Electro-optomechanical transduction & Quantum hard-sphere model for dissipative Rydberg-EIT media

PhD thesis

Emil Zeuthen

Niels Bohr Institute (NBI)
Faculty of Science
University of Copenhagen, Denmark
Supervisor: Prof. Anders S. Sørensen

This thesis has been submitted to
the PhD School of The Faculty of Science, University of Copenhagen

Contents

0.1 Abstract

This theoretical thesis consists of two parts which concern rather different topics belonging to the field of quantum optics.

Part I: Electro-optomechanical transduction

Using the techniques of optomechanics, there has been significant recent progress in coupling nano- and micro-scale mechanical oscillators to electromagnetic radiation modes ranging from radio to optical frequencies. By arranging two such couplings in tandem, a high-Q mechanical oscillator can serve as an efficient transducer between electromagnetic modes of different frequencies. This approach has successfully been exploited for frequency conversion of classical signals [1] and also has the potential of enabling quantum state transfer between superconducting circuitry and traveling optical signals.

In this thesis we present a detailed theoretical description of the interconversion between itinerant radiation modes using an intermediary mechanical mode. In order to characterize the performance of such transducers, suitable figures of merit must be established. We find here that a transducer can be characterized by two key parameters, the signal transfer efficiency η and added noise N. In terms of these, we evaluate its performance in various tasks ranging from classical signal detection to quantum conversion for quantum communication and information processing applications.

Having established the requirements for a transducer to perform efficiently, we turn to the question of optimizing the design of electro-optomechanical transducers in order to meet these demands. Moreover, given the hybrid nature of such systems, it is desirable to find a common framework for describing their dynamics. We address these questions by developing a unifying equivalent-circuit formalism for electro-optomechanical transducers, allowing us to optimize the design parameters of the transducer for its specific purpose. The equivalent circuit approach is suited for integrating the novel optomechanical transduction functionality into the well-established framework of electrical engineering, thereby facilitating its implementation in potential real-world applications such as nuclear magnetic resonance imaging (NMRI) and radio-astronomy. We consider such optomechanical sensing of weak electrical signals in detail using the equivalent circuit formalism to optimize the electrical circuit design.

Part II: Quantum hard-sphere model for dissipative Rydberg-EIT media

Effective photon-photon interactions can be engineered by combining long-range Rydberg interactions between atoms in a cold, optically dense cloud with light fields propagating under the condition of electromagnetically induced transparency (EIT). This can lead to strong and non-linear dissipative dynamics at the quantum level that prevent slow-light polaritons from coexisting within a blockade radius of one another.

Extending the work of Ref. [2], we introduce a new approach to analyzing this challenging quantum many-body problem in the limit of large optical depth

per blockade radius $d_b \gg 1$. The idea is to separate the single-polariton EIT physics from the Rydberg-Rydberg interactions in a serialized manner while using a hard-sphere model for the latter. We use our approach to analyze the saturation behavior of the transmission through one-dimensional Rydberg-EIT media in the experimentally relevant regime of non-perturbative single-polariton EIT-decay and compare our findings to recent experimental data. Next, we analyze a scheme for generating regular trains of single photons from continuous-wave input in the limit of perturbative single-polariton EIT-decay and derive its scaling behavior with d_b.

0.2 Resumé

Denne teoretiske afhandling består af to dele, der beskæftiger sig med forskellige emner inden for forskningsområdet kvanteoptik.

Del I:
Elektro-optomekanisk frekvensomformning

Ved at udnytte optomekanikkens metoder er der i de senere år gjort betydelige fremskridt med hensyn til at koble mekaniske oscillationer på nano- eller mikroskala til elektromagnetiske svingninger i et stort spektrum, der strækker sig fra radiobølger til synligt lys. På denne vis er det lykkedes at frekvensomforme klassiske radiosignaler [1] og metoden kan potentielt set benyttes til at overføre en kvantetilstand fra et superledende kredsløb til et optisk signal (og omvendt).

I denne afhandling præsenteres en detaljeret teoretisk beskrivelse af frekvensomformning mellem elektromagnetiske felter ved brug af et mekanisk mellemled. For at karakterisere ydeevnen for sådanne omformere må dertil passende parametre defineres. Vi finder her at vi kan karakterisere omformere ved deres signaloverførselseffektivitet η og tilføjede støj N. Udtrykt ved disse parametre evaluerer vi ydeevnen med henblik på en række anvendelser, deriblandt detektion af klassiske signaler og frekvensomformning på kvanteniveau med relevans for kvantekommunikation.

Efter således at have klarlagt kravene til en frekvensomformers ydeevne, betragter vi den optimeringsopgave der består i at få elektro-optomekaniske omformere til at leve op til disse. Eftersom disse omformere er hybrider af elektriske, optiske og mekaniske elementer, er det ydermere ønskværdigt at finde en samlet beskrivelse af disse. På denne baggrund udleder vi en ækvivalenskredsløbsformalisme for sådanne systemer som udgør et bekvemt værktøj til at optimere deres udformning med henblik på ydeevnen i en given anvendelse. Kredsløbsbilledet er velegnet til at anskueliggøre hvorledes optomekanisk omformning kan implementeres i konventionel elektronik og har potentielle anvendelser indenfor Magnetisk Resonans (MR) skanning og radioastronomi. Vi analyserer derfor optomekanisk detektion af svage elektriske signaler og anvender kredsløbsformalismen til at optimere udformningen af det elektriske kredsløb.

Del II:
Kvantekuglemodel for dissipative Rydberg-EIT-medier

Effektive vekselvirkninger mellem fotoner kan opnås ved at kombinere den langtrækkende Rydberg-vekselvirkning mellem atomer i en kold, optisk tæt sky med lysfelter der propagerer takket være elektromagnetisk induceret gennemsigtighed (EIT). Dette kan føre til en stærk og ikke-lineær dynamik på kvanteniveau der forhindrer fotoner i at befinde sig inden for en blokaderadius af hinanden.

Ved at bygge videre på Ref. [2] introducerer vi en ny tilgang til at analysere dette udfordrende mangelegemeproblem i grænsen hvor den optiske dybde per blokaderadius er stor, $d_\mathrm{b} \gg 1$. Idéen er at adskille enkeltfotonfysikken fra Rydberg-Rydberg-vekselvirkningerne på seriel vis og hvor sidstnævnte modelleres i stil med spredning af stive legemer. Vi anvender denne model til at analysere mætningen af transmissionen gennem endimensionelle Rydberg-EIT-medier i den eksperimentelt relevante grænse hvor EIT-henfald af enkelte fotoner spiller en stor rolle og sammenligner efterfølgende vores forudsigelser med eksperimentelle data. Derefter analyserer vi en metode til at generere pulstog af enkelte fotoner ud fra en Poisson-fordelt lyskilde i grænsen hvor EIT-henfald af enkelte fotoner spiller en mindre rolle, og vi udleder hvorledes metodens ydeevne skalerer med d_b.

0.3 Acknowledgments

This thesis is the third I complete under the supervision of Anders Sørensen, who deserves praise for being a most conscientious supervisor always willing to aid his students in their scientific woes. The collaboration with the inhabitants of the Quantum Membrane Lab at NBI have had a decisive influence on how my PhD study has unfolded. In particular, my discussions with Tolga Bagci, Anders Simonsen, Albert Schließer and Yeghishe Tsaturyan have taught me a lot about electro- and optomechanics in experimental reality. I would also like to acknowledge our collaborator Silvan Schmid from DTU in this context. As another important collaborator on the electro-optomechanics project, I would like to acknowledge Jake Taylor and thank Jake and the Joint Quantum Institute (JQI) at the University of Maryland for hosting me for my PhD exchange.

The work on Rydberg-EIT physics is part of an ongoing collaboration with Alexey Gorshkov, Michael Gullans and Mohammad Maghrebi, that was initiated when I was visiting the JQI. Our boisterous and youthful science sessions are among my fondest memories from my time in Maryland. I would also like to thank the Vuletić group for providing me with their experimental data and, in particular, Qi-Yu Liang, Jeff Thompson and Vladan Vuletić for discussions and details on the workings of the experiment.

During my approximately seven years as part of the QUANTOP family at the Bohr Institute, I have had the pleasure of meeting many talented, sweet and exotic people too numerous to mention exhaustively here. Let me thank the members of The Unresolved Sideband for our transformative experiences playing music together: William Nielsen, Andi Barg, Anne Fabricant, Miguel Carro, Jörg Helge Müller and last but not least our own rugged Frank Sinatra, Eugene Polzik. I am grateful to my *petit frère* Jean-baptiste Béguin for his good company and his wisdom in science and life alike. I would also like to thank my many good colleagues in the theory group for inspiring discussions: Anna Grodecka-Grad, Eran Kot, Florentin Reiter, Johannes Borregaard, Sumanta Das, Sasha Kyriienko, Ivan Iakoupov and Johan Ott. Special appreciation goes to my girlfriend Molly for her patience and support – it is not always easy to be the wife of a physicist.

Finally, an acknowledgment of the citizens of the European Union, who have funded my PhD study via The European Union Seventh Framework Programme through SIQS (Grant No. 600645) and ERC Grant QIOS (Grant No. 306576).

0.4 Publications

- Silvan Schmid, Tolga Bagci, Emil Zeuthen, Jacob M. Taylor, Patrick K. Herring, Maja Cassidy, Charles M. Marcus, Luis Guillermo Villanueva, Bartolo Amato, Anja Boisen, Yong Cheol Shin, Jing Kong, Anders S. Sørensen, Koji Usami, and Eugene S. Polzik
  Graphene on silicon nitride for optoelectromechanical micromembrane resonators
  [*J. Appl. Phys.* **115**, 054513 (2014)], referenced as [3].

- T. Bagci, A. Simonsen, S. Schmid, L. G. Villanueva, E. Zeuthen, J. Appel, J. M. Taylor, A. Sørensen, K. Usami, A. Schliesser, E. S. Polzik
  Optical detection of radio waves through a nanomechanical transducer
  [*Nature* **507**, 8185 (06 March 2014)], referenced as [1].

Part I

Transduction and its implementation in electro-optomechanical systems

Chapter 1

Introduction to transduction and electro-optomechanics

This chapter will provide the background and motivation for Part I of the thesis. In Section 1.1, recent experimental and theoretical developments regarding transduction in the realm of quantum optics will be reviewed. Next, in Section 1.2, we will discuss the physical mechanisms that allow efficient coupling between a mechanical mode and electromagnetic fields of various frequencies. Used in combination they form the basis for electro-optomechanical hybrid systems and we will provide an overview of the transduction physics of such devices. Having reviewed current research in transduction and the physical principles behind it, we give in Section 1.3 an overview of the work to be presented in the remaining chapters of Part I.

1.1 Transduction

1.1.1 Motivation and experimental review

Frequency conversion of signals is an ubiquitous task in electronics and optics applications, respectively. Moreover, interconversion between the electrical and optical parts of the electromagnetic spectrum is of utmost technological importance as the essential process enabling, e.g., long-distance fiber-based telecommunications forming the backbone of the Internet. With the conception of quantum communication and computing, frequency conversion has received renewed interest as an important ingredient in realizing an optically based "quantum internet" among quantum computers [4]. This imposes much more demanding requirements on the conversion process than in the case of the classical communication. Recently, a promising path towards frequency-conversion which can be extended to the quantum level has been demonstrated in Refs. [5, 1, 6] and is provided by coupling electromagnetic radiation to nano- or micro-scale mechanical oscillators (with typical resonance frequencies in the MHz-GHz range), as pursued in the field of *cavity optomechanics* [7, 8]. Such interaction can be made very efficient in the sense that it has enabled cooling of an individual mechanical oscillation mode to the vicinity of its quantum ground state [9, 10, 11, 12] as well as reversible coherent state transfer from electromagnetic fields into such a mechanical mode [13]. Remarkably, this coupling technique may be applied in a wide range of the electromagnetic spectrum and has seen a variety of implementations in both electrical circuits operating at radio [14, 15] or microwave [16, 9, 10] frequencies as well as in optical cavities [11, 12]. The universality of the coupling technique furthermore allows for hybrid systems involving several radiation modes with potentially different frequencies interacting with a common mechanical mode [17, 18, 19, 20]. Such hybrid devices have applications in the quantum-limited optical detection of weak electrical signals [19] such as in nuclear magnetic resonance imaging and radio astronomy. They are also envisioned to play an important role as transducers in quantum information processing including conversion between stationary and flying qubits in quantum networks [21]. At the classical level, such mechanically mediated transduction has already been realized with input and output modes both in the optical domain in optomechanical crystals [22] and silica microspheres [23] or discs [24], and with input and output modes respectively in the optical and the radio-frequency [1] or microwave domain [5, 6]. Although quantum-level transduction has yet to be achieved in these systems, they offer a promising alternative to electro-optic modulation, which is the established technique for classical signal conversion between the electrical and the optical domain, involving no intermediate mechanical resonance. While in principle quantum operation can be achieved in such systems [25], obtaining a quantum efficiency approaching unity has yet to be realized experimentally (see Refs. in [6]).

1.1.2 Steady-state transduction of itinerant signals

In the previous section we introduced the basic ideas behind mechanically mediated transduction. Within this general setting there are, however, a number of different ways in which the transducer can be operated. The bias optical and electrical frequency fields need to be oscillating in time to bridge the frequency gaps, but in addition their amplitudes can be varied in time. A variety of schemes for choosing the drive field parameters, including their time-dependence, have been discussed. In the simplest possible scheme, *steady-state transduction*, the cavity-mechanical coupling strengths are kept constant throughout the process [18]. This mode of operation is experimentally convenient and does not require knowledge of the temporal mode of the input. If, on the other hand, we have knowledge of the temporal input mode, this can be exploited to further enhance signal transduction as compared to the noise (in particular that of mechanical origin). This can be done either by sequential swap operations [26] or by adiabatically modulating coupling parameters in time, i.e. either the cavity-mechanical couplings strengths as in a STIRAP procedure [27, 28, 29] or one of the drive field detunings [30]. Contrary to the steady state transduction, however, all of these time-modulated approaches require strong cavity-mechanical coupling $g \gg \kappa$ to effectively suppress the mechanical noise (here, g is the annihilation operator coupling rate and κ is the decay rate of the cavity). Yet a different approach is to operate the transducer as a parametric amplifier by tuning one of the drive fields to the blue mechanical sideband. In this way, a traveling two-mode squeezed microwave-optical state can be generated, which may subsequently be used for continuous-variable state transfer by teleportation [31].

As mentioned above varying the control parameters in time may offer certain advantages, but for simplicity we restrict ourselves to steady state operation. That such a scheme may accommodate efficient transfer of itinerant signals can be attributed to the existence of a dark mode with respect to mechanical dissipation [27, 28]. This effect is known as optomechanically induced transparency (OMIT) [32, 33, 34] and leads to the suppression of mechanical noise in the transducer output. In the following, we will review some important results for this scheme that have appeared before in the context of a chain of three coupled oscillators. Since the steady-state transduction scenario can be described by coupled linear equations with constant coefficients, the system is easily solvable in the Fourier domain. The transduction chain can be biased towards an effective beam splitter interaction by red-detuning the drive fields by the mechanical frequency, $\Delta_i = -\omega_\mathrm{m}$ (as will be discussed later in more detail). Assuming furthermore the resolved-sideband regime, the chain of three coupled bosonic oscillators obeys the equations of motion (in an appropriately rotating frame),

$$\begin{aligned}
\dot{\hat{a}} &= -\frac{\gamma_1}{2}\hat{a} - ig_1\hat{b} - \sqrt{\eta_1\gamma_1}\hat{a}_\mathrm{in} - \sqrt{(1-\eta_1)\gamma_1}\hat{a}'_\mathrm{in} \\
\dot{\hat{b}} &= -\frac{\gamma_{\mathrm{m},0}}{2}\hat{b} - ig_1\hat{a} - ig_2\hat{c} - \sqrt{\gamma_{\mathrm{m},0}}\hat{b}'_\mathrm{in} \\
\dot{\hat{c}} &= -\frac{\gamma_2}{2}\hat{c} - ig_2\hat{b} - \sqrt{\eta_2\gamma_2}\hat{c}_\mathrm{in} - \sqrt{(1-\eta_2)\gamma_2}\hat{c}'_\mathrm{in}.
\end{aligned} \tag{1.1}$$

Here the bosonic operator $\hat{b}$ represents the mechanical mode (with intrinsic damping rate $\gamma_{m,0}$) coupled to the cavity (or circuit) modes $\hat{a}, \hat{c}$ at rates g_1, g_2 (assumed real). Each of the latter modes ($i \in \{1,2\}$) decay at a rate γ_i with external coupling efficiency η_i. Signal and noise inputs are represented by operators $\hat{a}_\mathrm{in}, \hat{c}_\mathrm{in}$ and $\hat{a}'_\mathrm{in}, \hat{b}'_\mathrm{in}, \hat{c}'_\mathrm{in}$ respectively. The resolved-sideband condition in terms of the mechanical frequency ω_m is $\gamma_i/(4\omega_\mathrm{m}) \ll 1$, $i \in \{1,2\}$. For transduction, it is desirable to have a near-unity signal transfer efficiency η and a small amount of added noise N (to be defined below), however, the relative importance of these quantities depends on the particular application in which the transducer enters. In the case of the 3-oscillator chain, (1.1), the peak signal transfer efficiency $\eta_0^{(+)}$ from the external port of $\hat{a}$ to that of $\hat{c}$ (or vice versa) is [29, 28, 23, 22]

$$\eta_0^{(+)} = \eta_1\eta_2\frac{4\mathcal{C}_1\mathcal{C}_2}{(1+\mathcal{C}_1+\mathcal{C}_2)^2}, \tag{1.2}$$

where $\mathcal{C}_i \equiv 4g_i^2/(\gamma_{m,0}\gamma_i)$ is the cooperativity between the mechanical mode and cavity $i \in \{1,2\}$. Eq. (1.2) shows that unit signal conversion efficiency requires the simultaneous fulfillment of three conditions: 1) impedance matching the transducer chain, $\mathcal{C}_1 = \mathcal{C}_2$, 2) overwhelming the intrinsic mechanical dissipation rate, $\mathcal{C}_i \gg 1$, and 3) overcoupling of the cavities, $\eta_i \to 1$, for $i \in \{1,2\}$. The first two conditions can be understood intuitively noting that in the fully-resolved sideband regime the cooperativities $\mathcal{C}_i$ are dimensionless versions of the rates $\gamma_{\mathrm{m},i} \equiv \mathcal{C}_i\gamma_{\mathrm{m},0}$ at which a narrow-band signal is transferred between cavity i and the mechanical mode. From this point of view Eq. (1.2) can be seen as the competition between inducing a transfer rate through the mechanical mode (the numerator) and the ensuing associated broadening of the mechanical mode that tends to decrease the coupling (the denominator, which is the square of the effective dimensionless width of the mechanical mode). If conditions 1) and 2) are fulfilled, $\mathcal{C}_1 = \mathcal{C}_2 \gg 1$, the intrinsic mechanical loss (represented by the

'1' in the denominator) drops out of Eq. (1.2) leaving $\eta_0^{(+)} \to \eta_1\eta_2$; hence unit conversion efficiency is possible if $\eta_1, \eta_2 \to 1$.

It is important to stress that $\eta_0^{(+)}$ approaching unity is in itself insufficient to conclude that the transducer can operate coherently at the single-photon level. A full analysis must also consider the noise N added by the transducer, as a perfectly transduced signal photon is useless if swamped by a multitude of (transduced) noise photons. Moreover, outside the resolved sideband regime the efficiency $\eta_0^{(+)}$ can even exceed unity at the cost of amplification noise. Additionally, we remark that the signal transfer efficiency $\eta_0^{(+)}$ is of secondary importance for some transducer applications. These aspects will be treated in detail in a subsequent chapter.

1.2 Electro-optomechanics

1.2.1 Physics of cavity-mechanical interfaces

The physical basis for the transduction processes to be considered here is the force exerted by electromagnetic radiation on mechanical objects; in turn, mechanical deflection will affect electromagnetic fields whereby mutual interaction may result. As this phenomenon pertains, in principle, to any wavelength in the spectrum, this system allows a mechanically mediated cross-coupling between electromagnetic modes [17]. In this way, a mechanical element may serve as a link between two electromagnetic fields. As we will describe in some detail, it is in general advantageous to couple the mechanical element to the input and output fields via appropriate electromagnetic cavities (or circuits) rather than directly to these itinerant fields.

To illustrate the notion of a cavity-mechanical interface between itinerant electromagnetic modes, we now turn to a concrete implementation of electro-optomechanical transduction as proposed in Ref. [19] and realized in Refs. [5, 1, 6]. The setup is illustrated in Fig. 1.1: Traveling radio or microwave frequency photons are fed to an LC circuit via a transmission line of characteristic impedance Z_{tx}. A mechanical mode of high quality factor ($Q_{\mathrm{m}} \gg 1$) is coupled capacitively to the LC circuit, whereby charge fluctuations in the circuit and mechanical vibrations become coupled. An electrical DC or AC source (not shown) induces a macroscopic steady-state charge (for DC bias) or charge oscillations (for AC drive) on the capacitor; since the electromechanical (EM) interaction is non-linear (as we will return to below) this will enhance the effect of the small (possibly quantum) fluctuations induced by a signal arriving via the transmission line. Effectively, these signal fluctuations in the circuit will thus see an enhanced linear coupling with the mechanical motion. Moreover, in the case where mechanical and circuit resonances do not coincide in frequency, the AC drive field will supply the energy necessary to convert between these two different frequencies. At the same time, the mechanical mode is read out optically through its coupling to the field fluctuations in the optical cavity. A laser drive (not shown) populates the cavity to enhance the effective linear coupling to the mechanical mode, while also ensuring energy conservation in a manner analogous to the AC-driven EM interface.

Mathematically, the essential physics of both radiation fields and mechanical motion are captured by a harmonic oscillator formulation; hence the transduc-

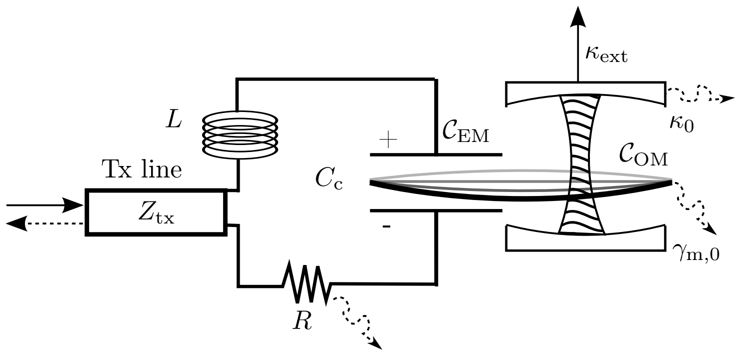

Figure 1.1: Sketch of an electro-optomechanical transduction apparatus. A mechanical vibration mode of a micromembrane couples simultaneously to both charge fluctuations in the electrical circuit (left) and intensity fluctuations of the optical cavity (right) thereby enabling transduction between electrical and optical frequencies (here using an optomechanical membrane-in-the-middle configuration [35]). Electrical and optical sources that bridge the frequency gaps are not shown. The input signal enters from the left via a transmission line of characteristic impedance Z_{tx}. A fraction of the signal is reflected due to impedance mismatch (dashed arrow on the left). The electrical circuit (left) is characterized by the inductance L, the coupling capacitance C_{c}, and ohmic resistance R; this corresponds to an electrical coupling efficiency of $\eta_{\mathrm{el}} = Z_{\mathrm{tx}}/(Z_{\mathrm{tx}} + R)$. The optical cavity (right) has external coupling rate κ_{ext} and intrinsic loss κ_0, corresponding to an optical coupling efficiency of $\eta_{\mathrm{opt}} = \kappa_{\mathrm{ext}}/(\kappa_{\mathrm{ext}} + \kappa_0)$. The electromechanical and optomechanical coupling strengths are quantified by the cooperativity parameters $\mathcal{C}_{\mathrm{EM}}$ and $\mathcal{C}_{\mathrm{OM}}$, respectively. The mechanical mode has intrinsic damping rate $\gamma_{\mathrm{m},0}$. Damping losses are represented by wavy, dashed arrows.

tion process can be thought of as the successful propagation of an incoming signal through a cascade of coupled oscillators yielding, ideally, an unperturbed but frequency-converted outgoing signal (as in the example given above, Eqs. (1.1)). The coupled oscillator model considered here is rather general and has previously been used to model optical-to-optical [23] and electrical-to-optical [6] transduction (or its reverse). The mapping of an electro-optomechanical system to an oscillator model can be easily understood for the setup depicted in Fig. 1.1, i.e. a serial RLC circuit coupled to a single mechanical mode which is, in turn, coupled to a single mode of an optical cavity; this is simply a string of three linearly coupled harmonic oscillators with the signal entering the first and leaving through the last. On the other hand more complex electrical circuits are often used and part of the motivation for the work to be presented below is to be able to deal with a more general class of electrical circuits.

1.2.2 Parametric cavity-mechanical couplings

In this section we will elaborate on the introductory description of cavity-mechanical coupling given in Section 1.2.1 and illustrated in Fig. 1.1. We do this by introducing a Hamiltonian description of the electromechanical (EM) and optomechanical (OM) couplings, highlighting the formal equivalence between the two.

We will now consider the nature of these cavity-mechanical couplings. They can be characterized as parametric in the sense that one or more canonical variables of the mechanical mode modulate a cavity parameter. In the typical coupling scheme, one arranges for the canonical position of a mechanical mode to modulate the cavity resonance frequency, i.e. a dispersive coupling, but other approaches have been considered including dissipative coupling [36] and mechanical multimode schemes [37, 38, 39]. In this thesis we will mainly focus on dispersive cavity couplings involving a single mechanical mode, although several of the ideas developed here likely to be extendable to accommodate other kinds of parametric couplings as well as multiple mechanical modes.

The standard parametric cavity-mechanical interaction Hamiltonian can be arrived at in a perturbative fashion by Taylor-expanding the mechanically modulated parameter around the classical steady state configuration of the hybrid system. For the canonical optomechanical setup consisting of an optical cavity (of which we confine attention to a single mode of frequency ω_c) with a movable mirror (described by canonical position operator $\hat{x}$), we may in this way find the radiation pressure Hamiltonian from that of a single optical mode (described by the field annihilation operator $\hat{a}$) as [7]

$$H_\mathrm{cav} = \hbar\omega_\mathrm{c}(\hat{x})\hat{a}^\dagger\hat{a} \approx \hbar\left[\omega_{\mathrm{c},0} + \left.\frac{d\omega_\mathrm{c}}{dx}\right|_{x=\bar{x}}\delta\hat{x}\right]\hat{a}^\dagger\hat{a}$$

hence this corresponds to an effective interaction Hamiltonian

$$H_\mathrm{OM} = \hbar\left.\frac{d\omega_\mathrm{c}}{dx}\right|_{x=\bar{x}}\delta\hat{x}\hat{a}^\dagger\hat{a}, \tag{1.3}$$

where $\bar{x}$ is the steady-state value of the position coordinate to which the mechanical fluctuations are referenced, $\delta\hat{x} \equiv \hat{x} - \bar{x}$. A more rigorous treatment shows that this is indeed the correct radiation pressure interaction Hamiltonian in the limit where the mechanical oscillation amplitude is small relative to the equilibrium cavity length and the mechanical frequency is small relative to the cavity mode spacing [40].

To derive the electromechanical coupling, we will again apply the simple perturbative procedure. Motivated by recent experiments [9, 37, 13, 1, 6], we will further specialize our treatment to capacitive coupling, i.e. a capacitor in the circuit has its capacitance modulated by a mechanical normal mode coordinate. Our approach should however work equally well for inductive coupling [41]. Expanding the charging energy of the capacitor (with capacitance C_c and canonical charge $\hat{Q}_\mathrm{c}$) yields

$$H_\mathrm{C} = \frac{\hat{Q}_\mathrm{c}^2}{2C_\mathrm{c}(\hat{x})} \approx \frac{\hat{Q}_\mathrm{c}^2}{2\bar{C}_\mathrm{c}} - \frac{1}{2}\frac{\hat{Q}_\mathrm{c}^2}{\bar{C}_\mathrm{c}^2}\left.\frac{dC_\mathrm{c}}{dx}\right|_{x=\bar{x}}\delta\hat{x} \tag{1.4}$$

from which we read off the capacitive coupling Hamiltonian

$$H_\mathrm{EM} = -\frac{1}{2}\frac{\hat{Q}_\mathrm{c}^2}{\bar{C}_\mathrm{c}^2}\left.\frac{dC_\mathrm{c}}{dx}\right|_{x=\bar{x}}\delta\hat{x}; \tag{1.5}$$

as above, $\hat{x}$ is a canonical position operator for the mechanical mode, $\bar{x}$ is its steady-state value, wrt. to which we define the mechanical fluctuations, $\delta\hat{x} \equiv \hat{x} - \bar{x}$, as in the optomechanical case; $\bar{C}_\mathrm{c} \equiv C_\mathrm{c}(\bar{x})$ denotes the steady-state value of the coupling capacitance. The notion of a position-dependent charging energy, presumed in Eq. (1.4), is meaningful in the quasi-electrostatic limit, where the electromagnetic field surrounding the capacitive element equilibrates much faster than the timescale of the mechanical modulation $2\pi/\omega_\mathrm{m}$. The physical mechanism underlying the position dependence in $C_\mathrm{c}(\hat{x})$ depends on the implementation; examples include the Kelvin polarization force from a inhomogeneous electric field on a dielectric mechanical element [15, 42], the electrostatic interaction with a conductive mechanical element [9, 10, 37, 34, 3], and the piezoelectric effect [16, 5], but the precise nature of the coupling is not important for this study.

1.2.3 Enhanced linearized interaction in presence of cavity drive fields

Now we discuss the important role played by drive fields. The cavity-mechanical interaction Hamiltonians (1.3) and (1.5) are non-linear in nature; for sensing or cooling purposes, however, linear interaction is typically desirable, in particular since they can be easily enhanced by applying strong classical drive fields to the cavity and the circuit. For an optical cavity, this can be achieved by adding a large mean intracavity field amplitude $\alpha e^{-i\omega_\mathrm{l}t}$, whereas for the mechanically coupled capacitor a charge response $\bar{Q}_\mathrm{c}(t)$ of large amplitude is induced (α is assumed real without loss of generality). By transforming to displaced dynamical variables corresponding to the fluctuations around the classical response to the drive fields,

$$\hat{x} \to \bar{x} + \delta\hat{x}, \quad \hat{Q}_\mathrm{c} \to \bar{Q}_\mathrm{c}(t) + \delta\hat{Q}_\mathrm{c}, \quad \hat{a} \to \alpha e^{-i\omega_\mathrm{l}t} + \delta\hat{a},$$

we can derive the effective Hamiltonians governing the interactions among the fluctuation variables $\delta\hat{x}, \delta\hat{Q}_\mathrm{c}, \delta\hat{a}$. For simplicity we assume a monochromatic electrical drive so as to induce a fluctuating charge on the coupling capacitor

$$\bar{Q}_{\mathrm{c}}(t) \equiv \begin{cases} \bar{Q}_{\mathrm{c},0} & \text{[DC bias]} \\ \bar{Q}_{\mathrm{c},0}[e^{i\omega_{\mathrm{d}}t} + e^{-i\omega_{\mathrm{d}}t}] & \text{[AC bias]} \end{cases}, \tag{1.6}$$

where ω_{d} is the frequency of the AC drive (we have taken $\bar{Q}_{\mathrm{c},0}$ to be real without loss of generality). Eq. (1.6) assumes that in the AC case we have a simple harmonic response in spite of (1.4) being non-linear. This will be the case if the mechanical response at frequencies $\geq 2\omega_{\mathrm{d}}$ is negligible leaving only a static displacement due to the mean force. Note that the notational convention for $\bar{Q}_{\mathrm{c}}(t)$ (1.6) implies that

$$\langle \bar{Q}_{\mathrm{c}}^2(t) \rangle = \begin{cases} \bar{Q}_{\mathrm{c},0}^2 & \text{[DC bias]} \\ 2\bar{Q}_{\mathrm{c},0}^2 & \text{[AC bias]} \end{cases}, \tag{1.7}$$

where $\langle \cdot \rangle$ denotes time-averaging over a period. Eqs. (1.3) and (1.5) lead to linear interaction among the fluctuation variables to lowest order in the latter:

$$H_{\mathrm{OM}}^{(\mathrm{lin})} \approx \frac{\hbar}{x_{\mathrm{ZPF}}} g_{\mathrm{OM}} \delta\hat{x}(e^{i\omega_{\mathrm{l}}t}\delta\hat{a} + e^{-i\omega_{\mathrm{l}}t}\delta\hat{a}^\dagger) \tag{1.8}$$

$$H_{\mathrm{EM}}^{(\mathrm{lin})} \approx G\delta\hat{Q}_{\mathrm{c}}\delta\hat{x} \cdot \begin{cases} 1 & \text{[DC bias]} \\ e^{i\omega_{\mathrm{d}}t} + e^{-i\omega_{\mathrm{d}}t} & \text{[AC drive]} \end{cases}, \tag{1.9}$$

where we have introduced the drive-enhanced cavity-mechanical OM and EM coupling parameters g_{OM} (units of s^{-1}) and G (units of V/m):

$$\begin{aligned} g_{\mathrm{OM}} &\equiv \alpha \left. \frac{d\omega_{\mathrm{c}}}{dx} \right|_{x=\bar{x}} x_{\mathrm{ZPF}} \\ G &\equiv -\frac{\bar{Q}_{\mathrm{c},0}}{\bar{C}_{\mathrm{c}}^2} \left. \frac{dC_{\mathrm{c}}}{dx} \right|_{x=\bar{x}}, \end{aligned} \tag{1.10}$$

with $x_{\mathrm{ZPF}} \equiv \sqrt{\hbar/(2m\omega_{\mathrm{m}})}$ being the mechanical zero-point amplitude in terms of the mechanical mass m and an appropriate mechanical frequency ω_{m} (including static shifts from the interaction as will be discussed later). We see from Eqs. (1.10) that the linear cavity mechanical interaction strengths are enhanced by the drive-induced intra-cavity amplitudes α and $\bar{Q}_{\mathrm{c},0}$, respectively.

Throughout we attempt to emphasize both the similarities and differences between DC- and AC-biased EM interfaces. Eq. (1.6) implies that in the AC-driven case we define $\bar{Q}_{\mathrm{c},0}$ to be half of the charge amplitude whereas in the DC case it is the full amplitude; this choice allows for a simpler presentation below. Physically, the factor of 1/2 by which the AC and DC definitions differ can be understood as a Rotating Wave Approximation penalty for AC operation; for $\omega_{\mathrm{m}} \ll \omega_{\mathrm{d}}$, any process in which the creation/annihilation of an electrical quantum is not accompanied by the annihilation/creation of a drive photon will be strongly energy non-conserving and hence suppressed; as a consequence only half the field amplitude will contribute.

The electromechanical coupling strength G introduced here will play a central role in several of the following chapters as it characterizes the strength of the interaction. An advantage of this quantity is that it can be meaningfully defined without specifying an electrical circuit resonance. Let us, however, discuss how G relates to the more familiar quantum optics system of two coupled quantum oscillators with coupling rate g. To relate the coupling strength G to this more familiar coupling rate g between bosonic annihilation and creation operators, we consider briefly the scenario where the electrical system is a serial RLC circuit as in Fig. 1.1 (but without the optical system). The electrical resonance frequency is $\omega_{\mathrm{LC}} = (L\bar{C}_{\mathrm{c}})^{-1/2}$, where L is the inductance and $\bar{C}_{\mathrm{c}}$ is the steady-state value of C_{c}. We then seek to express Eq. (1.9) as

$$H_{\mathrm{EM}}^{(\mathrm{lin})} \approx \hbar g(\delta\hat{a} + \delta\hat{a}^{\dagger})(\delta\hat{b} + \delta\hat{b}^{\dagger}), \tag{1.11}$$

in a suitably rotating frame (again assuming the mechanical response to be negligible at frequencies $\geq 2\omega_{\mathrm{d}}$ if AC-driven). Using that the quantized dynamical variables are given by $\delta\hat{x} = x_{\mathrm{ZPF}}(\delta\hat{a} + \delta\hat{a}^{\dagger})$ and $\delta\hat{Q}_{\mathrm{c}} = q_{\mathrm{ZPF}}(\delta\hat{b} + \delta\hat{b}^{\dagger})$, where $x_{\mathrm{ZPF}} \equiv \sqrt{\hbar/(2m\omega_{\mathrm{m}})}$ and $q_{\mathrm{ZPF}} = \sqrt{\hbar/(2L\omega_{\mathrm{LC}})}$, we find that Eqs. (1.9) and (1.11) are identical if

$$g = \frac{G x_{\mathrm{ZPF}} q_{\mathrm{ZPF}}}{\hbar} = \frac{G}{2\sqrt{L\omega_{\mathrm{LC}} m\omega_{\mathrm{m}}}}. \tag{1.12}$$

1.2.4 Energy conservation, sideband resolution and amplification effects

As mentioned several times above, the time dependence of drive fields is crucial in efficiently coupling oscillators of different frequencies. If the drive frequencies are chosen appropriately, then in a rotating frame wrt. these, the three subsystems can be made to oscillate at the same frequency. This occurs when red-detuning both drive fields by the mechanical frequency, see Fig. 1.2a. Hence, from this point of view, the operation of the transducer can be made energy conserving corresponding in the resolved-sideband regime to effective beam splitter interactions (where appropriate rotating frame annihilation and creation operators are introduced via $\delta\hat{x} = x_{\mathrm{ZPF}}(\delta\hat{b} + \delta\hat{b}^{\dagger})$ and $\delta\hat{Q}_{\mathrm{c}} = q_{\mathrm{ZPF}}(\delta\hat{c} + \delta\hat{c}^{\dagger})$)

$$\hat{H}_{\mathrm{int}} \sim \hbar g_{\mathrm{OM}}(\delta\hat{a}^{\dagger}\delta\hat{b} + \delta\hat{a}\delta\hat{b}^{\dagger}) + \hbar g_{\mathrm{EM}}(\delta\hat{b}^{\dagger}\delta\hat{c} + \delta\hat{b}\delta\hat{c}^{\dagger}) \tag{1.13}$$

and can thus operate efficiently. The Hamiltonian (1.13) results in the same type of coupling considered in Eqs. (1.1) above. This coupling technique allows bridging the energy gap between a mechanical oscillator and vastly different parts of the electromagnetic spectrum. Ideally, then, an incoming traveling electrical photon will be resonantly transmitted through the apparatus and finally leave as an optical photon (and vice versa) as in the all-optical analogy shown in Fig. 1.2b.

The above characterization is only correct in the fully resolved sideband regime, i.e. when the cavity susceptibilities are negligible for frequencies $\sim \omega_{\mathrm{d},i} - \omega_{\mathrm{m}}$ as compared to frequencies $\sim \omega_{\mathrm{d},i} + \omega_{\mathrm{m}}$, where $\omega_{\mathrm{d},i}$ are the respective drive field frequencies (see Fig. 1.3). The degree of sideband resolution can be quantified by the ratios $\gamma_{\mathrm{LC}}/(4\omega_{\mathrm{m}})$ and $\kappa/(4\omega_{\mathrm{m}})$. If either of these differ appreciably from zero, the presence of the lower sideband will introduce parametric signal amplification alongside the beam splitter interaction. Moreover, (signal) squeezing will occur: Lack of sideband resolution for the input cavity will cause the output to be a mixture of frequency components of the upper and lower

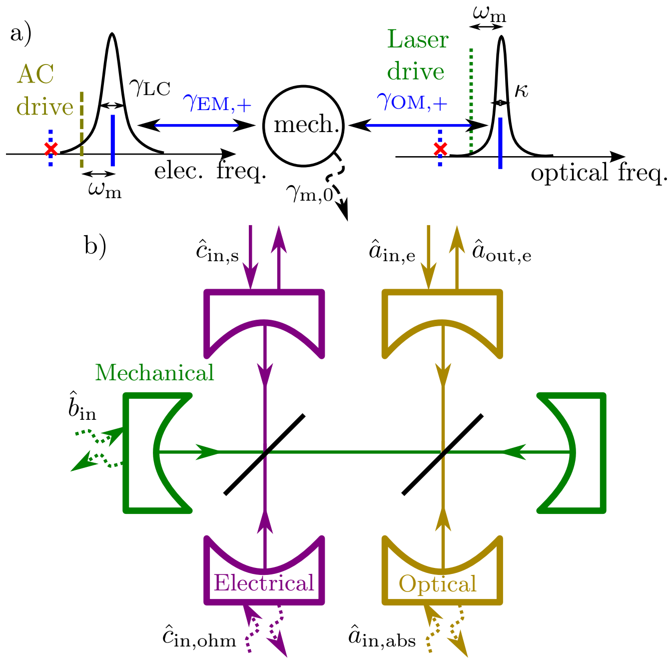

Figure 1.2: a) Circuit and cavity line shape functions of widths γ_{LC} and κ in the fully EM and OM resolved-sideband regime entailing beam splitter interaction, Eq. (1.13), when operated red-detuned by $-\omega_{\mathrm{m}}$ inducing anti-Stokes rates $\gamma_{\mathrm{EM},+}$ and $\gamma_{\mathrm{OM},+}$. b) Cascaded optical beam splitter analogy for the interaction Hamiltonian (1.13) between optical ($\delta\hat{a}$), mechanical ($\delta\hat{b}$) and electrical ($\delta\hat{c}$) modes. The input and output fields associated with signal and noise ports are indicated.

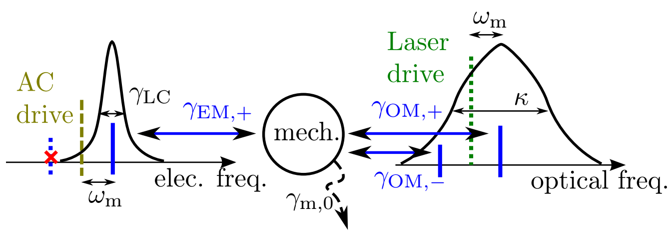

Figure 1.3: Scenario similar to Fig. 1.2a, but where the EM sidebands are resolved while the OM ones are not (both are operated red-detuned by $-\omega_{\mathrm{m}}$). Under these circumstances an electrical input signal at the electrical cavity resonance will be upconverted in a 1:2 fashion, appearing at both OM sidebands reflecting simultaneous anti-Stokes and Stokes processes. The mechanical coupling to the lower optical sideband moreover leads to parametric amplification at the price of increased optical noise.

(input) sidebands. Signal amplification may be desirable but will in general result in additional added noise [43]. The signal squeezing is unwanted in typical quantum transduction schemes, but can be exploited for teleportation-based transduction as mentioned previously.

In terms of cavity and electrical frequencies, the scenarios we consider will have either 1) The electrical signal frequency coinciding with the mechanical resonance frequency, in which case a DC electrical bias should be applied, or 2) The electrical signal frequency ω_{s} being much larger than the mechanical frequency, $\omega_{\mathrm{s}} \gg \omega_{\mathrm{m}}$, in which case an AC electrical drive of frequency $\omega_{\mathrm{d}} \sim \omega_{\mathrm{s}} - \omega_{\mathrm{m}}$ should be applied. For MHz mechanical oscillators, the former driving scheme is relevant for the transduction of radio-frequency signals (at MHz), while the latter applies to microwave transduction (at GHz). On the other hand, if a mechanical oscillator resonant in the GHz domain is used, direct (DC biased or piezoelectric) conversion to microwave radiation can be achieved.

1.2.5 Loss channels and noise sources

Finally, we briefly consider the loss and noise processes competing with the desired signal transduction. For studying cavity-mechanical transducers, an important part of the analysis is to consider damping and reflection losses and the associated noise inputs. The absolute frequencies of the subsystems of the transducer are important since they set the occupancies of the thermal reservoirs, $n(\omega) \approx k_{\mathrm{B}}T/(\hbar\omega)$, where ω is the bare (angular) signal frequency of the subsystem in question. In this sense, the thermal reservoir of the optical cavity is "cold" even at room temperature (vacuum fluctuations, to excellent approximation). In comparison, the occupancies of the thermal reservoirs coupled to the mechanical and electrical degrees of freedom (MHz or GHz), respectively, are typically much more severe. Hence, transduction is an inherently non-equilibrium situation.

Loss channels of the optical cavity include internal absorption and mode mismatch, with vacuum noise leaking in accordingly. The electrical cavity may suffer from ohmic losses resulting in Johnson noise leaking in. The mechanical oscillator will suffer from damping such as clamping losses, although this loss channel can be mitigated by phononic bandgap engineering [44, 45]. Additionally, reflection may occur due to lack of impedance matching in the transducer and amplification noise may arise due to finite sideband resolution in the AC-driven case. In summary, the various complications mentioned above conspire to make transduction a non-trivial optimization problem even within the linearized theory considered here.

1.3 Overview of Part I

Above we have reviewed recent experiments realizing transduction in hybrid systems involving a mechanical mode. We also discussed the basic physical mechanisms underlying them as well as some of the detrimental effects preventing ideal transduction in such systems. Part I of this theoretical thesis explores different aspects concerning the implementation of transduction in electro-optomechanical hybrid systems, but also considers transduction more generally. The presentation of the work is organized in four chapters:

Chapter 2: Framework for calculating electromechanical couplings This chapter establishes the details of the electromechanical coupling. We then present a simple procedure for calculating mode-specific coupling strengths and induced mechanical frequency shifts for electromechanical interfaces. While these quantities could be extracted from more cumbersome finite-element simulations, our approach provides intuition about the influence of geometry and material choices and requires little or no input from numerical simulations. The method has been applied in recent experiments involving vibrating micromembranes [3, 1].

Chapter 3: Figures of merit for transduction Before considering the specifics of electro-optomechanical transduction, we give a general discussion of linear transducers. Staring from the scattering matrix of a linear transducer, we characterize it generically in terms of its signal transfer efficiency and added noise temperature. To make connection to the language of quantum optics, we consider how these figures of merit are related to conditional and unconditional state fidelities and heterodyne sensitivity. These relations establish the requirements on a transducer for it to perform efficiently in various applications and show that the noise temperature of the transducer tends to be more important than its signal transfer efficiency.

Chapter 4: Equivalent circuit formalism for electro-optomechanics Focusing henceforth on electro-optomechanical transduction, we introduce an equivalent circuit formalism for electro-optomechanical transducers, thereby integrating the transduction functionality of optomechanical systems into the toolbox of electrical engineering. This unifying impedance description naturally accommodates the amplification effects that arise due to finite cavity-mechanical sideband resolution and which are crucial in analyzing transduction in the quantum regime. The formalism allows us to determine the scattering matrix of the transducer using standard circuit analysis, and from this we can assess the performance of the transducer as discussed in the preceding chapter.

Chapter 5: Optimizing electro-optomechanical receiver circuits Here we apply the equivalent circuit formalism as a design tool to optimize electro-optomechanical transduction. In particular, we focus on optimizing the optical detection of weak radio or microwave signals, considering both classical and quantum regimes. By evaluating the figure of merit for this and other transducer applications (discussed in a previous chapter), we can assess the feasibility of electro-optomechanical transduction in various scenarios.

Chapter 2

Framework for calculating electromechanical couplings

The work presented in this chapter has been carried out in collaboration with Jacob M. Taylor and Anders S. Sørensen.

2.1 Introduction

The introductory chapter touched upon the basic principles for achieving efficient electromechanical (EM) coupling. In this chapter we will revisit these ideas in the context of actual interface geometries that have appeared in recent experiments and discuss their characterization. We present a simple procedure for calculating mode-specific coupling strengths and induced mechanical frequency shifts for electromechanical interfaces involving 2-dimensional mechanical modes. These quantities could be extracted from full numerical simulations, but our analytical approach is calculationally simpler and provides a direct intuition about the influence of geometry on the coupling. The method presented here has already proven useful in the analysis of recent experiments [3, 1] involving vibrating micromembranes.

2.1.1 Overview of chapter

We present our approach to characterizing EM interfaces in two steps. First, in Section 2.2, we formulate the generic scenario of interest: a circuit resonance for which the capacitance is modulated by the motion of a mechanical oscillator. The capacitance in question thus arises from the combined configuration of both electrical and mechanical elements. In terms of this effective capacitance, C_{eff}, we can derive perturbative formulas for coupling strengths and frequency shifts. Second, in Section 2.3, we discuss how C_{eff} and its derivatives can be calculated efficiently by decomposing the capacitive interface into small unit cells. Example geometries from recent experiments are discussed in Section 2.4 followed by concluding remarks in Section 2.5.

2.2 Capacitive electromechanical interfaces

Here we will establish a Hamiltonian description of the electromechanical system, revisiting the calculation from the introductory Section 1.2.2. With careful attention to the mechanical and electrical modes involved in the interaction, we will perturbatively derive formal expressions for the coupling parameters of interest. These are the coupling strengths and mechanical frequency shifts induced by the interaction.

2.2.1 Overview of capacitively coupled systems

To begin our discussion of capacitive electromechanical coupling, we consider first the paradigmatic parallel plate capacitor. It consists of two conductive plates of small separation d compared to the transverse dimensions. Its capacitance is given by

$$C = \frac{\epsilon A}{d}, \tag{2.1}$$

where ϵ is the electrical permittivity of the separating medium and A is the area of each plate. The energy stored in the capacitor when the plates carry charge $\pm Q$, respectively, is

$$H'_{\mathrm{C}} = \frac{Q^2}{2C}. \tag{2.2}$$

We now extend this well-known scenario to the situation illustrated in Fig. 2.1a. Here, the upper plate has been mounted on a (conductive) spring allowing displacements along the normal of the plates. Hence, the plate separation is now $d = \bar{d} + \delta z$, where $\bar{d}$ is the equilibrium separation and δz is the spring displacement relative to equilibrium. This leads to the capacitance, (2.1), acquiring a dependence on the spring displacement δz, $C \to C(\delta z)$. In turn, this leads the charging energy (2.2) to depend on δz and, ultimately, coupling between the motion of the spring δz and the charge Q flowing to and from the capacitor (assumed to be connected to some electrical circuit).

While the plates of the parallel capacitor are 2-dimensional (2-d), the motion of the top plate considered in the scenario of Fig. 2.1a is essentially 1-d or, equivalently, corresponds to a flat 2-d mode. One of the main purposes of this chapter is to deal with generalizations of the simple 1-d scenario to arbitrary 2-d modes and their coupling to more involved capacitor geometries. As an example of such a scenario, consider the system depicted in Fig. 2.1b in which a 2-dimensional conductive membrane serves as one "plate" of a capacitor (the capacitor is part of an electrical circuit as will be relevant for the discussion of electrical biasing below). The effective capacitance of the circuit C_{eff} will hence depend on the (2-d) configuration $z(\vec{r})$ of the mechanical membrane, where $\vec{r} = (x, y)$ is a point in the plane of the membrane. In this case, the charging energy (2.2) takes the form

$$H_{\mathrm{C}} = \frac{Q^2}{2C_{\mathrm{eff}}[z(\vec{r})]}, \tag{2.3}$$

where C_{eff} is a functional of $z(\vec{r})$.

In the typical mode of operation, an electrical AC or DC voltage bias is applied to the circuit in order to enhance the electromechanical coupling, see

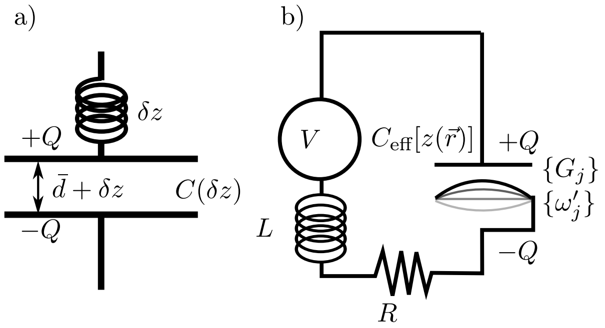

Figure 2.1: a) Parallel-plate capacitor where one plate has a one-dimensional vibratory degree of freedom δz around the steady-state separation $\bar{d}$ hence modulating the capacitance $C(\delta z)$ leading to coupling between δz and the charge on the plates Q. b) Illustration of an electromechanical system in which the vibrations of a 2-dimensional mechanical object with configuration $z(\vec{r})$ are capacitively coupled to the charge fluctuations Q in an electrical circuit. The circuit is a serial RLC resonance of resistance R, inductance L and with a voltage source V which biases the mechanically modulated capacitor $C_{\text{eff}}[z(\vec{r})]$. The interaction between the circuit and the mechanical vibration mode j is characterized by a coupling strength G_j and the effective mechanical frequency ω'_j.

Fig. 2.1b. This will induce a charge response $\bar{Q}(t)$ on the effective capacitor C_{eff} as has already been discussed in Section 1.2.3. This previous discussion carries over here, although in this chapter we will denote the amplitude of $\bar{Q}(t)$ by $\bar{Q}_{\text{c},0} \to \bar{Q}_0$. As previously, the charge amplitude $\bar{Q}_0$ is a large offset which serves to enhance the interaction and will appear in the expressions for the coupling strengths and effective frequencies below. Here we are interested in fluctuations δQ relative to the drive induced response $\bar{Q}(t)$,

$$\delta Q \equiv Q - \bar{Q}(t).$$

2.2.2 Mechanical vibrational modes

We now consider the mechanical system which couples to the capacitor, specializing to objects that are essentially 2-d. Taking the plane of the extended object to be the (x, y)-plane, we assume that it is only allowed to move in the out-of-plane direction, z. Under these circumstances, the 2-d mechanical object can be described in terms of a displacement field $z(\vec{r})$ and a momentum density field $\Pi(\vec{r})$, where $\vec{r} = (x, y)$. For a given boundary condition for the out-of-plane motion of the object, a complete set of normal modes, each characterized by frequency ω_j and mode shape $u_j(\vec{r})$, can be determined (see Appendix A.1 for details). Expanding the mechanical displacement relative to the steady-state configuration on this set we have,

$$\delta z(\vec{r}) = \sum_j \delta\beta_j u_j(\vec{r}), \tag{2.4}$$

in terms of canonical displacement coordinates $\{\delta\beta_j\}$. We can then state the Hamiltonian of the mechanical vibrational modes in diagonal form,

$$H_{\mathrm{m}}(\{\delta\beta_j, \delta p_j\}) = \sum_j \left[\frac{1}{2} m_j \omega_j'^2 \delta\beta_j^2 + \frac{\delta p_j^2}{2m_j}\right], \tag{2.5}$$

where $\delta p_j \equiv m_j \delta\dot{\beta}_j$ is the canonical momentum conjugate to $\delta\beta_j$. In this expression the mechanical mode frequencies $\omega_j^{'}$ are shifted from their non-interacting values ω_j due to the gradient of the bias-induced force field,

$$\omega_j'^2 = \omega_j^2 + \frac{\langle \bar{Q}^2(t)\rangle}{2m_j}\left[\frac{2}{\bar{C}_{\mathrm{eff}}^3}\left(\left.\frac{\partial C_{\mathrm{eff}}}{\partial(\delta\beta_j)}\right|_{\mathrm{eq.}}\right)^2 - \frac{1}{\bar{C}_{\mathrm{eff}}^2}\left.\frac{\partial^2 C_{\mathrm{eff}}}{\partial(\delta\beta_j)^2}\right|_{\mathrm{eq.}}\right], \tag{2.6}$$

as we will return to in Section 2.2.4. The gauge mass m_j in (2.5) depends on a scaling freedom in choosing $\delta\beta_j$. We can freely choose any point $\vec{r}_j$ whose displacement with respect to mode u_j represents the excursion of the mode as a whole. In doing so, however, we have to adjust for this choice in the gauge mass m_j and the physical interpretation of the canonical variables $\{\delta\beta_j, \delta p_j\}$ (see Appendix A.1 for details). We note, for purposes of expanding the charging energy (2.3) in terms of the canonical coordinates $\{\delta\beta_j, \delta p_j\}$ below, that the expansion (2.4) implies that these are chosen such that the $\{\delta\beta_j\}$ correspond to physical position. Below, we will work in the quasi-electrostatic limit, where the capacitance C_{eff} only depends on the spatial configuration of the mechanical object. As a consequence, C_{eff} is independent of $\{\delta p_j\}$.

We note here that intrinsic mechanical damping is most easily accounted for when considering the equations of motion rather than in the Hamiltonian description (2.5) [46]. This leads to the (classical) Langevin equations for each viscously damped mechanical mode (suppressing the mode index j for brevity)

$$\begin{aligned} \delta\dot{\beta} &= \delta p/m \\ \delta\dot{p} &= -m\omega'^2\delta\beta - \gamma\delta p + F(t) + \text{EM coupling}, \end{aligned} \tag{2.7}$$

where γ is the damping rate and F is the associated stochastic force.

2.2.3 Coupling strength G_j

In order to understand the interaction resulting from the mechanically modulated charging energy (2.3), we now expand this expression around the electromechanical steady-state configuration $\{\bar{Q}(t), \bar{z}(\vec{r})\}$ to second order in $\delta\beta_j$. By the definition of the steady state, there will be no linear terms in $\delta\beta_j$ or δQ as the net force on these relative variables must vanish (neglecting, in the case of AC drive, rapidly varying forces on the mechanical element of frequencies $\geq 2\omega_{\mathrm{d}}$ assumed to exceed all relevant mechanical frequencies). Here we first consider the coupling term, leaving the discussion of quadratic terms $\delta\beta_j^2$ for Section 2.2.4. The bilinear term in $\delta\beta_j, \delta Q$ yields the electromechanical coupling Hamiltonian

$$H_{\mathrm{int}} \equiv \sum_j H_{\mathrm{int}}^{(j)} \equiv \sum_j G_j \delta Q \delta\beta_j \cdot \begin{cases} e^{i\omega_{\mathrm{d}}t} + e^{-i\omega_{\mathrm{d}}t} & \text{[AC drive]} \\ 1 & \text{[DC bias]} \end{cases}, \tag{2.8}$$

where we have introduced the electromechanical coupling strength (units of electrical potential/length):

$$G_j \equiv -\frac{\bar{Q}_0}{\bar{C}_{\text{eff}}^2} \frac{\partial C_{\text{eff}}}{\partial(\delta\beta_j)}\bigg|_{z=\bar{z}} = -\frac{\bar{V}_0}{\bar{C}_{\text{eff}}} \frac{\partial C_{\text{eff}}}{\partial(\delta\beta_j)}\bigg|_{z=\bar{z}}, \tag{2.9}$$

which we see to be enhanced by the drive-induced charge $\bar{Q}_0$ of the coupling capacitor. In the last expression of (2.9) we have introduced the voltage amplitude

$$\bar{V}_0 \equiv \bar{Q}_0/\bar{C}_{\text{eff}}. \tag{2.10}$$

Eqs. (2.8,2.9) are a straightforward generalization of the derivation in Section 1.2.3, but here we have emphasized how the canonical position $\delta\beta \leftrightarrow \delta x$ and effective coupling capacitance $C_{\text{eff}} \leftrightarrow C_{\text{c}}$ arise and made their proper interpretation clear in the 2-d case. We thus have a general recipe for determining the most important coupling parameter. In Sections 2.3 and 2.4 we will use (2.9) to calculate the coupling strength for structures featured in recent experiments.

2.2.4 Effective mechanical frequency and electrical modes of the capacitive interface

The second quantity that we will use to characterize the interface is the effective frequency of the mechanical modes. To correctly determine this quantity for a given mechanical mode, we must carefully include all contributing factors, including both static and dynamic contributions. By the former we denote the drive-induced electrical force gradient experienced by the mechanical object for a given charge (an "electrical spring" effect). The dynamical shifts are those that arise because the mechanical motion also modifies the charge on the capacitor. The latter depends on the interaction between the mechanical mode and the various modes of the electrical circuit and in particular on their relative timescales.

In view of the above we need to consider more carefully the electrical modes of the capacitive interface as shown in Fig. 2.2. We start by specifying two kinds of modes that appear in that basic circuit layout: Firstly, there are the internal modes of the electrical part of the capacitive element, which rearrange the charge distribution on the electrodes, but does not alter their net charge. Their significance will be discussed in Subsection 2.2.4.1. Secondly, there is a mode associated with the voltage bias V responsible for inducing the (static or oscillating) bias charge on the coupling capacitor and hence does alter the net charge on the electrodes, i.e. the loop in Fig. 2.1b. The time-scale of this mode relative to that of the mechanical mode will determine to which extent the voltage bias can react to the mechanical modulation of the capacitance as we will see in Subsection 2.2.4.2 below.

2.2.4.1 Internal modes of the electrodes

As mentioned initially, we will approach the calculation of C_{eff} and its derivatives by subdividing the EM interface into small unit cells. This prompts us to consider the internal charge movements on the electrodes as illustrated in Fig. 2.2. We assume that the internal charge movements on the respective

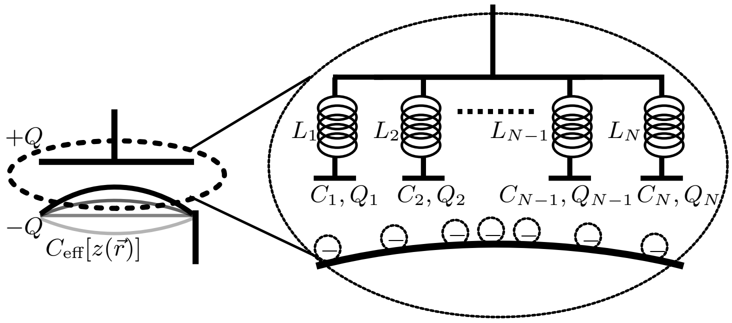

Figure 2.2: Close-up of the electromechanical interface of Fig. 2.1. We model each of the electrodes as a parallel connection of a number of LC arms with parameters $L_i, C_i[z(\vec{r}_i)]$, the latter being dependent on the local mechanical displacement $z(\vec{r}_i)$. The internal modes of the electrodes correspond to charge movement of the charges Q_i between arms belonging to the same electrode, thus conserving its net charge Q. The figure indicates that the charge distribution on a conductive membrane will mirror that of the electrodes.

electrodes occur without dissipation, but account for their finite time-scale by the inductances L_i as shown in the figure.

If the mechanical object moves in a manner that affects the capacitive elements asymmetrically it will in general cause internal charge redistribution on the electrodes, i.e. the mechanical modes couple to the internal modes of the electrodes. In turn, this alters the dynamics of the mechanical motion. In particular, these modes will dynamically shift the mechanical resonance frequency. In this work, we are interested in the limit where the internal electrode dynamics occurs on a time-scale much faster than those of both the mechanical motion and the bias mode of the circuit. As shown rigorously in previous work [47], this amounts to applying the limit $L_i \to 0$ in the circuit diagram of Fig. 2.2 and eliminating the internal modes by combining the capacitances $\{C_i\}_{i\in\{1,\ldots,N\}}$ using standard impedance combination rules; this yields the effective capacitance functional $C_{\text{eff}}[z(\vec{r})]$, which is just the capacitance for a static displacement $z(\vec{r})$. In particular, this procedure will lead to the correct effective mechanical resonance frequencies, where the dynamical shift due to the eliminated internal modes now enters as part of the static shift of the coupling as described by $C_{\text{eff}}[z(\vec{r})]$, Eq. (2.6). Hence, in the limit of fast internal capacitor dynamics, we may represent the electromechanical interface by a single effective capacitance $C_{\text{eff}}[z(\vec{r})]$ associated with a single electrical mode Q as shown on the left-hand side of Fig. 2.2.

2.2.4.2 Time-scale of the voltage bias

Given the conclusion of the previous subsection, we may conveniently return to the simple circuit diagram in Fig. 2.1b for the remainder of the present discussion. We will now consider the interplay between the voltage bias mode and each of the mechanical modes. This is most easily done by considering the Fourier transformed electromechanical equations of motion. In the DC-biased case we find from Eqs. (2.7,2.8) and the electrical circuit impedance in Fig.

2.1b,

$$\begin{aligned} m_j[\omega_j'^2 - \Omega^2 - i\Omega\gamma_j]\delta\beta_j(\Omega) &= -G_j\delta Q(\Omega) + F_j(\Omega) \\ L[\omega_{\rm LC}^2 - \Omega^2 - i\Omega R/L]\delta Q(\Omega) &= -G_j\delta\beta_j(\Omega), \end{aligned} \tag{2.11}$$

where $\omega_{\rm LC} \equiv (L\bar{C}_{\rm eff})^{-1/2}$, Ω is the Fourier frequency and we neglect Johnson noise, which is irrelevant to the present analysis (the details of setting up these equations will be treated when we derive the equivalent circuit in a later chapter). Solving Eqs. (2.11) for the effective mechanical response to $F_j(\Omega)$ we find in the limit $L \to 0$

$$m_j\left[\omega_j'^2 - \Omega^2 - i\Omega\gamma_j - \frac{G_j^2\bar{C}_{\rm eff}}{m_j}\frac{1+i\Omega R\bar{C}_{\rm eff}}{1+(\Omega R\bar{C}_{\rm eff})^2}\right]\delta\beta_j(\Omega) = F_j(\Omega). \tag{2.12}$$

The bracketed term in (2.12) is the (inverse) effective mechanical susceptibility. Assuming the dependence of its last term on Ω to be negligible, it can be interpreted as an electrically induced dynamical frequency shift (the real part) as well as dynamically induced broadening (the imaginary part). Under these circumstances we find the effective mechanical frequency to be (for DC biasing)

$$\Omega_j^2 \equiv \omega_j'^2 - \frac{\bar{C}_{\rm eff}G_j^2}{m_j}\frac{1}{1+(\omega_j' R\bar{C}_{\rm eff})^2}. \tag{2.13}$$

Eq. (2.13) shows how the effective mechanical frequency depends on the ratio of the mechanical oscillation period $\propto 1/\omega_j'$ and the RC time of the bias circuit, $R\bar{C}_{\rm eff}$. The dynamical shift interpolates between $-G_j^2\bar{C}_{\rm eff}/m_j$, in the limit of short RC time $\omega_j' R\bar{C}_{\rm eff} \ll 1$, and zero, in the limit of sufficiently long RC time $\omega_j' R\bar{C}_{\rm eff} \to \infty$. In the former limit, the bias voltage source responds instantaneously to mechanical motion leading to "fixed voltage" dynamics. In the latter limit, the mechanical oscillation period $2\pi/\omega_j'$ is much shorter than the response time $R\bar{C}_{\rm eff}$ of the voltage source leading to "fixed charge" dynamics. The derivation of (2.13) can be generalized to the AC-driven scenario. In the typical limit of $\omega_{\rm d} \gg \Omega_j$ this yields a factor of 2 relative to the shift found in the DC case, (2.13).

2.2.4.3 Effective mechanical frequency

As discussed above, the observed frequency shift of a mechanical mode is generally comprised of several contributions: 1) From the electrostatic field gradient induced by the bias voltage, 2) the adiabatic effect of the fast internal modes of the capacitive circuit element as discussed in Section 2.2.4.1, and 3) interaction with the main LC circuit mode, Eq. (2.13), as depends on the relative time-scale of the voltage bias as discussed above. Working in the limit where the internal capacitor modes are much faster than the mechanical time-scale, we can neglect the internal dynamics and work at the level of the effective capacitance $C_{\rm eff}$, as mentioned above. In this limit, shifts 1) and 2) combine to produce ω_j' given by Eq. (2.6), which we will, in turn, combine with 3) in what follows.

The static shift $\omega_j \to \omega_j'$, (2.6), arises from the "diagonal" second order derivatives of the charging energy (2.3), $(\partial^2/\partial(\delta\beta_j)^2)Q^2/[2C_{\rm eff}(\{\delta\beta_j\})]$. These quadratic terms $\propto (\delta\beta_j)^2$ combine with the "free" evolution of the mechanical

Hamiltonian, which has the same form as Eq. (2.5), to produce the shift $\omega_j \rightarrow \omega'_j$. To facilitate the combination with the dynamical shift, we rewrite the static shift (2.6) as

$$\omega_j'^2 \quad = \quad \omega_j^2 + \frac{\langle \bar{Q}^2(t) \rangle}{\bar{Q}_0^2} \frac{\bar{C}_{\text{eff}} G_j^2}{m_j} - \frac{1}{2m_j} \frac{\langle \bar{Q}^2(t) \rangle}{\bar{C}_{\text{eff}}^2} \frac{\partial^2 C_{\text{eff}}}{\partial(\delta\beta_j)^2}\bigg|_{\text{eq.}}, \tag{2.14}$$

where the second term has been expressed in terms of in terms of G using (2.9). Substituting Eq. (2.14) into the expression for the dynamical shift (2.13) we find the effective mechanical frequency including all contributions (assuming $\omega_{\text{d}} \gg \Omega_j$ in the case of AC bias)

$$\Omega_j^2 = \omega_j^2 + \frac{\langle \bar{Q}^2(t) \rangle}{\bar{Q}_0^2} \frac{\bar{C}_{\text{eff}} G_j^2}{m_j} \frac{(\omega'_j R \bar{C}_{\text{eff}})^2}{1 + (\omega'_j R \bar{C}_{\text{eff}})^2} - \frac{1}{2m_j} \frac{\langle \bar{Q}^2(t) \rangle}{\bar{C}_{\text{eff}}^2} \frac{\partial^2 C_{\text{eff}}}{\partial(\delta\beta_j)^2}\bigg|_{\text{eq.}}. \tag{2.15}$$

The second term contains the dependence on the relative time scale of the voltage source. In the limit of fixed charge dynamics, $\omega'_j R \bar{C}_{\text{eff}} \gg 1$, this contribution is finite and depends on G_j. In the opposite limit of fixed voltage dynamics, $\omega'_j R \bar{C}_{\text{eff}} \ll 1$, this contribution vanishes. In contrast, the third term of (2.15) only depends on the bias-induced voltage across the capacitor and is independent of the details of the circuit. For this reason, seeing as the focus of this chapter is to characterize the electromechanical interface, we will henceforth consider the fixed voltage limit, where (2.15) reduces to

$$\Omega_j^2 = \omega_j^2 - \frac{\langle V^2(t) \rangle}{2m_j} \frac{\partial^2 C_{\text{eff}}}{\partial(\delta\beta_j)^2}\bigg|_{\text{eq.}}, \tag{2.16}$$

where we have introduced the bias voltage $V(t) \equiv \bar{Q}(t)/\bar{C}_{\text{eff}}$ for brevity. For small relative shifts $|\Omega_j - \omega_j| \ll \omega_j$ we may approximate the shift in (2.16) by

$$\Delta\omega_j \equiv \Omega_j - \omega_j \approx -\frac{\langle V^2(t) \rangle}{4m_j\omega_j} \frac{\partial^2 C_{\text{eff}}}{\partial(\delta\beta_j)^2}\bigg|_{\text{eq.}}, \tag{2.17}$$

which is the formula we will use below.

2.3 Decomposing the effective capacitance C_{eff} into capacitive unit cells

With the above results we have a characterization of how the dependence of C_{eff} on $\delta z(\vec{r})$ affects the dynamics of the system. To apply the expressions derived for the electromechanical coupling strengths G_j and the mechanical frequency shifts $\Delta\omega_j$, we must be able to calculate C_{eff} and its derivatives and will now address how to evaluate these quantities. We introduce our approach by means of an example and consider a wired, conductive membrane above a fixed electrode. An instance of this coupling geometry is depicted in Fig. 2.3 (left). In this figure, we see a capacitive element consisting of a tensioned circular aluminum membrane above a fixed electrode (not visible) [10]. Since this mechanical oscillator is metalized and thus conducting, we can make it part of a capacitor. Because it is allowed to vibrate, the associated degrees of freedom

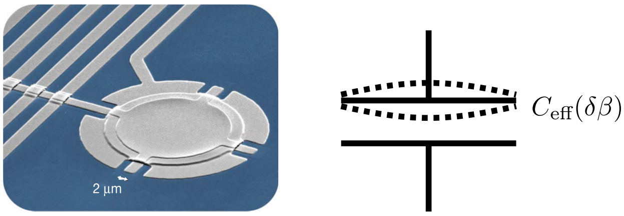

Figure 2.3: Plate capacitor with an elastic upper plate: (left) Aluminum circular drum capacitor where the upper electrode is free to vibrate whereas the lower electrode (not shown) is fixed (this figure has been reprinted from Ref. [10]). (right) Stylized depiction of the setup as a plate capacitor with a "wobbly" upper plate. Focusing on a single 2-d vibrational mode, $\delta\beta$ is a suitable canonical position coordinate.

will modulate the capacitance of the arrangement. A simpler, but equivalent, pictorial representation of this scenario is provided in Fig. 2.3 (right), where a plate capacitor with one elastic plate is shown. This illustration intentionally alludes to the paradigmatic parallel plate capacitor discussed in Section 2.2.1, but it is not equivalent to it. Let us, nonetheless, return to this standard textbook example.

The parallel plate capacitance, as given by Eq. (2.1), describes the scenario where the parallel plates are so close that the electric field lines are essentially all pointing along the normal of the plates. While field lines near the edges will deviate from this direction, the associated contributions to the stored energy are vanishingly small in the limit $d \ll \sqrt{A}$ and (2.1) accurately describes the capacitance. Turning now to the more complicated geometry of Fig. 2.3 (right), we will for simplicity continue to neglect edge effects, thus assuming the plate separation to be much smaller than the plate dimensions. In order to account for the mechanical modulation of the capacitance, we must necessarily account for changes induced by the variable configuration of the upper plate. Imagine that we freeze the motional state of the vibrating element in one of the configurations shown in Fig. 2.3 (right), as is appropriate for the quasi-static limit. The exact determination of the resulting capacitance with a frozen motional state is analytically complicated for an arbitrary configuration of the upper plate and will in general require a numerical solution. To circumvent this complication we will now construct an analytical approximation: If the configuration of the upper plate is such that its radius of curvature is large compared to the plate separation, then locally we may approximate the field density by that of a parallel plate capacitor. Hence, we are led to assign a capacitance contribution $dC(\vec{r})$ to an infinitesimal area dA in the neighborhood of the point $\vec{r} = (x, y)$ in the plane of the plate. Expressed as capacitance per unit area we have

$$\frac{dC[\delta z(\vec{r})]}{dA} = \frac{\epsilon}{\bar{z}(\vec{r}) + \delta z(\vec{r})}. \tag{2.18}$$

In calculating the total capacitance from (2.18) we wish to account for imperfect overlap between the electrodes or regions of the oscillating plate where metallization is absent. In the simplest possible approximation we only count contributions from the metalized regions of the mechanical oscillator that overlap with the fixed electrode. By introducing a mask function $\xi(\vec{r})$ that equals

1 for points in the plane of the mechanical oscillator that are metalized and overlap with the fixed electrode, we can express the total capacitance as

$$C_{\rm c} = \int_A \frac{dC[\delta z(\vec{r})]}{dA} \xi(\vec{r}) dA, \tag{2.19}$$

where the integral is over the entire mechanical mode area.

We can express the k'th derivative of $C[\delta z(\vec{r})]/dA$ wrt. $\delta\beta_j$ using the mode expansion (2.4) as

$$\frac{\partial^k}{\partial(\delta\beta_j)^k} \frac{dC[\delta z(\vec{r})]}{dA} = \left[\frac{d^k}{d(\delta z)^k} \frac{dC[\delta z]}{dA}\right] u_j^k(\vec{r}), \tag{2.20}$$

which is proportional to the k'th power of the mode function $u_j(\vec{r})$. For the parallel plate capacitance density (2.18) we have

$$\frac{d^k}{d(\delta z)^k} \frac{dC[\delta z]}{dA} = (-1)^k k! \frac{\epsilon}{(\bar{z}(\vec{r}) + \delta z)^{k+1}}. \tag{2.21}$$

The derivatives of $C_{\rm c}$ (2.19) for the locally parallel-plate conditions (2.18) then follow from (2.20) and (2.21); evaluating at the equilibrium configuration we arrive at

$$\begin{aligned} \left.\frac{\partial^k C_{\rm c}}{\partial(\delta\beta_j)^k}\right|_{\rm eq.} &= \int_A \left.\left(\frac{d^k}{d(\delta z)^k} \frac{dC[\delta z]}{dA}\right)\right|_{\rm eq.} u_j^k(\vec{r}) \xi(\vec{r}) dA \\ &= \int_A (-1)^k k! \frac{\epsilon}{[\bar{z}(\vec{r})]^{k+1}} u_j^k(\vec{r}) \xi(\vec{r}) dA. \end{aligned} \tag{2.22}$$

To evaluate (2.22) one needs to determine the mechanical equilibrium configuration $\bar{z}(\vec{r})$ induced by the electrical drive. The exact determination of $\bar{z}(\vec{r})$ is as difficult as calculating the capacitance of any given configuration. If the static deflection of the mechanical element is small, however, we may approximate $\bar{z}(\vec{r}) \approx d$ when evaluating (2.22), whereby the derivatives of the capacitance per unit area $dC[\delta z]/dA$ can be taken outside the integral. Thereby we get

$$\left.\frac{\partial^k C_{\rm c}}{\partial(\delta\beta_j)^k}\right|_{\rm eq.} \approx \left.\frac{d^k}{d(\delta z)^k} \frac{dC[\delta z]}{dA}\right|_{\bar{z}(\vec{r}) \approx d} A O_A^{(k,j)} = (-1)^k k! \frac{\epsilon A}{d^{k+1}} O_A^{(k,j)}, \tag{2.23}$$

where the overlap is given by

$$O_A^{(k,j)} \equiv A^{-1} \int_A u_j^k(\vec{r}) \xi(\vec{r}) dA'. \tag{2.24}$$

Eq. (2.23) shows that within the stated approximations, the derivatives of $C_{\rm c}$ are those of a standard parallel plate capacitor of area A and separation d, but with a correction from the mode-dependent factor $O_A^{(k,j)}$. Within the same approximation, the (steady-state) capacitance is that of a parallel-plate capacitor multiplied by the overlap fraction:

$$\bar{C}_{\rm c} \equiv C_{\rm c}|_{\rm eq.} \approx \frac{\epsilon A}{d} O_A^{(0)}.$$

Allowing for additional parasitic and/or tuning capacitance C_0 in parallel with the coupling capacitance we have $C_{\rm eff}(\delta\beta) = C_{\rm c}(\delta\beta) + C_0$ and $\bar{C}_{\rm eff} \equiv C_{\rm eff}|_{\rm eq.} =$

$\bar{C}_{\mathrm{c}}+C_0$, assuming that only C_{c} is modulated by $\delta\beta$. Using the derivatives (2.23) to evaluate the coupling strength (2.9) and the frequency shift (2.17) we arrive at the results,

$$G = \frac{\bar{V}_0}{\bar{C}_{\mathrm{c}} + C_0} \frac{\epsilon A}{d^2} O_A^{(1)}, \quad \Delta\omega \approx -\frac{\langle V^2(t)\rangle}{4m\omega} 2\frac{\epsilon A}{d^3} O_A^{(2)}, \tag{2.25}$$

for a particular mechanical mode of (unperturbed) frequency ω and mass m.

2.4 Additional examples

We have previously applied the framework presented here in the analysis of experiments involving vibrating micromembranes above one or more pairs of coplanar electrodes [3, 1], with the membrane acting as an intermediate floating electrode; in this section we will describe the details of these analyses. In such floating electrode scenarios, we must for calculational purposes distinguish between two scenarios: 1) Comparable or large membrane-electrode separation compared to inter-electrode gap(s). 2) Small membrane-electrode separation compared to the inter-electrode gap(s). The former case (1) applies, e.g., to a floating membrane electrode above a fixed electrode mask of high spatial frequency [3]. The approach presented here is still applicable, even for non-metalized membranes, but requires some input from numerical simulation; this case was treated in detail in previous work [47]. In what follows, we will therefore treat case (2) (we focus on a single mechanical mode j and therefore write $\delta\beta \equiv \delta\beta_j$ and $\omega = \omega_j$ for brevity).

2.4.1 Floating, conductive membrane close to fixed electrode mask

In this section we consider an EM coupling geometry which was used in a recent radio-to-optical transducer experiment [1], see Fig. 2.4. Here the electromechanical capacitance arises from a slightly more involved geometry than what was considered in Section 2.3. In this scenario, the conductive membrane is not electrically wired to the circuit. It is the electromechanical equivalent of the optomechanical membrane-in-the-middle setup [35]. This is typically an advantage for practical reasons since no wires are connected to the membrane [3].

If the metalized membrane is significantly closer to the plane of the electrodes than the inter-electrode gap, the capacitance between the respective electrodes and the membrane dominates over the inter-electrode capacitance. In this case the electrical field lines will be approximately normal to the electrode and membrane planes, although their direction will be different for the two electrode polarities. Hence, neglecting edge effects once again, the capacitance between electrodes and the membrane will locally be that of a parallel plate capacitor (2.18). In contrast to the simpler geometry in Fig. 2.3, however, little of the field energy resides directly between the positive and negative electrodes, but mainly between the membrane and the respective electrodes. Therefore the membrane acts to serially connect the capacitances of the electrodes so that the coupling capacitance now takes the form

$$C_{\mathrm{c}}(\delta\beta) = \left[C_+^{-1}(\delta\beta) + C_-^{-1}(\delta\beta)\right]^{-1}, \tag{2.26}$$

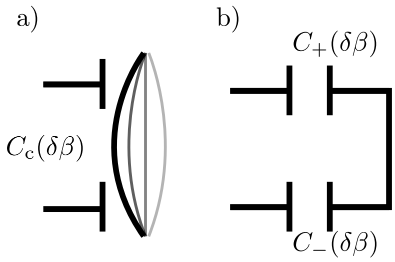

Figure 2.4: a) Electrically floating conductive membrane above fixed pair of electrodes. Note that, crucially, in the actual experiment the membrane-electrode separation is much smaller than the inter-electrode gap. The electrodes interact indirectly via the conductive mechanical object by polarizing it. b) Capacitance model for a) in which the capacitances between the membrane and the positive/negative electrode $C_\pm(\delta\beta)$ combine in series to determine $C_c(\delta\beta)$, see Eq. (2.26).

where $C_\pm(\delta\beta)$ is the capacitance between the membrane and the positive/negative electrode. Adding a membrane-independent capacitance C_0 in parallel to account for tuning and/or parasitic capacitance including direct capacitance between electrodes, the effective capacitance becomes

$$C_{\text{eff}}(\delta\beta) = C_0 + C_c(\delta\beta) = C_0 + \left[C_+^{-1}(\delta\beta) + C_-^{-1}(\delta\beta)\right]^{-1}. \tag{2.27}$$

We will model $C_\pm(\delta\beta)$ using the parallel plate capacitance per unit area (2.18), defining in analogy with (2.19),

$$C_\pm(\delta\beta) \equiv \int_{A_\pm} \frac{dC[\delta z(\vec{r})]}{dA}\xi(\vec{r})dA,$$

where $A_\pm$ is the region above the positive/negative electrode. From here we may apply the procedure of Section 2.3 to approximate $C_\pm(\beta)$ and its derivatives for each electrode polarity individually (amounting to the modification $C_c \to C_\pm, A \to A_\pm$ in (2.22)). Neglecting the static displacement as in (2.23), we find the approximation

$$\left.\frac{\partial^k C_\pm}{\partial(\delta\beta)_j^k}\right|_{\text{eq.}} \approx \frac{d^k}{d(\delta z)^k}\left.\frac{dC[\delta z]}{dA}\right|_{\bar{z}(\vec{r})=d} AO_\pm^{(k,j)} = (-1)^k k! \frac{\epsilon A}{d^{k+1}} O_\pm^{(k,j)} \tag{2.28}$$

$$O_\pm^{(k,j)} \equiv A^{-1}\int_{A_\pm} [u_j(\vec{r})]^k \xi(\vec{r})dA'. \tag{2.29}$$

Note that the partial overlap factors $O_{A_\pm}^{(k,j)}$ (2.29) are related to the full overlap factors of (2.24) as $O_A^{(k,j)} = O_{A_+}^{(k,j)} + O_{A_-}^{(k,j)}$. By applying the chain rule to Eq. (2.27) we can relate the derivatives of $C_\pm(\delta\beta)$ to those of $C_{\text{eff}}(\delta\beta)$. Evaluating the required derivatives of $C_{\text{eff}}(\delta\beta)$ at the equilibrium configuration and using the approximation (2.28) we arrive at the coupling strength (2.9)

$$G \equiv \bar{V}_0 \frac{\bar{C}_c}{C_0 + \bar{C}_c} \frac{1}{d} \frac{[O_+^{(0)}]^{-2}O_+^{(1)} + [O_-^{(0)}]^{-2}O_-^{(1)}}{[O_+^{(0)}]^{-1} + [O_-^{(0)}]^{-1}}, \tag{2.30}$$

containing the participation ratio $\bar{C}_c/(C_0 + \bar{C}_c)$ and the weighted average of the *renormalized* overlap factors for the first derivative $O_\pm^{(1)}/O_\pm^{(0)}$ with weight factors $[O_\pm^{(0)}]^{-1}$. The frequency shifts are given by (2.17)

$$\Delta\omega \approx -\frac{\langle V^2(t)\rangle}{2m\omega}\frac{\epsilon A}{d^3}\left[\frac{[O_+^{(0)}]^{-2}O_+^{(2)} + [O_-^{(0)}]^{-2}O_-^{(2)}}{\left([O_+^{(0)}]^{-1} + [O_-^{(0)}]^{-1}\right)^2} - \frac{1}{O_+^{(0)} + O_-^{(0)}}\left(\frac{[O_+^{(0)}]^{-1}O_+^{(1)} - [O_-^{(0)}]^{-1}O_-^{(1)}}{[O_+^{(0)}]^{-1} + [O_-^{(0)}]^{-1}}\right)^2\right]. \tag{2.31}$$

This expression was used in Ref. [3] to analyze mode-shape and misalignment corrections for floating electrodes made from SiN membranes metalized with Al or graphene.

In some experimental circumstances [1] it is easier to measure the electrically induced mechanical frequency $\Delta\omega$ than the coupling strength G. We can, however, infer G from $\Delta\omega$ using Eqs. (2.30,2.31):

$$G = -\frac{\bar{V}_0}{\langle V^2(t)\rangle}\frac{2\omega m d}{(C_0 + \bar{C}_c)}\frac{\frac{[O_+^{(0)}]^{-2}O_+^{(1)}+[O_-^{(0)}]^{-2}O_-^{(1)}}{[O_+^{(0)}]^{-1}+[O_-^{(0)}]^{-1}}}{\frac{[O_+^{(0)}]^{-2}O_+^{(2)}+[O_-^{(0)}]^{-2}O_-^{(2)}}{[O_+^{(0)}]^{-1}+[O_-^{(0)}]^{-1}} - \left(\frac{[O_+^{(0)}]^{-1}O_+^{(1)}-[O_-^{(0)}]^{-1}O_-^{(1)}}{\sqrt{O_+^{(0)}/O_-^{(0)}}+\sqrt{O_-^{(0)}/O_+^{(0)}}}\right)^2}\Delta\omega,$$

where the prefactor equals $\bar{V}_0^{-1}$ for DC bias and $(2\bar{V}_0)^{-1}$ for AC bias, see Eqs. (2.10) and (1.7). In an experimental context, this expression is a means to infer the possible coupling strength G which may be obtained. This procedure was used in Ref. [1] as an additional check that the system performance was well understood.

2.5 Concluding remarks

In this chapter we have given a rather careful treatment of the linearized capacitive coupling between charge fluctuations and 2-d mechanical vibration modes with emphasis on coupling strengths and mechanical frequency shifts, which are important quantities in characterizing such interfaces. We also introduced a semi-analytical approach to obtaining approximate predictions for these quantities, which has already been applied in the analysis of various interface geometries appearing in experiment [3, 1]. The method is a useful tool for achieving quick estimates of the influence of geometry and material choices and also provides a model linking coupling strength G and frequency shift $\Delta\omega$ for situations where the former is difficult to measure directly in experiment. The derivation was given here in the context of (thin) vibrating membranes, but can likely be extended to other types of oscillatory motion.

Chapter 3

Figures of merit for transduction

The work presented in this chapter has been carried out in collaboration with Albert Schließer, Jacob M. Taylor, and Anders S. Sørensen.

3.1 Introduction

Having considered the specifics of achieving effective EM coupling, the remainder of Part I will turn to hybrid electro-optomechanical systems and their application as transducers. Before specializing to electro-optomechanical transducers, however, it is worthwhile to discuss transduction more generically. Part of the motivation for taking a more general viewpoint here are the alternative approaches in current research to realizing quantum transduction between electrical and optical frequencies. In these systems the intermediary mechanical degree of freedom is replaced by, e.g., an erbium-doped crystal [48, 49] or a ferromagnetic magnon [50].

This chapter addresses the question of theoretically characterizing the performance of a quantum transducer. Given that we in practice cannot attain ideal one-to-one quantum conversion, we will explore how well the transducer performs in various scenarios ranging from classical signal detection to applications for quantum information processing. The performance of the transducer depends on the particular application in which the transducer enters but regardless of the application the performance of the transducer can be characterized by two simple parameters, the signal transfer efficiency η and the added noise N.

3.2 Scattering matrix formulation

The essential feature of a transducer is that it uses oscillating bias fields to modulate an incoming field and thereby connects different frequency components as shown in Fig. 3.1a (and discussed previously in the context of electro-optomechanics in Section 1.2). Here we are interested in the typical linear regime where a weak (bosonic) field is transduced to a different frequency through the modulation with a much stronger bias field. In this case the Hamiltonian can be truncated at the second order in the involved field operators and the equations of motion become linear. As a result, the solution to the Heisenberg-Langevin equations will take the form

$$\vec{A}_{\text{out}}(\Omega) = \int d\Omega' \mathbf{S}(\Omega, \Omega') \vec{A}_{\text{in}}(\Omega'), \tag{3.1}$$

where $\vec{A}_{\text{in (out)}}(\Omega)$ is a vector containing the input (output) of the involved annihilation and creation operators $\hat{a}_i$ and $\hat{a}_i^\dagger$ of all the involved modes, including decay channels, at a frequency Ω. In this expression the operation of the transducer is completely captured by the scattering matrix $\mathbf{S}(\Omega, \Omega')$ which describes how different frequency components are connected and this will form the basis of the discussion below. We will for simplicity assume the drive amplitude of the bias fields to be independent of time [18], and as a result the scattering matrix will take a simple form in the frequency representation. In practice there are, however, a variety of different approaches, e.g., involving time varying amplitudes [26, 27, 28, 29] or detunings [30] or using quantum teleportation [31] (see discussion in Section 1.1.2). Regardless of the specifics of the transducer, however, it is always possible to derive a similar scattering matrix in the linear regime and most of our conclusions can therefore easily be generalized to other situations.

In the ideal limit, a transducer merely converts photons from one frequency to another. In reality, however, photons may not be converted with unit efficiency $\eta < 1$. As a simple example of this let us consider a model where the scattering relation (3.1) does not mix creation and annihilation operators. In this case the transducer can be understood by the simple beam splitter model in Fig. 3.1a where the efficiency η is captured by a transmittance η. The loss at the beam splitter is complemented by the addition of noise from the other port as described by the beam splitter relation

$$\hat{a}_{\text{out},e}(\Omega_e) = \sqrt{\eta}\hat{a}_{\text{in},s}(\Omega_s) + \hat{F}(\Omega_e), \tag{3.2}$$

where $\hat{a}_{\text{out},e}$ and $\hat{a}_{\text{in},s}$ are annihilation operators for the output and input signal respectively and where $\hat{F}(\Omega_e)$ is a stationary noise operator accounting or all other contributions to $\hat{a}_{\text{out},e}(\Omega_e)$. Eq. (3.2) is a particular component of (3.1) representing the output of a particular port. Suppose that we are interested in measuring the time-integrated number flux from this output port. It will have two contributions $\int dt' I(t) = \eta \int (d\Omega/2\pi)(\langle \hat{a}_{\text{in},s}^\dagger \hat{a}_{\text{in},s}\rangle(\Omega) + N(\Omega))$, where $\langle \hat{a}_{\text{in},s}^\dagger \hat{a}_{\text{in},s}\rangle(\Omega)\delta(\Omega - \Omega') \equiv \langle \hat{a}_{\text{in},s}^\dagger(\Omega)\hat{a}_{\text{in},s}(\Omega')\rangle$ and

$$N(\Omega)\delta(\Omega - \Omega') = \frac{\langle \hat{\mathcal{F}}^\dagger(\Omega)\hat{\mathcal{F}}(\Omega')\rangle}{\eta} \tag{3.3}$$

describes the added noise relative to the signal. For measuring the input signal we are interested in knowing the output signal relative to the noise. This is exactly what is described by N, which measures how many photons an input signal should have per mode in order to exceed the noise. N is thus the central quantity of interest in this case, and in particular $N \lesssim 1$ is required for applications in the quantum regime, where we are sensitive to single photons. Here we will generalize this result, finding the full form of η and N, and show that

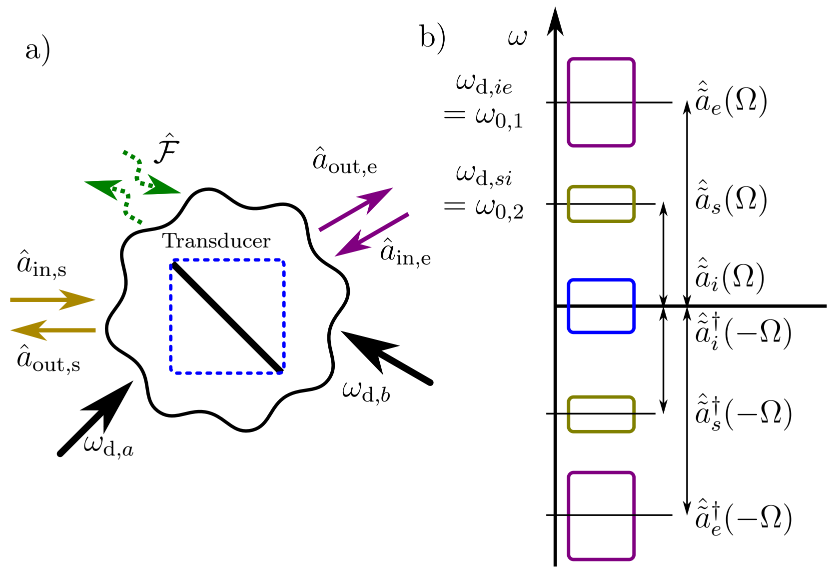

Figure 3.1: Generic transduction scenario. a) A transducer is driven by harmonically varying drive frequencies $\omega_{\mathrm{d},i}$ which connect different frequency components. In an idealized limit the transducer acts as a beam splitter transforming an input signal $\hat{a}_{\mathrm{in,s}}$ at a certain frequency to an output signal $\hat{a}_{\mathrm{out,e}}$ at a different frequency by addition or subtraction of the drive frequencies. A finite transduction efficiency $\eta < 1$ leads to admixture of noise $\hat{\mathcal{F}}$ from the other port of the beam splitter. b) The dynamics of the modes of the transducer are assumed to occur in narrow frequency bands (boxes) centered around $\{\omega_{0,m}\}$, relative to which the corresponding slowly-varying bosonic operators $\hat{\tilde{a}}_m(\Omega)$ are defined. The harmonic driving terms $\omega_{\mathrm{d},k}$ connect the different frequency bands. Drive terms not matching the difference between the bands are discarded in the rotating wave approximation. In the instance depicted here, the internal modes s and e that couple to the itinerant fields $\hat{a}_{\mathrm{in,s}}$ and $\hat{a}_{\mathrm{out,e}}$, respectively, are linked via the internal transducer mode i.

these are the two essential parameters for describing the performance of a linear transducer.

3.3 Time-stationary transduction

To be concrete we first derive the input-output scattering relation [51] for a general time-stationary transducer driven by bias fields of constant amplitude. We consider an open, linear system obeying the Heisenberg-Langevin equation of motion

$$\dot{\vec{V}}(t) = \sum_{k,l} \mathbf{M}_{l,k} \mathrm{e}^{il\omega_{d,k}t} \vec{V}(t) - \mathbf{\Gamma} \vec{A}_{\mathrm{in}}(t). \tag{3.4}$$

Here $\vec{V}$ is a vector of bosonic operators describing the internal degrees of the freedom of the transducer. Decay of the modes means that the internal degrees are coupled to the input vector $\vec{A}_{\rm in}(t)$ as described by the matrix $\mathbf{\Gamma}$, as per input-output theory [51]. The dynamics of the transducer is described by the coupling matrices $\mathbf{M}_{l,k}$ which include the part of the coupling which is modulated by all the different harmonic driving fields of frequency $\omega_{{\rm d},k}$ which may enter to various order $l = 0, \pm 1, \pm 2, \ldots$. To proceed we will make the assumption that the different field operators can be divided into a finite number of narrow bands denoted by an index m centered around a frequency $\omega_{0,m}$ (possibly zero). Each central frequency is connected to the center of another by an integer number of drive frequencies. This scenario is depicted in Fig. 3.1b and refers to the situation typically desired where bias fields are used to bridge different components of the spectra. Furthermore we make the rotating wave approximation (RWA) and neglect all couplings which are not resonantly connecting the different frequency bands. After introducing the Fourier representation of all operators in the equation of motion (3.4), it is convenient to change to a rotating frame where all field annihilation operators for a particular band $\hat{a}(\Omega + \omega_{0,m})$ are replaced by slowly varying operators $\tilde{\hat{a}}(\Omega) = \hat{a}(\Omega + \omega_{0,m})$ with commutation relation $[\tilde{\hat{a}}(\Omega), \tilde{\hat{a}}^\dagger(\Omega')] = \delta(\Omega - \Omega')$. We assume here that after having performed the RWA, all operators $\hat{a}(\omega), \hat{a}^\dagger(\omega)$ enter the equations of motion only via one slowly varying representation $\tilde{\hat{a}}(\Omega), \tilde{\hat{a}}^\dagger(\Omega)$. In this case, all oscillating components in Eq. (3.4) can be absorbed and the resulting equation of motion only involves the slow frequency component Ω. Solving Eq. (3.4) in the Fourier domain and using the input-output relation $\vec{A}_{\rm out}(t) = \mathbf{\Gamma}'\vec{V}(t) + \vec{A}_{\rm in}(t)$ [51] with a suitable matrix $\mathbf{\Gamma}'$ we arrive at a scattering relation of the form given in Eq. (3.1) with the scattering matrix

$$\mathbf{S}(\Omega, \Omega') \equiv \left(\mathbf{1} + \mathbf{\Gamma}' \frac{1}{i\Omega\mathbf{1} + \mathbf{M}} \mathbf{\Gamma}\right) \delta(\Omega - \Omega'). \tag{3.5}$$

Here $\mathbf{M} = \sum_{\langle l,k \rangle} \tilde{\mathbf{M}}_{l,k}$ is the sum over terms $\langle k, m \rangle$ in (3.4) not discarded in the RWA and the tilde on $\tilde{\mathbf{M}}_{l,k}$ denotes that terms corresponding to the central frequencies $\omega_{0,m}$ have been removed. Note, that since annihilation operators enter with the time dependence $\tilde{\hat{a}}(\Omega) \exp(-i\Omega t)$ whereas the creation operators, in the convention used here, are $\tilde{\hat{a}}^\dagger(\Omega) \exp(i\Omega t)$, the annihilation operators $\tilde{\hat{a}}(\Omega)$ will in general couple to $\tilde{\hat{a}}^\dagger(-\Omega)$ and the input (output) vectors $\vec{A}_{\rm in}(\Omega)$ ($\vec{A}_{\rm out}(\Omega)$) thus contain $\tilde{\hat{a}}(\Omega)$ and $\tilde{\hat{a}}^\dagger(-\Omega)$ (see Appendix B.1 regarding the Fourier convention). Since within the stated assumptions we can work in terms of the slowly varying operators alone, we will for notational simplicity omit the tilde henceforth.

3.4 Transducer characterization

We now return to the question of characterizing a transducer based on its scattering matrix $\mathbf{S}$ and a specification of the noise input fields. For simplicity we will assume that we only have signal input near a single positive frequency, i.e. confined to a particular band (see Fig. 3.1b). Furthermore, since we will typically be interested in the output of a particular port, it suffices to consider only a single row of the scattering matrix $\mathbf{S}$. Denoting the output field of the "exit" port $\hat{a}_{\rm out,e}$, we will write the corresponding scattering relation in a manner that singles out the input on the "signal" port $\hat{a}_{\mathrm{in,s}}$ (generalizing 3.2)

$$\hat{a}_{\mathrm{out,e}}(\Omega) = \begin{cases} U_{\mathrm{s}}(\Omega)\hat{a}_{\mathrm{in,s}}(|\Omega|) + \hat{\mathcal{F}}(\Omega) & \text{for } \Omega > 0 \\ V_{\mathrm{s}}(\Omega)\hat{a}^{\dagger}_{\mathrm{in,s}}(|\Omega|) + \hat{\mathcal{F}}(\Omega) & \text{for } \Omega < 0 \end{cases}, \tag{3.6}$$

where all noise contributions have been collected in a single noise operator

$$\hat{\mathcal{F}}(\Omega) \equiv \sum_{i \neq \mathrm{s}} \left[U_i(\Omega)\hat{a}_{\mathrm{in},i}(\Omega) + V_i(\Omega)\hat{a}^{\dagger}_{\mathrm{in},i}(-\Omega) \right]. \tag{3.7}$$

Here U_i (V_i) denote the contribution of $\hat{a}_{\mathrm{in},i}$ to $\hat{a}_{\mathrm{out,e}}$ in the scattering relation (3.1) and any possible input in the signal port at negative frequencies is treated as noise and thus contained in the sum. Furthermore we have used that the slowly varying annihilation operators $\hat{a}(\Omega)$ at negative frequencies $\Omega < 0$ couple to creation operators at positive frequencies $\hat{a}^{\dagger}(|\Omega|)$. The operators $\hat{a}_{\mathrm{in,s}}(\Omega), \hat{a}^{\dagger}_{\mathrm{in,s}}(\Omega)$ will be assumed uncorrelated with $\hat{\mathcal{F}}(\Omega'), \hat{\mathcal{F}}^{\dagger}(\Omega')$ for all Ω, Ω'. We see from Eq. (3.6) that if we consider the upper (lower) output sideband alone, $\Omega > 0$ ($\Omega < 0$), the transducer is phase-preserving (phase-conjugating) [43].

The scattering relation (3.6) allows the generalization of the two generic transducer parameters introduced above. Firstly, the *signal transfer efficiency* $\eta(\Omega)$ is

$$\eta(\Omega) \equiv \begin{cases} |U_{\mathrm{s}}(\Omega)|^2 & \text{for } \Omega > 0 \\ |V_{\mathrm{s}}(\Omega)|^2 & \text{for } \Omega < 0 \end{cases} \tag{3.8}$$

Secondly, we define the *added noise* flux per unit bandwidth referenced to the input

$$N(\Omega)\delta(\Omega - \Omega') \equiv \frac{\langle \hat{\mathcal{F}}^{\dagger}(\Omega)\hat{\mathcal{F}}(\Omega') \rangle}{\eta(\Omega)}. \tag{3.9}$$

The expectation value $\langle \hat{\mathcal{F}}^{\dagger}(\Omega)\hat{\mathcal{F}}(\Omega') \rangle$, which must be calculated to determine $N(\Omega)$ can straightforwardly be evaluated under the assumption of time-stationary thermal reservoirs,

$$\langle \hat{a}_i(\Omega)^{\dagger}\hat{a}_i(\Omega') \rangle = n_i(\Omega + \omega_{0,i})\delta(\Omega - \Omega'), \tag{3.10}$$

in terms of the thermal mean number of excitations $n_i(\omega) = (\exp[\hbar\omega/k_{\mathrm{B}}T_i] - 1)^{-1}$, which depends on the frequency in the lab frame. With this we find

$$\begin{aligned} \langle \hat{\mathcal{F}}^{\dagger}(\Omega)\hat{\mathcal{F}}(\Omega') \rangle = \delta(\Omega - \Omega')(&\sum_{i \neq \mathrm{s}} |T_i(\Omega)|^2 n_i(\Omega + \omega_{0,i}) \\ &+ \sum_i |V_i(\Omega)|^2 [n_i(-\Omega + \omega_{0,i}) + 1]), \end{aligned} \tag{3.11}$$

where in the second sum we include the noise due to the coupling to the lower sideband of the input port (assumed to be subject to thermal input).

3.5 Quantum-mechanical constraints on transduction

With these results we are now in a position to evaluate the performance of transducers for various applications. Before going into the details of particular applications we note that the the scattering matrix elements are subject to a number of constraints imposed by quantum mechanics [43]. In particular, if we consider the specific case where the scattering relation (3.6,3.7) can be described by a beam splitter interaction ($V_i = 0$ for all i), corresponding to the fully resolved sideband limit, as discussed in Section 1.2.4, unitarity implies the sum rule ($\Omega > 0$)

$$1 = \eta(\Omega) + \sum_{i \neq \mathrm{s}} |U_i(\Omega)|^2, \tag{3.12}$$

where we have used the definition (3.8). Hence if we achieve unit signal transfer efficiency $\eta(\Omega) = 1$ the contribution from the noise sources (contained in $\hat{\mathcal{F}}(\Omega)$) must vanish and we have an ideal transducer. On the other hand if we consider imperfect transducers, $\eta(\Omega) < 1$, noise will necessarily enter. Since the transducer connects vastly different frequency scales, we will have to consider the different number of thermal excitations in the noise reservoirs, $n_i(\Omega + \omega_{0,i})$, entering $N(\Omega)$, see Eq. (3.11). E.g., this is due to the vast gap between optical ($\gtrsim$ 300 THz), mechanical and electrical frequencies (∼1 MHz – 10 GHz). For this reason, maximizing $\eta(\Omega)$ will in general not lead to minimization of $N(\Omega)$ and, hence, a trade-off has to be made between maximizing signal transfer efficiency η and minimizing the added noise N. Outside the resolved-sideband regime, Eq. (3.12) generalizes to ($\Omega > 0$)

$$1 = \eta(\Omega) + \sum_{i \neq \mathrm{s}} \left(|U_i(\Omega)|^2 - |V_i(\Omega)|^2 \right),$$

allowing $\eta(\Omega) > 1$ at the cost of amplification noise (as discussed in Section 1.2.4). This further emphasizes the above conclusion that maximization of $\eta(\Omega)$ in itself is not a meaningful optimization strategy in general.

3.6 Transducer applications

Now that we have established the generic transducer parameters $\eta(\Omega)$ and $N(\Omega)$ from the scattering matrix and discussed their general features in the previous section, we will finally consider a number of transducer applications and their figures of merit.

3.6.1 Heterodyne detection

As a particular application we first consider sensing of weak signals, e.g., detection of upconverted electrical signals by optical means. We are interested in measuring both quadratures of the incoming signal and will therefore consider heterodyne detection. Alternatively if only a single quadrature is desired, homodyne detection may be advantageous. Heterodyning relies on beating the transducer output with a local oscillator (LO) of amplitude $\alpha_{\mathrm{LO}} = |\alpha_{\mathrm{LO}}|e^{i\theta_{\mathrm{LO}}}$ at a well-defined frequency which we take to be at the center of the output band $\omega_{0,\mathrm{e}}$. With this choice the LO lies in between the two sidebands $\omega_{0,\mathrm{e}} \pm \Omega$ carrying the information to be measured. For simplicity we confine our attention to setups involving a single photo-detector as shown in Fig. 3.2a. At the detector the associated photocurrent is given by

$$\hat{I}(\Omega) \approx \alpha_{\mathrm{LO}}^* \hat{a}_{\mathrm{out,e}}(\Omega) + \alpha_{\mathrm{LO}} \hat{a}_{\mathrm{out,e}}^\dagger(-\Omega), \tag{3.13}$$

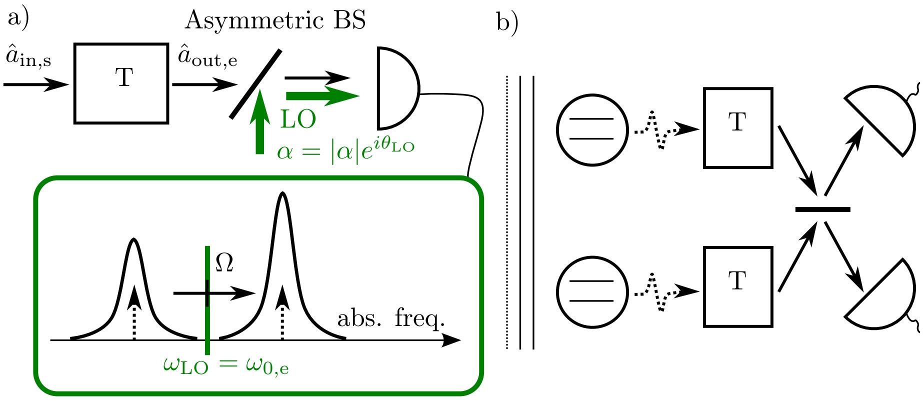

Figure 3.2: a) Interferometric detection of the output of the transducer mixed with a LO of frequency $\omega_{0,\text{e}}$ via a beam splitter. In general the Fourier component of the photocurrent $I(\Omega)$ at a frequency Ω will contain contributions from both the upper and lower sideband. b) Entanglement generation by transducing the output from two qubits to optical frequencies and interfering the signals on a beam splitter.

here the LO phase determines the relative phase with which the sidebands enter the linear combination. Assuming the transducer input to be confined to a single band, the scattering relation (3.6) and (3.13) imply that this will result in a simultaneous measurement of both input quadratures:

Substituting the former into the latter, we see that the spectral component $I(\Omega)$ is phase preserving and directly proportional to the signal input we want to measure $\hat{I}(\Omega) \propto \hat{a}_s(\Omega)$. Moreover, assuming an input coherent state $\langle \hat{a}_s \rangle = \alpha$ the signal-to-noise ratio is phase independent and is given by $\delta(\Omega - \Omega')|\langle I_\alpha(\Omega)\rangle|^2 / \langle I_{\alpha=0}(\Omega) I_{\alpha=0}(\Omega')\rangle = |\alpha|^2/P$ where I_α is the current with an incoming coherent state α and the power spectral noise density relative to the signal is given by

$$P(\Omega) = \frac{1}{2} + \frac{1}{|t_{\theta_{\text{LO}}}(\Omega)|^2}\Bigg[\eta(\Omega)N(\Omega) + \eta(-\Omega)N(-\Omega) + \frac{1}{2} + \frac{1 - \eta(\Omega) + \eta(-\Omega)}{2} + \text{Re}\left[e^{-2i\theta_{\text{LO}}} f(\Omega)\right]\Bigg]; \quad (3.14)$$

here the transfer function is defined as

$$t_{\theta_{\text{LO}}}(\Omega) \equiv e^{-i\theta_{\text{LO}}} U_{\text{s}}(\Omega) + e^{i\theta_{\text{LO}}} V_{\text{s}}^*(-\Omega), \quad (3.15)$$

and

$$f(\Omega)\delta(\Omega - \Omega') \equiv \langle \hat{\mathcal{F}}(\Omega)\hat{\mathcal{F}}(-\Omega')\rangle + \langle \hat{\mathcal{F}}(-\Omega)\hat{\mathcal{F}}(\Omega')\rangle,$$

is the interference between the noise in the sidebands. We notice that both the noise and efficiency has a phase dependence. This reflects the possible different degree to which the signals and noise are mapped to different quadratures of the output. If for instance the signal is mapped to one quadrature and the noise to another, the phase of the local oscillator can be set so that the heterodyne detection does not see the noise. Such details depend on the specifics of the transducer and we shall not enter this discussion here. In general, however, the interference term can be bounded by the Cauchy-Schwarz inequality and by setting the phase to have constructive interference for the signal we arrive at (see Appendix B.3 for details)

$$P(\Omega) \leq \frac{1}{2}+ \left(\frac{\sqrt{\eta(\Omega)}\sqrt{N(\Omega)+\frac{1}{2}[\frac{1}{\eta(\Omega)}-1]}+\sqrt{\eta(-\Omega)}\sqrt{N(-\Omega)+\frac{1}{2}[\frac{1}{\eta(-\Omega)}+1]}}{\sqrt{\eta(\Omega)}+\sqrt{\eta(-\Omega)}} \right)^2 . \tag{3.16}$$

Thus the sensitivity is primarily determined by a suitably weighted combination of the added noises $N(\pm\Omega)$, whereas the signal transfer efficiencies $\eta(\pm\Omega)$ mainly enter into the vacuum noise contributions $\propto [\eta(\pm\Omega)]^{-1} \mp 1$.

3.6.2 Deterministic transduction of coherent states

As an application for quantum information processing, we consider deterministic transduction of an incident coherent state of amplitude α [27] as e.g., required for continuous variable quantum information protocols. For simplicity, we only consider the upper-sideband output of the transducer although a better performance might in principle be achieved by also including the lower sideband. For a spectrally narrow input pulse at the upper sideband, for which the transducer parameters have the values $\eta_0^{(+)}, N_0^{(+)}$, we find that the output has the same noise in all quadratures and a resulting fidelity of

$$F_{\text{uc}} = \frac{1}{1+\eta_0^{(+)}N_0^{(+)}} \exp\left[-|\alpha|^2 \frac{|1-\sqrt{\eta_0^{(+)}}|^2}{1+\eta_0^{(+)}N_0^{(+)}} \right], \tag{3.17}$$

where we have included a phase rotation of the output that maximizes the fidelity. Hence the parameters $N_0^{(+)}$ and $\eta_0^{(+)}$ are again the crucial parameters for describing how well the transducer performs. However, the input amplitude $|\alpha|$ also enters Eq. (3.17) showing that larger amplitude states are more sensitive to signal attenuation or amplification, $\eta_0^{(+)} \neq 1$.

3.6.3 Discrete-variable transduction

We now turn to discrete variable photon counting of the output signal. The role of the transducer in this case is to perform frequency conversion of each photon. To this end, beam splitter interaction ($V_i \approx 0$) is desirable since it directly converts quanta from one frequency to another. We shall therefore consider transducers which are reasonably sideband-resolved. Nevertheless nonzero temperature as well as imperfect sideband resolution will still lead to noise photons leaving the transducer giving rise to an effective dark count rate. As opposed to the heterodyne measurement considered above, photon counting is not mode-selective and will count photons of all modes impinging on the detector. Using the scattering relation in Eq. (3.6) the dark count rate can be expressed as $r_{\mathrm{N}} = \eta_0^{(+)} N_0^{(+)} B$, where we have separated out the peak efficiency $\eta_0^{(+)}$ and added noise $N_0^{(+)}$ at that frequency and introduced

$$B = \int \frac{d\Omega}{2\pi} \frac{\eta(\Omega)}{\eta_0^{(+)}} \frac{N(\Omega)}{N_0^{(+)}}. \tag{3.18}$$

If the added noise $N(\Omega)$ can be considered constant over the entire bandwidth of the transducer, then B is just a measure of the bandwidth. On the other hand B may deviate significantly from this if, e.g., the transducer involves near-DC components with rapid variations in the thermal population near zero frequency.

We now consider an incoming temporal mode and express the annihilation operator of the mode through its spectral decomposition $\hat{a}_{\mathrm{s}} = \int h_{\mathrm{in}}(\Omega)\hat{a}_{\mathrm{in,s}}(\Omega)d\Omega$. Here $\hat{a}_{\mathrm{s}}$ obeys the desired discrete mode commutation relations given the normalization convention $\int |h_{\mathrm{in}}(\Omega)|^2 d\Omega = 1$. If we integrate over the entire output at the upper sideband, the mode dependent efficiency is given by $\eta_h = \int_0^\infty \eta(\Omega)|h_{\mathrm{in}}(\Omega)|^2 d\Omega$. Introducing the normalized mode function $h_{\mathrm{out}}(t)$ for the output and considering a single photon in the input, we may express the number of photons counted during a time interval ΔT as

$$\bar{n}_{\mathrm{out}} = \eta_0^{(+)} \left(\frac{\eta_h}{\eta_0^{(+)}} \int_0^{\Delta T} |h_{\mathrm{out}}(t)|^2 dt + N_0^{(+)} B \Delta T \right). \tag{3.19}$$

Here the first term in the parenthesis represents the desired component. This term is upper-bounded by unity, which can only be reached in the limit of a long time interval ΔT. Hence the added noise relative to the signal is again given by the added noise $N_0^{(+)}$, but now it is increased by a factor of $B\Delta T \gtrsim 1$, since photon counters are not mode selective.

3.6.4 Entanglement generation

As an application for quantum information processing in the discrete variable regime, we consider the remote entanglement of two, e.g., superconducting qubits by transducing the signal to optical frequencies for long distance communication as shown in Fig. 3.2b. A number of different protocols have been suggested for this [52]. In particular protocols relying on a single click are advantageous for low $\eta \ll 1$ since they give a higher success probability, whereas two click protocols are advantageous in terms of the resulting fidelity. Optimizing the protocols in the presence of dark counts we find (see Appendix B.4 for details)

$$\begin{aligned} F_{1\mathrm{c}} &\approx 1 - 2\sqrt{N_0^{(+)} B \Delta T} \\ F_{2\mathrm{c}} &\approx 1 - 6 N_0^{(+)} B \Delta T \end{aligned} \tag{3.20}$$

for the one- and two-click protocols respectively. Here we have assumed $\eta \ll 1$, as is typical in schemes for long-distance communication using quantum repeaters, and that $1/\Delta T$ is small compared to the bandwidth, so that the the pulse fits within both the spectral and temporal windows. As is evident, the key quantity for the quality of the generated entanglement is the added noise, whereas the efficiency of the transducer mainly enters into the success probability.

3.7 Concluding remarks

In this chapter we have given a generic characterization of time-stationary transducers in terms of signal transfer efficiency η and added noise N. We have pointed out that the non-equilibrium character of transduction requires us to make a trade-off in optimizing these quantities. By deriving the figures of merit for various quantum optics applications in terms of η and N, we have clarified the requirements on a transducer to perform efficiently in each of these contexts. This is important for a proper assessment of which applications a given transducer is suited for. Importantly, the examples considered here show that the added noise N often plays a more important role than the signal transfer efficiency η in determining the performance.

The figures of merit derived here will be evaluated for example electro-optomechanical transducer systems in Chapter 5 below.

Chapter 4

Electro-optomechanical equivalent circuits for transduction

The work presented in this chapter has been carried out in collaboration with Albert Schließer, Jacob M. Taylor, and Anders S. Sørensen.

4.1 Introduction

In the previous chapter we gave a general treatment of transducers without reference to the particulars of its individual components. The mathematical description used there is a generic input/output scattering formalism. Henceforth, we will focus on electro-optomechanical realizations of transducers. In this more specific context, we will introduce another unifying formalism: As an analysis and design tool for such electro-optomechanical transducers, we develop an equivalent circuit formalism, where the entire transducer is represented as an electrical circuit. Thereby we integrate the transduction functionality of optomechanical systems into the toolbox of electrical engineering allowing the use of the well-established techniques of that field. This unifying impedance description can be applied both for static (DC) and harmonically varying (AC) fields, accommodates arbitrary linear circuits, and is not restricted to the resolved sideband limit. Furthermore, by establishing the quantized input/output formalism for the equivalent circuit, we obtain the scattering matrix for linear transducers using standard circuit analysis, and thereby have a complete quantum mechanical characterization of the transducer (as discussed in Chapter 3). Hence, this mapping of the entire transducer to the language of electrical engineering both sheds light on how the transducer performs and can at the same time be used to optimize its performance by aiding the design of a suitable electrical circuit.

4.1.1 Equivalent circuits and circuit theory

In the formalism to be developed here, the entire coupled system of electrical modes, mechanical vibrations, and optical fields can be described in terms of a linear electrical circuit obeying Kirchhoff's laws. The formal reason that such an equivalent-circuit formulation is possible is that all the involved systems are conveniently described in the Heisenberg-Langevin input-output formalism for coupled oscillators. For an arbitrary linear circuit the Heisenberg-Langevin equations are nothing but a quantized version of Kirchhoff's well-known circuit laws. As a consequence all the involved degrees of freedom can be mapped to electrical analogs thereby allowing a common equivalent circuit description of the full electro-optomechanical system. Hence we may adequately describe the system by Kirchhoff's laws with impedances specified by the electro-optomechanical couplings.

A similar representation of mechanical oscillation modes coupled to an electrical circuit by an equivalent circuit element is already an established tool in the MEMS community [53, 54], known as the Butterworth-van Dyke circuit, and has also been applied in the context of cavity-electromechanics [14, 16]. We take this idea further by making the following important extensions: Firstly, we derive a quite general, yet simple, equivalent circuit for AC-driven electromechanical (EM) systems. Secondly, we derive the impedance of an optical mode, allowing us to construct a full electro-optomechanical equivalent circuit. Moreover, we will discuss how to quantize the theory.

A quantum theory for electrical circuits can be established by applying the canonical quantization procedure to appropriate charge and flux variables [55], where a suitable set of canonical variables can be identified by graph theoretical considerations [56]. Analogously to quantum optical input-output theory, an open system description can be developed to account for the dissipation induced by resistive circuit elements. While this approach fully accommodates nonlinear circuit elements such as Josephson junctions [57], we will in this article restrict ourselves to effectively linear circuits (w.r.t. displaced variables). In this case the Heisenberg-Langevin equations closely resemble the classical equations of motion. By solving the classical equations of motion we can thus find the complete scattering matrix representing the transducer. As a result we only need to quantize the incoming and outgoing fields to get a complete characterization of the transducer even in the quantum regime.

4.1.2 Structure of chapter

We will establish the electro-optomechanical equivalent circuit formalism gradually in the following steps: First we give an intuitive derivation of the mechanical equivalent impedance for a DC-biased interface in Section 4.2. Next, we extend the electromechanical equivalent circuit to the case of an AC electrical drive in Section 4.3. Then, in Section 4.4, we supplement the impedance formalism by introducing electrical input-output theory, which allows us to consider the in- and outcoupling of signals and noise. Following that, we describe how to quantize the theory in Section 4.5. Having established all aspects of the electromechanical equivalent circuit, we then introduce the optical subsystem by analogy in Section 4.6, thereby arriving at the full electro-optomechanical equivalent circuit. We use this, in Section 4.7, to derive the general structure of the scattering matrix for electro-optomechanical transducers using impedance rules. For demonstration we apply the formalism to a simple transducer in Section 4.8. In Section 4.9 we derive a reduced equivalent circuit by adiabatic elimination of the electrical and optical modes. Finally, we conclude the chapter in Section 4.10 with an outlook.

4.2 Intuitive derivation of electromechanical equivalent circuit for DC bias

We will now give a simple derivation of the equivalent circuit representation of a mechanical system coupled to an electrical circuit based on the treatment of capacitive electromechanical interfaces presented in Sections 1.2.3 and 2.2 above. Throughout the chapter we will consider only a single mechanical mode. For simplicity we start with the case of DC-biased coupling, postponing the AC-driven scenario until Section 4.3. In essence, we are looking for a way to describe the linear response of the system depicted in Fig. 4.1a with a circuit diagram consisting of standard components (capacitors, inductors, etc.). Consider adding charge δQ to the equilibrium charge $\bar{Q}_{\mathrm{c},0}$ already present on the EM capacitor of capacitance $C_{\mathrm{c}} \equiv C_{\mathrm{c}}(\bar{x})$. In this case the additional charge will introduce a force on the oscillator which pushes it towards a larger capacitance in order to reduce the charging energy. As a consequence the voltage fluctuation induced on the capacitor $\delta V(x)$ will be less than anticipated from naive expectation $\delta V(\bar{x}) = \delta Q / C_{\mathrm{c}}(\bar{x})$. Instead of modeling this as a capacitance which depends on δx we instead introduce a fixed capacitance $\bar{C}_{\mathrm{c}}$ and model the reduced voltage fluctuations as being due to a part of the charge $-\delta Q_{\mathrm{m}}$ not sitting on the capacitor but instead being diverted to an equivalent *mechanical* circuit branch *in parallel* to the coupling capacitor as shown in Fig. 4.1b [54]. Since the charge diverted to the parallel mechanical arm represents the mechanical motion we expect it to obey similar equations of motion as the viscously damped harmonic oscillator (2.7) considered in Section 2.2.2. Such an oscillator is mathematically equivalent to a serial RLC circuit and we therefore tentatively assume the mechanical arm to be simply a serial RLC,

$$Z_{\mathrm{m}}(\omega) = -i\omega L_{\mathrm{m}} + R_{\mathrm{m}} + \frac{1}{-i\omega C_{\mathrm{m}}}, \tag{4.1}$$

where $L_{\mathrm{m}}, R_{\mathrm{m}}, C_{\mathrm{m}}$ are mechanical equivalent circuit parameters (see Fig. 4.1b). Below we confirm this ansatz for the mechanical impedance and derive explicit expressions for the individual components in terms of the known physical parameters.

4.2.1 Dynamical variables of the equivalent circuit

The (non-dissipative) Hamiltonian corresponding to the circuit in Fig. 4.1b is

$$\begin{aligned} H' &= \frac{(\delta Q + \delta Q_{\mathrm{m}})^2}{2\bar{C}_{\mathrm{c}}} + \frac{\delta Q_{\mathrm{m}}^2}{2C_{\mathrm{m}}} + \frac{\phi_{\mathrm{m}}^2}{2L_{\mathrm{m}}} \\ &= \frac{\delta Q^2}{2\bar{C}_{\mathrm{c}}} + \frac{1}{2}\left(\frac{1}{\bar{C}_{\mathrm{c}}} + \frac{1}{C_{\mathrm{m}}}\right)\delta Q_{\mathrm{m}}^2 + \frac{\phi_{\mathrm{m}}^2}{2L_{\mathrm{m}}} + \frac{\delta Q \delta Q_{\mathrm{m}}}{\bar{C}_{\mathrm{c}}}, \end{aligned} \tag{4.2}$$

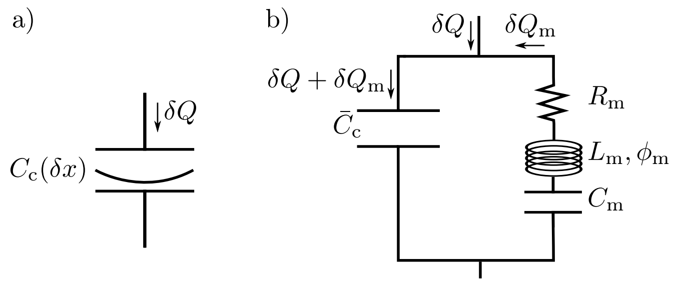

Figure 4.1: a) Sketch of a mechanically modulated coupling capacitor, $C_{\mathrm{c}}(x)$, where x is a suitable mechanical position coordinate. b) Equivalent circuit model with a serial RLC circuit in parallel to the *unmodulated* coupling capacitor $\bar{C}_{\mathrm{c}}$.

where $\delta Q_{\mathrm{m}}, \phi_{\mathrm{m}}$ are charge and magnetic flux variables of the virtual mechanical branch. The first two terms of Eq. (4.2) can be regarded as the charging energy of two capacitors, and the third term is the virtual magnetic field energy of the equivalent mechanical inductor. The fourth term, which is essential for the transducer, is a bilinear coupling between the mechanical oscillation and the capacitor. We can check the ansatz (4.1) and find expressions for the equivalent circuit parameters in terms of EM quantities by comparing Eq. (4.2) to the mechanical Hamiltonian (2.5) for a single mode combined with the coupling in Eq. (2.8) and the charging energy of the (steady-state) coupling capacitor $\bar{C}_{\mathrm{c}}$,

$$H_{\mathrm{C}} + H_{\mathrm{m},0} \approx \frac{\delta Q^2}{2\bar{C}_{\mathrm{c}}} + \frac{1}{2} m\omega_{\mathrm{m},Q}^2 \delta x^2 + \frac{p^2}{2m} + G\delta Q\delta x. \tag{4.3}$$

This is the the linearized Hamiltonian describing the mechanical system and the coupling capacitor, where in this chapter we use the notation $\delta\beta_j \leftrightarrow \delta x, m_j \leftrightarrow m, C_{\mathrm{eff}} \leftrightarrow C_{\mathrm{c}}, \bar{Q}(t) \leftrightarrow \bar{Q}_{\mathrm{c}}(t)$ relative to that of Chapter 2. Here we have defined a modified mechanical frequency $\omega_{\mathrm{m},Q}$,

$$\omega_{\mathrm{m},Q}^2 = \omega_{\mathrm{m},0}^2 + \frac{\bar{C}_{\mathrm{c}} G^2}{m} - \frac{\langle \bar{Q}_{\mathrm{c}}^2(t)\rangle}{2m\bar{C}_{\mathrm{c}}^2} \left.\frac{d^2 C_{\mathrm{c}}}{dx^2}\right|_{\mathrm{eq.}}, \text{ [DC bias]} \tag{4.4}$$

which is the "fixed charge" frequency ω' (2.14) discussed in Section 2.2.4.3. We will return to the interpretation of this frequency below.

We can now compare each of the terms of Eq. (4.2) with the corresponding term in Eq. (4.3) (the two expressions are written in the same order). We first compare the last (coupling) terms. These become identical if we make the identification

$$\delta Q_{\mathrm{m}} = \bar{C}_{\mathrm{c}} G\delta x, \tag{4.5}$$

that is, the charge variable of the virtual mechanical arm is proportional to the mechanical displacement.

Given the above correspondence, we expect a similar relationship among the canonical conjugates, $\phi_{\mathrm{m}} \propto p$. Taking the time derivative we indeed find

$$p = m\delta\dot{x} = \frac{m}{\bar{C}_{\mathrm{c}} G}\delta\dot{Q}_{\mathrm{m}} = \frac{m}{\bar{C}_{\mathrm{c}} G} I_{\mathrm{m}} = \frac{m}{\bar{C}_{\mathrm{c}} G L_{\mathrm{m}}}\phi_{\mathrm{m}}, \tag{4.6}$$

using $\phi_{\mathrm{m}} = L_{\mathrm{m}}\delta\dot{Q}_{\mathrm{m}}$ and $I_{\mathrm{m}} \equiv \delta\dot{Q}_{\mathrm{m}}$. Equating the inductive energy term of Eq. (4.2) with the kinetic of Eq. (4.3) and substituting using (4.6) we find an expression for L_{m}

$$\frac{p^2}{2m} = \frac{\phi_{\mathrm{m}}^2}{2L_{\mathrm{m}}} \Leftrightarrow L_{\mathrm{m}} = \frac{m}{\bar{C}_{\mathrm{c}}^2 G^2}. \tag{4.7}$$

Substituting L_{m} into Eq. (4.6) we then find

$$\phi_{\mathrm{m}} = \frac{1}{\bar{C}_{\mathrm{c}} G} p. \tag{4.8}$$

Taken together, Eqs. (4.5,4.8) show that the dynamical variables of the equivalent circuit $\{\delta Q_{\mathrm{m}}, \phi_{\mathrm{m}}\}$ are related to the original coordinates $\{\delta x, p\}$ by a simple canonical scaling transformation.

Finally, we determine the equivalent mechanical resistance R_{m}, which is most easily done by comparing equations of motion (where damping can be incorporated straightforwardly). Equating the viscous dissipation rate in the mechanical Langevin equation (2.7) with $\dot{\phi}_{\mathrm{m}} = -(R_{\mathrm{m}}/L_{\mathrm{m}})\phi_{\mathrm{m}} + \ldots$ we get

$$R_{\mathrm{m}} = \gamma_{\mathrm{m},0} L_{\mathrm{m}} = \frac{m\gamma_{\mathrm{m},0}}{\bar{C}_{\mathrm{c}}^2 G^2}, \tag{4.9}$$

using the expression in Eq. (4.7) for L_{m} and denoting the intrinsic mechanical damping rate $\gamma_{\mathrm{m},0}$. In the same way, the associated mechanical Johnson noise is found by comparison with $\dot{\phi}_{\mathrm{m}} = 2V_{\mathrm{m}} + \ldots$ to be

$$2V_{\mathrm{m}} \equiv \frac{F}{G\bar{C}_c}, \tag{4.10}$$

where the factor of two has been included to conform with the electrical input-output formalism to be presented in Section 4.4 below, cf. Eq. (4.33).

4.2.2 Effective mechanical resonance frequencies

In Section 2.2.4.2 we discussed a subtlety of the effective mechanical resonance frequency regarding its dependence on the time-scale of the mechanical mode (here represented by δQ_{m}) in relation to that of the electrical mode δQ. In the present context of the EM equivalent circuit, this discussion comes out naturally: Two different limits can be understood from Fig. 4.1b and Eqs. (4.2), namely fixed voltage vs. fixed charge dynamics. Fixed voltage across the terminals of Fig. 4.1b corresponds to the situation where the voltage bias in the circuit acts much faster than the mechanical modulation, i.e. supplying and absorbing charge instantaneously so as to maintain a fixed voltage. Hence the voltage across the mechanical arm will in this case be independent of the coupling capacitor arm; therefore we may read off the *fixed voltage* mechanical resonance frequency as the resonance frequency of the mechanical branch of Fig. 4.1b:

$$\omega_{\mathrm{m},V}^2 = \frac{1}{L_{\mathrm{m}} C_{\mathrm{m}}}, \tag{4.11}$$

sometimes referred to as the mechanical series resonance [54]. For given applied voltage across the coupling capacitor the maximal mechanical response occurs at $\omega_{\mathrm{m},V}$. If, on the other hand, the time-scale of mechanical modulation is much faster than that of δQ (thus preventing the voltage bias from reacting), we may effectively set $\delta Q \to 0$ and the *fixed charge* mechanical resonance frequency will be the resonance frequency of the entire loop in Fig. 4.1b in which case the capacitances $\bar{C}_{\rm c}, C_{\rm m}$ are added in series

$$\omega_{{\rm m},Q}^2 = \frac{1}{L_{\rm m}}\left(\frac{1}{\bar{C}_{\rm c}} + \frac{1}{C_{\rm m}}\right). \text{ [DC bias]} \tag{4.12}$$

This is sometimes referred to as the mechanical parallel resonance [54]. This is the same relation obtained by equating the second terms in Eq. (4.2) and Eq. (4.3). For a given current running into the (physical) coupling capacitor $C_{\rm c}(x)$, the maximal mechanical response occurs at $\omega_{{\rm m},Q}$. By comparing Eqs. (4.11) and (4.12) we see that the two limiting mechanical frequencies are related by

$$\omega_{{\rm m},Q}^2 - \omega_{{\rm m},V}^2 = \frac{1}{L_{\rm m}\bar{C}_{\rm c}} = \frac{\bar{C}_{\rm c}G^2}{m}, \text{ [DC bias]} \tag{4.13}$$

from which we conclude that $\omega_{{\rm m},Q} \geq \omega_{{\rm m},V}$. The mechanical oscillator thus has a different resonance frequency depending on the circuit to which it is coupled (as we also concluded in Section 2.2.4). For instance if the bias voltage is applied via a low-pass filter with cut-off frequency below the mechanical frequency (as in Ref. [1]) this entails fixed charge conditions.

From the expression for $\omega_{{\rm m},Q}^2$ in Eq. (4.4) and the relation in Eq. (4.13) we can find an expression for $\omega_{{\rm m},V}$ in terms of the known physical quantities

$$\omega_{{\rm m},V}^2 = \omega_{{\rm m},0}^2 - \frac{\langle \bar{Q}_{\rm c}^2(t)\rangle}{2m\bar{C}_{\rm c}^2}\left.\frac{d^2C_{\rm c}}{dx^2}\right|_{\rm eq.}, \tag{4.14}$$

consistent with Eq. (2.16). Using Eqs. (4.7,4.11) we can then express the mechanical capacitance through quantities which can be calculated from first principles

$$C_{\rm m} = \frac{\bar{C}_{\rm c}^2|G|^2}{\omega_{{\rm m},V}^2 m}. \tag{4.15}$$

4.3 Electromechanical equivalent circuit for AC drive

Above we have given an intuitive derivation of the equivalent circuit in the case of a DC-biased capacitor. This allows us to describe how electrical signals are converted into mechanical motion at the same frequency. The main purpose of a transducer is, however, to convert signals from one frequency Ω to another $\omega_{\rm d} \pm \Omega$ by harmonically driving the system with a frequency $\omega_{\rm d}$. In the following we shall develop an equivalent circuit formalism to describe such a situation. To this end we will consider a system corresponding to a low frequency mechanical oscillator, e.g. in the MHz regime, driven by a high frequency bias field, e.g. in the microwave regime.

When the capacitor is driven by an alternating voltage the charge on the capacitor will take the form

$$Q(t) = \bar{Q}_{\rm c}(t) + \delta Q(t) = \bar{Q}_{{\rm c},0}\left(e^{-i\omega_d t} + e^{i\omega_d t}\right) + \delta Q(t), \tag{4.16}$$

as in Section 1.2.3. As previously, this amplitude should be found by self-consistently solving for the equilibrium configuration of the electrical and mechanical system, and $\delta Q(t)$ then represents the fluctuations around this value.

It will be convenient to work in the Fourier domain. Using that all charges, currents, and voltages are real valued, we introduce the Fourier transform as an integral over positive frequencies so that, e.g., the voltage fluctuations are denoted by

$$\delta V(t) = \int_0^\infty \frac{d\omega}{\sqrt{2\pi}} \left[V(\omega)\mathrm{e}^{-i\omega t} + V^*(\omega)\mathrm{e}^{i\omega t} \right] \tag{4.17}$$

with similar expressions for the charge δQ and current δI fluctuations as well as the position δx and momentum p fluctuations. To proceed it is convenient not to deal with the specifics of the rest of the circuit and we therefore replace it with its Thévenin equivalent as shown in Fig. 4.2a, where the rest of the circuit is represented by the ideal voltage source δV and the input impedance Z.

If we now consider the contribution to Kirchhoff's voltage law coming from the coupled EM system we have

$$\delta V(t) = ... + \frac{Q(t)}{C_{\mathrm{c}}(x)} - \frac{\bar{Q}_{\mathrm{c},0}\left(\mathrm{e}^{-i\omega_d t} + \mathrm{e}^{i\omega_d t}\right)}{\bar{C}_{\mathrm{c}}} \tag{4.18}$$

$$\approx ... + \frac{\delta Q(t)}{\bar{C}_{\mathrm{c}}} + G\delta x(t)\left(\mathrm{e}^{-i\omega_d t} + \mathrm{e}^{i\omega_d t}\right) \tag{4.19}$$

Here we have in the last line expanded to lowest order in the fluctuations and introduced the coupling constant G as defined in (2.9).

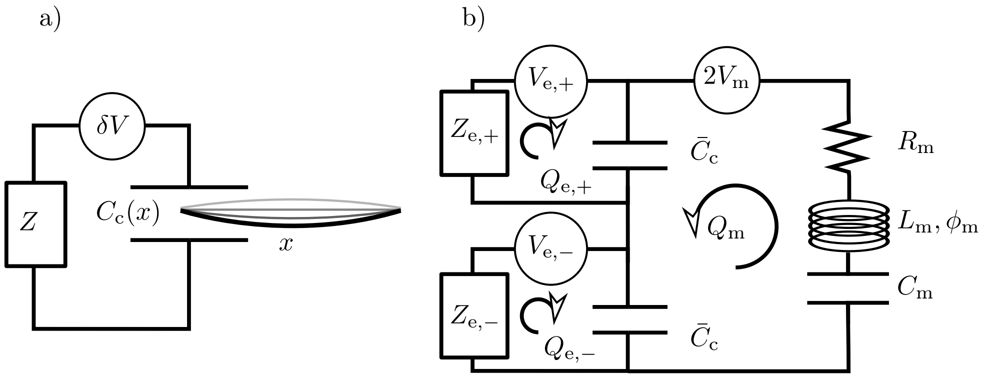

Figure 4.2: a) Thévenin equivalent circuit considered for the AC-driven system. An ideal voltage source $\delta V(\omega)$ in series with an impedance $Z(\omega)$ drives the coupled membrane capacitor system. b) Electromechanical equivalent circuit. The mechanical motion is replaced by the central loop current $I_{\mathrm{m}}(\Omega)$. Through capacitors of capacitance $\bar{C}_c$ the mechanical current is connected to loop currents $I_{\mathrm{e},+}$ and $I_{\mathrm{e},-}$ representing the upper and lower sidebands of the electrical current, which are driven by voltage sources $V_{\mathrm{e},+}(\Omega) = \delta V(\omega_d + \Omega)$ and $V_{\mathrm{e},-}(\Omega) = \delta V^*(\omega_d - \Omega)$.

We will now assume that the mechanical component is the slowest frequency scale in the problem so that we can neglect the mechanical response, $\delta x(\omega) \approx 0$, at high frequencies $\omega > \omega_d$, this amounts to the assumption that the mechanical linewidth is narrow compared to $\omega_{\rm d}$. With this assumption, the frequency components of the voltage $\delta V(\omega)$ with $\omega > \omega_d$ are according to Eq. (4.19) only coupled to the positive frequency component of the mechanical motion $\delta x(\omega - \omega_d)$. Similarly, the negative frequency component of the voltage $\delta V^*(\omega)$ with $\omega < \omega_d$ is only coupled to $\delta x(\omega_d - \omega)$. We thus arrive at

$$\delta V(\omega_d + \Omega) = Z(\omega_d + \Omega)\delta I(\omega_d + \Omega) + \frac{\delta Q(\omega_d + \Omega)}{\bar{C}_{\rm c}} - G\delta x(\Omega) \quad (4.20)$$

$$\delta V^*(\omega_d - \Omega) = Z^*(\omega_d - \Omega)\delta I^*(\omega_d - \Omega) + \frac{\delta Q^*(\omega_d - \Omega)}{\bar{C}_{\rm c}} - G\delta x(\Omega) \quad (4.21)$$

From this expression the principle of the transducer is apparent: the oscillating drive connects different frequency components of the mechanical and electrical circuit. Eqs. (4.20,4.21) also show that electrical frequency components are mapped into the mechanical mode in a non-invertible, 2-to-1 manner. This characteristic permits us to avoid the use of matrix-valued impedance functions and is hence the key to establishing a relatively simple equivalent circuit for the AC case below. The two components represent the two sidebands to which the mechanical mode couples as illustrated in Fig. 1.3 on page 20. Essentially, as we will see below, we may consider the upper and lower electrical sidebands, (4.20) and (4.21), as distinct degrees of freedom coupling to the mechanical mode. In terms of the generic transducer discussion in Section 3.3, these two equations represent symmetrically placed bands that couple to a single band centered around zero frequency as illustrated in Fig. 3.1b on page 39.

We now turn to the mechanical oscillator. By combining the interaction Hamiltonian (2.8) with the mechanical Langevin equation (2.7) we may derive the equation of motion for the mechanical momentum

$$\dot{p} = -m\omega_{{\rm m},V}^2\delta x - \gamma_{{\rm m},0}p + F(t) - G\big(\mathrm{e}^{-i\omega_d t} + \mathrm{e}^{i\omega_d t}\big)\delta Q - 2G^2\bar{C}_{\rm c}\delta x. \quad (4.22)$$

In the above expression we have averaged over oscillations occurring with a frequency $2\omega_d$ in accordance with the assumption that the mechanical response only happens on a slower time scale. Compared to the DC-biased case, where $\omega_{{\rm m},Q}$ and $\omega_{{\rm m},V}$ are related by (4.13), this averaging in the AC case gives a factor of two appearing on the right-hand side of (4.13) and hence in the last term of Eq. (4.22). This merely reflects the difference in the average of the square of the charge oscillation which is $\langle\bar{Q}_{\rm c}^2(t)\rangle = 2\bar{Q}_{{\rm c},0}^2$ with the definition in Eq. (4.16) whereas it is $\bar{Q}_{{\rm c},0}^2$ in the DC case. For later convenience we have here introduced $\omega_{{\rm m},V}$ in (4.22) from Eq. (4.14) which we will again identify as the resonance frequency at fixed voltage. Converting Eq. (4.22) to Fourier space and introducing the electrical analogs of the mechanical parameters as defined in Eqs. (4.5,4.6,4.7,4.9,4.10,4.15) we find

$$2V_{\rm m}(\Omega) = -i\Omega L_{\rm m}I_{\rm m}(\Omega) + R_{\rm m}I_{\rm m}(\Omega) + \frac{Q_{\rm m}(\Omega)}{C_{\rm m}} + \frac{2Q_{\rm m}(\Omega) + \delta Q(\omega_d + \Omega) + \delta Q^*(\omega_d - \Omega)}{\bar{C}_{\rm c}}. \quad (4.23)$$

The equation of motion for the momentum (4.23) resembles Kirchhoff's Voltage Law, except for the mixing of different frequency components and the appearance of the complex conjugate. To absorb the differences in frequency and the complex conjugate we define new voltages and charges for the upper and lower sidebands of the drive

$$V_{\mathrm{e},+}(\Omega) = \delta V(\omega_d + \Omega) \qquad V_{\mathrm{e},-}(\Omega) = \delta V^*(\omega_d - \Omega) \tag{4.24}$$

$$Q_{\mathrm{e},+}(\Omega) = \delta Q(\omega_d + \Omega) \qquad Q_{\mathrm{e},-}(\Omega) = \delta Q^*(\omega_d - \Omega). \tag{4.25}$$

For the current we wish to retain the standard relation $Q_{\mathrm{e},l} = -i\Omega I_l$ with $l = \pm$. We achieve this with the choice

$$I_{\mathrm{e},+}(\Omega) = \frac{\Omega}{\omega_d + \Omega} I(\omega_\mathrm{d} + \Omega) \qquad I_{\mathrm{e},-}(\Omega) = -\frac{\Omega}{\omega_d - \Omega} I^*(\omega_\mathrm{d} - \Omega), \tag{4.26}$$

where the minus sign in the last expression is a consequence of the complex conjugation. Correspondingly we have the impedances

$$Z_{\mathrm{e},+}(\Omega) = \frac{\omega_d + \Omega}{\Omega} Z(\omega_\mathrm{d} + \Omega) \qquad Z_{\mathrm{e},-}(\Omega) = -\frac{\omega_d - \Omega}{\Omega} Z^*(\omega_\mathrm{d} - \Omega). \tag{4.27}$$

Here the combination of the negative sign and the complex conjugation in $Z_{\mathrm{e},-}$ means that reactances retain their sign whereas resistances get a negative sign. This reflects the instability associated with the lower sideband which gives rise to parametric amplification. Furthermore the factor in front means that capacitors keep their usual expression for the impedance $1/(-i\Omega C)$ whereas inductances and resistances are scaled up to reflect that it is harder to induce a given current at a higher frequency. Combining these definitions with the equations of motion in Eq. (4.20), (4.21), and (4.23) we finally achieve

$$2V_\mathrm{m}(\Omega) = \left[-i\Omega L_\mathrm{m} + R_\mathrm{m} + \frac{1}{-i\Omega C_\mathrm{m}}\right] I_\mathrm{m}(\Omega) + \frac{2I_\mathrm{m}(\Omega) + I_{\mathrm{e},+}(\Omega) + I_{\mathrm{e},-}(\Omega)}{-i\Omega \bar{C}_c} \tag{4.28}$$

$$\begin{aligned} V_{\mathrm{e},+}(\Omega) &= Z_{\mathrm{e},+}(\Omega) I_{\mathrm{e},+}(\Omega) + \frac{I_{\mathrm{e},+}(\Omega) + I_\mathrm{m}(\Omega)}{-i\Omega \bar{C}_\mathrm{c}} & (4.29) \\ V_{\mathrm{e},-}(\Omega) &= Z_{\mathrm{e},-}(\Omega) I_{\mathrm{e},-}(\Omega) + \frac{I_{\mathrm{e},-}(\Omega) + I_\mathrm{m}(\Omega)}{-i\Omega \bar{C}_\mathrm{c}}. & (4.30) \end{aligned}$$

These equations of motion have a straightforward interpretation in terms of the equivalent circuit diagram in Fig. 4.2b, where the mechanical system is represented by the loop current I_m in the central loop, whereas the outer loops represent the upper and lower sidebands of the electrical system.

From the circuit it is immediately apparent that $\omega_{\mathrm{m},V} = 1/\sqrt{L_\mathrm{m} C_\mathrm{m}}$ is the mechanical resonance frequency in the limit where the capacitor is connected to an ideal voltage source $Z_{\mathrm{e},+} = Z_{\mathrm{e},-} = 0$, so that the outer arms are replaced by short circuits bypassing $\bar{C}_\mathrm{c}$. On the other hand, for fixed charge $Z_{\mathrm{e},+}, Z_{\mathrm{e},-} \to \infty$ the mechanical resonance frequency at fixed charge $\omega_{m,Q}$ is shifted from $\omega_{m,V}$ by twice the amount given in Eq. (4.13) since $\bar{C}_\mathrm{c}$ appears for both sidebands (as remarked above). The limit of resolved sidebands is obtained by taking $Z_{\mathrm{e},-}(Z_{\mathrm{e},+}) \to \infty$ for red-detuned (blue-detuned) electrical drive (for finite $V_{\mathrm{e},-}, V_{\mathrm{e},+}$).

This completes the derivation of the equivalent circuit. With the results developed here the analysis of the coupled EM system can now be reduced to finding voltages and currents of linear circuits. This gives a very direct description of how voltage fluctuations are transduced to the mechanical system and vice versa.

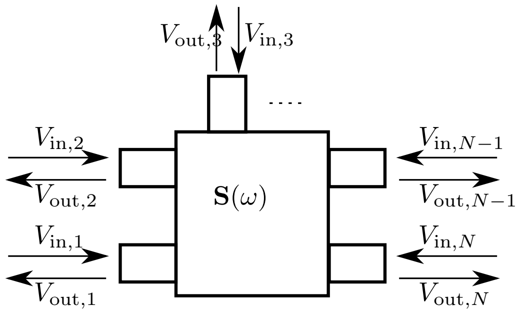

Figure 4.3: Illustration of the scattering matrix $\mathbf{S}(\omega)$ for an N-port system.

4.4 Electrical input-output formalism

In the preceding sections we have derived an equivalent impedance description of electromechanical systems. We will now establish the equations that describe how signals and noise enter and exit the system via its various ports, which is essential to the analysis of transducers. Physically, the ports of the circuit correspond to transmission lines, resistive elements and mechanical dissipation. In order to have an equivalent circuit description we shall establish a common mathematical description of these sources. Input-output formalism is a well-established tool for describing open quantum optical systems [51] (see also Section 3.3). A formally equivalent formalism is employed in the characterization of radio-frequency and microwave circuits [58]. In the context of a linear N-port network, with the i'th port connected to a transmission line of characteristic impedance $Z_{\text{tx},i}$, the outgoing signals can be related to the incoming ones by the classical scattering matrix

$$\vec{V}_{\text{out}}(\Omega) = \mathbf{S}(\Omega)\vec{V}_{\text{in}}(\Omega), \tag{4.31}$$

where $\vec{V}_{\text{in/out}}(\Omega)$ is a vector containing the complex amplitudes of the incoming and outgoing traveling waves. Note that this vector should be understood in the framework of the preceding section where $V_{\text{in/out},i}(\Omega)$ is in a rotating frame wrt. to the central frequency $\omega_{\text{d},i}$ (specific to subsystem i), and the lower sideband enter as an independent input containing the complex conjugate of the voltage $\delta V^*(\omega_d - \Omega)$. This is foreign to ordinary linear circuit theory but arises here due to the driven electromechanical nonlinearity and allows us to capture the frequency conversion of the transducer. Once the scattering matrix $\mathbf{S}(\Omega)$ in (4.31) has been obtained, we have a full characterization of the dynamics of the transducer. When the initial state of all the involved reservoirs is specified, the scattering matrix can then be used to evaluate the performance of the transducer for whichever application one is interested in, as discussed in Chapter 3.

To link the external input and output fields in $\vec{V}_{\text{in/out}}(\Omega)$ to the internal currents and voltages in the impedance formalism of the preceding two sections, we must derive how the presence of a port in the circuit modifies Kirchhoff's equations. To this end, we observe that the voltage V_i across and the net current amplitude I_i into the i'th terminal can be expressed in terms of the traveling

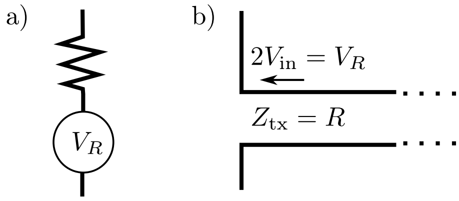

Figure 4.4: Illustration of the mapping between a) resistor R with Johnson voltage noise V_R and b) a semi-infinite lossless transmission line with characteristic impedance $Z_{\text{tx}} = R$ and incoming signal $2V_{\text{in}} = V_R$.

wave amplitudes at the terminal as

$$\begin{aligned} V_i &= V_{\text{in},i} + V_{\text{out},i} \\ I_i &= \frac{1}{Z_{\text{tx},i}} \left[V_{\text{in},i} - V_{\text{out},i} \right]. \end{aligned} \tag{4.32}$$

From Eqs. (4.32) we can derive the equivalent of a fluctuation-dissipation theorem for each port [55],

$$V_i = -Z_{\text{tx},i} I_i + 2V_{\text{in},i}. \tag{4.33}$$

Eq. (4.33) is the key to extending Kirchhoff's laws to an open system setting, i.e. to derive the classical Langevin equations for linear circuits. Specifically, for Kirchhoff's Voltage Law for any loop including one of the ports, it tells us that the port introduces dissipation corresponding to the real-valued resistance $R = Z_{\text{tx},i}$, as well as a source term $2V_{\text{in},i}$. Conversely, as pointed out by Nyquist, this implies that any resistive element R in the circuit can be mapped to an equivalent semi-infinite transmission line of characteristic impedance $Z_{\text{tx},j} = R$ (for which we will specify a thermal mixed state for the corresponding source term $V_{\text{in},j}$); this idea is illustrated in Fig. 4.4. Hence, the resulting open circuit formalism accommodates both noise and signal inputs exactly as its quantum optical counterpart. From Eqs. (4.32) we can also derive the input-output relations for the ports,

$$V_{\text{out},i} = -Z_{\text{tx},i} I_i + V_{\text{in},i}, \tag{4.34}$$

that allow us to determine the outgoing voltages.

With the above in place, we may, for an arbitrary N-port passive linear circuit, use Kirchhoff's circuit laws supplemented with Eqs. (4.33) and (4.34) to derive the scattering matrix $\mathbf{S}(\omega)$, Eq. (4.31). In practice this can, e.g., be done by applying voltage and current division rules to the equivalent circuit diagram under consideration as will be demonstrated for the full electro-optomechanical circuit in Section 4.7.

4.5 Quantization of the equivalent circuit

Turning now to the quantization of the circuit theory, we remark that this task is greatly facilitated by the great degree parallelism between the classical and quantum cases. One way to see this is to note that for a bilinear Hamiltonian, the Heisenberg-Langevin equations of the system are form-equivalent to their classical counterpart, Hamilton's equations of motion. As a consequence, the linearity of the equations entails that the method for deriving the scattering matrix $\mathbf{S}(\omega)$ in the classical case carries through quantum mechanically. Hence the scattering matrix $\mathbf{S}(\omega)$ is the same quantum mechanically as it is classically. Put differently, due to the linearity the scattering matrix is independent of the amplitude. Therefore the quantum mechanical equations of motion are in the macroscopic correspondence limit for all amplitudes of the fields (within the validity of the linearized theory), and must give the same as the classical solution according to the correspondence principle. This circumstance simplifies the problem considerably, as we do not have to explicitly quantize the internal degrees of freedom of the circuit prior to solving for $\mathbf{S}(\omega)$, which contains all desired information about the dynamics of the system. Hence, the quantum circuit theory simply consists of a scattering relation (of the form (4.31)) relating the quantized input and output fields [55]. To complete the theory we thus have to provide a quantum description of the incoming and outgoing modes.

To this end, we expand the quantized voltage amplitudes for the incoming and outgoing fields into frequency components according to

$$\hat{V}_{\mathrm{in/out},i}(t) = \int_0^\infty \frac{d\omega}{\sqrt{2\pi}} \sqrt{\frac{\hbar\omega Z_{\mathrm{tx},i}}{2}} \left[\hat{b}_{\mathrm{in/out},i}(\omega) e^{-i\omega t} + \mathrm{H.C.}\right], \tag{4.35}$$

where the annihilation operators $\hat{b}_{\mathrm{in/out},i}(\omega)$ obey the commutation relations

$$[\hat{b}_{\mathrm{in/out},i}(\omega), \hat{b}^\dagger_{\mathrm{in/out},j}(\omega')] = \delta(\omega - \omega')\delta_{i,j}, \tag{4.36}$$

with all other commutators involving these being zero. Eqs. (4.35,4.36) specify the correct ohmic noise operator that enters the quantum version of (4.33) within the First Markov Approximation [46]. This expansion has the same form as the Fourier transform introduced in Eq. (4.17), and hence we can immediately identify the corresponding voltage operators which replace their classical counterparts

$$V_{\mathrm{in/out},i}(\omega) \to \hat{V}_{\mathrm{in/out},i}(\omega) = \sqrt{\frac{\hbar\omega Z_{\mathrm{tx},i}}{2}} \hat{b}_{\mathrm{in/out},i}(\omega) \tag{4.37}$$

$$V^*_{\mathrm{in/out},i}(\omega) \to \hat{V}^\dagger_{\mathrm{in/out},i}(\omega) = \sqrt{\frac{\hbar\omega Z_{\mathrm{tx},i}}{2}} \hat{b}^\dagger_{\mathrm{in/out},i}(\omega). \tag{4.38}$$

From these expressions we can then find the corresponding rotating frame operators entering into the equivalent circuit using Eq. (4.24). To characterize the noise we will assume that all reservoirs are in their thermal state as specified by the expectation values

$$\langle \hat{V}^\dagger_{\mathrm{in},i}(\omega) \hat{V}_{\mathrm{in},j}(\omega')\rangle = \frac{\hbar\omega' Z_{\mathrm{tx},i}}{2} \bar{N}_i(\omega')\delta(\omega - \omega')\delta_{i,j} \tag{4.39}$$

and $\langle \hat{V}_{\mathrm{in},i}(\omega)\hat{V}_{\mathrm{in},j}(\omega')\rangle = 0$, where the thermal flux pr. unit bandwidth is $\bar{N}_i(\omega) \equiv (e^{\hbar\omega/k_{\mathrm{B}}T_i} - 1)^{-1}$. The thermal expectation values of the mechanical Johnson voltage $V_{\mathrm{m}}(\Omega)$, (4.10), take on the same form as (4.39) with the replacements $Z_{\mathrm{tx},i} \to R_{\mathrm{m}}, T_i \to T_{\mathrm{m}}$ [59].

4.6 Optical impedance and full electro-optomechanical equivalent circuit

In Section 4.3 we derived the equivalent circuit for an AC-driven electromechanical interface involving an arbitrary linear electrical circuit. We now turn to the optomechanical coupling, assuming we may consider a single optical cavity mode whose frequency $\omega_{\rm cav}(\hat{x})$ is modulated by the same mechanical position $\hat{x}$ entering the electromechanical coupling (paralleling the discussion in Sections 1.2.2 and 1.2.3). Following the standard procedure [7], we take as our starting point the quantum Hamiltonian for the optical mode,

$$H_{\rm opt} = \hbar\omega_{\rm cav}(\hat{x})\hat{a}^\dagger\hat{a}. \tag{4.40}$$

Applying a coherent optical laser drive of frequency $\omega_{\rm l}$ to the optical cavity (represented by a Hamiltonian $H_{\rm l}$), we expand the total Hamiltonian of the optomechanical system $H = H_{\rm opt} + H_{\rm m,0} + H_{\rm l} + \ldots$ around the ensuing steady-state configuration $(\bar{x}, \alpha)$ (ignoring the terms in the Hamiltonian responsible for coupling to the environment of the hybrid system). The linearized dynamics of the displaced variables, $\hat{x} = \bar{x} + \delta\hat{x}$ and $\hat{a} = \alpha + \delta\hat{a}$, is then described by the Hamiltonian

$$H_{\rm OM} = \hbar\bar{\omega}_{\rm cav}\delta\hat{a}^\dagger\delta\hat{a} + \left[\frac{\delta\hat{p}^2}{2m} + \frac{1}{2}m\omega_{\rm m}^2\delta\hat{x}^2\right] + H_{\rm OM,int} \tag{4.41}$$

$$H_{\rm OM,int} \equiv G_{\rm OM}\delta\hat{x}(e^{i\omega_{\rm l}t}e^{-i\theta}\delta\hat{a} + e^{-i\omega_{\rm l}t}e^{i\theta}\delta\hat{a}^\dagger)/\sqrt{2} \tag{4.42}$$

in terms of the steady-state cavity resonance $\bar{\omega}_{\rm cav}$, the optically shifted mechanical frequency $\omega_{\rm m}$ and the optomechanical coupling strength $G_{\rm OM}$ (units of energy per length)

$$\omega_{\rm m}^2 \equiv \omega_{\rm m,0}^2 + \frac{\hbar|\alpha|^2}{m}\left.\frac{d^2\omega_{\rm cav}}{dx^2}\right|_{x=\bar{x}},\ G_{\rm OM} \equiv \sqrt{2}\hbar\left.\frac{d\omega_{\rm cav}}{dx}\right|_{x=\bar{x}}|\alpha|,\ \theta \equiv {\rm Arg}[\alpha]. \tag{4.43}$$

The coupling strength $G_{\rm OM}$ is related to the more familiar coupling rate $g_{\rm OM}$ between creation and annihilation operators that occurs in the following restatement of (4.42),

$$H_{\rm OM,int} = \hbar g_{\rm OM}(\delta\hat{c} + \delta\hat{c}^\dagger)(e^{i\omega_{\rm l}t}e^{-i\theta}\delta\hat{a} + e^{-i\omega_{\rm l}t}e^{i\theta}\delta\hat{a}^\dagger), \tag{4.44}$$

where $\delta\hat{x} = x_{\rm ZPF}(\delta\hat{c} + \delta\hat{c}^\dagger)$ and $x_{\rm ZPF} \equiv \sqrt{\hbar/2m\omega_{\rm m}}$. Comparing (4.42) and (4.44), the two optomechanical coupling parameters are seen to be related by

$$g_{\rm OM} = G_{\rm OM}/\sqrt{4\hbar m\omega_{\rm m}}. \tag{4.45}$$

The first and second terms of (4.41) are the "free-evolution" Hamiltonians of the displaced optical and mechanical modes whereas the third term, $H_{\rm OM,int}$, is the drive-enhanced linear coupling between them. In order to achieve equations of motion equivalent to those governing the electromechanical coupling considered in Section 4.3, we note that within the rotating wave approximation (RWA), we may approximate the interaction Hamiltonian (4.42) as

$$H_{\rm OM,int} \approx G_{\rm OM}\delta\hat{x}(e^{i\omega_{\rm l}t} + e^{-i\omega_{\rm l}t})\hat{X}, \tag{4.46}$$

where we have introduced the dimensionless light quadratures

$$\hat{X} \equiv (e^{-i\theta}\delta\hat{a} + e^{i\theta}\delta\hat{a}^\dagger)/\sqrt{2},\ \hat{P} \equiv (e^{-i\theta}\delta\hat{a} - e^{i\theta}\delta\hat{a}^\dagger)/(\sqrt{2}i), \tag{4.47}$$

obeying $[\hat{X}, \hat{P}] = i$. Note that here we go in the opposite direction of what is typically done in the RWA, where the standard procedure is to replace Eq. (4.46) by Eq. (4.42). In optomechanics the RWA is typically a very good approximation since the dynamics on the mechanical timescale $2\pi/\omega_\mathrm{m}$ are much slower than that of the optical drive $2\pi/\omega_\mathrm{l}$. Hence the starting point of the derivation of the coupling assumed the RWA from the beginning, and there is a priori no reason to prefer one form over the other. By choosing the form in Eq. (4.46), however, the Hamiltonian linearly couples $\delta\hat{x}$ to $\hat{X}$ with strength G_OM in a manner similar to the linearized electromechanical interaction Hamiltonian (1.9) considered above. With the form in Eq. (4.46) we can thus obtain the equivalent circuit in a similar manner.

We also need to specify how the optical mode couples to its environment via its loss and drive ports, as can be conveniently treated using quantum optical input/output formalism. Traditionally this is again only discussed within the RWA, and the microscopic details of the optical bath coupling is in general not known, leaving it an open question how the bath couples to the quadrature variables $(\hat{X}, \hat{P})$ [46]. Assuming linear coupling to the bath modes, however, the precise microscopic model is unimportant within the RWA. Thus, in a spirit similar to (4.46), this permits us to assume that the optical bath modes couple to the quadrature $\hat{X}$, resulting in the usual viscous damping and noise terms in the equation of motion of the conjugate quadrature $\hat{P}$

$$\begin{aligned}\dot{\hat{X}} &= \bar{\omega}_\mathrm{cav}\hat{P}\\ \dot{\hat{P}} &= -\bar{\omega}_\mathrm{cav}\hat{X} - \kappa\hat{P} + \sqrt{2\kappa}\hat{P}_\mathrm{in} + \ldots,\end{aligned} \tag{4.48}$$

where κ is the decay rate of the optical mode and the operator $\hat{P}_\mathrm{in}$ represents the noise and/or signal input leaking into the mode. The input operator $\hat{P}_\mathrm{in}$ and its output counterpart $\hat{P}_\mathrm{out}$ can be expanded on a set of itinerant bosonic modes in analogy to (4.35) as

$$\hat{P}_\mathrm{in/out}(t) = \int_0^\infty \frac{d\omega}{\sqrt{2\pi}}\sqrt{\frac{\omega}{\bar{\omega}_\mathrm{cav}}}\left[\hat{a}_\mathrm{in/out}(\omega)e^{-i\omega t} + \hat{a}^\dagger_\mathrm{in/out}(\omega)e^{i\omega t}\right], \tag{4.49}$$

where we have introduced bosonic field operators obeying $[\hat{a}_\mathrm{in/out}(\omega), \hat{a}^\dagger_\mathrm{in/out}(\omega')] = \delta(\omega - \omega')$ and $[\hat{a}_\mathrm{in/out}(\omega), \hat{a}_\mathrm{in/out}(\omega')] = 0$. If $\hat{P}_\mathrm{in}$ is in a thermal state then Eq. (4.49) represents an ohmic bath with the following expectation value in Fourier space

$$\langle \hat{P}_\mathrm{in}(\omega)\hat{P}_\mathrm{in}(\omega')\rangle = \frac{\omega'}{\bar{\omega}_\mathrm{cav}}\bar{N}_\mathrm{opt}(\omega')\delta(\omega + \omega'),$$

where in analogy to Eq. (4.39) we define $\bar{N}_\mathrm{opt}(\omega) \equiv (e^{\hbar\omega/k_\mathrm{B}T_\mathrm{opt}} - 1)^{-1}$ in terms of the temperature of the optical system T_opt. For all practical purposes the magnitude of optical frequencies is such that $|\hbar\omega/k_\mathrm{B}T_\mathrm{opt}| \gg 1$, which entails that to very good approximation we may take the optical noise to be vacuum, $\bar{N}_\mathrm{opt}(\omega) \approx -\Theta(-\omega)$. For consistency with the conventions implicit in (4.47,4.48,4.49), the optical input-output relation reads (for $\omega > 0$, $\omega < 0$ simply yield the Hermitian conjugate equations)

$$\hat{a}_{\text{out}}(\omega) = i\sqrt{\frac{\omega}{\bar{\omega}_{\text{cav}}}}\sqrt{\kappa}e^{-i\theta}\hat{a}(\omega) + \hat{a}_{\text{in}}(\omega). \tag{4.50}$$

Having achieved optomechanical equations of motion equivalent to an ohmically damped serial RLC circuit capacitively coupled to a mechanical mode, we may straightforwardly retrace the steps of Section 4.3 to derive an optomechanical equivalent circuit. Rather than considering this on its own, we proceed immediately to the transduction scenario of simultaneous electro- and optomechanical couplings. In this case the displaced variables $\delta Q, \delta x, \delta a$ are defined wrt. the equilibrium configuration of the 3-part hybrid system subjected to simultaneous electrical and optical driving (we again neglect the higher harmonics of the system response). Kirchhoff's law for the mechanical loop (4.28) then generalizes to

$$\begin{aligned} 2V_{\text{m}}(\Omega) = &\left[-i\Omega L_{\text{m}} + R_{\text{m}} + \frac{1}{-i\Omega C'_{\text{m}}}\right] I_{\text{m}}(\Omega) \\ &+ \frac{2I_{\text{m}}(\Omega) + I_{\text{e},+}(\Omega) + I_{\text{e},-}(\Omega)}{-i\Omega\bar{C}_{\text{c}}} + \frac{2I_{\text{m}}(\Omega) + I_{\text{o},+}(\Omega) + I_{\text{o},-}(\Omega)}{-i\Omega\bar{C}_{\text{opt}}}, \end{aligned} \tag{4.51}$$

whereas the effective electrical equations (4.29,4.30) are unaltered, but supplemented by the following optical counterparts

$$V_{\text{o},+}(\Omega) = Z_{\text{o},+}(\Omega)I_{\text{o},+}(\Omega) + \frac{I_{\text{o},+}(\Omega) + I_{\text{m}}(\Omega)}{-i\Omega\bar{C}_{\text{opt}}} \tag{4.52}$$

$$V_{\text{o},-}(\Omega) = Z_{\text{o},-}(\Omega)I_{\text{o},-}(\Omega) + \frac{I_{\text{o},-}(\Omega) + I_{\text{m}}(\Omega)}{-i\Omega\bar{C}_{\text{opt}}}. \tag{4.53}$$

Here we define optical upper/lower sideband quantities $V_{\text{o},\pm}(\Omega), Q_{\text{o},\pm}(\Omega), I_{\text{o},\pm}(\Omega)$ and $Z_{\text{o},\pm}(\Omega)$ analogously to the similar electrical quantities in Eqs. (4.24-4.27) with the replacements $\omega_{\text{d}} \to \omega_{\text{l}}, Z \to Z_{\text{opt}}, \delta V \to 2V_{\text{o,in}}, \delta Q \to \delta Q_{\text{o}}, I_{\text{o}} \to \delta\dot{Q}_{\text{o}}$ and according to the definitions

$$\delta Q_{\text{o}} \equiv \hbar\bar{\omega}_{\text{cav}}\frac{\bar{C}_{\text{c}}G}{G_{\text{OM}}}\hat{X} \tag{4.54}$$

$$Z_{\text{opt}}(\omega) = -i\omega L_{\text{opt}} + R_{\text{opt}} \tag{4.55}$$

$$L_{\text{opt}} \equiv \frac{G_{\text{OM}}^2}{\bar{C}_{\text{c}}^2 G^2 \hbar\bar{\omega}_{\text{cav}}^3},\ \bar{C}_{\text{opt}} \equiv \hbar\bar{\omega}_{\text{cav}}\frac{\bar{C}_{\text{c}}^2 G^2}{G_{\text{OM}}^2},\ R_{\text{opt}} \equiv \kappa L_{\text{opt}} \tag{4.56}$$

and

$$1/C'_{\text{m}} \equiv 1/C_{\text{m}} - 2/\bar{C}_{\text{opt}}. \tag{4.57}$$

The mechanical frequency $\omega_{\text{m},V}$ entering the definition of C_{m} contains static shifts from both the EM and OM interaction, (4.14) and (4.43). Note that the need to define the modified C'_{m} (4.57) appearing in Eq. (4.51), which was not required for the electrical coupling, can be traced to the difference in how we define the coupling constant (whether we take derivatives of the resonance

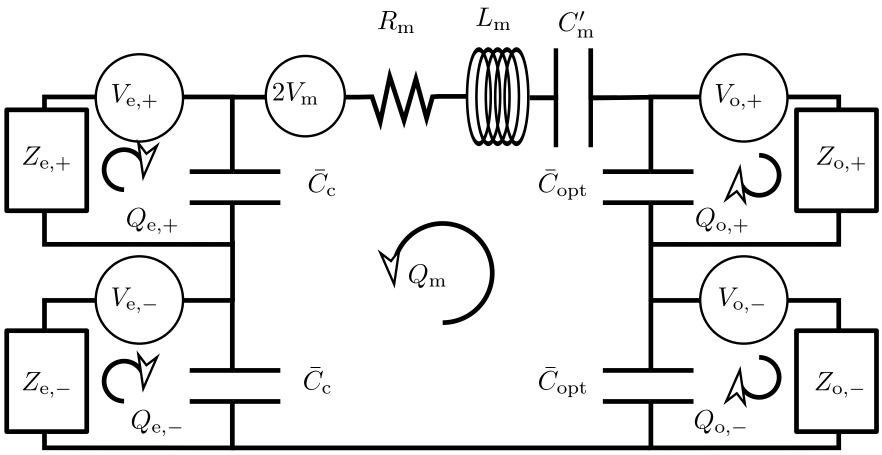

Figure 4.5: Electro-optomechanical equivalent circuit for a mechanical mode acting as an intermediary between an arbitrary linear electrical circuit and a single optical mode. Each of the electrical or optical sidebands are represented by a loop current $I_{\mathrm{e},\pm}$ or $I_{\mathrm{o},\pm}$ in the diagram and are coupled capacitively to the mechanical loop current I_{m} via $\bar{C}_{\mathrm{c}}$ or $\bar{C}_{\mathrm{opt}}$. The effective voltage sources $V_{\mathrm{e},\pm}, V_{\mathrm{o},\pm}, V_{\mathrm{m}}$ represent electrical, optical and mechanical noise or signal inputs. Using standard circuit rules to determine the current in an external loop, expressed as a linear combination of voltage sources, we may determine the output at the corresponding sideband.

frequency or the capacitance). Converting (4.49) to electrical units we obtain the equivalent optical input and output voltage fields

$$\begin{aligned} V_{\mathrm{o,in/out}}(t) &\equiv \sqrt{\frac{\hbar\bar{\omega}_{\mathrm{cav}} R_{\mathrm{opt}}}{2}} P_{\mathrm{in/out}}(t) \\ &= \int_0^\infty \frac{d\omega}{\sqrt{2\pi}} \sqrt{\frac{\hbar\omega R_{\mathrm{opt}}}{2}} \left[\hat{a}_{\mathrm{in/out}}(\omega) e^{-i\omega t} + \hat{a}^\dagger_{\mathrm{in/out}}(\omega) e^{i\omega t}\right], \quad (4.58) \end{aligned}$$

which is completely analogous to (4.35). We likewise convert the optical input-output relation (4.50) into electrical units using (4.47,4.54,4.58),

$$V_{\mathrm{o,out}}(\omega) = -R_{\mathrm{opt}} I_{\mathrm{o}}(\omega) + V_{\mathrm{o,in}}(\omega), \quad (4.59)$$

completely analogous to its electrical counterpart, (4.34). Again these equations can be interpreted as a combined electro-optomechanical equivalent circuit diagram that generalizes Fig. (4.2). This equivalent circuit is shown in Fig. (4.5).

4.7 Scattering matrix

Here we will demonstrate how the scattering matrix of an electro-optomechanical transducer can be determined by applying circuit rules to the generic equivalent circuit in Fig. 4.5. This analysis will already determine the main features of the scattering matrix even without specifying a particular circuit. Later, in Section 4.8, we will consider a concrete example transducer.

Defining the mechanical impedance in the presence of OM coupling (compare to (4.1)),

$$Z'_{\mathrm{m}}(\Omega) \equiv -i\Omega L_{\mathrm{m}} + R_{\mathrm{m}} + \frac{1}{-i\Omega C'_{\mathrm{m}}},$$

a useful first observation based on Fig. 4.5 is that each sideband can be viewed as adding additional loads to Z'_{m}. The resulting effective mechanical impedance $Z_{\mathrm{m,eff}}$ determines how I_{m} will respond to V_{m}. Applying standard impedance combination rules to Fig. 4.5, we find $Z_{\mathrm{m,eff}}(\Omega) = Z'_{\mathrm{m}}(\Omega) + \Delta Z(\Omega)$, where

$$\begin{aligned}\Delta Z(\Omega) &= \sum_l \left[-i\Omega C_l + 1/Z_l(\Omega)\right]^{-1} \\ &= \frac{1}{-i\Omega}\left(\frac{2}{\bar{C}_{\mathrm{c}}} + \frac{2}{\bar{C}_{\mathrm{opt}}}\right) + \sum_l \left[-\frac{1/(-i\Omega C_l)^2}{Z_l(\Omega) + 1/(-i\Omega C_l)}\right], \end{aligned} \tag{4.60}$$

where in the second line we have expressed the load from loop l as the serial combination of the impedance of the relevant coupling capacitor C_l and an impedance transformed version of $Z_l(\Omega)$. Under circumstances where the electrical and optical modes can be adiabatically eliminated (see Section 4.9 below for details), the effective mechanical resonance frequency Ω_{m}, i.e. including all static and dynamical shifts from the electrical and optical interactions, can be found from (4.60) as the solution to the equation

$$\mathrm{Im}[Z_{\mathrm{m,eff}}(\Omega_{\mathrm{m}})] = 0. \tag{4.61}$$

leading us to define the effective mechanical resistance

$$R_{\mathrm{m,eff}} \equiv Z_{\mathrm{m,eff}}(\Omega_{\mathrm{m}}), \tag{4.62}$$

which yields the effective transducer bandwidth $\gamma_{\mathrm{m,eff}} \equiv R_{\mathrm{m,eff}}/L_{\mathrm{m}}$ in the adiabatic regime.

Let us consider the current $I_{l'}^{(l)}$ in the loop of l' induced by the voltage source V_l. Note that V_l induces the voltage $-V_l(\Omega)(-i\Omega C_l)^{-1}/[Z_l(\Omega) + (-i\Omega C_l)^{-1}]$ across its coupling capacitor C_l into the mechanical loop, adding to $2V_{\mathrm{m}}(\Omega)$. Conversely, the mechanical loop current I_{m} induces a voltage $-I_{\mathrm{m}}/(-i\Omega C_{l'})$ in loop l'. Thus, putting these three observations together, we find the admittance relating $I_{l'}^{(l)}$ and V_l,

$$I_{l'}^{(l)}(\Omega) = \mathcal{Q}_{l'}(\Omega)\left[\frac{\mathcal{Q}_l(\Omega)}{Z_{\mathrm{m,eff}}(\Omega)} - i\Omega C_{l'}\delta_{l,l'}\right] V_l(\Omega), \tag{4.63}$$

where we have introduced the line shape functions

$$\mathcal{Q}_l(\Omega) \equiv -\frac{(-i\Omega C_l)^{-1}}{Z_l(\Omega) + (-i\Omega C_l)^{-1}}, \tag{4.64}$$

which can be interpreted as the resonant voltage enhancement at Ω by the resonator and sideband represented by loop l (as will become clearer in the context of the example circuit considered below in Section 4.8). The factor $1/Z_{\mathrm{m,eff}}(\Omega)$ in (4.63) is the effective admittance of the electro-optically loaded mechanical mode defined in (4.60). The arguments above Eq. (4.63) also imply that the mechanical Johnson voltage V_{m} induces the current $I_{l'}^{(\mathrm{m})}$ in loop l' given by

$$I_{l'}^{(\mathrm{m})}(\Omega) = \frac{\mathcal{Q}_{l'}(\Omega)}{Z_{\mathrm{m,eff}}(\Omega)} 2V_{\mathrm{m}}(\Omega). \tag{4.65}$$

The total current in loop l' follows from (4.63,4.65) by linearity,

$$I_{l'}(\Omega) = \sum_{l} I_{l'}^{(l)}(\Omega) + I_{l'}^{(\mathrm{m})}(\Omega). \tag{4.66}$$

Since the $Z_{l'}(\Omega)$ in general represents the combined impedance of several output ports, we cannot proceed to determine the scattering matrix without specifying the structure of the $Z_{l'}(\Omega)$. For this reason, we now turn to a concrete example of a transducer in the following section.

4.8 Example of application

To demonstrate the circuit formalism we now consider a specific example transducer with the aim of determining its scattering matrix. We choose the well-known scenario of a single mechanical mode serving as the intermediary between, on the one hand, a serial RLC circuit via its capacitance $C_{\mathrm{c}}(x)$ and, on the other, a single mode of an optical cavity via a parametric dispersive coupling, see Fig. 4.6 (other electrical circuit layouts will be considered in Chapter 5). The serial RLC circuit contains two resistive loads, an ohmic loss resistance R_{LC} and a transmission line load given by its characteristic impedance Z_{tx}; hence, our example circuit is characterized by the following Thévenin impedance $Z(\omega)$ entering the formalism through Eqs. (4.27) (see also Fig. 4.2a)

$$Z(\omega) = -i\omega L + R_{\mathrm{LC}} + Z_{\mathrm{tx}}, \tag{4.67}$$

where L is the inductance in the electrical circuit and, for later convenience, we define $\bar{\omega}_{\mathrm{LC}} \equiv (L\bar{C}_{\mathrm{c}})^{-1/2}$.

Since the electrical circuit in itself only has one loop, Eq. (4.67) implies the electrical coupling efficiency $\eta_{\mathrm{el}} \equiv Z_{\mathrm{tx}}/(R_{\mathrm{LC}} + Z_{\mathrm{tx}})$. Each of the decay channels induce a (Johnson) voltage source contributing to δV

$$\delta V(\omega) = 2V_{\mathrm{e,in}}^{(\mathrm{LC})}(\omega) + 2V_{\mathrm{e,in}}^{(\mathrm{tx})}(\omega), \tag{4.68}$$

as derived in Section 4.4. Analogously, we specify the optical mode to have two (optical) decay channels, $\kappa = \kappa_0 + \kappa_{\mathrm{ext}}$, where κ_0 is the intrinsic loss rate and κ_{ext} is the coupling rate to the optical signal port. Hence, in our example, (4.55) reads

$$Z_{\mathrm{opt}}(\omega) = -i\omega L_{\mathrm{opt}} + R_0 + Z_{\mathrm{ext}}, \tag{4.69}$$

where from (4.56) we have been led to define $R_0 \equiv \kappa_0 L_{\mathrm{opt}}, Z_{\mathrm{ext}} \equiv \kappa_{\mathrm{ext}} L_{\mathrm{opt}}$, and hence the optical coupling efficiency $\eta_{\mathrm{opt}} \equiv Z_{\mathrm{ext}}/(R_0 + Z_{\mathrm{ext}}) = \kappa_{\mathrm{ext}}/(\kappa_0 + \kappa_{\mathrm{ext}})$. Accordingly, the equivalent optical input and output voltages $V_{\mathrm{o,in/out}}$ each split into two independent contributions of the same form (4.58) obtained by the replacements $R_{\mathrm{opt}} \to R_0, Z_{\mathrm{ext}}$ and introducing appropriate bosonic operators.

Having specified $Z(\omega), Z_{\mathrm{opt}}(\omega)$ we are now in a position to determine the output fields of the signal ports. The electrical output fields are given by the

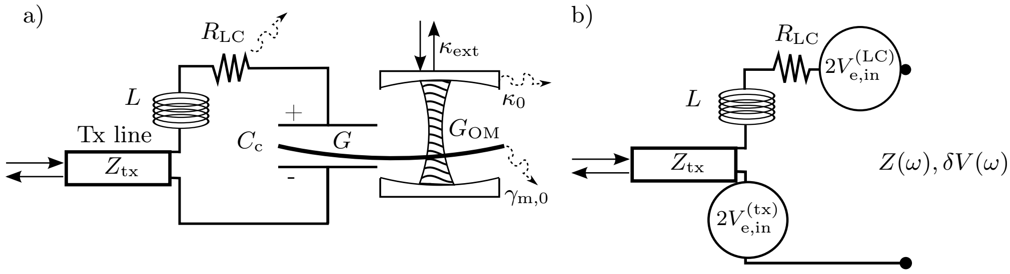

Figure 4.6: a) Example electro-optomechanical transducer: The electrical subsystem is a serial RLC circuit with intrinsic resistance R_{LC} loaded by a semi-infinite transmission line of characteristic impedance Z_{tx}. The circuit is capacitively coupled to a mechanical mode of intrinsic linewidth $\gamma_{m,0}$ with coupling strength G. Analogously, the optical mode has an intrinsic loss rate κ_0 and a readout rate κ_{ext} and couples to the mechanical mode with strength G_{OM}. b) The electrical part of a) that determines the Thévenin equivalent quantities $Z(\omega)$ and $\delta V(\omega)$; these enter the formalism through Eqs. (4.24) and (4.27). Each of the electrical loss ports has an associated voltage source contributing to $\delta V(\omega)$, Eq. (4.68). Note that the subcircuit b) does not include the coupling capacitor.

input-output relations (4.34) found above. For the serial RLC considered here, (4.67), which only has one loop current, the electrical transmission line output is given by

$$V_{e,out}^{(tx)}(\omega_d + \Omega) = -\frac{\omega_d + \Omega}{\Omega} Z_{tx} I_{o,+}(\Omega) + V_{e,in}^{(tx)}(\omega_d + \Omega) \tag{4.70}$$

$$V_{e,out}^{(tx)}(\omega_d - \Omega) = \frac{\omega_d - \Omega}{\Omega} Z_{tx} I_{o,-}^{\dagger}(\Omega) + V_{e,in}^{(tx)}(\omega_d - \Omega), \tag{4.71}$$

in terms of the upper and lower sideband electrical loop currents $I_{e,\pm}(\Omega)$. Analogously, the optical readout is found by reexpressing (4.59) in terms of the upper and lower sideband optical currents $I_{o,\pm}(\Omega)$ to find ($\Omega > 0$)

$$V_{o,out}^{(ext)}(\omega_l + \Omega) = -\frac{\omega_l + \Omega}{\Omega} Z_{ext} I_{o,+}(\Omega) + V_{o,in}^{(ext)}(\omega_l + \Omega) \tag{4.72}$$

$$V_{o,out}^{(ext)}(\omega_l - \Omega) = \frac{\omega_l - \Omega}{\Omega} Z_{ext} I_{o,-}^{\dagger}(\Omega) + V_{o,in}^{(ext)}(\omega_l - \Omega). \tag{4.73}$$

Eqs. (4.70-4.73) provide the missing relations needed to determine the scattering matrix; combining these with the solution for $I_{l'}(\Omega)$, (4.66), we can find the rows of the scattering matrix corresponding to the sidebands of the electrical and optical transmission lines. Let us evaluate, e.g., the optical output at the upper sideband (4.72) at the effective mechanical resonance frequency Ω_m defined in (4.61), assuming red-sideband operation $\bar{\omega}_{LC} - \omega_d = \Omega_m = \bar{\omega}_{cav} - \omega_l$. The current $I_{o,+}$, as can be evaluated via (4.66), depends on the functions $\mathcal{Q}_l(\Omega)$, (4.64). At the mechanical peak they take the values

$$\mathcal{Q}_{\mathrm{o},+}(\Omega_{\mathrm{m}}) = -i\frac{\bar{\omega}_{\mathrm{cav}}}{\kappa} \equiv -iQ_{\mathrm{cav}},\ \mathcal{Q}_{\mathrm{o},-}(\Omega_{\mathrm{m}}) \approx \frac{iQ_{\mathrm{cav}}}{1-4i\Omega_{\mathrm{m}}/\kappa} \tag{4.74}$$

$$\mathcal{Q}_{\mathrm{e},+}(\Omega_{\mathrm{m}}) = -i\frac{\bar{\omega}_{\mathrm{LC}}L}{R_{\mathrm{LC}}+Z_{\mathrm{tx}}} \equiv -iQ_{\mathrm{LC}},\ \mathcal{Q}_{\mathrm{e},-}(\Omega_{\mathrm{m}}) \approx \frac{iQ_{\mathrm{LC}}}{1-4i\Omega_{\mathrm{m}}L/(R_{\mathrm{LC}}+Z_{\mathrm{tx}})}, \tag{4.75}$$

where the approximations are valid in the limit $Q_{\mathrm{cav}} \equiv \bar{\omega}_{\mathrm{cav}}/\kappa, Q_{\mathrm{LC}} \equiv \bar{\omega}_{\mathrm{LC}}L/(R_{\mathrm{LC}}+Z_{\mathrm{tx}}) \gg 1, \Omega_{\mathrm{m}} \ll \bar{\omega}_{\mathrm{cav}}, \bar{\omega}_{\mathrm{LC}}$. These quantities signify the strength of the various sidebands. Let us, in our example, assume the optomechanically resolved-sideband regime, $\kappa/(4\Omega_{\mathrm{m}}) \ll 1$. From (4.74) we see that this implies that $|\mathcal{Q}_{\mathrm{o},-}(\Omega_{\mathrm{m}})/\mathcal{Q}_{\mathrm{o},+}(\Omega_{\mathrm{m}})| \ll 1$ and hence we may disregard the loop (o,−) altogether (however, for applications where quantum noise is important, one has to carefully consider to which extent this limit is fulfilled). In this scenario, we arrive at a scattering relation of the form

$$\begin{aligned}\hat{a}^{(\mathrm{ext})}_{\mathrm{out}}(\bar{\omega}_{\mathrm{cav}}) &= S_{\mathrm{tx},U}\hat{b}^{(\mathrm{tx})}_{\mathrm{in}}(\bar{\omega}_{\mathrm{LC}}) + S_{\mathrm{LC},U}\hat{b}^{(\mathrm{LC})}_{\mathrm{in}}(\bar{\omega}_{\mathrm{LC}}) + S_{\mathrm{tx},L}\hat{b}^{(\mathrm{tx})\dagger}_{\mathrm{in}}(\bar{\omega}_{\mathrm{LC}}-2\Omega_{\mathrm{m}})\\ &+ S_{\mathrm{LC},L}\hat{b}^{(\mathrm{LC})\dagger}_{\mathrm{in}}(\bar{\omega}_{\mathrm{LC}}-2\Omega_{\mathrm{m}}) + S_{\mathrm{m}}\hat{c}_{\mathrm{in}}(\Omega_{\mathrm{m}}) + S_{\mathrm{ext},U}\hat{a}^{(\mathrm{ext})}_{\mathrm{in}}(\bar{\omega}_{\mathrm{cav}}) + S_{0,+}\hat{a}^{(0)}_{\mathrm{in}}(\bar{\omega}_{\mathrm{cav}}),\end{aligned} \tag{4.76}$$

where $\hat{c}_{\mathrm{in}}$ is the bosonic input operator for the mechanical noise. Defining the dimensionless voltage mapping factor T from the mechanical loop to the upper optical sideband,

$$T \equiv -2\frac{\bar{\omega}_{\mathrm{cav}}}{\Omega_{\mathrm{m}}}Z_{\mathrm{ext}}\frac{-iQ_{\mathrm{cav}}}{R_{\mathrm{m,eff}}} = i\eta_{\mathrm{opt}}\frac{4g^2_{\mathrm{OM}}}{\bar{\omega}_{\mathrm{cav}}\gamma_{\mathrm{m,eff}}}, \tag{4.77}$$

in terms of $g_{\mathrm{OM}} = G_{\mathrm{OM}}/\sqrt{4\hbar m\Omega_{\mathrm{m}}}$ and $\gamma_{\mathrm{m,eff}}$, defined below (4.62), the scattering matrix elements are

$$S_{\mathrm{m}} = T\sqrt{\frac{\Omega_{\mathrm{m}}R_{\mathrm{m}}}{\bar{\omega}_{\mathrm{cav}}Z_{\mathrm{ext}}}} \tag{4.78}$$

$$S_{\mathrm{tx},+} = T\sqrt{\frac{\bar{\omega}_{\mathrm{LC}}Z_{\mathrm{tx}}}{\bar{\omega}_{\mathrm{cav}}Z_{\mathrm{ext}}}}\mathcal{Q}_{\mathrm{e},+}(\Omega_{\mathrm{m}}) \quad S_{\mathrm{tx},-} = T\sqrt{\frac{(\bar{\omega}_{\mathrm{LC}}-2\Omega_{\mathrm{m}})Z_{\mathrm{tx}}}{\bar{\omega}_{\mathrm{cav}}Z_{\mathrm{ext}}}}\mathcal{Q}_{\mathrm{e},-}(\Omega_{\mathrm{m}}) \tag{4.79}$$

$$S_{\mathrm{LC},+} = T\sqrt{\frac{\bar{\omega}_{\mathrm{LC}}R_{\mathrm{LC}}}{\bar{\omega}_{\mathrm{cav}}Z_{\mathrm{ext}}}}\mathcal{Q}_{\mathrm{e},+}(\Omega_{\mathrm{m}}) \quad S_{\mathrm{LC},-} = T\sqrt{\frac{(\bar{\omega}_{\mathrm{LC}}-2\Omega_{\mathrm{m}})R_{\mathrm{LC}}}{\bar{\omega}_{\mathrm{cav}}Z_{\mathrm{ext}}}}\mathcal{Q}_{\mathrm{e},-}(\Omega_{\mathrm{m}}) \tag{4.80}$$

$$S_{\mathrm{ext},+} = 1-2\eta_{\mathrm{opt}}-iQ_{\mathrm{cav}}T \quad S_{0,+} = \sqrt{\eta^{-1}_{\mathrm{opt}}-1}\left[-2\eta_{\mathrm{opt}}-iQ_{\mathrm{cav}}T\right], \tag{4.81}$$

where the electrical sideband strengths $\mathcal{Q}_{\mathrm{e},\pm}(\Omega_{\mathrm{m}})$ were calculated in Eq. (4.75). All of the scattering elements contain a frequency and impedance conversion factor of the form $\sqrt{\omega_{\mathrm{in}}R_{\mathrm{in}}/\omega_{\mathrm{out}}R_{\mathrm{out}}}$; it is the ratio of the voltage zero-point amplitudes, appearing as the prefactor in (4.35). For the optical sources this factor takes the values unity and $\sqrt{\eta^{-1}_{\mathrm{opt}}-1}$, respectively, as expressed in terms of η_{opt} introduced below Eq. (4.69). The electrical and mechanical scattering

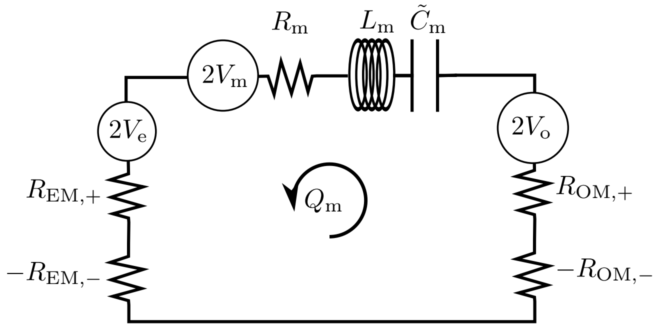

Figure 4.7: Reduced electro-optomechanical equivalent circuit in which electrical and optical modes have been adiabatically eliminated. It consists of an effective mechanical loop of shifted resonance frequency loaded by a resistive element for each sideband coupling. The resistances are positive for the upper sidebands, $R_{\rm EM/OM,+}$, and negative for the lower ones, $-R_{\rm EM/OM,-}$, leading to amplification effects. Each sideband coupling drives the effective mechanical loop with a Thévenin voltage representing the noise and signal ports of that subsystem. The readout of the system corresponds to the signal dissipated in the various ports.

coefficients (4.78-4.80) consist only of single terms because for these sources only a single path exists to the optical readout port 'ext'. In contrast, the effective reflection coefficient for the 'ext' port $S_{\rm ext,+}$, (4.81), results as the interference between three paths and hence three terms; in order of appearance: Direct reflection, reflection in the cavity, and reflection from the electromechanical system. (In the case of $S_{0,+}$, only the latter two apply.)

Given the scattering relation (4.76) we may calculate the transducer parameters η and N and, in turn, evaluate figures of merit for transducer applications of interest as discussed in Chapter 3. Several examples of this will be given in Chapter 5 below.

4.9 Adiabatic elimination of electrical and optical modes

In the preceding two sections, 4.7 and 4.8, we have demonstrated how the electro-optomechanical equivalent circuit in Fig. 4.5 can be used to deduce the elements of the scattering matrix. In the present section we will proceed to derive an even simpler, reduced equivalent circuit (Fig. 4.7) by adiabatically eliminating the electrical and optical modes in Fig. 4.5. Such elimination is warranted when their loading of the mechanical mode has negligible frequency dependence over the bandwidth of interest (typically, the effective bandwidth of the transducer) and simply amounts to neglecting this weak dependence.

In the effective description that results (see Fig. 4.7), the electrical and optical modes enter as effective loads attached to the mechanical loop. The combined electrical and optical loading of the mechanical current loop $\Delta Z(\Omega)$ was derived in (4.60). The real part of $\Delta Z(\Omega)$ adds resistance while the imaginary part shifts the mechanical resonance frequency. The effective resistance of the mechanical loop thus has a contribution from each sideband of each coupled subsystem, positive from the upper sidebands and negative for the lower ones

$$R_{\mathrm{m,eff}} = R_{\mathrm{m}} + R_{\mathrm{EM},+} - R_{\mathrm{EM},-} + R_{\mathrm{OM},+} - R_{\mathrm{OM},-}. \tag{4.82}$$

These resistances $R_{\mathrm{EM/OM},\pm}$ are the electrical equivalents of the EM/OM anti-Stokes and Stokes rates for the scattering of mechanical phonons into the respective sidebands as electrical/optical photons,

$$\gamma_{\mathrm{EM/OM},\pm} \equiv R_{\mathrm{EM/OM},\pm}/L_{\mathrm{m}}. \tag{4.83}$$

Moreover, each of the eliminated loops contribute a voltage source term to the effective mechanical loop. However, we lump the two electrical and the two optical contributions, respectively, into effective quantities $V_{\mathrm{e}}(\Omega)$ and $V_{\mathrm{o}}(\Omega)$. Finally, to be able to calculate the electrical and optical readout from the reduced circuit, we need to obtain effective input-output relations. We will establish these effective quantities and relations in what follows.

4.9.1 Elimination of optical mode

The optomechanical resistances in (4.60),

$$R_{\mathrm{OM},\pm} \equiv \pm\mathrm{Re}\left[-\frac{1/(-i\Omega_{\mathrm{m}}\bar{C}_{\mathrm{opt}})^2}{Z_{\mathrm{o},\pm}(\Omega_{\mathrm{m}}) + 1/(-i\Omega_{\mathrm{m}}\bar{C}_{\mathrm{opt}})}\right], \tag{4.84}$$

can be put on a more specific form since we are assuming a single cavity mode, (4.55). Considering optical frequencies ω close to the cavity resonance, $|\omega - \bar{\omega}_{\mathrm{cav}}| \ll \bar{\omega}_{\mathrm{cav}}$, the optical line shape is well-approximated by a Lorentzian. Ignoring corrections of order $\Omega_{\mathrm{m}}/\omega_{\mathrm{l}}$, this allows us to reexpress (4.84) as

$$R_{\mathrm{OM},\pm} = L_{\mathrm{m}}\gamma_{\mathrm{OM},\pm} \tag{4.85}$$

$$\gamma_{\mathrm{OM},\pm} \equiv \gamma_{\mathrm{m},0}\mathcal{C}_{\mathrm{OM}}\mathcal{L}_{\pm}^2, \quad \mathcal{C}_{\mathrm{OM}} \equiv \frac{4g_{\mathrm{OM}}^2}{\gamma_{\mathrm{m},0}\kappa}, \tag{4.86}$$

where $\gamma_{\mathrm{OM},\pm}$ are the OM anti-Stokes and Stokes rates in terms of the OM cooperativity $\mathcal{C}_{\mathrm{OM}}$ and the Lorentzian line shape strengths $\mathcal{L}_{\pm}$ and phases $\theta_{\pm}$ at the upper/lower OM sidebands,

$$\mathcal{L}(\omega) \equiv \frac{\kappa/2}{-i(\omega - \bar{\omega}_{\mathrm{cav}}) + \kappa/2}, \tag{4.87}$$

$$\mathcal{L}_{\pm} \equiv |\mathcal{L}(\omega_{\mathrm{l}} \pm \Omega_{\mathrm{m}})|, \quad \theta_{\pm} \equiv \mathrm{Arg}[\mathcal{L}(\omega_{\mathrm{l}} \pm \Omega_{\mathrm{m}})]. \tag{4.88}$$

The effective optical Thévenin voltage V_{o}, which has contributions from $V_{\mathrm{o},\pm}$, can be determined by voltage division as discussed in Section 4.7,

$$V_{\mathrm{o}}(\Omega) \approx -iQ_{\mathrm{cav}}[e^{i\theta_+}\mathcal{L}_+V_{\mathrm{o},+}(\Omega) - e^{-i\theta_-}\mathcal{L}_-V_{\mathrm{o},-}(\Omega)], \tag{4.89}$$

where we have ignored the frequency dependence of $\mathcal{L}(\omega)$ over the bandwidth of interest. For the typical example of an optical mode with two decay channels considered in Section 4.8, $V_{\mathrm{o}}(\Omega)$ in (4.89) can be stated explicitly in terms of the bosonic operators of the itinerant optical fields as (again ignoring corrections of order $\Omega_\mathrm{m}/\omega_\mathrm{l}$)

$$V_\mathrm{o}(\Omega) \approx -i\frac{2g_\mathrm{OM}}{\sqrt{\kappa}}\frac{\sqrt{\hbar m\Omega_\mathrm{m}/2}}{\bar{C}_\mathrm{c}G}[e^{i\theta_+}\mathcal{L}_+\hat{a}_\mathrm{in}(\omega_\mathrm{l}+\Omega) - e^{-i\theta_-}\mathcal{L}_-\hat{a}^\dagger_\mathrm{in}(\omega_\mathrm{l}-\Omega)], \quad (4.90)$$

where $\hat{a}_\mathrm{in}(\omega) = \sqrt{\eta_\mathrm{opt}}\hat{a}^{(\mathrm{ext})}_\mathrm{in}(\omega) + \sqrt{1-\eta_\mathrm{opt}}\hat{a}^{(0)}_\mathrm{in}(\omega)$ is a linear combination of the two optical input fields. The effective optomechanical input-output relation can be found by combining (4.59) with (4.52,4.53) and the optical counterparts of (4.26). For the readout port 'ext' we find the outgoing field

$$\begin{aligned}\hat{a}^{(\mathrm{ext})}_\mathrm{out}(\omega_\mathrm{l}+\Omega) &= ie^{i\theta_+}\sqrt{\eta_\mathrm{opt}}\sqrt{\frac{2R_{\mathrm{OM},+}}{\hbar\Omega_\mathrm{m}}}\frac{\Omega_\mathrm{m}}{\Omega}I_\mathrm{m}(\Omega) + \hat{a}^{(\mathrm{eff})}_\mathrm{in}(\omega_\mathrm{l}+\Omega) \quad (4.91)\\ \hat{a}^{(\mathrm{ext})}_\mathrm{out}(\omega_\mathrm{l}-\Omega) &= -ie^{i\theta_-}\sqrt{\eta_\mathrm{opt}}\sqrt{\frac{2R_{\mathrm{OM},-}}{\hbar\Omega_\mathrm{m}}}\frac{\Omega_\mathrm{m}}{\Omega}I^\dagger_\mathrm{m}(\Omega) + \hat{a}^{(\mathrm{eff})}_\mathrm{in}(\omega_\mathrm{l}-\Omega) \quad (4.92)\end{aligned}$$

where we have defined the effective optical noise operator

$$\hat{a}^{(\mathrm{eff})}_\mathrm{out}(\omega_\mathrm{l}\pm\Omega) \equiv \left[1 - 2\eta_\mathrm{opt}\mathcal{L}_\pm e^{i\theta_\pm}\right]\hat{a}^{(\mathrm{ext})}_\mathrm{in}(\omega_\mathrm{l}\pm\Omega) - 2\sqrt{\eta_\mathrm{opt}(1-\eta_\mathrm{opt})}\mathcal{L}_\pm e^{i\theta_\pm}\hat{a}^{(0)}_\mathrm{in}(\omega_\mathrm{l}\pm\Omega). \quad (4.93)$$

Eqs. (4.91,4.92) show that the power dissipated from the mechanical loop into the resistors $R_{\mathrm{OM},\pm}$ is proportional to $R_{\mathrm{OM},\pm}|I_\mathrm{m}|^2$ in the classical limit as one would expect.

4.9.2 Elimination of electrical modes

We define the effective electromechanical resistances from (4.60) as

$$\begin{aligned}R_{\mathrm{EM},\pm} &\equiv \pm\,\mathrm{Re}\left[\left(-i\Omega\bar{C}_\mathrm{c} + 1/Z_{\mathrm{e},\pm}(\Omega)\right)^{-1}\right]\Big|_{\Omega=\Omega_\mathrm{m}}\\ &= \pm\,\mathrm{Re}\left[-\frac{1/(-i\Omega\bar{C}_\mathrm{c})^2}{Z_{\mathrm{e},\pm}(\Omega) + 1/(-i\Omega\bar{C}_\mathrm{c})}\right]\Bigg|_{\Omega=\Omega_\mathrm{m}}, \quad (4.94)\end{aligned}$$

where the two expressions are related by the impedance transformation in (4.60), allowing us (in terms of the calculation) to combine $Z_{\mathrm{e},\pm}(\Omega)$ with the impedance owing to $\bar{C}_\mathrm{c}$ either parallelly or serially. From these expressions we find in terms of electrical frequencies ω and actual circuit impedances that

$$\begin{aligned}R_{\mathrm{EM},\pm} &= \frac{\omega_\mathrm{d}\pm\Omega_\mathrm{m}}{\Omega_\mathrm{m}}\,\mathrm{Re}\left[\left(-i\omega\bar{C}_\mathrm{c} + 1/Z(\omega)\right)^{-1}\right]\Big|_{\omega=\omega_\mathrm{d}\pm\Omega_\mathrm{m}}\\ &= \frac{\omega_\mathrm{d}\pm\Omega_\mathrm{m}}{\Omega_\mathrm{m}}\,\mathrm{Re}\left[\frac{1/(\omega\bar{C}_\mathrm{c})^2}{Z(\omega) + 1/(-i\omega\bar{C}_\mathrm{c})}\right]\Bigg|_{\omega=\omega_\mathrm{d}\pm\Omega_\mathrm{m}} \quad (4.95)\end{aligned}$$

where $Z(\omega)$ is the arbitrary impedance illustrated in Fig. 4.2a. The denominators of the first and second expressions in Eq. (4.95) contain, respectively, the parallel and serial combinations of $Z(\omega)$ with the coupling capacitor impedance (complex conjugated and multiplied by -1 in the case of the lower sideband).

The Thévenin voltage V_e of the reduced circuit, Fig. 4.7, is easily derived in terms of the Thévenin voltages $V_{\mathrm{e},\pm}$ of Fig. 4.5 following Section 4.7,

$$2V_\mathrm{e}(\Omega) = \mathcal{Q}_{\mathrm{e},+}(\Omega)V_{\mathrm{e},+}(\Omega) + \mathcal{Q}_{\mathrm{e},-}(\Omega)V_{\mathrm{e},-}(\Omega). \quad (4.96)$$

For purposes of practical calculation, however, it is more natural to calculate V_e directly without the intermediate step of determining $V_{\mathrm{e},\pm}$. This is done by including the coupling capacitor $\bar{C}_\mathrm{c}$ in, e.g., Fig. 4.6b, leading to a new Thévenin voltage $\delta V'(\omega)$. In terms of this quantity, the electrical Thévenin voltage of the reduced equivalent circuit is

$$2V_\mathrm{e}(\Omega) = \delta V'(\omega_\mathrm{d} + \Omega) + \delta V'^{*}(\omega_\mathrm{d} - \Omega). \tag{4.97}$$

The effective electromechanical input-output relations can be determined as in the optomechanical case once the electrical circuit has been specified.

The reduced equivalent circuit will be applied in the following chapter to analyze various circuits.

4.10 Concluding remarks and outlook

In this chapter we have developed an equivalent circuit formalism for electro-optomechanical transducers, thus unifying the elements of such hybrid systems in a common framework native to electrical engineering while capturing all the relevant physics. The scattering matrix $\mathbf{S}$ of the transducer can therefore be determined by linear circuit analysis. The common language provided by the equivalent circuit formulation is valuable in the cross-disciplinary work of implementing the low-noise sensing capabilities and optical fiber compatibility of optomechanics [1] in real-world applications such as nuclear magnetic resonance imaging (NMRI) and radio-astronomy. We have given a prescription for quantizing the theory, thus making it applicable to analyzing transduction in the quantum limit. This is important for assessing the potential of electro-optomechanical transducers in future quantum communication applications in optically-based networks [21]. The formalism was developed assuming capacitive coupling to a single mechanical mode, but it should be straightforward to generalize to inductive coupling [41] or situations involving several spectrally well-separated mechanical modes.

In the following chapter we will further demonstrate the formalism by applying it in optimizing electro-optomechanical receiver circuits.

Chapter 5

Optimizing electro-optomechanical receiver circuits

The work presented in this chapter has been carried out in collaboration with Albert Schließer, Jacob M. Taylor, and Anders S. Sørensen.

5.1 Introduction

In the course of the previous two chapters we have: 1) established how to characterize transducers and assess their performance in various applications based on their scattering matrix **S** (Chapter 3), and 2) we have derived an equivalent circuit formalism that allows us to obtain **S** in terms of the (equivalent) impedances of the various components of the transducer (Chapter 4), which can be advantageous in the design of the transducer. Now is the time to put these these tools to work by applying them to an actual design problem.

In this chapter we will consider a family of simple receiver circuits coupled to an optomechanical system and apply the circuit formalism to determine the transducer parameters η and N. On this basis we could optimize the circuit design for, e.g., any of the applications discussed in Chapter 3. For specificity, however, we will here focus on optimizing the circuit design of the receiver circuit for indirect optical heterodyning of weak incoming electrical signals, considering both the high-temperature and quantum limits of operation. We will also evaluate the performance in the deterministic state transfer scheme relevant for quantum communication applications although without optimization.

5.2 Contents of chapter

First we review, in Section 5.3, the equivalent circuit formalism developed in the previous chapter. Then, in Section 5.4, we introduce the family of electrical receiver circuits with optomechanical readout that we will analyze: Serial and parallel RLC circuits and a non-resonant RC circuit. Using the equivalent-circuit formalism, we will in Section 5.5 derive the scattering matrix elements relating signal and noise input fields to the output port, from which we extract the transducer parameters η and N, the signal transfer efficiency and added noise, in Section 5.6. We then specialize, in Section 5.7, to the application of indirect optical heterodyne detection of electrical signals, for which we optimize the circuit design over the family of receiver circuits. Afterwards, in Section 5.8, we estimate the performance of the detection scheme using parameter values inspired by recent experiments. As an example of a quantum application, we also evaluate the unconditional state transfer fidelity. Finally, we conclude on the results in Section 5.9.

5.3 Summary of equivalent circuit formulation

We will now demonstrate how the equivalent circuit formalism can be used to determine and optimize the performance of electro-optomechanical transducers. The present section provides an overview of the conceptual and calculational steps leading from a given physical system (Fig. 5.1a) to the generic transducer parameters $\eta(\Omega)$ and $N(\Omega)$ (Fig. 5.2b).

Fig. 5.1 illustrates the conceptual transition from electro-optomechanical transducer system (a) to its full equivalent-circuit representation (b) as derived in Section 4.6. In the latter, each sideband of each electromagnetic subsystem is represented by a circuit loop with loop charge $Q_{\mathrm{e},\pm}$ or $Q_{\mathrm{o},\pm}$ connecting to the central mechanical loop with loop charge Q_{m} by capacitive couplings. The electrical voltages $V_{\mathrm{e},\pm}(\Omega)$ and charges $Q_{\mathrm{e},\pm}(\Omega)$ in (b) are proportional to the actual Thévenin voltage and charge fluctuations in (a) on the the coupling capacitor $\bar{C}_{\mathrm{c}}$ at the sidebands around the electrical drive $\omega_{\mathrm{d}} \pm \Omega$ (although with complex conjugation applied to the lower sideband quantities). The optical equivalent voltages $V_{\mathrm{o},\pm}$ and charges $Q_{\mathrm{o},\pm}(\Omega)$ are proportional to the optical input fields and cavity field fluctuations at the upper/lower sidebands. Let us now consider the mapping of the (actual) electrical circuit impedance in (a) into the equivalent description of (b): The electrical impedance across the open terminals shown in Fig. 5.1a (in absence of coupling to the optomechanical system but with $C_{\mathrm{c}} \to \bar{C}_{\mathrm{c}}$) maps into the equivalent circuit (Fig. 5.1b) as indicated by the solid dots, but with a frequency conversion prefactor referencing the electrical impedance to the mechanical frequency scale (relevant for AC-driven scenarios). In the case of electrical AC drive, this frequency-converted electrical impedance manifests itself a second time as the lower-sideband impedance across the open dots in (b), where this time the electrical resistances enter with a flipped sign, $R \to -R$, giving rise to amplification effects. The impedance contributions across the two pairs of dots represent the dynamical back-action from the upper and lower electrical sidebands, respectively. Noting that the equations of motion for an optical cavity mode are mathematically equivalent to those of a serial RLC circuit, the couplings to the two optical sidebands enter the equivalent circuit analogously to those of the electrical subsystem.

While the full equivalent circuit (Fig. 5.1b) is general and elucidates the physics of the hybrid system, we may in the adiabatic limit work with the reduced equivalent circuit derived in Section 4.9 and shown in Fig. 5.1c. I.e. its regime of applicability is when the frequency dependence of the electrical and optical loading is negligible over the bandwidth of interest. In this case, the loading of the mechanical loop by each sideband can be approximated as

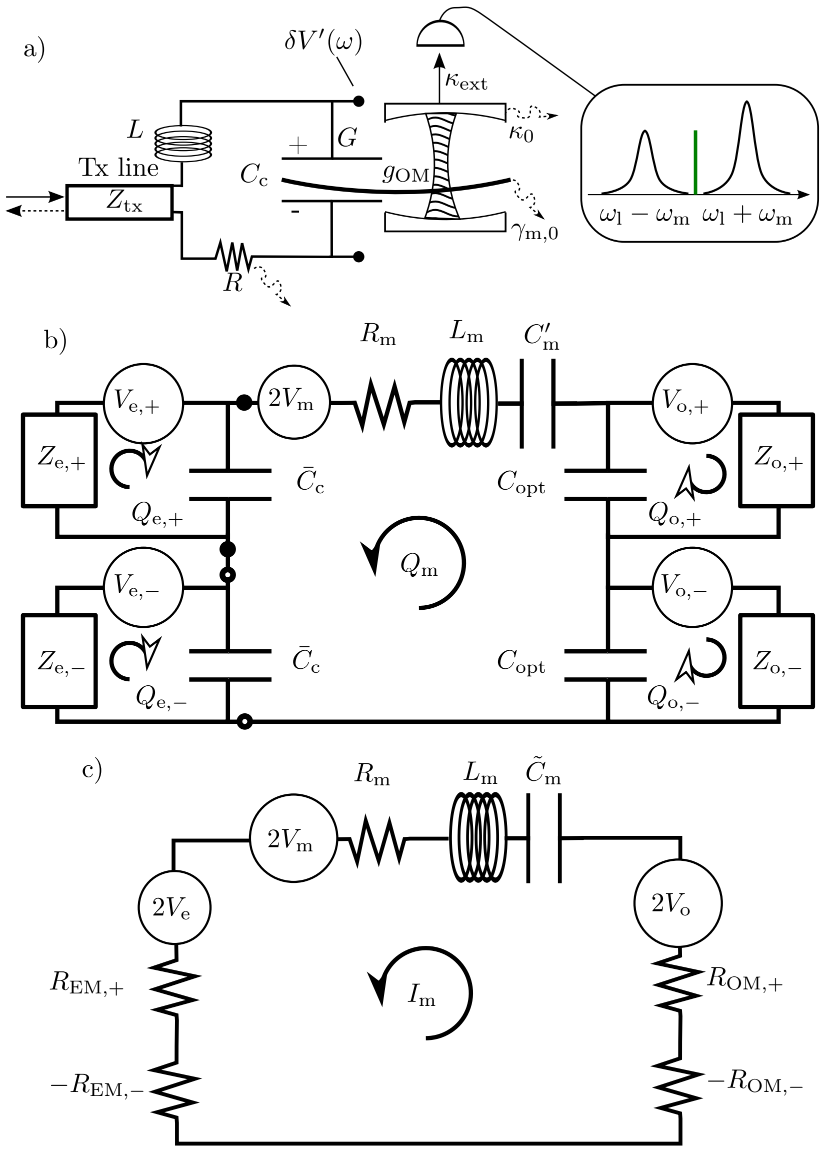

Figure 5.1: Relating component parameters to effective transducer parameters, step by step: a) The electro-optomechanical apparatus is defined by its circuit layout and the parameters of its various components as well as coupling and dissipation rates; the optical readout will in general feature two mechanical sidebands at $\omega_{\mathrm{l}} \pm \omega_{\mathrm{m}}$. b) Electro-optomechanical equivalent circuit for a mechanical mode acting as an intermediary between an arbitrary linear electrical circuit and a single optical mode. Each of the electrical or optical sidebands are represented by a loop charge $Q_{\mathrm{e},\pm}$ or $Q_{\mathrm{o},\pm}$ in the diagram and are coupled capacitively to the mechanical loop charge Q_{m} via $\bar{C}_{\mathrm{c}}$ or C_{opt}. The effective voltage sources $V_{\mathrm{e},\pm}, V_{\mathrm{o},\pm}, V_{\mathrm{m}}$ represent electrical, optical and mechanical noise or signal inputs. Using standard circuit rules to determine the current in an external loop, expressed as a linear combination of voltage sources, we may determine the output at the corresponding sideband. c) By eliminating the electrical and optical loops in b), a reduced equivalent circuit for the transducer is achieved in the weak-coupling regime. It consists of an effective mechanical loop of shifted resonance frequency loaded by a resistive element for each sideband coupling. The resistances are positive for the upper sidebands, $R_{\mathrm{EM/OM},+}$, and negative for the lower ones, $-R_{\mathrm{EM/OM},-}$, leading to amplification effects. Each sideband coupling drives the effective mechanical loop with a Thévenin voltage representing the noise and signal ports of that subsystem. The readout of the system corresponds to the signal dissipated in the various ports.

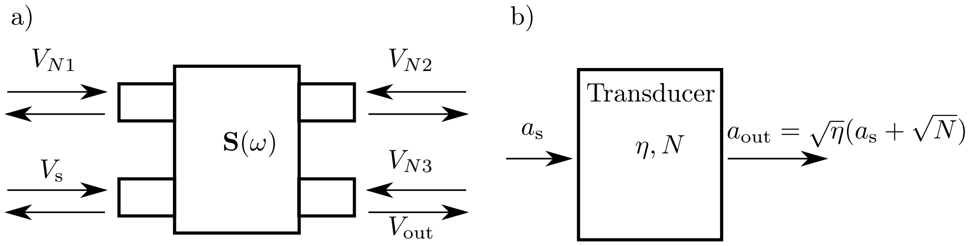

Figure 5.2: a) By applying voltage division rules to the reduced equivalent circuit, Fig. 5.1c, we may obtain the transfer functions that relate voltage sources to the fluctuations they induce at each port; these are exactly the entries of the scattering matrix $\mathbf{S}(\omega)$. b) From the particular row of the scattering matrix $\mathbf{S}(\omega)$ corresponding to the desired output port, we can extract the signal transfer efficiency $\eta(\omega)$ and the added noise spectral density $N(\omega)$; focusing on their peak values, we arrive at the effective transducer parameters from which the figure of merit can be calculated.

an effective positive/negative resistance $\pm R_{\mathrm{EM},\pm}$ or $\pm R_{\mathrm{OM},\pm}$ and a frequency shift (which we combine into the net shift $C'_{\mathrm{m}} \to \tilde{C}_{\mathrm{m}}$). The reduced electrical Thévenin voltage is given by $V_{\mathrm{e}}(\Omega) = \delta V'(\omega_{\mathrm{d}} + \Omega) + \delta V'^{*}(\omega_{\mathrm{d}} - \Omega)$ where $\delta V'(\omega)$ is the Thévenin voltage across the coupling capacitor $\bar{C}_{\mathrm{c}}$ of the original circuit as indicated by the open terminals in the example circuit of Fig. 5.1a. When applicable, the reduced equivalent circuit (Fig. 5.1c) offers two (related) advantages: It is a very compact and simple representation of the transducer as a single damped, driven oscillator. As a result, calculating the system dynamics is trivial once the quantities defining the reduced circuit have been determined.

In this chapter, we will assume the adiabatic limit where the reduced equivalent circuit applies, i.e. that the effective width of the mechanical mode $\gamma_{\mathrm{m,eff}} \equiv R_{\mathrm{m,eff}}/L_{\mathrm{m}}$ does not become comparable to the widths of the circuit and cavity modes ($(Z_{\mathrm{tx}} + R)/L$ and κ, respectively, in the notation of Fig. 5.1a). This is not a severe limitation when analyzing steady-state transduction of itinerant fields because signals anyway cannot enter or leave the system faster than dictated by the external coupling rates of the circuit/cavity (Z_{tx}/L and κ_{ext}, respectively).

We will now outline the calculational procedure that we will follow in our analysis of the receiver circuits below. Working in the adiabatic limit, we start by establishing the reduced equivalent circuit (Fig. 5.1c) from the physical system, e.g., Fig. 5.1a. Using the effective input-output relations connecting the itinerant fields to the response of the reduced circuit loop (see Section 4.9), we derive the scattering matrix $\mathbf{S}(\Omega)$ relating incoming and outgoing itinerant signal and noise fields (as illustrated in Fig. 5.2a and discussed in Chapter 3). Finally, by specifying the state of the noise reservoirs, we can extract the effective transducer parameters $\eta(\Omega)$ and $N(\Omega)$ from the scattering matrix $\mathbf{S}(\Omega)$, yielding the generic transducer characterization illustrated in Fig. 5.2b. The results $\eta(\Omega), N(\Omega)$ and $\mathbf{S}(\Omega)$ serve as the starting point for the optimization of the receiver circuits.

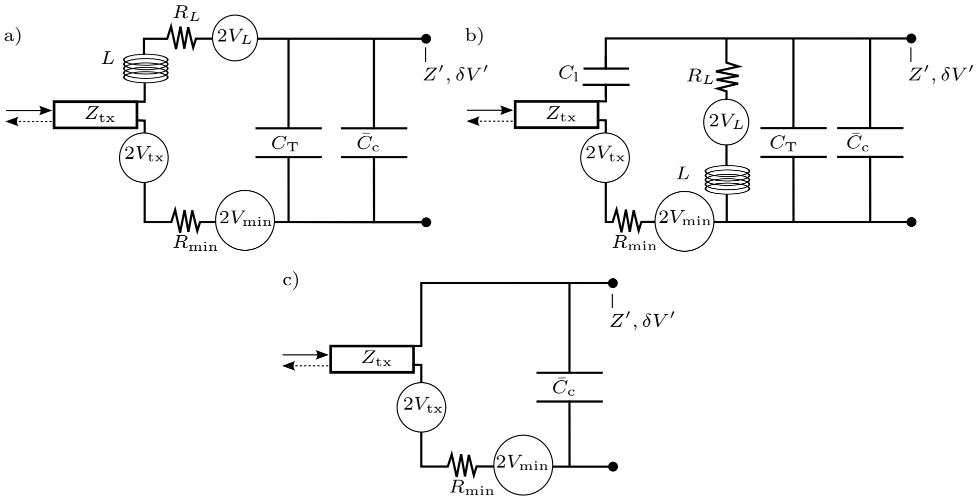

Figure 5.3: Electrical receiver circuits: A transmission line (characteristic impedance $Z_{\rm tx}$) coupled into either a serial RLC (a), parallel RLC (b) via a "loading" capacitor of capacitance $C_{\rm l}$, or an RC circuit (c). The inductor is assumed to be the primary source of ohmic resistance, R_L, whereas the coupling capacitor of steady-state capacitance $\bar{C}_{\rm c}$ is assumed lossless. The resonant circuits (a&b) include a tuning capacitor of capacitance $C_{\rm T}$. In all three circuits we include a serial ohmic resistance $R_{\rm min}$ at the input accounting for the incoupling loss. The Thévenin impedance Z' and voltage $\delta V'$ across the open terminals in the circuit diagram determine the electrical loading and driving of the mechanical mode across the two pairs of dots in the full equivalent circuit (Fig. 5.1b) and the effective electromechanical resistances $R_{{\rm EM},\pm}$ and $V_{\rm e}$ in the reduced equivalent circuit (Fig. 5.1c).

5.4 Receiver circuits

The electrical circuits we will consider can be thought of as matching circuits for the efficient coupling of the optomechanical system to the signal input. For the purposes of our analysis below, we will assume the incoming signal (central frequency $\omega_{\rm s}$) to be supplied by a transmission line of characteristic impedance $Z_{\rm tx} \in \mathbb{R}_+$. The signal will be assumed narrow with respect to the transducer bandwidth and to be confined to the upper EM sideband. In addition, we assume a semi-infinite transmission line so that signals reflected from the transducer are simply lost. This conveniently separates the transducer design from the specifics of the source, under the additional assumption that the effects of back-action and noise from the transducer on the source are negligible (e.g. this is clearly valid for radio-astronomical sensing applications, whereas the coupling to a single super-conducting emitter may warrant a more detailed analysis).

In our analysis we will consider the three simple receiver circuits in Fig. 5.3: The resonant serial (a) and parallel (b) RLC circuits as well as the non-resonant RC circuit (c). Regarding the resonant circuits, the labels serial and parallel are determined by the incoupling position of the electrical signal source, i.e. the transmission line, relative to the inductor (inductance L) and the coupling capacitor (steady-state capacitance $\bar{C}_{\rm c}$). The combined (ohmic and/or radiative) resistance R_L of the inductor is in either case assumed to be the dominant electrical loss port, whereas we take the coupling capacitor to be lossless. We also include an incoupling resistance $R_{\rm min}$ to account for the residual ohmic loss present even in absence of an inductor as in the RC circuit. Each signal or noise port has an associated voltage source representing its input. As a means to the resonance frequency, a tuning capacitor of capacitance $C_{\rm T}$ has been included in the RLC circuits. We will use the symbol $C_{\rm tot}$ to denote the total electrical capacitance in the resonant circuits, i.e., $C_{\rm tot}^{\rm (ser)} \equiv \bar{C}_{\rm c} + C_{\rm T}$ and $C_{\rm tot}^{\rm (par)} \equiv \bar{C}_{\rm c} + C_{\rm T} + C_{\rm l}$. Here, $C_{\rm T}$ is a tuning capacitance serving the purpose of aligning the electrical resonance with the signal frequency $\omega_{\rm s}$. Based on these definitions, we define the LC impedance $Z_0 \equiv \sqrt{L/C_{\rm tot}}$ for the resonant circuits, and $Z_0' \equiv 1/(\omega_{\rm s}\bar{C}_{\rm c})$ for the RC circuit.

In comparing the circuits, we will always assume the values of $\omega_{\rm s}, Z_{\rm tx}, R_{\rm min}$ and $\bar{C}_{\rm c}$ to be fixed. This corresponds to the situation of a given signal that we wish to transduce using a given EM coupling interface, whereas we are free to build any linear circuit around this interface. Also, we will implicitly assume the drive-enhanced optomechanical (annihilation operator) coupling strength $g_{\rm OM}$ (units of $\rm s^{-1}$) [7] and the EM coupling strength G (units of V/m) [1] to be constant across choices of optical detuning Δ and circuit layouts. Effectively, this amounts to assuming the same intracavity fields for different circuits. By doing this, we ignore that the intracavity field may depend on detuning and that the resonant enhancement of the drive field will be different for different circuits. This is a meaningful comparison if the coupling strength is limited by competing non-linearities and instabilities a realistic scenario. Fixed G then corresponds to the EM biasing being limited by a maximal (rms) voltage that can be applied as dictated e.g. by the mechanical pull-in instability. Moreover, we assume the noise flux spectral densities n_i of the dissipative channels in the system to be given (evaluated at suitable frequencies). For the resonant circuits, we will assume their resonance frequencies $\omega_{\rm LC} \equiv (LC_{\rm tot})^{-1/2}$ to align with the electrical signal carrier $\omega_{\rm LC} = \omega_{\rm s}$. This still leaves the quantities L and $C_{\rm l}$ as tunable parameters as will be discussed in detail when we optimize the circuits in Section 5.7.

5.5 Deducing scattering matrix elements

We will now determine the scattering matrix elements starting from the circuit diagrams in Fig. 5.3. The scattering matrix $\mathbf{S}(\Omega)$ contains all information about the transducer when combined with a specification of the input fields as discussed in Section 5.3. A convenient way to derive $\mathbf{S}(\Omega)$ is to use the reduced equivalent circuit Fig. 5.1c. The quantities appearing in the reduced circuit, which we need to determine in order to apply this method, are the Thévenin equivalent voltage $\delta V'(\omega)$ of the electrical subcircuit and the EM resistances $R_{\rm EM,\pm}$. These will be derived in the following two subsections, after which we obtain the scattering matrix elements of interest in Subsection 5.5.3.

5.5.1 Thévenin voltages

Physically, the Thévenin voltage simply corresponds to the net force due to electrical sources experienced by the (loaded) mechanical mode. We will determine this for each receiver circuit as the voltage across the coupling capacitor, i.e. the voltage across $\bar{C}_{\rm c}$ in absence of the mechanical loop, accounting for the contributions from each of the "bare" voltage sources appearing in the respective diagrams, Figs. 5.3. Each contribution can be determined by iterative application of the voltage transfer rule for impedances. The sources entering the Thévenin voltage are seen in Figs. 5.3: The Johnson noise of the inductor V_L and the incoupling resistance $V_{\rm min}$, and the incoming transmission line signal $V_{\rm tx}$. In the following we will derive the transfer functions $\mathcal{T}_i(\omega)$ for each of these voltage sources for each of the three circuit designs, writing the Thévenin voltage $\delta V'$ as defined in Fig. 5.3 as the linear combination

$$\delta V'(\omega) = 2\mathcal{T}_{\rm tx}(\omega)V_{\rm tx}(\omega) + 2\mathcal{T}_L(\omega)V_L(\omega) + 2\mathcal{T}_{\rm min}(\omega)V_{\rm min}(\omega). \tag{5.1}$$

This determines the electrical voltage source $V_{\rm e}$ that appears in the reduced equivalent circuit (Fig. 5.1c) via Eq. (4.97), which we reproduce here:

$$2V_{\rm e}(\Omega) = \delta V'(\omega_{\rm d} + \Omega) + \delta V'^*(\omega_{\rm d} - \Omega). \tag{5.2}$$

Since, by the adiabatic assumption, the frequency dependence of the transfer functions $\mathcal{T}_i(\omega)$ is negligible over the transducer bandwidth, we see from Eq. (5.2) that we will only need to evaluate $\mathcal{T}_i(\omega_{\rm d} \pm \Omega_{\rm m})$ in our calculations.

5.5.1.1 Serial RLC

Starting with the serial RLC, in which all electrical sources enter the diagram equivalently (Fig. 5.3a), we find using the voltage division rule in terms of impedances

$$\mathcal{T}^{\rm (ser)} \equiv \mathcal{T}^{\rm (ser)}_{\rm tx} = \mathcal{T}^{\rm (ser)}_{L} = \mathcal{T}^{\rm (ser)}_{\rm min}, \tag{5.3}$$

$$\mathcal{T}^{\rm (ser)}(\omega) = \frac{1/(-i\omega C_{\rm tot})}{1/(-i\omega C_{\rm tot}) - i\omega L + Z_{\rm tx} + R_L + R_{\rm min}} \xrightarrow{\omega=\omega_{\rm LC}} i\frac{Z_0}{Z_{\rm tx} + R_L + R_{\rm min}}, \tag{5.4}$$

in terms of the LC impedance $Z_0 \equiv \sqrt{L/C_{\rm tot}}$ introduced previously. Evaluating the transfer function $\mathcal{T}^{\rm (ser)}$ at the electrical resonance $\omega_{\rm LC} = (LC_{\rm tot})^{-1/2}$ in Eq. (5.4), we find that it equals the (loaded) electrical Q-factor. Since all electrical inputs of the serial circuit have the same transfer function $\mathcal{T}^{\rm (ser)}$, signal and ohmic noise enjoy the same enhancement and no other part of the transducer may alter this one-to-one ratio between signal and ohmic noise. Hence the resonance does not improve the input signal relative to the other electrical noise sources; it does, however, increase the electrical signal relative to the optical and mechanical equivalent voltages $V_{\rm o}$ and $V_{\rm m}$ (see Fig. 5.1c).

5.5.1.2 RC circuit

Now we consider the inductorless RC circuit (Fig. 5.3c) for which we define the characteristic impedance $Z'_0 \equiv 1/(\omega_{\rm s}\bar{C}_{\rm c})$ in terms of the electrical signal carrier frequency $\omega_{\rm s}$. In this case there is no inductor, and from the circuit diagram in Fig. 5.3c, we find:

$$\mathcal{T}^{\rm (RC)}(\omega) \equiv \mathcal{T}^{\rm (RC)}_{\rm tx} = \mathcal{T}^{\rm (RC)}_{\rm min},\ \mathcal{T}^{\rm (RC)}_{L} = 0$$

$$\mathcal{T}^{\rm (RC)}(\omega) = \frac{1/(-i\omega\bar{C}_{\rm c})}{1/(-i\omega\bar{C}_{\rm c}) + Z_{\rm tx} + R_{\rm min}} \xrightarrow{\omega=\omega_{\rm s}} \left(1 - i\frac{Z_{\rm tx} + R_{\rm min}}{Z'_0}\right)^{-1} \approx 1,$$

where in the approximation we have taken the limit of short RC time of the loaded circuit compared to the signal period, $(Z_{\text{tx}} + R_{\text{min}})\bar{C}_{\text{c}}\omega_{\text{s}} = (Z_{\text{tx}} + R_{\text{min}})/Z'_0 \ll 1$. We thus see that in this limit the input voltage is mapped with a factor of unity, which is smaller than in the resonant case discussed above, since we do not gain from the resonant buildup in the circuit. On the other hand this circuit has the advantage that it completely gets rid of the inductor, whereby this circuit has the minimum amount of electrical noise corresponding to the reduced residual resistance R_{min}. Furthermore this circuit has the additional advantage that there is no need to tune the circuit into resonance.

5.5.1.3 Parallel RLC

Turning now to the parallel RLC circuit, we start by discussing the role of the loading capacitor of capacitance C_{l} (see Fig. 5.3b). This capacitor is inserted in the circuit to transform the transmission line impedance Z_{tx}, thereby providing a practical knob for tuning the effective loading of the circuit. This can be seen by rewriting the admittance Y_{l} of the arm containing these circuit elements

$$\begin{aligned} Y_{\text{l}}(\omega) = 1/Z_{\text{l}}(\omega) &= \left(\frac{1}{-i\omega C_{\text{l}}} + Z_{\text{tx}} + R_{\text{min}}\right)^{-1} \\ &= \frac{[\omega C_{\text{l}}(Z_{\text{tx}} + R_{\text{min}})]^2}{1 + [\omega C_{\text{l}}(Z_{\text{tx}} + R_{\text{min}})]^2} \frac{1}{Z_{\text{tx}} + R_{\text{min}}} - i\omega \frac{C_{\text{l}}}{1 + [\omega C_{\text{l}}(Z_{\text{tx}} + R_{\text{min}})]^2}, \end{aligned} \quad (5.5)$$

showing that $\text{Re}[Y_{\text{l}}(\omega)]$ can be tuned in the interval $[0; 1/(Z_{\text{tx}} + R_{\text{min}})]$ by scanning C_{l} between the limits $[\omega C_{\text{l}}(Z_{\text{tx}} + R_{\text{min}})]^2 \ll 1$ and $[\omega C_{\text{l}}(Z_{\text{tx}} + R_{\text{min}})]^2 \gg 1$. The latter limit amounts to removing the loading capacitor so that $\text{Re}[Y_{\text{l}}(\omega)] = 1/(Z_{\text{tx}} + R_{\text{min}})$, resulting in performance which we find to be essentially identical to the inductorless RC circuit (see below). For this reason we focus on the limit $[\omega C_{\text{l}}(Z_{\text{tx}} + R_{\text{min}})]^2 \ll 1$ in which case we may approximate Eq. (5.5) by

$$Y_{\text{l}}(\omega) \approx \frac{[\omega C_{\text{l}}(Z_{\text{tx}} + R_{\text{min}})]^2}{Z_{\text{tx}} + R_{\text{min}}} - i\omega C_{\text{l}}, \quad (5.6)$$

which is equivalent to a resistance $(Z_{\text{tx}} + R_{\text{min}})/[\omega C_{\text{l}}(Z_{\text{tx}} + R_{\text{min}})]^2$ in parallel to a capacitance C_{l} (assuming $\omega C_{\text{l}}[Z_{\text{tx}} + R_{\text{min}}]$ can be taken constant over the bandwidth of interest); this means that C_{l} combines in parallel with $\bar{C}_{\text{c}}$ and C_{T}, as presumed in the definition of C_{tot}, and hence affects the circuit resonance frequency ω_{LC}. By similar steps we approximate the admittance Y_L of the arm containing the inductor in the limit $Q_L \equiv \omega_{\text{LC}} L/R_L = Z_0/R_L \gg 1$ by

$$Y_L(\omega) = 1/Z_L(\omega) = (-i\omega L + R_L)^{-1} \approx \frac{R_L}{Z_0^2} + (-i\omega L)^{-1}, \quad (5.7)$$

which amounts to converting the serial inductive resistance R_L into a parallel resistance Z_0^2/R_L (ignoring a small shift in L of relative size $1/Q_L^2$, see Appendix C.1). To get the most efficient transducer we are interested in overcoupling the circuit by the transmission line (in some cases, coupling critically). From the above expression we see that this requires $\text{Re}[Y_{\text{l}}(\omega_{\text{LC}})] < \text{Re}[Y_L(\omega_{\text{LC}})]$ since these arms combine in parallel (see Fig. 5.3b). To achieve this, Eqs. (5.6,5.7) imply that C_{l} must exceed

$$C_{\text{crit}} = \frac{\bar{C}_{\text{c}} + C_{\text{T}}}{\sqrt{\frac{Z_{\text{tx}} + R_{\text{min}}}{R_L}} - 1}. \quad (5.8)$$

For typical non-superconducting rf circuits R_L is likely to be sizable and hence this implies that $C_l > \bar{C}_c + C_T$ (for Z_{tx} larger than but comparable to R_L), which would cause a large shift of the circuit resonance. To compare different circuits we shall therefore assume that the sum of the capacitances C_{tot} is fixed so that also the resonance frequency is fixed, but for the typical rf scenario this entails $C_l \gg \bar{C}_c + C_T$. As we shall see this essentially renders the circuit similar to a serial RLC circuit. In contrast, for superconducting MW circuit which may have $(Z_{tx} + R_{min})/R_L \gg 1$ the parallel RLC configuration allows for overcoupling while keeping the loading capacitance small, $C_l \ll \bar{C}_c + C_T$.

Having discussed the role of C_l, we now turn to the transfer functions for the parallel RLC circuit using the approximations (5.6,5.7) and assuming $\omega C_l(Z_{tx} + R_{min}) \ll 1$. Since V_{tx} and V_{min} enter in series, we immediately have

$$\mathcal{T}_{tx}^{(par)} = \mathcal{T}_{min}^{(par)}.$$

The signal transfer function $\mathcal{T}_{tx}^{(par)}$ is found as the ratio of the loading arm admittance to the sum of all admittances $Y_l/\sum_i Y_i$:

$$\mathcal{T}_{tx}^{(par)}(\omega) = \frac{\frac{[\omega C_l(Z_{tx}+R_{min})]^2}{Z_{tx}+R_{min}} - i\omega C_l}{\frac{[\omega C_l(Z_{tx}+R_{min})]^2}{Z_{tx}+R_{min}} - i\omega C_{tot} + \frac{1}{-i\omega L} + \frac{R_L}{Z_0^2}} \xrightarrow{\omega=\omega_{LC}} \approx \frac{-i\omega_{LC} C_l}{\frac{[\omega_{LC} C_l(Z_{tx}+R_{min})]^2}{Z_{tx}+R_{min}} + \frac{R_L}{Z_0^2}}. \quad (5.9)$$

Assuming that the loading capacitance C_l can be varied at will, we consider which value optimizes the magnitude of $\mathcal{T}_{tx}^{(par)}(\omega_{LC})$ to have the maximal transfer. This is achieved at the critical coupling condition $C_l = C_{crit}$, (5.8), yielding (for fixed C_{tot})

$$\mathcal{T}_{tx}^{(par)}(\omega_{LC})\Big|_{crit.} = -i\frac{1}{2}\frac{Z_0}{\sqrt{R_L(Z_{tx}+R_{min})}}, \quad (5.10)$$

in magnitude this exceeds what is achieved with the corresponding serial circuit, Eq. (5.4), by a factor greater than unity, $\approx \sqrt{(Z_{tx}+R_{min})/R_L}/2$ in the regime $Z_{tx} \gg R_L$, hence allowing for greater relative suppression of the mechanical noise. Similarly, we find the transfer function of the inductor as $Y_L/\sum_i Y_i$

$$\mathcal{T}_{L}^{(par)}(\omega) = \frac{\frac{1}{-i\omega L} + \frac{R_L}{Z_0^2}}{\frac{[\omega C_l(Z_{tx}+R_{min})]^2}{Z_{tx}+R_{min}} - i\omega C_{tot} + \frac{1}{-i\omega L} + \frac{R_L}{Z_0^2}} \xrightarrow{\omega=\omega_{LC}} \approx \frac{i/Z_0}{\frac{[\omega_{LC} C_l(Z_{tx}+R_{min})]^2}{Z_{tx}+R_{min}} + \frac{R_L}{Z_0^2}}. \quad (5.11)$$

From here we see that the ratio between the transfer functions for the inductive Johnson noise and the transmission line signal is

$$\frac{\mathcal{T}_{L}^{(par)}(\omega_{LC})}{\mathcal{T}_{tx}^{(par)}(\omega_{LC})} \approx \frac{(-i\omega_{LC}L)^{-1}}{-i\omega_{LC}C_l} = \frac{C_{tot}}{C_l}. \quad (5.12)$$

Since the ratio (5.12) exceeds unity, the parallel RLC offers less electrical noise suppression than its serial counterpart, for which the corresponding ratio (5.3) is unity. Eq. (5.12) approaches unity in the limit $C_\mathrm{l} \gg \bar{C}_\mathrm{c} + C_\mathrm{T}$, whereas for critical coupling $C_\mathrm{l} = C_\mathrm{crit}$, (5.8), it takes the value

$$\left.\frac{\mathcal{T}_L^{(\mathrm{par})}(\omega_\mathrm{LC})}{\mathcal{T}_\mathrm{tx}^{(\mathrm{par})}(\omega_\mathrm{LC})}\right|_\mathrm{crit.} = \sqrt{\frac{Z_\mathrm{tx} + R_\mathrm{min}}{R_L}}.$$

For fixed circuit resonance frequency ω_s, the electrical signal-to-noise ratio of the parallel RLC approximately interpolates between that of the serial RLC in the limit $\omega_\mathrm{LC} C_\mathrm{l}(Z_\mathrm{tx}+R_\mathrm{min}) \ll 1$ (and $C_\mathrm{l} \gg \bar{C}_\mathrm{c}+C_\mathrm{T}$) and that of the RC circuit when $\omega C_\mathrm{l}(Z_\mathrm{tx} + R_\mathrm{min}) \gg 1$.

In conclusion we thus find that choosing $C_\mathrm{l} = C_\mathrm{crit}$, (5.8), in order to have critical coupling, the parallel RLC circuit enhances the electrical signal relative to the mechanical noise by the factor (5.10), but this comes at a similar cost in the electrical noise from the inductor. On the other hand, taking $C_\mathrm{l} > C_\mathrm{crit}$ we decrease the gain in the signal relative to the mechanical, but at the same time we decrease the electrical noise from the inductor. Hence the value of the coupling capacitor can be chosen to optimize the performance depending on the dominant imperfection of the particular device at hand.

5.5.2 Electromechanical resistances, $R_{\mathbf{EM},\pm}$

Having determined the Thévenin voltages of the electrical circuits above, we now turn to the second ingredient of the reduced equivalent circuit, the electromechanical resistances $R_{\mathrm{EM},\pm}$. These can be evaluated from the Thévenin impedances of the electrical circuits using Eq. (4.95).

Considering first the resonant circuits, Fig. 5.3a&b, we note that their Thévenin impedances $Z'(\omega)$ include the coupling capacitor in parallel to the remainder of the circuit. Hence, to relate to the notation of Section 4.9.2, we have $Z'(\omega) = [-i\omega\bar{C}_\mathrm{c} + 1/Z(\omega)]^{-1}$, where $Z(\omega)$ is the electrical impedance excluding the coupling capacitor, which determines $Z_{\mathrm{e},\pm}$ in the full equivalent circuit (Fig. 5.1b). Then, in terms of $Z'(\omega)$, Eq. (4.95) reads

$$R_{\mathrm{EM},\pm} = \frac{\omega_\mathrm{d} \pm \Omega_\mathrm{m}}{\Omega_\mathrm{m}} \,\mathrm{Re}\left[Z'(\omega)\right]\big|_{\omega=\omega_\mathrm{d}\pm\Omega_\mathrm{m}}.$$

Using this expression we find that the effective EM resistances for the resonant circuits are given by

$$R_{\mathrm{EM},\pm} = \frac{Z_0^2}{R_\mathrm{LC}^{(\mathrm{X})}} \cdot \begin{cases} \delta_{+,\pm} & [\text{DC bias}] \\ \frac{\omega_\mathrm{d}\pm\Omega_\mathrm{m}}{\Omega_\mathrm{m}}[\mathcal{K}_\pm^{(\mathrm{X})}]^2 & [\text{AC drive}] \end{cases}, \tag{5.13}$$

where the loaded LC circuit resistances are

$$R_\mathrm{LC}^{(\mathrm{ser})} \equiv R_L + Z_\mathrm{tx} + R_\mathrm{min}, \quad R_\mathrm{LC}^{(\mathrm{par})} \equiv R_L + (Z_\mathrm{tx} + R_\mathrm{min})\,(C_\mathrm{l}/C_\mathrm{tot})^2\,,$$

respectively, and we have defined $\mathcal{K}_\pm^{(\mathrm{X})} \equiv |\mathcal{K}^{(\mathrm{X})}(\pm\Omega_\mathrm{m})|$ from the Lorentzian $\mathcal{K}^{(\mathrm{X})}(\omega)$ for circuit 'X' in analogy to the optical $\mathcal{L}(\Omega)$,

$$\mathcal{K}^{(\mathrm{X})}(\Omega) \equiv \frac{R_\mathrm{LC}^{(\mathrm{X})}/2L}{-i(\omega_\mathrm{d} + \Omega - \omega_\mathrm{LC}) + R_\mathrm{LC}^{(\mathrm{X})}/2L}, \tag{5.14}$$

valid for $|\omega_\mathrm{d}+\Omega-\omega_\mathrm{LC}| \ll \omega_\mathrm{LC}$. Note that $\mathcal{K}^{(\mathrm{X})}(\omega)$ is closely related to the line shape function $\mathcal{Q}_l(\Omega)$ of Chapter 4, see Eqs. (4.64,4.75). For the non-resonant RC circuit we find the following resistances

$$R^{(\mathrm{RC})}_{\mathrm{EM},\pm} \approx \frac{Z_\mathrm{tx}+R_\mathrm{min}}{1+(Z_\mathrm{tx}+R_\mathrm{min})^2/Z_0'^2} \quad \text{[AC drive]}, \tag{5.15}$$

and likewise for DC bias except that in that case $R^{(\mathrm{RC})}_{\mathrm{EM},-}=0$.

The EM resistances are the electrical analogs of the anti-Stokes and Stokes rates (4.83) for the scattering of a phonon into the upper and lower EM sidebands, respectively, $\gamma_{\mathrm{EM},\pm} \equiv R_{\mathrm{EM},\pm}/L_\mathrm{m}$. In terms of these rates, the net EM broadening of the mechanical mode by the circuits is given by

$$\Gamma_\mathrm{EM} = \begin{cases} \gamma_{\mathrm{EM},+} & \text{[DC bias]} \\ \gamma_{\mathrm{EM},+}-\gamma_{\mathrm{EM},-} & \text{[AC drive]} \end{cases}. \tag{5.16}$$

5.5.3 Scattering matrix elements

Having determined the reduced Thévenin voltage V_e and the EM resistances $R_{\mathrm{EM},\pm}$, we have now reduced the three electro-optomechanical receiver circuits to the simple form of a driven, damped oscillator shown in Fig. 5.1c (the optical equivalent components were derived in Section 4.9.1). It is therefore clear that quantities of interest will share a common form. We will now derive the scattering relation (3.6) giving the output field at the desired optical port in terms of the various inputs and thereby explicitly determine the scattering matrix elements of interest. To do so we combine the effective mechanical response as described by the equivalent current,

$$I_\mathrm{m}(\Omega) = \frac{1}{Z_{\mathrm{m,eff}}(\Omega)}\left[2V_\mathrm{e}(\Omega)+2V_\mathrm{o}(\Omega)+2V_\mathrm{m}(\Omega)\right],$$

with the effective OM input-output relations, Eqs. (4.91,4.92); in terms of the quantized source terms this yields

$$\hat{a}^{(\mathrm{ext})}_\mathrm{out}(\omega_\mathrm{l}+\Omega) = ie^{i\theta_+}\sqrt{\eta_\mathrm{opt}}\sqrt{\frac{2R_{\mathrm{OM},+}}{\hbar\Omega_\mathrm{m}}}\frac{\Omega_\mathrm{m}}{\Omega}2\frac{\hat{V}_\mathrm{e}(\Omega)+\hat{V}_\mathrm{o}(\Omega)+\hat{V}_\mathrm{m}(\Omega)}{Z_{\mathrm{m,eff}}(\Omega)} + \hat{a}^{(\mathrm{eff})}_\mathrm{in}(\omega_\mathrm{l}+\Omega) \tag{5.17}$$

$$\hat{a}^{(\mathrm{ext})}_\mathrm{out}(\omega_\mathrm{l}-\Omega) = -ie^{i\theta_-}\sqrt{\eta_\mathrm{opt}}\sqrt{\frac{2R_{\mathrm{OM},-}}{\hbar\Omega_\mathrm{m}}}\frac{\Omega_\mathrm{m}}{\Omega}2\frac{\hat{V}^\dagger_\mathrm{e}(\Omega)+\hat{V}^\dagger_\mathrm{o}(\Omega)+\hat{V}^\dagger_\mathrm{m}(\Omega)}{Z^*_{\mathrm{m,eff}}(\Omega)} + \hat{a}^{(\mathrm{eff})}_\mathrm{in}(\omega_\mathrm{l}-\Omega), \tag{5.18}$$

where the itinerant electrical (5.2), optical (4.90), and mechanical input fields enter via ($R_\mathrm{tx} \equiv Z_\mathrm{tx}$)

$$\hat{V}_\mathrm{e}(\Omega) = \sum_{i\in\{\mathrm{tx},L,\mathrm{min}\}}\Bigg[\mathcal{T}_i(\omega_\mathrm{d}+\Omega)\sqrt{\frac{\hbar(\omega_\mathrm{d}+\Omega)R_i}{2}}\hat{a}^{(i)}_\mathrm{in}(\omega_\mathrm{d}+\Omega) + \mathcal{T}^*_i(\omega_\mathrm{d}-\Omega)\sqrt{\frac{\hbar(\omega_\mathrm{d}-\Omega)R_i}{2}}\hat{a}^{(i)\dagger}_\mathrm{in}(\omega_\mathrm{d}-\Omega)\Bigg] \tag{5.19}$$

$$\hat{V}_{\rm o}(\Omega) = -i\frac{2g_{\rm OM}}{\sqrt{\kappa}}\frac{\sqrt{\hbar m\Omega_{\rm m}/2}}{\bar{C}_{\rm c}G}[e^{i\theta_+}\mathcal{L}_+\hat{a}_{\rm in}^{(\rm opt)}(\omega_{\rm l}+\Omega) - e^{-i\theta_-}\mathcal{L}_-\hat{a}_{\rm in}^{(\rm opt)\dagger}(\omega_{\rm l}-\Omega)], \tag{5.20}$$

$$\hat{V}_{\rm m}(\Omega) = \sqrt{\frac{\hbar\Omega R_{\rm m}}{2}}\hat{a}_{\rm in}^{(\rm m)}(\Omega), \tag{5.21}$$

where the optical input operator $\hat{a}_{\rm in}^{(\rm opt)}(\omega) \equiv \sqrt{\eta_{\rm opt}}\hat{a}_{\rm in}^{(\rm ext)}(\omega) + \sqrt{1-\eta_{\rm opt}}\hat{a}_{\rm in}^{(0)}(\omega)$ is a linear combination of the two decay channels of the cavity and the effective optical noise operator $\hat{a}_{\rm in}^{(\rm eff)}$ is defined in Eq. (4.93). Eqs. (5.17-5.21) are effectively a statement of the two columns in the scattering matrix $\mathbf{S}(\Omega)$ that relate the two optical output sidebands $\hat{a}_{\rm out}^{(\rm ext)}(\omega_{\rm l}\pm\Omega)$ to all the inputs of the system.

To calculate the peak signal transfer efficiencies $\eta_0^{(\pm)}$ (as defined via Eq. (3.8)), we only need to track how $\hat{a}_{\rm in}^{(\rm tx)}(\omega_{\rm d}+\Omega)$ maps into the optical output sidebands, i.e. two particular elements of $\mathbf{S}(\Omega)$. Let us now consider these matrix elements in detail as an example. From the Eqs. (5.17-5.19) we find (as always assuming the incoming electrical signal to be confined to the upper EM sideband)

$$\hat{a}_{\rm out}^{(\rm ext)}(\omega_{\rm l}+\Omega) = ie^{i(\theta_++\phi_+)}\sqrt{\eta_{\rm opt}\eta_{\rm el}}\frac{\Omega_{\rm m}}{\Omega}\frac{2\sqrt{R_{\rm OM,+}R_{\rm EM,+}}}{Z_{\rm m,eff}(\Omega)}\hat{a}_{\rm in}^{(\rm tx)}(\omega_{\rm d}+\Omega) + \text{noise} \tag{5.22}$$

$$\hat{a}_{\rm out}^{(\rm ext)}(\omega_{\rm l}-\Omega) = -ie^{i(\theta_--\phi_+)}\sqrt{\eta_{\rm opt}\eta_{\rm el}}\frac{\Omega_{\rm m}}{\Omega}\frac{2\sqrt{R_{\rm OM,-}R_{\rm EM,+}}}{Z^*_{\rm m,eff}(\Omega)}\hat{a}_{\rm in}^{(\rm tx)\dagger}(\omega_{\rm d}+\Omega) + \text{noise}, \tag{5.23}$$

where we have introduced the electrical coupling efficiency (for the upper EM sideband) as

$$\eta_{\rm el} \equiv \frac{\omega_{\rm d}+\Omega_{\rm m}}{\Omega_{\rm m}}\frac{|\mathcal{T}_{\rm tx}(\omega_{\rm d}+\Omega_{\rm m})|^2 Z_{\rm tx}}{R_{\rm EM,+}}. \tag{5.24}$$

This is the fraction of the electrical loading caused by the transmission line and, conversely, the efficiency with which transmission line signals can be mapped into the system relative to the electrical noise sources. Eqs. (5.22,5.23) reflect the simplicity of the reduced equivalent circuit, Fig. 5.1c. We may eliminate the electrical units in these equations by introducing the EM and OM anti-Stokes and Stokes rates (4.83), $\gamma_{\rm EM/OM,\pm} \equiv R_{\rm EM/OM,\pm}/L_{\rm m}$,

$$\hat{a}_{\rm out}^{(\rm ext)}(\omega_{\rm l}+\Omega) \approx ie^{i(\theta_++\phi_+)}\sqrt{\eta_{\rm opt}\eta_{\rm el}}\frac{\sqrt{\gamma_{\rm OM,+}\gamma_{\rm EM,+}}}{-i(\Omega-\Omega_{\rm m})+\gamma_{\rm m,eff}/2}\hat{a}_{\rm in}^{(\rm tx)}(\omega_{\rm d}+\Omega) + \text{noise} \tag{5.25}$$

$$\hat{a}_{\rm out}^{(\rm ext)}(\omega_{\rm l}-\Omega) \approx -ie^{i(\theta_--\phi_+)}\sqrt{\eta_{\rm opt}\eta_{\rm el}}\frac{\sqrt{\gamma_{\rm OM,-}\gamma_{\rm EM,+}}}{i(\Omega-\Omega_{\rm m})+\gamma_{\rm m,eff}/2}\hat{a}_{\rm in}^{(\rm tx)\dagger}(\omega_{\rm d}+\Omega) + \text{noise}, \tag{5.26}$$

where we for simplicity have made the mechanical narrow-band approximation, $|\Omega-\Omega_{\rm m}| \ll \Omega_{\rm m}$. The scattering matrix elements in Eqs. (5.25,5.26) have the following straightforward interpretation: Transmission line signal at the upper sideband couples at rate $\eta_{\rm el}\gamma_{\rm EM,+}$ into the mechanical mode, whose response is governed by the detuning $\Omega - \Omega_{\rm m}$ and effective width $\gamma_{\rm m,eff}$ and is read out optically at rates $\eta_{\rm opt}\gamma_{\rm OM,\pm}$ at the upper/lower sideband. Note that the lower optical sideband reads out the Hermitian conjugate of the transmission line input operator. The remaining coefficients of the scattering relation (5.17-5.21) can be put on a similar form (with the exception of the optical-to-optical elements, see discussion below Eqs. (4.81) in Section 4.8).

5.6 Calculating transducer parameters η and N

The scattering relation derived above, given by Eqs. (5.17-5.21), can be used to determine the transduction for all frequency components within the mechanical bandwidth. Henceforth we will, however, restrict our attention to the transducer peak, corresponding to input signals that are narrow compared to the transducer bandwidth. Hence, now that the scattering relation has been established, we can extract the (peak) transducer parameters $\eta_0^{(\pm)}$ and $N_0^{(\pm)}$ at the upper/lower output sideband as defined in Section 3.4.

5.6.1 Peak signal transfer efficiency, $\eta_0^{(\pm)}$

First of all, Eqs. (5.25,5.26) allow to us to directly read off $\eta_0^{(\pm)}$ (3.8), and hence the peak signal transfer efficiency into the upper/lower OM sideband for the circuits takes the common form,

$$\eta_0^{(\pm)} = \eta_{\rm opt}\eta_{\rm el}\frac{4\gamma_{\rm OM,\pm}\gamma_{\rm EM,+}}{(\gamma_{\rm m,0} + \Gamma_{\rm OM} + \Gamma_{\rm EM})^2}. \tag{5.27}$$

in terms of the cavity-mechanical anti-Stokes/Stokes rates, $\gamma_{\rm EM/OM,\pm}$. The net EM and OM broadening are given by

$$\Gamma_{\rm EM/OM} \equiv \gamma_{\rm EM/OM,+} - \gamma_{\rm EM/OM,-}. \tag{5.28}$$

$\eta_{\rm el/opt}$ in (5.27) are the cavity coupling efficiencies which determine the fraction of the signal in the cavities that makes it into the desired channel as opposed to being dissipated into the cavity loss channels, i.e. a fraction $1 - \eta_{\rm el}$ of the electrical cavity signal will be dissipated ohmically, see Eq. (5.24). Analogously, a fraction $1 - \eta_{\rm opt}$ of the signal in the optical cavity will be dissipated into loss channels. In the notation of Fig. 5.1a), the optical coupling efficiency is $\eta_{\rm opt} = \kappa_{\rm ext}/(\kappa_{\rm ext} + \kappa_0) = \kappa_{\rm ext}/\kappa$.

Eq. (5.27) is valid for arbitrary degree of sideband resolution as determined by the ratio of the sideband separation $2\Omega_{\rm m}$ to the respective circuit and cavity linewidths. In the regime of resolved EM and OM sidebands operated red-detuned by $-\Omega_{\rm m}$, we observe that $\Gamma_{\rm EM/OM} \to \gamma_{\rm EM/OM,+}$, thereby recovering the situation described by Eq. (1.2) in Section 1.1.2. Hence, under these circumstances, we get a transfer efficiency $\eta_0^{(+)}$, (5.27), only limited by $\eta_{\rm el}\eta_{\rm opt}$ in the impedance-matched, overdamped regime $\gamma_{\rm OM,+} = \gamma_{\rm EM,+} \gg \gamma_{\rm m,0}$. Outside the resolved sideband regime, however, the net cavity-mechanical broadening $\Gamma_{\rm EM/OM}$ (5.28) also has a negative contribution from $\gamma_{\rm EM/OM,-}$ leading to amplification effects whenever we have $\gamma_{\rm EM,-} > 0$ and/or $\gamma_{\rm OM,-} > 0$. This means that $\eta_0^{(\pm)}$ can exceed $\eta_{\rm el}\eta_{\rm opt}$ (and possibly even exceed unity), but this comes at the price of amplification noise and small bandwidth as discussed previously. The quantities $\eta_{\rm el}, \gamma_{\rm EM,+}, \Gamma_{\rm EM}$ in (5.27) depend on the circuit in question and will be presented below in Table 5.1.

5.6.2 Added noise, $N_0^{(\pm)}$

We now turn to the second transducer characteristic, the added noise N flux per unit bandwidth referenced to the input, (3.9), focusing on its values at the transducer peak of the upper/lower output sideband $N_0^{(\pm)}$. To determine these, we combine the scattering functions of the noise inputs into the optical output port, implicitly given by Eqs. (5.17-5.21), with the thermal expectation values of the input operators, see Eqs. (3.10,3.11), under the usual assumption of uncorrelated inputs. In the DC-driven or AC-driven EM resolved-sideband limit we find that for all circuits the added noise can be described by

$$N_0^{(\pm)} = \frac{R_{\rm min}}{Z_{\rm tx}}\left(n_{\rm min}(\omega_{\rm d}+\Omega_{\rm m}) + \delta_{-,\pm}\right) + \frac{R_L}{Z_{\rm tx}}\frac{|\mathcal{T}_L|^2}{|\mathcal{T}_{\rm tx}|^2}\left(n_L(\omega_{\rm d}+\Omega_{\rm m}) + \delta_{-,\pm}\right) \\ + \frac{1}{\gamma_{\rm EM,+}\eta_{\rm el}}\left[\gamma_{\rm m,0}\left(n_{\rm m}(\Omega_{\rm m}) + \delta_{-,\pm}\right) + \gamma_{\rm OM,\mp}\right]. \text{ [EM RSB]} \quad (5.29)$$

If the EM sidebands are not fully resolved additional electrical noise contributions will arise, as discussed previously. If we assume that the mechanical frequency is much smaller than the drive frequency $\Omega_{\rm m} \ll \omega_{\rm d}$ and take the high-temperature limit for the circuit $k_{\rm B}T_{\rm circ} \gg \hbar(\omega_{\rm d}+\Omega_{\rm m}) \Leftrightarrow n_i(\omega_{\rm d}+\Omega_{\rm m}) \gg 1$, in which $\langle\delta\hat{a}_{\rm in}^{(i)\dagger}(\omega)\delta\hat{a}_{\rm in}^{(i)}(\omega')\rangle \approx \langle\delta\hat{a}_{\rm in}^{(i)}(\omega)\delta\hat{a}_{\rm in}^{(i)\dagger}(\omega')\rangle \Rightarrow n_i[\omega_{\rm d}+\Omega_{\rm m}] + 1 \approx n_i[\omega_{\rm d}+\Omega_{\rm m}]$, then we may approximate $n_i(\omega_{\rm d}-\Omega_{\rm m})+1 \approx n_i(\omega_{\rm d}-\Omega_{\rm m}) \approx n_i(\omega_{\rm d}+\Omega_{\rm m}) \approx n_i(\omega_{\rm d})$ in Eq. (3.11), whereby in the fully EM unresolved-sideband regime (5.29) is replaced by[1]

$$N_0^{(\pm)} \approx n_{\rm tx}(\omega_{\rm d}-\Omega_{\rm m}) + 2\frac{R_{\rm min}}{Z_{\rm tx}}n_{\rm min}(\omega_{\rm d}) + 2\frac{R_L}{Z_{\rm tx}}\frac{|\mathcal{T}_L|^2}{|\mathcal{T}_{\rm tx}|^2}n_L(\omega_{\rm d}) \\ + \frac{1}{\gamma_{\rm EM,+}\eta_{\rm el}}\left[\gamma_{\rm m,0}n_{\rm m}(\Omega_{\rm m}) + \gamma_{\rm OM,\mp}\right], \text{ [EM unRSB]} \quad (5.30)$$

the first term being the tx line noise impinging at the lower electrical sideband. The result (5.30) determines the added noise for the EM unresolved-sideband regime in the classical, high-temperature limit. It shows that in this case the Johnson noise contribution is essentially doubled compared to the sideband-resolved case (5.29) (assuming the difference in drive enhancement to be unimportant).

Another regime of interest is that of low-temperature circuits, potentially near the quantum ground state. Working in this regime, it is important to note that the EM sideband resolution will determine the Johnson noise contributions to $N_0^{(\pm)}$ that persist even at absolute zero temperature $T \to 0$, where all $n_i \to 0$. In this limit, e.g. for red-detuned operation (both electrically and optically),

[1] The different frequency arguments for the thermal electrical occupancies have been chosen for didactical reasons although within the approximations stated above they are indistinguishable: We write $n_{\rm tx}(\omega_{\rm d}-\Omega_{\rm m})$ to indicate that this is the noise from the lower sideband of the tx line. Since the other sources, e.g., n_L have contributions from both sidebands $\omega_{\rm d} \pm \Omega_{\rm m}$, we make the symmetric choice $\omega_{\rm d}$.

$N_0^{(+)}$ will be bounded from below by the squeezed vacuum contribution from the lower electrical sideband. For AC drive where we can ignore corrections of order $\Omega_\mathrm{m}/\omega_\mathrm{d}$ by assuming $n_i(\omega_\mathrm{d}+\Omega_\mathrm{m}) \approx n_i(\omega_\mathrm{d}-\Omega_\mathrm{m}) \approx n_i(\omega_\mathrm{d})$, we find for the resonant circuits (assuming $R_\mathrm{min} \ll Z_\mathrm{tx}$)

$$N_0^{(+)} \approx \left(\frac{1}{\eta_\mathrm{el}} - 1\right)\left[1 + \frac{\mathcal{K}_-^2}{\mathcal{K}_+^2}\right] n_L(\omega_\mathrm{d}) + \frac{\mathcal{K}_-^2}{\mathcal{K}_+^2} n_\mathrm{tx}(\omega_\mathrm{d} - \Omega_\mathrm{m}) + \frac{1}{\eta_\mathrm{el}}\frac{\mathcal{K}_-^2}{\mathcal{K}_+^2} + \frac{1}{\gamma_{\mathrm{EM},+}\eta_\mathrm{el}}\left[\gamma_{\mathrm{m},0} n_\mathrm{m}(\Omega_\mathrm{m}) + \gamma_{\mathrm{OM},-}\right], \quad (5.31)$$

$$N_0^{(-)} \approx \left(\frac{1}{\eta_\mathrm{el}} - 1\right)\left[1 + \frac{\mathcal{K}_-^2}{\mathcal{K}_+^2}\right] n_L(\omega_\mathrm{d}) + \frac{\mathcal{K}_-^2}{\mathcal{K}_+^2} n_\mathrm{tx}(\omega_\mathrm{d} - \Omega_\mathrm{m}) + \left(\frac{1}{\eta_\mathrm{el}} - 1\right) + \frac{1}{\gamma_{\mathrm{EM},+}\eta_\mathrm{el}}\left[\gamma_{\mathrm{m},0}\left(n_\mathrm{m}(\Omega_\mathrm{m}) + 1\right) + \gamma_{\mathrm{OM},+}\right], \quad (5.32)$$

where $\mathcal{K}_\pm$ are electrical sideband strengths defined in Eq. (5.14). Considering the electrical and mechanical contributions in Eqs. (5.31,5.32), we notice that the finite-temperature contributions, i.e. those proportional to n_i for some i, are the same for the two sidebands, $(\pm)$. Thus, in the high-temperature limit where all $n_i \gg 1$ we have approximate equality between the EM contributions to $N_0^{(\pm)}$ at the upper and lower sidebands, $N_{\mathrm{EM},0}^{(+)} \approx N_{\mathrm{EM},0}^{(-)}$. The vacuum contributions of Eqs. (5.31,5.32), that persist even when all $n_i \to 0$, are different, however. The asymmetry between the third terms in Eqs. (5.31,5.32) is due to our assumption that the upper electrical sideband contains signal whereas the lower contains noise and the convention that the input of the former does not contribute to $N(\Omega)$.

5.7 Optimizing heterodyne detection sensitivity P

As mentioned above, to consider a specific application we will optimize the electro-optomechanical receiver circuits for the optical detection of transduced electrical signals. We now specify the homodyne detection scheme that we will apply to the optical output of the transducer (see Fig. 5.4). An important first consideration is how the electrical input signal is mapped to the optical sidebands. As mentioned previously, we will restrict the discussion to narrow electrical input signals (wrt. the transducer bandwidth) with carrier frequency at the upper EM sideband. A transducer in the OM resolved-sideband regime will simply translate the signal spectrum by adding an optical carrier frequency and subtracting an electrical ditto (with some gain and added noise), yielding an output spectrum as in Fig. 5.4b. Outside the resolved-sideband regime the signal spectrum will be mapped into two optical sidebands, which are in some sense scaled mirror images of one another (see Fig. 5.4c). As will be demonstrated below, the two-sideband (optical) homodyne measurement depicted in Fig. 5.4c, where the LO frequency is in between the sidebands $\omega_\mathrm{LO} = (\omega_+ + \omega_-)/2$, collects the same quadrature information from the transducer output as would a direct electrical heterodyne measurement corresponding to Fig. 5.4b with ω_LO

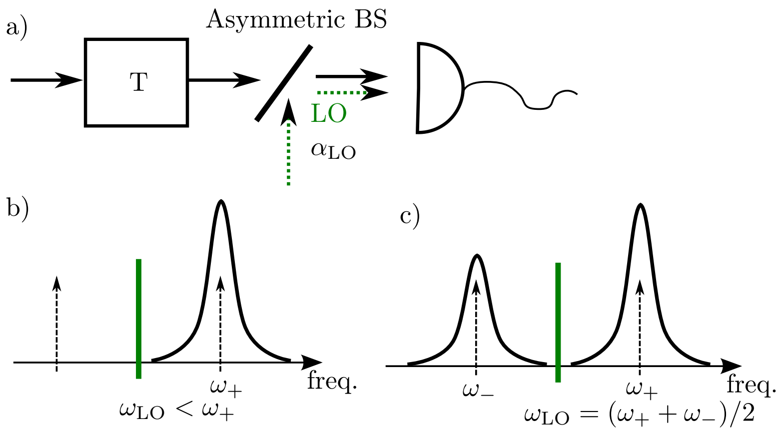

Figure 5.4: Illustration of homo- and heterodyning setups involving a single photodetector. a) The optical transducer output is combined with a local oscillator (LO) field using a highly asymmetric beam splitter; b) Heterodyning of a single isolated sideband at ω_+ using a LO at some $\omega_{\mathrm{LO}} < \omega_+$ causing the admixture of vacuum noise. The measurement b) simultaneously captures both quadratures at the cost of an extra quantum of vacuum noise; c) Two-sideband homodyning using a LO frequency in between the sidebands at $\omega_\pm$, $\omega_{\mathrm{LO}} = (\omega_+ + \omega_-)/2$.

representing an electrical LO (but, crucially, the optical measurement allows for increased sensitivity). This choice can be regarded as a practical method of measuring both quadratures of the input signal simultaneously at the cost of adding an additional quantum of vacuum noise. Note that this addition of a quantum of vacuum noise is a fundamental requirement of quantum mechanics for any simultaneous measurement of two conjugate quadratures.

We now turn to analyzing the signal and noise content of the homodyne photo-current spectrum $\hat{I}(\Omega)$ obtained using a local oscillator state α_{LO} of frequency $\omega_{\mathrm{LO}} = \omega_{\mathrm{l}}$ and phase angle $\theta_{\mathrm{LO}} = \mathrm{Arg}[\alpha_{\mathrm{LO}}]$ (see Appendix C.2.1 for details). Using the generic scattering relation (3.6) to substitute for $\hat{a}_{\mathrm{out,e}}$ in $\hat{I}(\Omega) \approx \alpha^*_{\mathrm{LO}}\hat{a}_{\mathrm{out,e}}(\Omega) + \alpha_{\mathrm{LO}}\hat{a}^\dagger_{\mathrm{out,e}}(-\Omega)$, we find for $\Omega > 0$

$$\hat{I}(\Omega)/|\alpha_{\mathrm{LO}}| = t_{\mathrm{s},\theta_{\mathrm{LO}}}(\Omega)\hat{a}_{\mathrm{in,s}}(\Omega) + \hat{\mathcal{N}}_{\theta_{\mathrm{LO}}}(\Omega), \tag{5.33}$$

with

$$t_{\mathrm{s},\theta_{\mathrm{LO}}}(\Omega) \equiv e^{-i\theta_{\mathrm{LO}}}U_{\mathrm{s}}(\Omega) + e^{i\theta_{\mathrm{LO}}}V^*_{\mathrm{s}}(-\Omega), \tag{5.34}$$

$$\hat{\mathcal{N}}_{\theta_{\mathrm{LO}}}(\Omega) \equiv e^{-i\theta_{\mathrm{LO}}}\hat{\mathcal{F}}(\Omega) + e^{i\theta_{\mathrm{LO}}}\hat{\mathcal{F}}^\dagger(-\Omega), \tag{5.35}$$

where $t_{\mathrm{s},\theta_{\mathrm{LO}}}(\Omega)$ characterizes how the signal part of the sidebands interfere when recombined in the homodyne measurement. Note that even though $\hat{I}(\Omega)$ contains information from two output sidebands, Eq. (5.33) resembles Eq. (5.22) for the upper sideband readout, $\Omega > 0$. Thus, by including the homodyne system in what we define as "the transducer", its overall action is seen to be phase-preserving. Moreover, the noise $\hat{\mathcal{N}}_{\theta_{\mathrm{LO}}}(\Omega)$ is time-stationary as it inherits this property from $\hat{\mathcal{F}}$ (see Appendix B.3). This constitutes the mathematical derivation of the statement given previously in this section: That two-sideband homodyning of the transduced spectrum (Fig. 5.4c) contains the same quadrature information as a direct heterodyne measurement of the input spectrum (Fig. 5.4b). In the limit of no lower output sideband, $V_s^*(-\Omega_m) \approx 0$, i.e. a sideband-resolved output cavity, the situation described by Eq. (5.33) becomes simply a heterodyning scenario like in (Fig. 5.4b), as already discussed. Hence, no matter the sideband-resolution, the photo-current $\hat{I}(\Omega)$, Eq. (5.33), constitutes a simultaneous measurement of both quadratures of the input spectrum.

Each input quadrature of the form $\hat{X}_{s,\varphi}(\Omega) \equiv [e^{-i\varphi}\hat{a}_{\mathrm{in,s}}(\Omega)+e^{i\varphi}\hat{a}^\dagger_{\mathrm{in,s}}(\Omega)]/\sqrt{2}$ is mapped to an output quadrature $\hat{Z}_{\phi,\theta_{\mathrm{LO}}}(\Omega) \equiv [e^{i\phi}\hat{I}(\Omega)+e^{-i\phi}\hat{I}^\dagger(\Omega)]/(2|\alpha_{\mathrm{LO}}|)$ for some ϕ and fixed θ_{LO}. Since the noise is time-stationary it will be quadrature independent. We are now in a position to characterize the performance of this "indirect heterodyne" measurement, by defining a figure of merit: The sensitivity $P(\Omega)$ of the indirect heterodyne measurement to incoming signals of the transducer[2]

$$P(\Omega)\delta(\Omega-\Omega') \equiv \frac{1}{2}\delta(\Omega-\Omega') + \frac{\langle\hat{\mathcal{N}}_{\theta_{\mathrm{LO}}}(\Omega)\hat{\mathcal{N}}^\dagger_{\theta_{\mathrm{LO}}}(\Omega')\rangle + \langle\hat{\mathcal{N}}^\dagger_{\theta_{\mathrm{LO}}}(\Omega)\hat{\mathcal{N}}_{\theta_{\mathrm{LO}}}(\Omega')\rangle}{2|t_{s,\theta_{\mathrm{LO}}}(\Omega)|^2}, \tag{5.36}$$

i.e. the combined transducer and measurement noise referenced to the input; the first term on the right-hand side of (5.36) is the fundamental vacuum noise of the input field, $\langle\hat{X}_{s,\Theta}(\Omega)\hat{X}_{s,\Theta}(\Omega')\rangle_{\mathrm{vac}} = (1/2)\delta(\Omega-\Omega')$, while the second is the transducer noise, with $\hat{\mathcal{N}}_{\theta_{\mathrm{LO}}}(\Omega)$ given by (5.35). Hence, $P(\Omega)$ quantifies the minimum spectral density that must be present in the input for it to be detectable. For example, for an incoming mode much narrower than the transducer bandwidth, $P(\Omega_m)$ is simply the minimum number of signal photons that must be present in that mode for the signal to rise above the noise of the combined transduction/homodyne measurement process. The added noise $N_0^{(\pm)}$ was defined to be proportional to the excess number of photons leaving the upper/lower sideband as, e.g, measured by photon counting. The sensitivity P, on the other hand, expresses the noise as measured by heterodyne measurements and thus contain additional vacuum noise contributions.

Whereas the expression in Eq. (5.36) is completely general we shall now simplify it for the reduced equivalent circuit in Fig. 5.1c. To this end we note once more from the circuit that the ratio and phase of electrical signal relative to electrical and mechanical noise sources are determined by the combination V_e+V_m. Hence the ratio between the electrical and mechanical noise sources are unaffected by the details of the optical readout process.[3] From this it follows that the electrical and mechanical contributions to $N(\Omega)$, $N_e(\Omega)$ and $N_m(\Omega)$, are independent of optical parameters as seen in, e.g., the expressions in Section 5.6.2. In this sense, the only non-trivial sideband interference is between the optical back-action and the imprecision shot noise. The choice of LO phase angle θ_{LO} will therefore only influence the optical noise contribution to P. The above considerations imply that the homodyne sensitivity $P(\Omega)$, (5.36), simplifies to

[2]The definition (5.36) given here is equivalent to the one in Section 3.6.1, as remarked in Appendix B.3 above Eq. (B.13).

[3]The only exception is the Hermitian conjugation brought about by lower-sideband readout that lead to the asymmetry in, e.g., the expressions for $N_0^{(\pm)}$ in Section 5.6.2.

(see Appendix C.2.2 for details)

$$P(\Omega)\delta(\Omega-\Omega') = \left[\frac{1}{2} + \bar{N}_\mathrm{e}(\Omega) + \bar{N}_\mathrm{m}(\Omega) + N_\mathrm{opt}^{(\mathrm{h})}(\Omega)\right]\delta(\Omega-\Omega'). \tag{5.37}$$

Here $\bar{N}_\mathrm{e}(\Omega) \equiv [N_\mathrm{e}(\Omega) + N_\mathrm{e}(-\Omega)]/2$ and $\bar{N}_\mathrm{m}(\Omega) \equiv [N_\mathrm{m}(\Omega) + N_\mathrm{m}(-\Omega)]/2$ are the symmetrized versions of the Johnson and mechanical noise contributions $N_\mathrm{e}(\Omega), N_\mathrm{m}(\Omega)$ to $N(\Omega)$, whose peak values $N_0^{(\pm)} \equiv N(\pm\Omega_\mathrm{m})$ we have already determined in Section 5.6.2. The optical noise contribution $N_\mathrm{opt}^{(\mathrm{h})}(\Omega)$ will be considered later, in Section 5.7.2.

Since the EM noise is independent of the optical parameters, we can independently analyze the classical regime where the transducer is dominated by thermal EM excitation making the optical (vacuum) noise negligible in comparison, $N_\mathrm{opt}^{(\mathrm{h})} \ll \bar{N}_\mathrm{e} + \bar{N}_\mathrm{m}$; we will do this in Section 5.7.1. It remains to calculate $N_\mathrm{opt}^{(\mathrm{h})}(\Omega)$, which is the optical contribution to $P(\Omega)$, and we will do so in Section 5.7.2.1, allowing us to finally perform a full optimization of the sensitivity. We note that the added optical noise $N_\mathrm{opt}^{(\mathrm{h})}$ *does* depend on the electrical parameters since the noise is referenced to the electrical input and since $N_\mathrm{opt}^{(\mathrm{h})}$ includes contributions from reflected input noise operators.

5.7.1 Classical regime: Electromechanical noise contributions

In this section we analyze the transducer sensitivity P derived above, in the limit where the electrical and mechanical noise contributions dominate, i.e. at high temperatures. We focus henceforth on the value of P at the transducer peak, $P_0 \equiv P(\Omega_\mathrm{m})$. We note that in the high-temperature limit considered here we have $\bar{N}_i \approx N_i^{(+)} \approx N_i^{(-)}$ for $i \in \{\mathrm{e,m}\}$, as noted previously in Section 5.6.2. Hence, in this limit, the peak sensitivity (5.37) is simply given by

$$P_0 \approx N_{\mathrm{e},0} + N_{\mathrm{m},0},$$

where we have dropped the $(\pm)$ for brevity as we will for the remainder of this section.

To compare the different circuits, it is useful to introduce dimensionless EM cooperativity parameters. We define the externally loaded cooperativities $\mathcal{C}_\mathrm{EM}$ of the respective receiver circuits as the ratio of the on-resonant sideband loading to R_m,

$$\mathcal{C}_\mathrm{EM} \equiv \left.\frac{R_{\mathrm{EM},+}}{R_\mathrm{m}}\right|_{\mathcal{K}_+^{(\mathrm{X})}\to 1}, \tag{5.38}$$

where $R_{\mathrm{EM},+}$ is given by Eq. (5.13) or (5.15). For the resonant circuits, Eq. (5.13) implies that $\mathcal{C}_\mathrm{EM}$ can be expressed as

$$\mathcal{C}_\mathrm{EM} = \frac{Z_0^2}{R_{\mathrm{m},0}R_\mathrm{LC}^{(\mathrm{X})}} \cdot \begin{cases} 1 & [\text{DC bias}] \\ \frac{\omega_\mathrm{d}+\Omega_\mathrm{m}}{\Omega_\mathrm{m}} & [\text{AC bias}] \end{cases}, \tag{5.39}$$

where $Z_0 \equiv \sqrt{L/C_\mathrm{tot}}$ and the loaded circuit resistances for the serial and parallel circuits are given by

$$\begin{aligned} R_\mathrm{LC}^{(\mathrm{ser})} &= R_L + Z_\mathrm{tx} + R_\mathrm{min} \\ R_\mathrm{LC}^{(\mathrm{par})} &= R_L + (Z_\mathrm{tx} + R_\mathrm{min})\,(C_\mathrm{l}/C_\mathrm{tot})^2 . \end{aligned} \tag{5.40}$$

$\mathcal{C}_{\rm EM}$ for the RC circuit follows from Eq. (5.15) and is given in Table 5.1 below. We note that the loaded resistance $R_{\rm LC}^{(\rm par)}$ of the circuit resonance (5.40) shows how the loading of the parallel circuit is controlled by the ratio $C_{\rm l}/C_{\rm tot}$. Increasing the external loading of the circuit will tend to decouple it from the mechanical mode, resulting in smaller coupling rates $\gamma_{\rm EM,\pm}$ and less broadening $\Gamma_{\rm EM}$, (5.16). Since $R_{\rm LC}^{(\rm par)} < R_{\rm LC}^{(\rm ser)}$, the parallel circuit offers larger transducer bandwidths at the price of less electrical noise suppression. As a common reference for comparing different circuits, we define the serial RLC cooperativity in the absence of the transmission line load ($Z_{\rm tx}, R_{\rm min} \to 0$), so that $R_{\rm LC}^{(\rm ser)} \to R_L$ from (5.39)

$$\mathcal{C}_{\rm EM,0} \equiv \frac{Z_0^2}{R_{\rm m,0}R_L} \cdot \begin{cases} 1 & [\text{DC bias}] \\ \frac{\omega_{\rm d}+\Omega_{\rm m}}{\Omega_{\rm m}} & [\text{AC bias}] \end{cases}. \tag{5.41}$$

From the results of Section 5.6.2 for the added noise contributions $N_{\rm e,0}, N_{\rm m,0}$ along with the transfer functions determined in 5.5.1, the definition of $\eta_{\rm el}$ and the above expressions for $\mathcal{C}_{\rm EM}, \mathcal{C}_{\rm EM,0}$, we assemble a simplified overview of the performance of the three receiver circuits in Table 5.1; the results apply to AC-driven operation in the EM resolved-sideband regime and for DC-biased operation. Considering the first set of rows in the table we include here, in the first column, the electrical coupling efficiency to the signal port $\eta_{\rm el}$ and, in the second, the EM cooperativity $\mathcal{C}_{\rm EM}$ characterizing the EM coupling strength relative to the intrinsic mechanical dissipation rate. The second set of rows states the ohmic and mechanical contributions to the added noise in the EM resolved-sideband limit (or DC-biased operation).

circuit/fig. of merit	$\eta_{\rm el}$	$\mathcal{C}_{\rm EM}$
Serial RLC	$\frac{Z_{\rm tx}}{Z_{\rm tx}+R_{\rm min}+R_L} \approx 1 - \frac{R_L}{Z_{\rm tx}}$	$\mathcal{C}_{\rm EM}^{\rm ser} = \mathcal{C}_{\rm EM,0}\frac{R_L}{Z_{\rm tx}+R_{\rm min}+R_L} \approx \mathcal{C}_{\rm EM,0}\frac{R_L}{Z_{\rm tx}}$
Parallel RLC	$\frac{Z_{\rm tx}}{Z_{\rm tx}+R_{\rm min}+R_L(C_{\rm tot}/C_{\rm l})^2}$	$\mathcal{C}_{\rm EM}^{\rm par} = \mathcal{C}_{\rm EM,0}\frac{R_L}{R_L+(Z_{\rm tx}+R_{\rm min})(C_{\rm l}/C_{\rm tot})^2}$
RC	$\frac{Z_{\rm tx}}{Z_{\rm tx}+R_{\rm min}} \approx 1$	$\mathcal{C}_{\rm EM}^{\rm RC} = \mathcal{C}_{\rm EM,0}\frac{R_L Z_{\rm tx}}{Z_0^2+Z_{\rm tx}^2}$

circuit/fig. of merit	$N_{\rm e,0}$	$N_{\rm m,0}$
Serial RLC	$\frac{R_L+R_{\rm min}}{Z_{\rm tx}} n_{\rm ohm}(\omega_{\rm s})$	$\frac{n_{\rm m}(\Omega_{\rm m})}{\mathcal{C}_{\rm EM,0}} \frac{(Z_{\rm tx}+R_{\rm min}+R_L)^2}{R_L Z_{\rm tx}} \approx \frac{n_{\rm m}(\Omega_{\rm m})}{\mathcal{C}_{\rm EM,0}} \frac{Z_{\rm tx}}{R_L}$
Parallel RLC	$\frac{R_L(C_{\rm tot}/C_{\rm l})^2+R_{\rm min}}{Z_{\rm tx}} n_{\rm ohm}(\omega_{\rm s})$	$\frac{n_{\rm m}(\Omega_{\rm m})}{\mathcal{C}_{\rm EM,0}} \frac{\left[Z_{\rm tx}+R_{\rm min}+R_L(C_{\rm tot}/C_{\rm l})^2\right]^2}{Z_{\rm tx}R_L(C_{\rm tot}/C_{\rm l})^2}$
RC	$\frac{R_{\rm min}}{Z_{\rm tx}} n_{\rm ohm}(\omega_{\rm s})$	$\frac{n_{\rm m}(\Omega_{\rm m})}{\mathcal{C}_{\rm EM,0}} \frac{Z_0^2+Z_{\rm tx}^2}{R_L Z_{\rm tx}}$

Table 5.1: Performance of the transducer for the three receiver circuits assuming equal EM coupling strength G. The approximations are valid in the regime $Z_0^2/R_L \gg Z_{\rm tx} \gg R_L \gg R_{\rm min}$. For the parallel circuit we assume $\omega C_{\rm l}(Z_{\rm tx} + R_{\rm min}) \ll 1$ for frequencies ω of interest. $\mathcal{C}_{\rm EM,0}$ is the serial RLC cooperativity in absence of external loading by $Z_{\rm tx}$ and $R_{\rm min}$, Eq. (5.41). For added ohmic noise $N_{\rm e,0}$ we assume DC or resolved EM sidebands (5.29) and that $n_{\rm ohm}(\omega) \equiv n_{\rm min}(\omega) = n_L(\omega)$. $\omega_{\rm s} = \omega_{\rm LC} = \omega_{\rm d} + \Omega_{\rm m}$ is the incoming signal frequency. More general expressions for the added noise contributions can be found in Section 5.6.2.

Let us discuss the relative strengths of the three receiver circuits of Fig. 5.3. The RLC circuits have the advantage of resonant enhancement of incoming signals, which is not a feature of the non-resonant RC circuit. On the other hand, the RC circuit does not suffer from the ohmic noise associated with the inductive element of the RLC circuits. Comparing now the two resonant circuits, serial vs. parallel, the latter offers tunable loading of the circuit by the transmission line impedance (fixed) $Z_{\rm tx}$ via the impedance transformation brought about by the loading capacitor $C_{\rm l}$. In the regime of interest, the parallel RLC is equivalent to the serial RLC but with an effective transmission line impedance $Z'_{\rm tx} \in [0; Z_{\rm tx}]$. As will emerge from the analysis, these characteristics imply that the three receiver circuits each have their advantages in different parameter regimes. To provide an overview, we may somewhat simplistically order the three receiver circuits in the following "spectrum": At one extreme, a critically coupled parallel RLC provides maximal mechanical noise suppression (suited for super-conducting circuits near the ground-state); as an intermediate choice, a serial RLC overcouples the circuit by the transmission line, suppressing Johnson noise, while still having good mechanical noise suppression due to resonant electrical enhancement (suited for room-temperature rf or microwave circuits); on the other extreme is the RC circuit with its near-perfect overcoupling (provided that $R_{\rm min} \ll Z_{\rm tx}$), but vanishing electrical electrical signal enhancement (suited for room-temperature DC-biased interfaces or AC-driven interfaces with a cold signal source in which large EM cooperativity $\mathcal{C}_{\rm EM,0}$ is available).

The results in Table 5.1 show that formulas for the serial and parallel circuits have the same form; i.e. the serial expressions hold for the parallel circuit under the replacements

$$Z_{\rm tx} \to Z'_{\rm tx} = Z_{\rm tx}(C_{\rm l}/C_{\rm tot})^2, \qquad R_{\rm min} \to R'_{\rm min} = R_{\rm min}(C_{\rm l}/C_{\rm tot})^2, \tag{5.42}$$

where the primed parameters are the effective resistances for the parallel circuit. The resistance $R_{\rm min}$ has been included in the receiver circuits as the residual resistance present even when there is no inductor. When comparing these circuits we will therefore mostly neglect $R_{\rm min}$ by assuming $R_{\rm min} \ll Z_{\rm tx}$, in which case inspection of Table 5.1 shows the following useful relation for the resonant circuits

$$\mathcal{C}_{\rm EM} = \mathcal{C}_{\rm EM,0}(1 - \eta_{\rm el}), \tag{5.43}$$

where the part of $\mathcal{C}_{\rm EM}$ dependent on the transmission line load has been factored out. These two observations, (5.42) and (5.43), will prove convenient shortly.

We will now consider how to minimize the sum $N_{\rm EM,0} \equiv N_{\rm e,0} + N_{\rm m,0}$ by the choice of the appropriate circuit in the classical high-temperature limit, where the optical (quantum) noise is negligible. To quantitatively compare the circuits in a meaningful way, we must keep certain properties fixed. The relevant properties are determined by practical restrictions or requirements and one can envision a multitude of different optimization constraints. Two scenarios will be discussed in some detail in the following subsections (both subject to the general constraints stated in Section 5.4).

5.7.1.1 Optimal $\eta_{\rm el}$ for fixed L, R_L

Here we will consider the case where the parameters of the inductor L, R_L are fixed, leaving as the only free parameter the loading capacitance $C_{\rm l}$ in the parallel circuit, which controls the external loading efficiency of the circuit, $\eta_{\rm el}$. The matching condition of the resonance frequency of the RLC circuits to the incoming signal, $\omega_{\mathrm{LC}} = \omega_{\mathrm{s}}$, fixes the tuning capacitance C_{T} for given C_{l} and determines the range of the latter, $C_{\mathrm{l}} \in [0; (\omega_{\mathrm{s}}^2 L)^{-1} - \bar{C}_{\mathrm{c}}]$.

As noted above, if we for simplicity neglect $R_{\min} \ll Z_{\mathrm{tx}}$, the expressions in Table 5.1 for the parallel circuit become equivalent to those for the serial, but with a variable loading, η_{el}. Conveniently, this allows us to treat the resonant circuits simultaneously. Subsequently, we will compare their performance with that of the non-resonant RC circuit.

To determine the optimal value of η_{el} for the resonant circuits, we will for specificity consider the two limits of EM resolved and unresolved sidebands, respectively (intermediate cases are a straightforward generalization). From the EM added noise $N_{\mathrm{e},0}$ and $N_{\mathrm{m},0}$ in Table 5.1 (Eq. (5.30) for unresolved EM sidebands), we have for the resonant circuits in the high-temperature limit (using the appropriate formulas for $\eta_{\mathrm{el}}, \mathcal{C}_{\mathrm{EM}}$ from Table 5.1 and assuming $\omega_{\mathrm{d}} = \omega_{\mathrm{LC}} - \Omega_{\mathrm{m}}$)

$$N_{\mathrm{EM},0} = \begin{cases} \left(\frac{1}{\eta_{\mathrm{el}}} - 1\right) n_{\mathrm{ohm}}(\omega_{\mathrm{d}} + \Omega_{\mathrm{m}}) + \frac{1}{\mathcal{C}_{\mathrm{EM},0}\eta_{\mathrm{el}}(1-\eta_{\mathrm{el}})} n_{\mathrm{m}}(\Omega_{\mathrm{m}}), & \text{[EM RSB]} \\ n_{\mathrm{tx}}(\omega_{\mathrm{d}} - \Omega_{\mathrm{m}}) + 2\left(\frac{1}{\eta_{\mathrm{el}}} - 1\right) n_{\mathrm{ohm}}(\omega_{\mathrm{d}}) + \frac{1}{\mathcal{C}_{\mathrm{EM},0}\eta_{\mathrm{el}}(1-\eta_{\mathrm{el}})} n_{\mathrm{m}}(\Omega_{\mathrm{m}}), & \text{[EM unRSB]} \end{cases} \tag{5.44}$$

where we have made the assumptions that $Z_{\mathrm{tx}} \gg R_{\min}$ and that the resistors R_L and $R_{\min}$ are at equal temperatures, $n_{\mathrm{ohm}}(\omega) \equiv n_L(\omega) = n_{\min}(\omega)$, allowing us to neglect $R_{\min}$ altogether; the EM resolved-sideband (RSB) regime is characterized by $R_{\mathrm{LC}}^{(\mathrm{par})}/2L \ll \omega_{\mathrm{m}}$, the EM unresolved-sideband (unRSB) regime being the opposite limit. Choosing a large value of η_{el} is desirable for minimizing the ohmic noise, but this comes at the expense of a reduced cooperativity and thus an increased mechanical noise. Minimizing $N_{\mathrm{EM},0}$ as a function of η_{el} the optimal value is found to be (henceforth denoting optimized quantities with a $\check{}$ accent)

$$\check{\eta}_{\mathrm{el}} = \begin{cases} \left[1 + \left(1 + \frac{\mathcal{C}_{\mathrm{EM},0} n_{\mathrm{ohm}}(\omega_{\mathrm{d}}+\Omega_{\mathrm{m}})}{n_{\mathrm{m}}(\Omega_{\mathrm{m}})}\right)^{-1/2}\right]^{-1}, & \text{[EM RSB]} \\ \left[1 + \left(1 + 2\frac{\mathcal{C}_{\mathrm{EM},0} n_{\mathrm{ohm}}(\omega_{\mathrm{d}})}{n_{\mathrm{m}}(\Omega_{\mathrm{m}})}\right)^{-1/2}\right]^{-1}, & \text{[EM unRSB]} \end{cases} \tag{5.45}$$

resulting in the minimum EM added noise

$$\begin{aligned} \check{N}_{\mathrm{EM},0} &\equiv N_{\mathrm{EM},0}\big|_{\eta_{\mathrm{el}}=\check{\eta}_{\mathrm{el}}} \\ &= \begin{cases} 2\frac{n_{\mathrm{m}}(\Omega_{\mathrm{m}})}{\mathcal{C}_{\mathrm{EM},0}}\left(1 + \sqrt{1 + \frac{\mathcal{C}_{\mathrm{EM},0} n_{\mathrm{ohm}}(\omega_{\mathrm{d}}+\Omega_{\mathrm{m}})}{n_{\mathrm{m}}(\Omega_{\mathrm{m}})}}\right), & \text{[EM RSB]} \\ n_{\mathrm{tx}}(\omega_{\mathrm{d}} - \Omega_{\mathrm{d}}) + 2\frac{n_{\mathrm{m}}(\Omega_{\mathrm{m}})}{\mathcal{C}_{\mathrm{EM},0}}\left(1 + \sqrt{1 + 2\frac{\mathcal{C}_{\mathrm{EM},0} n_{\mathrm{ohm}}(\omega_{\mathrm{d}})}{n_{\mathrm{m}}(\Omega_{\mathrm{m}})}}\right), & \text{[EM unRSB]} \end{cases} \end{aligned} \tag{5.46}$$

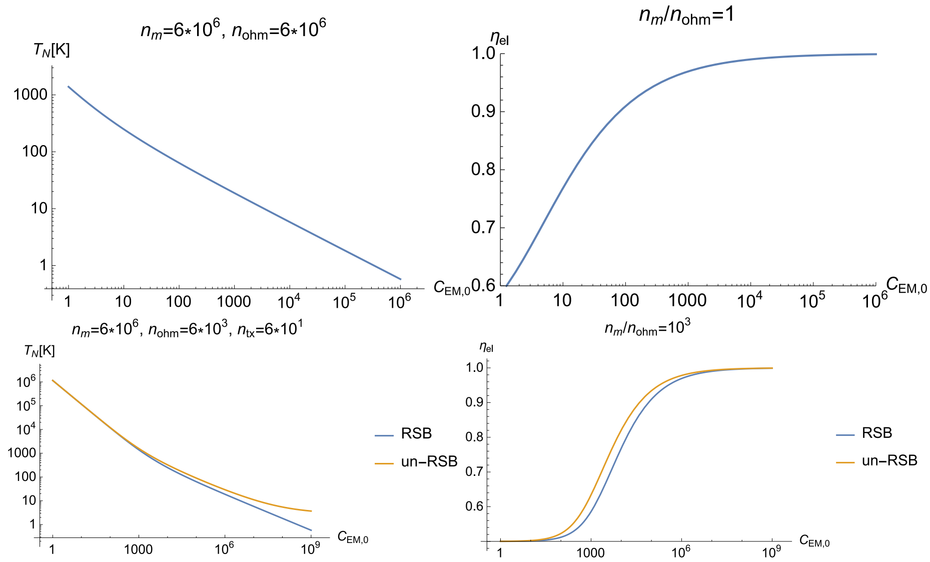

Figure 5.5: Plots of optimal electrical coupling efficiency $\check{\eta}_{\rm el}$ and minimal added EM noise temperature $\check{T}_{\rm N} \equiv \frac{\hbar\omega_{\rm s}}{k_{\rm B}}\check{N}_{\rm EM,0}$ as a function of the unloaded EM cooperativity $\mathcal{C}_{\rm EM,0}$, Eq. (5.41). Parameters represent a room-temperature transducer in which a MHz mechanical mode coupled to a MHz circuit (top row), DC-biased and hence automatically EM sideband resolved; and a GHz circuit (bottom row) loaded by a cold source, $n_{\rm tx}(\omega_{\rm d}-\Omega_{\rm m}) = 60$, for both EM resolved and unresolved sidebands.

We plot the minimum added noise and the optimal coupling efficiency $\check{\eta}_{\rm el}$, (5.45) and (5.46), in Fig. 5.5 in terms of the noise temperatures $T_{\rm N}$. In the classical regime this quantity is preferable over the sensitivity P_0 (equivalent flux of noise quanta per unit bandwidth) considered thus far; we define the (peak) added noise temperature (referenced to the signal frequency $\omega_{\rm s}$) as

$$T_{\rm N} \equiv \frac{\hbar\omega_{\rm s}}{k_{\rm B}} P_0, \tag{5.47}$$

with similarly definitions when referring to the individual contributions to P_0. The plots in Fig. 5.5 correspond to different scenarios of room-temperature transducers. The top row plots represent a DC-biased transducer consisting of 1 MHz mechanical and electrical modes, whereas the bottom row refers to AC-biased transduction from a 1 GHz circuit via a 1 MHz oscillator. In both cases, the noise temperature curves show two regimes as expected from (5.46): For small values of $\mathcal{C}_{\rm EM,0} \ll n_{\rm m}(\Omega_{\rm m})/n_{\rm ohm}(\omega_{\rm d})$ we should employ critical coupling $\check{\eta}_{\rm el} \approx 1/2$ and the noise temperature $\check{T}_{\rm N}$ decreases as $1/\mathcal{C}_{\rm EM,0}$, whereas for large values, $\mathcal{C}_{\rm EM,0} \gg n_{\rm m}(\Omega_{\rm m})/n_{\rm ohm}(\omega_{\rm d})$, the circuit must be overcoupled $\check{\eta}_{\rm el} > 1/2$ to gain further, leading to a decrease in $\check{T}_{\rm N}$ of only $\propto 1/\sqrt{\mathcal{C}_{\rm EM,0}}$. Fig. 5.5 demonstrates how a large electromechanical coupling as expressed by the cooperativity $\mathcal{C}_{\rm EM,0}$ allows for efficient transduction of electrical signals to optical fields. At large $\mathcal{C}_{\rm EM,0}$ the optimal coupling efficiency approaches unity and correspondingly the added noise temperature decreases, possibly reaching the quantum level where the added noise is less than a single photon, as will be analyzed in Section 5.7.2. For the MW-to-optical scenario (bottom row of Fig. 5.5) we note, however, that the unloaded cooperativity must be rather large $\mathcal{C}_{\mathrm{EM},0} \gtrsim 10^4$ for the noise temperature T_{N} to drop below room temperature. Unresolved EM sidebands call for larger coupling efficiency $\check{\eta}_{\mathrm{el}}$ than the resolved-sideband case because of the additional Johnson noise from the lower sideband, and thus an increased demand for suppression of Johnson noise. Furthermore in the unresolved-sideband case, the added noise temperature is ultimately bounded from below by the temperature of the lower sideband of the input signal port, which does not diminish as we increase the cooperativity. Note that the optimal coupling efficiency (5.45) is always in the range $\check{\eta}_{\mathrm{el}} \in [1/2; 1]$. Hence if mechanical noise is the bottleneck, $n_{\mathrm{m}}(\Omega_{\mathrm{m}})/\mathcal{C}_{\mathrm{EM},0} \gg n_{\mathrm{ohm}}(\omega_{\mathrm{d}})$, critical coupling $\check{\eta}_{\mathrm{el}} = 1/2$ is optimal since it allows the largest suppression of the mechanical noise. On the other hand, for large unloaded EM cooperativity $\mathcal{C}_{\mathrm{EM},0}$ such that $n_{\mathrm{m}}(\Omega_{\mathrm{m}})/\mathcal{C}_{\mathrm{EM},0} \ll n_{\mathrm{ohm}}(\omega_{\mathrm{d}})$ we have $\check{\eta}_{\mathrm{el}} \to 1$ reflecting a demand for suppression of Johnson noise by overcoupling. We must have in mind, however, that the resonant circuits considered here can at most provide a coupling efficiency $\eta_{\mathrm{el}}^{(\mathrm{ser})} = Z_{\mathrm{tx}}/(Z_{\mathrm{tx}} + R_{\mathrm{min}} + R_L)$. The values of $\mathcal{C}_{\mathrm{EM},0}$ for which we can no longer attain $\eta_{\mathrm{el}} = \check{\eta}_{\mathrm{el}}$ using a resonant circuit are

$$\check{\eta}_{\mathrm{el}} > \eta_{\mathrm{el}}^{(\mathrm{ser})} \Rightarrow \mathcal{C}_{\mathrm{EM},0} > \left[\left(\frac{Z_{\mathrm{tx}}}{R_L + R_{\mathrm{min}}}\right)^2 - 1\right] \frac{n_{\mathrm{m}}(\Omega_{\mathrm{m}})}{n_{\mathrm{ohm}}(\omega_{\mathrm{d}})}. \tag{5.48}$$

It should also be noted that under the constraints considered here, C_{l} is bounded from above such that the achievable values with the parallel circuit are $\eta_{\mathrm{el}} \leq [1 + (R_L/Z_{\mathrm{tx}})(1 - \bar{C}_{\mathrm{c}}/C_{\mathrm{tot}})^{-2}]^{-1} < \eta_{\mathrm{el}}^{(\mathrm{ser})}$, so that there is, in general, also a gap in the spectrum of achievable η_{el} separating the serial and parallel circuits.

The limit to the efficiency in Eq. (5.48) raises the question of whether we can achieve less added EM noise than offered by the resonant circuits by discarding the inductor which limits the efficiency and reverting to the non-resonant RC circuit (Fig. 5.3c). While the latter can provide superior overcoupling, as indicated by η_{el} in Table 5.1, it offers no resonant electrical signal enhancement and thus less EM cooperativity. By comparing the expressions in Table 5.1 for $N_{\mathrm{EM},0} \equiv N_{\mathrm{e},0} + N_{\mathrm{m},0}$ for the serial RLC against those of the inductorless RC, we find that the latter adds less EM noise if (assuming $2R_L Z_{\mathrm{tx}} \ll Z_0^2$ and $R_{\mathrm{min}} \ll Z_{\mathrm{tx}}$)

$$\mathcal{C}_{\mathrm{EM},0} > \left(\frac{Z_0^2}{R_L^2} - 2\frac{Z_{\mathrm{tx}}}{R_L} - 1\right) \frac{n_{\mathrm{m}}(\Omega_{\mathrm{m}})}{n_L(\omega_{\mathrm{d}})} \approx \frac{Z_0^2}{R_L^2} \frac{n_{\mathrm{m}}(\Omega_{\mathrm{m}})}{n_L(\omega_{\mathrm{d}})} = Q_L^2 \frac{n_{\mathrm{m}}(\Omega_{\mathrm{m}})}{n_L(\omega_{\mathrm{d}})}, \tag{5.49}$$

where $Q_L \equiv Z_0/R_L$ is the Q-factor of the unloaded serial resonance. We plot in Fig. 5.6 the smaller of the two values of $N_{\mathrm{e},0} + N_{\mathrm{m},0}$ as well as the crossover between the two regions for similar parameters as considered in Fig. 5.5. The crossover between the two desired regimes of operation expressed in Eq. (5.49) can be understood from the following argument: The appearance of Q_L^2 can be understood noting that dissipated power goes as $\propto V^2$ combined with the fact that the relative voltage enhancement in switching from a serial RLC to the RC circuit is $1/Q_L$. In order for the RC scenario to be desirable the increased mechanical load, which is now $\approx (R_L/Z_{\mathrm{tx}})(Q_L^2 n_{\mathrm{m}}(\Omega_{\mathrm{m}})/\mathcal{C}_{\mathrm{EM},0})$ for $Z_0 \gg Z_{\mathrm{tx}}$, must be lower than the ohmic load of the serial RLC circuit, $(R_L/Z_{\mathrm{tx}})n_L(\omega_{\mathrm{d}})$. It is important to note that the ratio of bath occupancies appearing in Eq. (5.49)

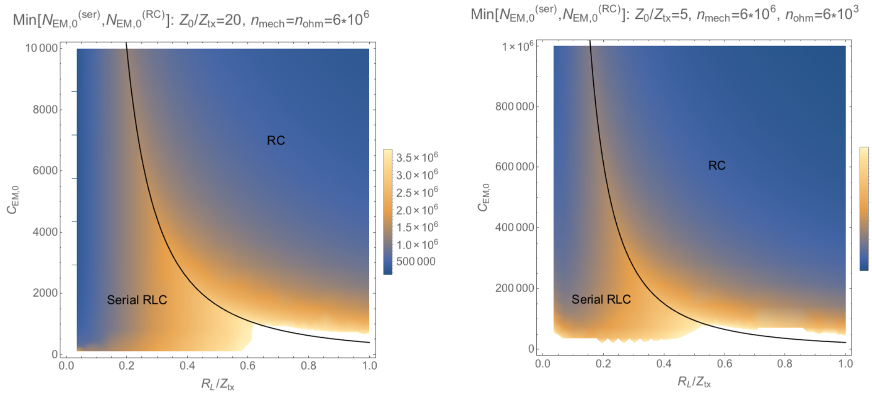

Figure 5.6: Optimal circuits for transduction when $\check{\eta}_{\rm el} \geq \eta_{\rm el}^{(\rm ser)}$: Phase diagram showing the respective parameter regimes where the serial RLC and RC circuits add the least noise, $N_{\rm EM,0}$, assuming room-temperature operation $T \sim 300$K and $R_{\rm min} \ll Z_{\rm tx}$. The left plot represents a typical DC-biased scenario with $Z_0/Z_{\rm tx} = 20$ and bath occupancies corresponding to $\Omega_{\rm m} = \omega_{\rm LC} = (2\pi)\cdot 1$MHz so that $n_{\rm m} = n_{\rm ohm} = 6\cdot 10^6$. The right plot corresponds to a typical AC-driven scenario with $Z_0/Z_{\rm tx} = 5$ and frequencies $\Omega_{\rm m} = (2\pi)\cdot 1\text{MHz}, \omega_{\rm d} = (2\pi)\cdot 1\text{GHz}$, resulting in $n_{\rm m} = 6\cdot 10^6$ and $n_{\rm ohm} = 6\cdot 10^3$, with the assumption that the transmission line noise at the lower EM sideband has been removed by filtering or cooling. The black curves demarcates the transition between serial RLC and RC being the preferable circuit layout according to Eq. (5.49). In interpreting the plots it is important to keep in mind that increasing R_L for fixed $\mathcal{C}_{\rm EM,0}$ entails decreasing $L_{\rm m}$ in the same proportion (assuming $\gamma_{\rm m,0}$ fixed, see Eq. (5.41)) corresponding to increasing the EM coupling strength G.

in the high-temperature limit equals the ratio of the electrical and mechanical frequencies, $n_{\rm m}(\Omega_{\rm m})/n_L(\omega_{\rm d}) \approx \omega_{\rm d}/\Omega_{\rm m}$ (assuming equal bath temperatures); hence for DC-biased operation the ratio is unity, whereas in the AC-driven case of, e.g., a GHz circuit coupled to a MHz mechanical mode this ratio will be $\sim 10^3$, making mechanical noise suppression more important. It must also be emphasized that for the AC-driven scenario, Eq. (5.49) assumes the serial RLC circuit to be sideband-resolved and for the RC circuit that the noise of the lower electrical sideband can be neglected $n_{\rm tx}(\omega_{\rm d} - \Omega_{\rm m}) \approx 0$ or filtered away.

5.7.1.2 Optimal L for fixed $C_{\rm l}$

While we have fixed the resonance frequency of the RLC circuits to the signal frequency, $\omega_{\rm LC} = \omega_{\rm s}$, thus fixing the product of L and $C_{\rm tot}$. Releasing the constraint of given L considered in the previous subsection, we may hence consider what their optimal ratio is, i.e. optimize over $Z_0 \equiv \sqrt{L/C_{\rm tot}}$. We will do so for the serial and parallel circuits for fixed (effective) transmission line impedance, $Z'_{\rm tx}$. For the analysis to have practical relevance, we must recognize that R_L will depend on L in some way, $R_L = f(L)$. Assuming, for specificity, that the inductors available to us are characterized by a fixed quality factor $Q_L \equiv \omega_{\rm s} L/R_L$, we have the relation $R_L = \gamma_L L$. It follows that increasing L will lead to a decreasing $\eta_{\rm el}$, due to increased ohmic resistance, and an increasing $\mathcal{C}_{\rm EM,0}$ reflecting stronger EM loading due to the increased R_L for fixed Q_L. With this in mind, we minimize $N_{\mathrm{EM},0}$, Eq. (5.44), wrt. L and find that the optimum $\check{L}$ is given by the root of a cubic polynomial. Expanding the result in the overcoupled limit $R_L \ll Z'_{\mathrm{tx}}$ we find (in the high-temperature regime, $n_{\mathrm{i}}(\omega) \approx k_{\mathrm{B}}T/(\hbar\omega)$, and considering the EM resolved-sideband regime for specificity)

$$\check{L} \approx \frac{Z'_{\mathrm{tx}}}{\gamma_L}\sqrt[3]{\frac{2R_{\mathrm{m}}}{Z'_{\mathrm{tx}}Q_L^2}}\left(1+\frac{1}{3}\sqrt[3]{\frac{2R_{\mathrm{m}}}{Z'_{\mathrm{tx}}Q_L^2}}\right), \tag{5.50}$$

valid when $\sqrt[3]{2R_{\mathrm{m}}/(Z'_{\mathrm{tx}}Q_L^2)} \ll 1$. The EM coupling strength enters (5.50) through $R_{\mathrm{m}} \propto G^{-2}$, (4.9). Evaluating (5.44) at $\check{L}$ (keeping only the lowest order term) yields the added noise minimum in the overcoupled limit $R_L \ll Z'_{\mathrm{tx}}$,

$$N_{\mathrm{EM},0} = \frac{3}{2}\sqrt[3]{\frac{2R_{\mathrm{m}}}{Z'_{\mathrm{tx}}Q_L^2}}\,n_{\mathrm{ohm}}[\omega_{\mathrm{s}}].$$

It is important to note that the practically achievable range of L under the given constraints is $L \in [0; (\omega_{\mathrm{s}}^2[\bar{C}_{\mathrm{c}} + C_{\mathrm{l}}])^{-1}]$ and may not include $\check{L}$, in which case one should choose the maximal value.

5.7.1.3 More general optimization

In the previous two subsections we have considered the minimization of the EM added noise $N_{\mathrm{EM},0}$ with respect to the component parameters C_{l} and L individually. If these values are both tunable, it is desirable to perform a simultaneous optimization over (C_{l}, L). This simultaneous optimization is more cumbersome and is better suited to be performed in the context of given experimental constraints, including a specification of the relation $R_L = f(L)$.

5.7.2 Quantum regime: Full minimization of the (peak) sensitivity P_0

Above we have found that the EM noise can ideally reach the quantum limit $P_0 \sim 1$. At such low noise levels one should also include the optical noise and minimizing the sensitivity requires a balance between the various noise sources. To investigate this the optical noise $N_{\mathrm{opt}}^{(\mathrm{h})}$ will be calculated in Subsection 5.7.2.1. Having calculated this, we may perform the full minimization of the (peak) sensitivity P_0, as given by Eq. (5.37),

$$P_0 = \frac{1}{2} + \bar{N}_{\mathrm{e},0} + \bar{N}_{\mathrm{m},0} + N_{\mathrm{opt},0}^{(\mathrm{h})} \tag{5.51}$$

As discussed in Section 5.7, for the case of electrical-to-optical conversion $N_{\mathrm{opt}}^{(\mathrm{h})}$ depends on electrical parameters (including Γ_{EM}), whereas $\bar{N}_{\mathrm{e},0}, \bar{N}_{\mathrm{m},0}$ are independent of optical parameters. Conveniently, this permits the following optimization strategy: First, we minimize $N_{\mathrm{opt},0}^{(\mathrm{h})}$ as a function of the OM cooperativity $\mathcal{C}_{\mathrm{OM}}$ for a given EM setup to obtain the minimum value $\check{N}_{\mathrm{opt},0}^{(\mathrm{h})}$ in terms of EM parameters. This will be done in Subsection 5.7.2.2 (in doing so we assume $\mathcal{C}_{\mathrm{OM}}$ to be freely tunable). Second, we minimize P_0, (5.51), with $N_{\mathrm{opt},0}^{(\mathrm{h})} = \check{N}_{\mathrm{opt},0}^{(\mathrm{h})}$ which then only depends on EM parameters, i.e. electrical parameters and choice of circuit design. This will be discussed in Subsection 5.7.2.3.

5.7.2.1 Optical heterodyne noise $N_{\mathbf{opt}}^{\mathbf{(h)}}$

In this section we will derive an explicit expression for the optical contribution $N_{\mathrm{opt},0}^{(\mathrm{h})}$ to the (peak) homodyne sensitivity P_0, Eq. (5.37). Before doing so, it is in order to comment on how the present analysis relates to the discussion of heterodyne detection already given in Section 3.6.1. There we derived an upper bound for P expressible in terms of η and N by (pessimistically) assuming constructive interference between the noise in the two sidebands. The precise value of P depends on the actual interference, as is manifest in Eq. (3.14), but this coherence information is lost when evaluating η and N. Hence, to obtain the precise value of P, the transducer parameters η and N do not suffice.[4]

To determine $N_{\mathrm{opt}}^{(\mathrm{h})}$ we must therefore return to the scattering relation for $\hat{I}(\Omega)$, (5.33), and evaluate the optical contribution to $P(\Omega)$, Eq. (5.36),

$$N_{\mathrm{opt}}^{(\mathrm{h})}(\Omega)\delta(\Omega-\Omega') \equiv \frac{\langle \hat{\mathcal{N}}_{\theta_{\mathrm{LO}}}^{(\mathrm{opt})}(\Omega)\hat{\mathcal{N}}_{\theta_{\mathrm{LO}}}^{(\mathrm{opt})\dagger}(\Omega')\rangle + \langle \hat{\mathcal{N}}_{\theta_{\mathrm{LO}}}^{(\mathrm{opt})\dagger}(\Omega)\hat{\mathcal{N}}_{\theta_{\mathrm{LO}}}^{(\mathrm{opt})}(\Omega')\rangle}{2|t_{\mathrm{s},\theta_{\mathrm{LO}}}(\Omega)|^2}, \quad (5.52)$$

where $\hat{\mathcal{N}}_{\theta_{\mathrm{LO}}}^{(\mathrm{opt})}$ is the optical component of $\hat{\mathcal{N}}_{\theta_{\mathrm{LO}}}$, Eq. (5.35). Evaluating (5.52) at the transducer peak we find (see Appendix C.2.2 for details)

$$\begin{aligned} N_{\mathrm{opt},0}^{(\mathrm{h})} \equiv N_{\mathrm{opt}}^{(\mathrm{h})}(\Omega_{\mathrm{m}}) = \frac{1}{\eta_{\mathrm{el}}\gamma_{\mathrm{EM},+}} \times \\ \Bigg(\frac{(\gamma_{\mathrm{m},0}+\Gamma_{\mathrm{EM}}+\Gamma_{\mathrm{OM}})^2}{4\mathcal{C}_{\mathrm{OM}}\gamma_{\mathrm{m},0}|\mathcal{L}_+ e^{-i(\theta_{\mathrm{LO}}-\theta_+)} - \mathcal{L}_- e^{i(\theta_{\mathrm{LO}}-\theta_-)}|^2} \left[(\frac{1}{\eta_{\mathrm{opt}}}-1) + \frac{\gamma_{\mathrm{m},0}+\Gamma_{\mathrm{EM}}-\Gamma_{\mathrm{OM}}}{\gamma_{\mathrm{m},0}+\Gamma_{\mathrm{EM}}+\Gamma_{\mathrm{OM}}} \right] \\ + \frac{\gamma_{\mathrm{m},0}\mathcal{C}_{\mathrm{OM}}}{2}(\mathcal{L}_+^2+\mathcal{L}_-^2) \Bigg), \quad (5.53) \end{aligned}$$

having set $n_{\mathrm{opt}} \approx 0$. Only the prefactor to the bracketed term depends on θ_{LO} and hence the extrema of $N_{\mathrm{opt},0}^{(\mathrm{h})}$ coincide with the extrema of the prefactor with respect to θ_{LO}. These correspond to constructive and destructive sideband-interference (wrt. the absolute size of the signal component),

$$|\mathcal{L}_+ e^{-i(\theta_{\mathrm{LO}}-\theta_+)} - \mathcal{L}_- e^{i(\theta_{\mathrm{LO}}-\theta_-)}|^2 \to (\mathcal{L}_+ \pm \mathcal{L}_-)^2,$$

and are achieved for

$$\theta_{\mathrm{LO}} = \frac{\theta_+ + \theta_-}{2} + \begin{cases} \pi/2 & \text{constructive} \\ 0 & \text{destructive} \end{cases}. \quad (5.54)$$

Evaluating (5.53) for constructive/destructive sideband interference (5.54), we find

$$N_{\mathrm{opt},0}^{(\mathrm{h})}\Big|_{\mathrm{constr./destruc.}} = (N_{\mathrm{opt},0}^{(+)} + N_{\mathrm{opt},0}^{(-)})/2 + N_{\mathrm{opt},0}^{(\mathrm{im})}\Big|_{\mathrm{constr./destruc.}} \quad (5.55)$$

[4]This only applies to the optical contribution $N_{\mathrm{opt}}^{(\mathrm{h})}$ to P because the EM signal-to-noise ratio cannot be altered in the optical readout, see discussion above Eq. (5.37).

$$N_{\mathrm{opt},0}^{(\mathrm{im})}\Big|_{\mathrm{constr./destruc.}} \equiv \frac{1}{\eta_{\mathrm{el}}\gamma_{\mathrm{EM},+}}\left(\frac{1}{\eta_{\mathrm{opt}}}\frac{(\gamma_{\mathrm{m},0}+\Gamma_{\mathrm{EM}}+\Gamma_{\mathrm{OM}})^2}{4\mathcal{C}_{\mathrm{OM}}\gamma_{\mathrm{m},0}(\mathcal{L}_+\pm\mathcal{L}_-)^2} - \frac{\gamma_{\mathrm{m},0}+\Gamma_{\mathrm{EM}}+\Gamma_{\mathrm{OM}}}{2}\frac{\mathcal{L}_+\mp\mathcal{L}_-}{\mathcal{L}_+\pm\mathcal{L}_-}\right), \tag{5.56}$$

where in Eq. (5.55) we have decomposed the (peak) optical homodyne added noise $N_{\mathrm{opt},0}^{(\mathrm{h})}$ into the average of the squeezed vacuum fluxes of the two sidebands (see, e.g., Eq. (5.29)),

$$\frac{N_{\mathrm{opt},0}^{(+)}+N_{\mathrm{opt},0}^{(-)}}{2} = \frac{\gamma_{\mathrm{m},0}\mathcal{C}_{\mathrm{OM}}}{2\eta_{\mathrm{el}}\gamma_{\mathrm{EM},+}}(\mathcal{L}_+^2+\mathcal{L}_-^2) = \frac{\gamma_{\mathrm{OM},-}+\gamma_{\mathrm{OM},+}}{2\eta_{\mathrm{el}}\gamma_{\mathrm{EM},+}}, \tag{5.57}$$

and a contribution $N_{\mathrm{opt},0}^{(\mathrm{im})}$ containing imprecision shot noise (first term) and an interference contribution (second term) due to the correlations between imprecision noise and the squeezed vacuum [60]. Imprecision noise arises from the quantized nature of light at low intensities and is due to the random arrival times of photons. In fact, by comparing to the peak transfer efficiencies $\eta_0^{(\pm)}$, (5.27), we see that the imprecision noise contribution in (5.56) is

$$\frac{1}{\eta_{\mathrm{el}}\eta_{\mathrm{opt}}}\frac{(\gamma_{\mathrm{m},0}+\Gamma_{\mathrm{EM}}+\Gamma_{\mathrm{OM}})^2}{4\gamma_{\mathrm{EM},+}\mathcal{C}_{\mathrm{OM}}\gamma_{\mathrm{m},0}(\mathcal{L}_+\pm\mathcal{L}_-)^2} = \frac{1}{\left(\sqrt{\eta_0^{(+)}}\pm\sqrt{\eta_0^{(-)}}\right)^2}, \tag{5.58}$$

showing that its impact diminishes with the absolute amount of signal transferred through the transducer. Hence, the imprecision (5.58) noise is minimized by impedance matching considerations. On the other hand, the squeezed vacuum contribution (5.57) is seen to be proportional to $\mathcal{C}_{\mathrm{OM}}/\mathcal{C}_{\mathrm{EM}}$, thus favoring small values of $\mathcal{C}_{\mathrm{OM}}$. We will consider this trade-off in the next section.

5.7.2.2 Extrema of the homodyne optical noise $N_{\mathrm{opt},0}^{(\mathrm{h})}$

In this section we will examine the extrema of $N_{\mathrm{opt},0}^{(\mathrm{h})}$ wrt. $\mathcal{C}_{\mathrm{OM}}$ and $\mathcal{L}_\pm$ for fixed EM parameters $\eta_{\mathrm{el}}, \mathcal{C}_{\mathrm{EM}}$. We therefore start by parametrizing Eq. (5.55) in terms of $\mathcal{C}_{\mathrm{OM}}$ and $\mathcal{L}_\pm$, which is equivalent to drive-induced intra-cavity field and laser detuning for fixed cavity width κ and mechanical frequency Ω_{m}:

$$\begin{aligned} N_{\mathrm{opt},0}^{(\mathrm{h})}\Big|_{\mathrm{constr./destruc.}} = &\frac{1}{4\eta_{\mathrm{el}}\gamma_{\mathrm{EM},+}}\left(\gamma_{\mathrm{m},0}\mathcal{C}_{\mathrm{OM}}\left[\left(\frac{1}{\eta_{\mathrm{opt}}}-1\right)(\mathcal{L}_+\mp\mathcal{L}_-)^2+(\mathcal{L}_+\pm\mathcal{L}_-)^2\right]\right. \\ &\left.+\frac{1}{\gamma_{\mathrm{m},0}\mathcal{C}_{\mathrm{OM}}}\frac{(\gamma_{\mathrm{m},0}+\Gamma_{\mathrm{EM}})^2}{\eta_{\mathrm{opt}}(\mathcal{L}_+\pm\mathcal{L}_-)^2}+2(\gamma_{\mathrm{m},0}+\Gamma_{\mathrm{EM}})\left[\frac{1}{\eta_{\mathrm{opt}}}-1\right]\frac{\mathcal{L}_+\mp\mathcal{L}_-}{\mathcal{L}_+\pm\mathcal{L}_-}\right). \end{aligned} \tag{5.59}$$

Eq. (5.59) has the following local minimum point $\check{\mathcal{C}}_{\mathrm{OM}}$ with respect to $\mathcal{C}_{\mathrm{OM}}$,

$$\begin{aligned} \check{\mathcal{C}}_{\mathrm{OM}}\big|_{\mathrm{constr./destruc.}} &= \frac{1+\Gamma_{\mathrm{EM}}/\gamma_{\mathrm{m},0}}{|\mathcal{L}_+^2-\mathcal{L}_-^2|\sqrt{1\pm\eta_{\mathrm{opt}}\frac{4\mathcal{L}_+\mathcal{L}_-}{(\mathcal{L}_+\mp\mathcal{L}_-)^2}}} \\ &= \frac{1+\Gamma_{\mathrm{EM}}/\gamma_{\mathrm{m},0}}{(\mathcal{L}_+\pm\mathcal{L}_-)^2\sqrt{1\mp(1-\eta_{\mathrm{opt}})\frac{4\mathcal{L}_+\mathcal{L}_-}{(\mathcal{L}_+\pm\mathcal{L}_-)^2}}}. \end{aligned} \tag{5.60}$$

Considering Eq. (5.60) in the limits of resolved and unresolved OM sidebands, $4\eta_{\text{opt}}\mathcal{L}_{\mp} \ll \mathcal{L}_{\pm} \approx 1$ (red/blue detuned) and $\mathcal{L}_{-} \approx \mathcal{L}_{+}$ respectively, we find

$$\check{\mathcal{C}}_{\text{OM}} \approx \begin{cases} 1 + \Gamma_{\text{EM}}/\gamma_{\text{m},0} & \text{[OM RSB]} \\ \frac{1+\Gamma_{\text{EM}}/\gamma_{\text{m},0}}{\mathcal{L}_+^2\sqrt{16\eta_{\text{opt}}}} & \text{[OM un-RSB]} \end{cases}. \tag{5.61}$$

Hence, in the RSB limit we recover the impedance matching condition that the optically induced width should match that of the electrically broadened mechanical mode, $\Gamma_{\text{OM}} \approx \gamma_{\text{OM},+} \approx \gamma_{\text{m},0}\check{\mathcal{C}}_{\text{OM}} = \gamma_{\text{m},0} + \Gamma_{\text{EM}}$ ($\approx \Gamma_{\text{EM}}$ when $\Gamma_{\text{EM}} \gg \gamma_{\text{m},0}$). From this we draw the important conclusion that for the heterodyning scheme considered here, impedance matching is only the optimal strategy to the extent that the readout cavity is sideband-resolved. The un-RSB limit of Eq. (5.61) reflects a trade-off between heating from squeezed vacuum (grows as $\mathcal{C}_{\text{OM}}$) and imprecision shot noise, as discussed in the previous section.

In the following we will analyze the minimized quantity $\check{N}^{(\text{h})}_{\text{opt}} \equiv N^{(\text{h})}_{\text{opt}}|_{\mathcal{C}_{\text{OM}}=\check{\mathcal{C}}_{\text{OM}}}$, assuming that the optimal OM cooperativity $\check{\mathcal{C}}_{\text{OM}}$ (5.60) is attainable; we find for constructive/destructive interference (assuming $\gamma_{\text{m},0} + \Gamma_{\text{EM}} > 0$),

$$\check{N}^{(\text{h})}_{\text{opt},0} = \frac{1}{\eta_{\text{el}}}\frac{\gamma_{\text{m},0} + \Gamma_{\text{EM}}}{\gamma_{\text{EM},+}}\sigma, \tag{5.62}$$

where, for later convenience, we have introduced the effective optical noise flux per unit bandwidth

$$\sigma|_{\text{constr./destruc.}} \equiv \frac{1}{2}\left(\frac{1}{\sqrt{\eta_{\text{opt}}}}\sqrt{1 + \left[\frac{1}{\eta_{\text{opt}}} - 1\right]\left(\frac{\mathcal{L}_+ \mp \mathcal{L}_-}{\mathcal{L}_+ \pm \mathcal{L}_-}\right)^2} + \left[\frac{1}{\eta_{\text{opt}}} - 1\right]\frac{\mathcal{L}_+ \mp \mathcal{L}_-}{\mathcal{L}_+ \pm \mathcal{L}_-}\right), \tag{5.63}$$

that only depends on the optical coupling efficiency η_{opt} and the optical sideband strengths $\mathcal{L}_{\pm}$. The interpretation of σ will become clear when we compare the optical noise to the other noise contributions later on. Before considering the choice of optical drive detuning, which will determine $\mathcal{L}_{\pm}$, we make the following observations: First, we remark that $\sigma|_{\text{constr.}} < \sigma|_{\text{destruc.}}$ for all applicable $\mathcal{L}_{\pm}$, meaning that constructive sideband interference results in less optical noise than destructive sideband interference for $\mathcal{C}_{\text{OM}} = \check{\mathcal{C}}_{\text{OM}}|_{\text{constr./destruc.}}$. Henceforth we will therefore restrict our attention to $\check{N}^{(\text{h})}_{\text{opt},0}|_{\text{constr.}}$ and omit the label. Second, we note by inspecting Eq. (5.63) that in the limit of perfect optical outcoupling, $\eta_{\text{opt}} \to 1$, we have $\sigma \to 1/2$ and (accordingly) the minimized added noise $\check{N}^{(\text{h})}_{\text{opt},0}$ is independent of the optical sideband strengths $\mathcal{L}_{\pm}$ (or, alternatively, the OM sideband resolution parameter $s \equiv \kappa/(4\Omega_{\text{m}})$ and the choice of optical detuning Δ):

$$\check{N}^{(\text{h})}_{\text{opt},0}\Big|_{\eta_{\text{opt}}\to 1} = \frac{1}{2\eta_{\text{el}}}\frac{\gamma_{\text{m},0} + \Gamma_{\text{EM}}}{\gamma_{\text{EM},+}}. \tag{5.64}$$

If we moreover take the limit of resolved EM sidebands, $\Gamma_{\text{EM}} \to \gamma_{\text{EM},+}$, high EM cooperativity, $\gamma_{\text{EM},+} \gg \gamma_{\text{m},0}$ and ideal electrical efficiency $\eta_{\text{el}} = 1$, we recover the fundamental quantum-mechanical limit $\check{N}^{(\text{h})}_{\text{opt},0} = 1/2$ for the simultaneous measurement of two quadratures. This is achieved since all incoming information is transduced and measured in the output regardless of the detuning Δ.

We now turn to the choice of optical drive detuning Δ. For $\eta_{\rm opt} < 1$ we note that $\check{N}^{(\rm h)}_{\rm opt,0}$ only depends on the sideband strengths through $l \equiv \mathcal{L}_-/\mathcal{L}_+$ and has no stationary points with respect to l for $l \in \mathbb{R}_+$, i.e. $d\check{N}^{(\rm h)}_{\rm opt,0}/dl \neq 0$. It then follows from the chain rule that the extremal points of $\check{N}^{(\rm h)}_{\rm opt,0}$, (5.62), with regard to the choice of optical detuning Δ coincide with those of the sideband ratio $l = \mathcal{L}_-/\mathcal{L}_+$. These extrema are $\Delta = \pm\Delta_0$ where for the Lorentzian line shape

$$\Delta_0 = \sqrt{\Omega_{\rm m}^2 + (\kappa/2)^2} = \Omega_{\rm m}\sqrt{1+4s^2},$$

where $s \equiv \kappa/(4\Omega_{\rm m})$ is the OM sideband resolution parameter. The minimum of $\check{N}^{(\rm h)}_{\rm opt,0}$ occurs for blue-sideband detuning $\Delta = +\Delta_0$, whereas the maximum occurs for red-sideband detuning $\Delta = -\Delta_0$. The reason for this is that blue detuning maximizes OM amplification of the signal before it is subject to loss due to the finite optical coupling efficiency $\eta_{\rm opt} < 1$. The gain achieved using blue-sideband detuning $\Delta = +\Delta_0$ thus counters the added noise floor due to imperfect optical coupling $\eta_{\rm opt} < 1$, thereby leading to the minimal value of $\check{N}^{(\rm h)}_{\rm opt,0}$. At the same time, however, it also diminishes the bandwidth of the transducer $\Gamma_{\rm EM} + \gamma_{\rm m,0}(1 + \mathcal{C}_{\rm OM}[\mathcal{L}_+^2 - \mathcal{L}_-^2])$. This implies a gain-bandwidth trade-off. In the resolved sideband limit $s \lesssim 1$, we have $\Delta_0 \to \Omega_{\rm m}$ and find that blue-detuned operation results in

$$\check{N}^{(\rm h)}_{\rm opt,0}\Big|_{\Delta=+\Delta_0} = \frac{1}{\eta_{\rm el}}\frac{\gamma_{\rm m,0}+\Gamma_{\rm EM}}{\gamma_{\rm EM,+}}\left[\frac{1}{2} + (1-\eta_{\rm opt})s^2\right] + \mathcal{O}(s^3). \tag{5.65}$$

Comparing Eq. (5.65) to the expression (5.64) for the $\eta_{\rm opt} \to 1$ limit, we see that blue-sideband operation in the OM resolved sideband regime allows us to approach the $\eta_{\rm opt} \to 1$ value of $\check{N}^{(\rm h)}_{\rm opt}$ even for an imperfect optical outcoupling $\eta_{\rm opt} < 1$. As mentioned above, this comes at the cost of a smaller bandwidth. Ultimately, as $s \to 0$ we have $\check{\mathcal{C}}_{\rm OM} \to (1 + \Gamma_{\rm EM}/\gamma_{\rm m,0})/\mathcal{L}_-^2$ and $\mathcal{L}_+/\mathcal{L}_- \to 0$ for blue-detuned operation whereby the transducer bandwidth approaches zero, $\Gamma_{\rm EM} + \gamma_{\rm m,0}(1 + \mathcal{C}_{\rm OM}[\mathcal{L}_+^2 - \mathcal{L}_-^2]) \to 0$.

Working red-detuned, on the other hand, has the benefit of increasing the bandwidth. In the resolved-sideband limit, $s \lesssim 1$, the largest optical broadening is obtained for $\Delta \approx -\Omega_{\rm m}$. In this case, for $s \ll 1$, the optical noise is

$$\check{N}^{(\rm h)}_{\rm opt,0}\Big|_{\Delta=-\Omega_{\rm m}} = \frac{1}{\eta_{\rm el}}\frac{\gamma_{\rm m,0}+\Gamma_{\rm EM}}{\gamma_{\rm EM,+}}\left[\frac{1}{2} + (\frac{1}{\eta_{\rm opt}} - 1)[1 - 2s(1 - s(1+\eta_{\rm opt}/2))]\right] + \mathcal{O}(s^3).$$

In the unresolved sideband regime, $s \gtrsim 1$, the difference between driving red and blue detuned naturally becomes less pronounced. In this regime, maximal optical broadening is achieved for $\Delta \approx -\kappa/\sqrt{12}$ yielding the optical noise ($s \gg 1$)

$$\check{N}^{(\rm h)}_{\rm opt,0}\Big|_{\Delta=-\kappa/\sqrt{12}} = \frac{1}{\eta_{\rm el}}\frac{\gamma_{\rm m,0}+\Gamma_{\rm EM}}{\gamma_{\rm EM,+}}\left[\frac{1}{2\sqrt{\eta_{\rm opt}}} + (\frac{1}{\eta_{\rm opt}} - 1)\frac{\sqrt{3}}{16}\frac{1}{s}\right] + \mathcal{O}(s^{-2}).$$

We collect simplified versions of the above results in Table 5.2, which shows how the sensitivity to imperfect optical coupling efficiency $\eta_{\rm opt} < 1$ decreases with increasing OM amplification. In one end of the spectrum, red-detuned operation in the fully resolved-sideband limit, the optical noise goes as $\eta_{\rm opt}^{-1}$, whereas for blue-detuned operation in the same limit, a narrowband signal can in principle be preamplified to the classical level. In the latter case, imprecision noise becomes negligible and the dependence on η_{opt} vanishes. As an intermediate choice, $\Delta = -\kappa/\sqrt{12}$ (which maximizes Γ_{OM} when $s \gg 1$) provides some amplification and results in the noise scaling as $(\eta_{\mathrm{opt}})^{-1/2}$. These consideration are important insofar as the optical noise dominates the sensitivity and a noise penalty on the order of $\sim \eta_{\mathrm{opt}}^{-1} - 1$ is a concern (assuming the electrical system to be perfectly coupled, $\eta_{\mathrm{el}} \to 1$).

Opt. regime/fig. of merit	$\check{N}^{(\mathrm{h})}_{\mathrm{opt},0}$
$\Delta = -\Omega_{\mathrm{m}}\ [s \lll 1]$	$\frac{1}{\eta_{\mathrm{el}}} \frac{\gamma_{\mathrm{m},0}+\Gamma_{\mathrm{EM}}}{\gamma_{\mathrm{EM},+}} \left[\frac{1}{\eta_{\mathrm{opt}}} - \frac{1}{2}\right]$
$\Delta = -\kappa/\sqrt{12}\ [s \ggg 1]$	$\frac{1}{\eta_{\mathrm{el}}} \frac{\gamma_{\mathrm{m},0}+\Gamma_{\mathrm{EM}}}{\gamma_{\mathrm{EM},+}} \left[\frac{1}{2\sqrt{\eta_{\mathrm{opt}}}}\right]$
$\Delta = +\Omega_{\mathrm{m}}\ [s \lll 1]$	$\frac{1}{\eta_{\mathrm{el}}} \frac{\gamma_{\mathrm{m},0}+\Gamma_{\mathrm{EM}}}{\gamma_{\mathrm{EM},+}} \left[\frac{1}{2}\right]$

Table 5.2: Optical noise for optimal $\mathcal{C}_{\mathrm{OM}} = \check{\mathcal{C}}_{\mathrm{OM}}$, $\check{N}^{(\mathrm{h})}_{\mathrm{opt}}$, evaluated at different optical detunings Δ in different limits of the OM sideband-resolution parameter s. The expressions show decreasing sensitivities to optical loss $\eta_{\mathrm{opt}} < 1$ from top to bottom due to an increasing degree of OM pre-amplification.

5.7.2.3 Full minimization of the sensitivity P_0

We will now minimize the homodyne peak sensitivity P_0, (5.37), taking into account all contributions at once. Such a full optimization is most relevant in the vicinity of the quantum regime, $P_0 \sim 1$, which is only likely to be achieved with an AC-driven resonant superconducting circuit and hence we specialize to this case. We will optimize over the parameters $\mathcal{C}_{\mathrm{OM}}$ and η_{el}, while leaving the result a function of drive detunings and cavity/circuit linewidths. Choosing the values of the latter parameters is a matter of gain-bandwidth trade-off, which we will not delve into here. Two cases will be discussed: 1) The scenario where we assume that we can always achieve the optimal OM cooperativity $\mathcal{C}_{\mathrm{OM}} = \check{\mathcal{C}}_{\mathrm{OM}}$, (5.60), but where $\mathcal{C}_{\mathrm{EM},0}$ is constrained by some upper (practical) bound $\mathcal{C}^{(\mathrm{max})}_{\mathrm{EM},0}$. 2) The scenario where OM cooperativity is limited $\mathcal{C}_{\mathrm{OM}} \leq \mathcal{C}^{(\mathrm{max})}_{\mathrm{OM}} \ll \check{\mathcal{C}}_{\mathrm{OM}}$ so that the optimal value of $\check{\mathcal{C}}_{\mathrm{OM}}$ cannot be attained (the latter being evaluated at $\mathcal{C}^{(\mathrm{max})}_{\mathrm{EM},0}$).

$\mathcal{C}_{\mathrm{OM}}$ freely tunable In Section 5.7.2.2 above, we considered the minimization of the optical noise contribution to P_0 for fixed electrical parameters $\mathcal{C}_{\mathrm{EM}}, \mathcal{K}_{\pm}$. The resulting minimum $\check{N}^{(\mathrm{h})}_{\mathrm{opt},0}$ as a function of $\check{\mathcal{C}}_{\mathrm{OM}}$, (5.62), is hence a function of the electrical parameters. Since in contrast, as discussed above, the electrical and mechanical noise contributions $\bar{N}_{\mathrm{e},0}, \bar{N}_{\mathrm{m},0}$ are independent of the parameters of the optical system, the full minimization of P_0 corresponds to minimizing

$$P_0|_{\mathcal{C}_{\mathrm{OM}}=\check{\mathcal{C}}_{\mathrm{OM}}} = \frac{1}{2} + \bar{N}_{\mathrm{e},0} + \bar{N}_{\mathrm{m},0} + \check{N}^{(\mathrm{h})}_{\mathrm{opt},0} \tag{5.66}$$

over the electrical parameters. This presumes, however, that $\mathcal{C}_{\mathrm{OM}} = \check{\mathcal{C}}_{\mathrm{OM}}$ is always achievable and this is the assumption we will make at present.

We start by expressing the minimized optical noise in terms of the electrical sideband strengths $\mathcal{K}_\pm$, which appeared first in Section 5.5.2, see Eq. (5.14). In terms of these symbols Eq. (5.62) reads,

$$\check{N}^{(\mathrm{h})}_{\mathrm{opt},0} = \frac{1}{\eta_{\mathrm{el}}}\frac{\gamma_{\mathrm{m},0}+\Gamma_{\mathrm{EM}}}{\gamma_{\mathrm{EM},+}}\sigma = \frac{1}{\eta_{\mathrm{el}}}\left(\frac{1}{\mathcal{C}_{\mathrm{EM}}\mathcal{K}_+^2} + \frac{\mathcal{K}_+^2-\mathcal{K}_-^2}{\mathcal{K}_+^2}\right)\sigma. \tag{5.67}$$

Here, the first term in the parenthesis equals $\gamma_{\mathrm{m},0}/\gamma_{\mathrm{EM},+}$ and is therefore suppressed as $1/\mathcal{C}_{\mathrm{EM}}$; the second term in the parenthesis is $\Gamma_{\mathrm{EM}}/\gamma_{\mathrm{EM},+}$ for which the dependence on $\mathcal{C}_{\mathrm{EM}}$ cancels out. Combining (5.67) with $\bar{N}_{\mathrm{e},0}+\bar{N}_{\mathrm{m},0}$ as follows from Eqs. (5.31,5.32), we evaluate Eq. (5.66) to find

$$\begin{aligned} P_0|_{\mathcal{C}_{\mathrm{OM}}=\check{\mathcal{C}}_{\mathrm{OM}}} &= \frac{1}{2} + \left(\frac{1}{\eta_{\mathrm{el}}}-1\right)\left[1+\frac{\mathcal{K}_-^2}{\mathcal{K}_+^2}\right]\left(n_L(\omega_{\mathrm{d}}+\Omega_{\mathrm{m}})+\frac{1}{2}\right) \\ &+ \frac{\mathcal{K}_-^2}{\mathcal{K}_+^2}\left(n_{\mathrm{tx}}(\omega_{\mathrm{d}}-\Omega_{\mathrm{m}})+\frac{1}{2}\right) + \frac{1}{\eta_{\mathrm{el}}}\left[\sigma+(1-\sigma)\frac{\mathcal{K}_-^2}{\mathcal{K}_+^2}\right] + \frac{n_{\mathrm{m}}(\Omega_{\mathrm{m}})+1/2+\sigma}{\mathcal{K}_+^2\mathcal{C}_{\mathrm{EM},0}(1-\eta_{\mathrm{el}})\eta_{\mathrm{el}}}. \end{aligned} \tag{5.68}$$

Here we have used $\gamma_{\mathrm{EM},+}=\gamma_{\mathrm{m},0}\mathcal{C}_{\mathrm{EM},0}(1-\eta_{\mathrm{el}})\mathcal{K}_+^2$ as follows from Eq. (5.43) and the definition of the anti-Stokes rate. Noting that (5.68) has the same functional form as (5.44) in terms of η_{el}, we may minimize P_0 using similar steps; hence, we rewrite (5.68) as

$$P_0 = P_{\mathrm{res}} + \left(\frac{1}{\eta_{\mathrm{el}}}-1\right)n_{\mathrm{EO}} + \frac{n_{\mathrm{OM}}}{\mathcal{C}_{\mathrm{EM},0}(1-\eta_{\mathrm{el}})\eta_{\mathrm{el}}}, \tag{5.69}$$

in terms of the residual sensitivity P_{res} and effective electro-optical n_{EO} and opto-mechanical n_{OM} noise fluxes per unit bandwidth,

$$\begin{aligned} P_{\mathrm{res}} &= \frac{1}{2} + \frac{\mathcal{K}_-^2}{\mathcal{K}_+^2}\left(n_{\mathrm{tx}}(\omega_{\mathrm{d}}-\Omega_{\mathrm{m}})+\frac{1}{2}\right) + \frac{\mathcal{K}_-^2}{\mathcal{K}_+^2} + \left[1-\frac{\mathcal{K}_-^2}{\mathcal{K}_+^2}\right]\sigma, \\ n_{\mathrm{EO}} &\equiv \left[1+\frac{\mathcal{K}_-^2}{\mathcal{K}_+^2}\right]\left(n_L(\omega_{\mathrm{d}})+\frac{1}{2}\right) + \frac{\mathcal{K}_-^2}{\mathcal{K}_+^2} + \left[1-\frac{\mathcal{K}_-^2}{\mathcal{K}_+^2}\right]\sigma,\ n_{\mathrm{OM}} \equiv \frac{n_{\mathrm{m}}(\Omega_{\mathrm{m}})+1/2+\sigma}{\mathcal{K}_+^2}. \end{aligned}$$

These definitions make it clear that σ (5.63) plays the role of an effective optical noise flux per unit bandwidth. The peak sensitivity, (5.69), is minimized by

$$\check{\eta}_{\mathrm{el}} = \left[1+\left(1+\frac{\mathcal{C}_{\mathrm{EM},0}n_{\mathrm{EO}}}{n_{\mathrm{OM}}}\right)^{-1/2}\right]^{-1}, \tag{5.70}$$

generalizing Eq. (5.45). The corresponding minimum value of P_0 is

$$\check{P}_0 = P_{\mathrm{res}} + 2\frac{n_{\mathrm{OM}}}{\mathcal{C}_{\mathrm{EM},0}}\left(1+\sqrt{1+\frac{\mathcal{C}_{\mathrm{EM},0}n_{\mathrm{EO}}}{n_{\mathrm{OM}}}}\right), \tag{5.71}$$

which is the generalization of (5.46) to the quantum regime (as well as arbitrary electrical drive detuning and sideband resolution). The expression (5.71) shows that $\mathcal{C}_{\mathrm{EM},0}$ should be made as large as possible provided that $\mathcal{C}_{\mathrm{OM}}=\check{\mathcal{C}}_{\mathrm{OM}}$, (5.60), can be maintained (this corresponds to the situation where the EM coupling strength is the bottleneck). In this sense, Eq. (5.71) is minimized wrt. the cooperativities $\mathcal{C}_{\mathrm{OM}}$ and $\mathcal{C}_{\mathrm{EM}}$, while the optical and electrical drive-tone frequencies will have to be chosen as a compromise between peak added noise and bandwidth.

$\mathcal{C}_{\mathrm{OM}}$ limited If we cannot tune $\mathcal{C}_{\mathrm{OM}}$ freely so as to achieve the value $\check{\mathcal{C}}_{\mathrm{OM}}$, the preceding analysis ceases to apply. Hence we now consider the scenario where practical considerations constrain the OM cooperativity $\mathcal{C}_{\mathrm{OM}} \leq \mathcal{C}_{\mathrm{OM}}^{(\mathrm{max})} \ll \check{\mathcal{C}}_{\mathrm{OM}}$ (where the latter is evaluated at $\mathcal{C}_{\mathrm{EM},0}^{(\mathrm{max})}$). In this case the optical noise is dominated by the imprecision shot noise. Focusing on red-detuned operation, (5.60) and the previous assumption imply $\Gamma_{\mathrm{OM}}^{(\mathrm{max})} \equiv \gamma_{\mathrm{m},0}\mathcal{C}_{\mathrm{OM}}^{(\mathrm{max})}(\mathcal{L}_+^2 - \mathcal{L}_-^2) \ll \gamma_{\mathrm{m},0} + \Gamma_{\mathrm{EM}}$; choosing $\mathcal{C}_{\mathrm{OM}} = \mathcal{C}_{\mathrm{OM}}^{(\mathrm{max})}$ we can therefore approximate (5.55)

$$N_{\mathrm{opt},0}^{(\mathrm{h})} \approx \frac{\gamma_{\mathrm{m},0}}{\eta_{\mathrm{el}}\eta_{\mathrm{opt}}\gamma_{\mathrm{EM},+}} \frac{(1+\Gamma_{\mathrm{EM}}/\gamma_{\mathrm{m},0})^2}{4\mathcal{C}_{\mathrm{OM}}^{(\mathrm{max})}(\mathcal{L}_+ + \mathcal{L}_-)^2}. \tag{5.72}$$

In this situation, $N_{\mathrm{opt},0}^{(\mathrm{h})} \to \infty$ for $\mathcal{C}_{\mathrm{EM}} \to \infty$ because EM broadening will decouple the mechanical mode from the optical field if $\mathcal{C}_{\mathrm{OM}}$ does not follow $\mathcal{C}_{\mathrm{EM}}$ (as we assumed in the previous minimization above). Since, obviously, we also require $\mathcal{C}_{\mathrm{EM}} > 0$ a trade-off exists with some optimal value of $\mathcal{C}_{\mathrm{EM}}$. To determine this, we must consider simultaneously all terms in P_0, (5.51), that depend on $\mathcal{C}_{\mathrm{EM}}$; these are the mechanical and optical contributions

$$\begin{aligned}\bar{N}_{\mathrm{m},0} + N_{\mathrm{opt},0}^{(\mathrm{h})} = \frac{1}{\eta_{\mathrm{el}}}\Bigg[&\frac{1}{\mathcal{K}_+^2\mathcal{C}_{\mathrm{EM}}}(n_{\mathrm{m}}(\Omega_{\mathrm{m}}) + \frac{1}{2} + n_{\mathrm{O}}) \\ &+ \mathcal{C}_{\mathrm{EM}} n_{\mathrm{O}} \frac{(\mathcal{K}_+^2 - \mathcal{K}_-^2)^2}{\mathcal{K}_+^2} + 2\left(1 - \frac{\mathcal{K}_-^2}{\mathcal{K}_+^2}\right) n_{\mathrm{O}}\Bigg],\end{aligned} \tag{5.73}$$

where we once again have introduced the electrical sideband strengths $\mathcal{K}_\pm$ and an equivalent optical noise flux per unit bandwidth

$$n_{\mathrm{O}} \equiv \frac{1}{4\eta_{\mathrm{opt}}\mathcal{C}_{\mathrm{OM}}^{(\mathrm{max})}(\mathcal{L}_+ + \mathcal{L}_-)^2}.$$

Eq. (5.73) is minimal as a function of $\mathcal{C}_{\mathrm{EM}}$ at

$$\begin{aligned}\check{\mathcal{C}}_{\mathrm{EM}} &= \frac{\sqrt{1 + (n_{\mathrm{m}}(\Omega_{\mathrm{m}}) + 1/2)/n_{\mathrm{O}}}}{|\mathcal{K}_+^2 - \mathcal{K}_-^2|} \\ &= \frac{\sqrt{1 + (n_{\mathrm{m}}(\Omega_{\mathrm{m}}) + 1/2)4\eta_{\mathrm{opt}}\mathcal{C}_{\mathrm{OM}}^{(\mathrm{max})}(\mathcal{L}_+ + \mathcal{L}_-)^2}}{|\mathcal{K}_+^2 - \mathcal{K}_-^2|},\end{aligned} \tag{5.74}$$

determining the effective transducer bandwidth (for red-detuned electrical drive) for $\mathcal{C}_{\mathrm{EM}} = \check{\mathcal{C}}_{\mathrm{EM}}$

$$\gamma_{\mathrm{m}} \approx \gamma_{\mathrm{m},0}(1+\check{\mathcal{C}}_{\mathrm{EM}}[\mathcal{K}_+^2-\mathcal{K}_-^2]) = \gamma_{\mathrm{m},0}\sqrt{1 + (n_{\mathrm{m}}(\Omega_{\mathrm{m}}) + 1/2)4\eta_{\mathrm{opt}}\mathcal{C}_{\mathrm{OM}}^{(\mathrm{max})}(\mathcal{L}_+ + \mathcal{L}_-)^2}.$$

Evaluating P_0, (5.51), at $\mathcal{C}_{\mathrm{EM}} = \check{\mathcal{C}}_{\mathrm{EM}}$, (5.74), we find

$$\begin{aligned}P_0 = \frac{1}{2} + \left(\frac{1}{\eta_{\mathrm{el}}} - 1\right)\left[1 + \frac{\mathcal{K}_-^2}{\mathcal{K}_+^2}\right]\left[n_L(\omega_{\mathrm{d}}) + \frac{1}{2}\right] + \frac{\mathcal{K}_-^2}{\mathcal{K}_+^2}\left[n_{\mathrm{tx}}[\omega_{\mathrm{d}} - \Omega_{\mathrm{m}}] + \frac{1}{2}\right] \\ + \frac{2}{\eta_{\mathrm{el}}}\left(1 - \frac{\mathcal{K}_-^2}{\mathcal{K}_+^2}\right)\sqrt{n_{\mathrm{O}}(n_{\mathrm{m}}(\Omega_{\mathrm{m}}) + 1/2 + n_{\mathrm{O}})}\left[1 + (1 + (n_{\mathrm{m}}(\Omega_{\mathrm{m}}) + 1/2)/n_{\mathrm{O}})^{-1/2}\right].\end{aligned} \tag{5.75}$$

Provided that $\mathcal{C}_{\rm EM} = (1-\eta_{\rm el})\mathcal{C}_{\rm EM,0} = \check{\mathcal{C}}_{\rm EM}$ can be fulfilled, $\eta_{\rm el}$ in (5.75) should be as large as possible, i.e. within the family of circuits considered here, the serial RLC should be chosen. Eq. (5.75) shows that if the OM cooperativity $\mathcal{C}_{\rm OM}$ is limited and P_0 is dominated by the OM contributions in (5.75), it can be advantageous to decrease the electrical sideband resolution (provided that we may still achieve $\mathcal{C}_{\rm EM} = \check{\mathcal{C}}_{\rm EM}$). This is because the electrical broadening of the mechanical mode (that takes place in the EM resolved-sideband regime) tends to decouple it from the optics.

This concludes our analysis of how to balance the noise contributions determining P_0 in the quantum regime where optical noise must be accounted for.

5.8 Numerical examples

We will now evaluate the figures-of-merit for some of the transducer applications discussed in Chapter 3, considering both examples of classical and quantum operation. To enable single-quantum operation of a transducer, noise sources must be suppressed to a degree that the probability of converting thermal excitations into output photons is small compared to that of converting input signal photons. In general, this requires careful engineering of the system and operating the system at cryogenic temperatures. On the other hand, sensing weak electrical signals with optical heterodyne detection can be advantageous even at room temperature. Here we will consider device parameters from recent experiments to assess the feasibility of some of the transduction schemes considered above.

5.8.1 Optical homodyne detection of RF and microwave signals

The task of designing an optical homodyne detector for MHz or GHz radiation was considered in some detail in the preceding parts of this section. Here we will calculate the expected performance of such an apparatus, considering both classical and quantum level scenarios.

5.8.1.1 RF to optical

For DC-biased RF-to-optical conversion at room temperature, where the mechanical resonance frequency equals that of the incoming electrical signal, we are typically in the classical scenario which was the focus of Section 5.7.1. Ohmic noise from the electrical circuit will dominate in the large EM cooperativity limit $\mathcal{C}_{\rm EM} > (1-\eta_{\rm el})^{-1}$. Using parameters similar to those of Ref. [1], $R_L = 20\Omega, Q_L = 130, \mathcal{C}_{\rm EM,0} = 6800, \omega_{\rm LC} = \Omega_{\rm m} = (2\pi)\cdot 0.72\text{MHz}$, the criteria (5.45) and (5.49) for picking the circuit layout with the least added noise favors the serial RLC circuit since $\check{\eta}_{\rm el} = 0.99$ but $\mathcal{C}_{\rm EM,0} < Q_L^2$. Feeding the serial RLC receiver by a transmission line of characteristic impedance $Z_{\rm tx} = 50\Omega$ we may evaluate the noise temperatures using Table 5.1 and 5.2 ($R_{\rm min} \to 0$ for simplicity)

$$T_{\rm ohm} \sim 120\text{K}, T_{\rm mech} \sim 0\text{K}, T_{\rm opt} \sim 0\text{K},$$

assuming that the optical noise minimum $\check{N}_{\rm opt}^{(\rm h)}$ can be achieved, Eq. (5.62). In this case, we find the optical noise to be negligible (irrespective of optical detuning) as long as $\eta_{\rm opt}$ is not very small,

$$\eta_{\rm opt} \gg \frac{1}{(1-\eta_{\rm el})n_{\rm ohm}(\omega_{\rm LC})}, \qquad \text{for } \Delta = -\omega_{\rm m}[s \ll 1]$$
$$\eta_{\rm opt} \gg \left(\frac{1}{2(1-\eta_{\rm el})n_{\rm ohm}(\omega_{\rm LC})}\right)^2, \qquad \text{for } \Delta = -\kappa/\sqrt{12}[s \gg 1]$$

referring to the limits of resolved and unresolved OM sidebands using a red-detuned optical drive, see Table 5.2.

Hence for RF-to-optical conversion, ohmic noise is typically the bottleneck for room-temperature operation, whereas the optomechanical system adds little noise. The ohmic noise can be suppressed by increasing the coupling efficiency of the circuit $\eta_{\rm el} = Z_{\rm tx}/(Z_{\rm tx} + R_L)$ or decreasing $n_{\rm ohm}$ by cooling the circuit below room temperature. Alternatively, if $\mathcal{C}_{\rm EM,0}$ can be increased, the lossy inductor can be dispensed with as discussed in Section 5.7.1.1.

5.8.1.2 MW to optical

For AC-driven receiver circuits operating in the GHz range of frequencies coupled to a MHz mechanical oscillator at equal temperature, the ohmic bath occupancy $n_{\rm ohm}$ will be several orders of magnitude smaller than its mechanical counterpart $n_{\rm m}$, $n_{\rm ohm} \approx (\Omega_{\rm m}/\omega_{\rm s})n_{\rm m}$. In this case, ohmic noise will only exceed the mechanical noise given that the latter can be suppressed by an EM cooperativity $\mathcal{C}_{\rm EM} > (\omega_{\rm s}/\Omega_{\rm m})(1-\eta_{\rm el})^{-1}$. Therefore, in GHz-to-optical conversion the noise contribution of the MHz mechanical mode will tend to be the bottleneck, which (in the absence of a very large EM cooperativity) can only be brought into the quantum regime by cooling the system to sub-Kelvin temperatures. Since we reference the added noise to the GHz signal, the noise temperature of the MHz oscillator may well exceed the temperature of the system, as we will see below.

The exact optimization of this scenario was performed in Section 5.7.2.3 as a function of $\mathcal{C}_{\rm OM}$ and $\eta_{\rm el}$. Assuming that $\mathcal{C}_{\rm OM}$ is freely tunable and choosing the value $\check{\mathcal{C}}_{\rm OM}$, (5.60), that minimizes the optical noise, we evaluate $\check{P}_0$ (5.71) corresponding to $\eta_{\rm el} = \check{\eta}_{\rm el}$, (5.70), for parameters similar to those in the experiment of Ref. [6],

$$\begin{gathered}\mathcal{C}_{\rm EM,0} = 20.000, \eta_{\rm opt} = 0.23, \Omega_{\rm m} = (2\pi)\cdot 1.24\text{MHz},\\ \omega_{\rm LC} = (2\pi)\cdot 7\text{GHz}, s_{\rm OM} = s_{\rm EM} = 0.3, \Delta = -\Omega_{\rm m} = \omega_{\rm d} - \omega_{\rm LC}.\end{gathered} \tag{5.76}$$

We do so for different system temperatures and the results are plotted in Fig. 5.7 with select values given in Table 5.3 specifying the noise contributions of the individual subsystems.

From the plot in Fig. 5.7 we see that mechanical noise dominates for temperatures $T \gtrsim 0.7$K, whereas for smaller temperatures the optical noise contribution dominates, which is mainly due to the imperfect optical coupling efficiency $\eta_{\rm opt} = 0.23$. Note that since $N^{(\rm h)}_{\rm opt,0} \geq 1/2$ for the chosen heterodyning scheme where two quadratures are measured simultaneously, the fundamental limit for P_0 is unity. It should be remarked that for system temperatures where the electrical system is near its ground state, it is at least in principle possible to perform all-electrical quantum-limited heterodyne detection.

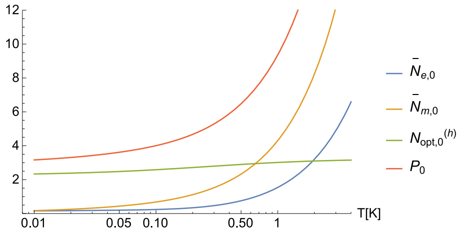

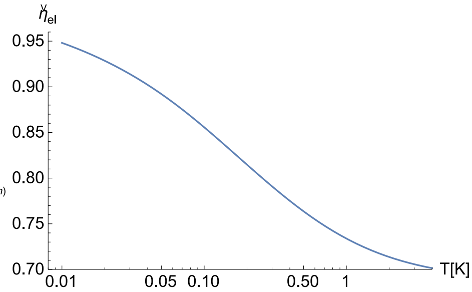

Figure 5.7: (left) Minimized (peak) heterodyne noise, $\check{P}_0$, in terms of its ohmic $\bar{N}_{\mathrm{e},0}$, mechanical $\bar{N}_{\mathrm{m},0}$ and optical $N^{(\mathrm{h})}_{\mathrm{opt},0}$ contributions. (right) The required value for the electrical coupling efficiency, $\check{\eta}_{\mathrm{el}}$.

Temp./Noise source	ohmic	mech.	opt.	total
$T = 300\mathrm{K}$ [$\check{\eta}_{\mathrm{el}} = 0.69$]	$T_{\mathrm{e},0} \sim 172\mathrm{K}$	$T_{\mathrm{m},0} \sim 394\mathrm{K}$	$T^{(\mathrm{h})}_{\mathrm{opt},0} \sim 1\mathrm{K}$	$\check{T}_0 \sim 568\mathrm{K}$
$T = 4\mathrm{K}$ [$\check{\eta}_{\mathrm{el}} = 0.70$]	$\bar{N}_{\mathrm{e},0} \sim 6.6$	$\bar{N}_{\mathrm{m},0} \sim 16.0$	$N^{(\mathrm{h})}_{\mathrm{opt},0} \sim 3.2$	$\check{P}_0 \sim 26.3$
$T = 40\mathrm{mK}$ [$\check{\eta}_{\mathrm{el}} = 0.90$]	$\bar{N}_{\mathrm{e},0} \sim 0.2$	$\bar{N}_{\mathrm{m},0} \sim 0.4$	$N^{(\mathrm{h})}_{\mathrm{opt},0} \sim 2.5$	$\check{P}_0 \sim 3.5$

Table 5.3: Transducer added noise contributions in MW-to-optical homodyning using parameters (5.76) similar to those of Ref. [6], assuming them to be temperature-independent (not necessarily true in practice). The total includes the vacuum fluctuations of the input field. The room-temperature values are stated as temperatures using Eq. (5.47).

5.8.2 Coherent state transfer

A task relevant for continuous-variable quantum information processing is the deterministic transduction of a coherent state. To get a sense of the feasibility of implementing such conversion with an electro-optomechanical transducer, we will now evaluate the unconditional fidelity F_{uc} given in Eq. (3.17), valid for a narrowband input signal. For $\eta_0^{(+)} \neq 1$, F_{uc} depends on the amplitude $|\alpha|$ of the state to be transduced. We choose to consider parameters such that the imperfect coupling efficiency $\eta_{\mathrm{el}}\eta_{\mathrm{opt}} < 1$ is countered by amplification effects, due to the circuit and cavity modes not being fully sideband resolved, with the result that $\eta_0^{(+)} = 1$ according to Eq. (5.27). Under these circumstances, the expression for the fidelity becomes independent of $|\alpha|$ and reduces to

$$F_{\mathrm{uc}}\big|_{\eta_0^{(+)}=1} = \frac{1}{1 + N_0^{(+)}}, \tag{5.77}$$

where $N_0^{(+)}$ will include an amplification noise penalty. Using Eq. (5.31) for $N_0^{(+)}$, we plot F_{uc} and $N_0^{(+)}$ in Fig. 5.8 as a function of the transducer temperature T (assumed to be the same for all subsystems) for the parameter set

$$\begin{aligned} &\mathcal{C}_{\mathrm{OM}} = \mathcal{C}_{\mathrm{EM}} = 5000, \eta_{\mathrm{opt}} = \eta_{\mathrm{el}} = 0.9, \Omega_{\mathrm{m}} = (2\pi)\cdot 1.24\mathrm{MHz}, \\ &\omega_{\mathrm{LC}} = (2\pi)\cdot 7\mathrm{GHz}, s_{\mathrm{OM}} = s_{\mathrm{EM}} = 0.34, \Delta = -\Omega_{\mathrm{m}} = \omega_{\mathrm{d}} - \omega_{\mathrm{LC}}. \end{aligned} \tag{5.78}$$

The plot shows that the fidelity saturates at $F_{\mathrm{uc}} \sim 0.8$ for $T \lesssim 10\mathrm{mK}$ when the mechanical noise contribution drops below the amplification noise floor. Note

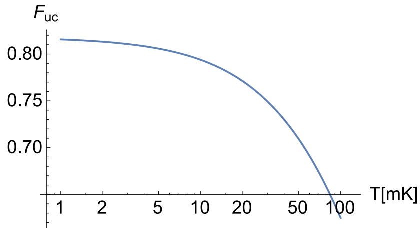

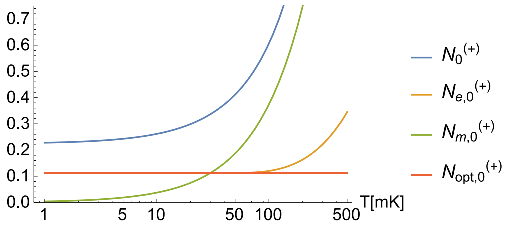

Figure 5.8: (left) Unconditional coherent state transfer fidelity F_{uc}, Eq. (5.77), as a function of temperature for the parameter set (5.78). (right) Noise contributions to $N_0^{(+)}$ from the various subsystems of the transducer.

from Fig. 5.8b that both the circuit and the optical cavity modes are in the ground-state for $T \lesssim 100$mK, meaning that the amplification noise that determines the asymptote $F_{\text{uc}} \sim 0.8$ is squeezed vacuum. To improve the performance the sideband resolution could be increased. In the fully sideband-resolved, high-cooperativity limit we see from (3.17) that

$$F_{\text{uc}} \to \exp\left[-|\alpha|^2(1-\sqrt{\eta_{\text{opt}}\eta_{\text{el}}})^2\right], \tag{5.79}$$

provided that the electrical system is in its ground state. For a coherent state with $|\alpha| \approx 1$ and a transducer with combined coupling efficiency $\eta_{\text{opt}}\eta_{\text{el}} = (0.9)^2$, as in (5.78), the limiting expression (5.79) yields a fidelity of $F_{\text{uc}} \sim 0.99$.

5.9 Conclusion and outlook for Part I

In this chapter we applied the equivalent circuit formalism for electro-optomechanical transducers to analyze receiver circuits. The formalism provides a straightforward way to extract the effective quantities that govern the dynamics of the hybrid system in a way that makes clear the influence of the electrical circuit design on the performance. We optimized the receiver circuits for optomechanical detection of electrical signals in both the high-temperature and quantum regimes. The resulting expressions for the achievable performance describes how the various noise sources should be balanced under various circumstances and constraints. These results can serve as a starting point to identify real-world applications in which such optomechanical sensing is advantageous, e.g., potentially in radio-astronomy or nuclear magnetic resonance imaging (as mentioned previously).

Part I of this thesis has addressed several important matters of relevance to current research in transduction, as we will now briefly summarize. We have discussed the characterization of transducers in terms of their signal transfer efficiency η and added noise N and related these quantities to figures of merit for applications of interest. Hereby we have established the requirements for a transducer to perform efficiently in various contexts, which is important for guiding experimental efforts. We also introduced an equivalent circuit formalism for electro-optomechanical transducers which could be crucial in realizing the potential of optomechanical sensing and conversion in the realm of electronics, both as a design tool and as a common language enabling cross-disciplinary collaborations. We also presented a thorough analysis of capacitive electromechanical interfaces along with an analytical method for predicting their coupling properties.

Part II

Dissipative Rydberg-EIT physics

Chapter 6

Quantum hard-sphere model for dissipative Rydberg-EIT media

The work presented in this chapter has been carried out in collaboration with Michael J. Gullans, Mohammad F. Maghrebi, and Alexey V. Gorshkov at JQI/QuICS/NIST, University of Maryland.

6.1 Introduction

The interaction between photons is under most circumstances completely negligible at the quantum level. In optically dense atomic media, however, strong non-linear inter-photon interactions at the single-quantum level can be engineered via the interactions of Rydberg-polaritons propagating due to Electromagnetically Induced Transparency (EIT) [61]. Such photon-photon interactions are highly desirable from the point of view of quantum information processing as they can be used to implement quantum gates between a pair of photons ("flying" qubits) or between a photon and a stored spin-wave in the atomic medium [62]. The strong photon-photon interaction can also be engineered to dynamically generate non-classical states of light [2]. The Rydberg-EIT technique accommodates the engineering of a rich variety of physical effects including both dissipative and dispersive Rydberg-Rydberg interactions, the former resulting in the scattering of photons out of the propagating mode [2], while the latter gives rise to both attractive and repulsive inter-photon potentials allowing the formation of many-body bound states [63].

The present work proposes a model for the many-body physics of the dissipative blockade in Rydberg-EIT media. Since general analytical solutions to this problem are unavailable, such an ansatz is valuable if it can shed light on the structure of these solutions.

The remainder of this introductory section will provide the background and foundation for this work. We start by discussing the mechanism that allows photons to interact via Rydberg-Rydberg interactions in Subsection 6.1.1. Subsequently, we will review important experimental realizations of the dissipative

Rydberg blockade in Subsection 6.1.2, as well as theoretical progress towards understanding the many-body physics of such systems in Subsection 6.1.3. Finally, an overview of the work presented in the remainder of this chapter is given in Subsection 6.1.4.

6.1.1 Rydberg-EIT physics

The Rydberg-EIT media we will consider here are optically dense ensembles of cold atoms for which the effective 3-level structure shown in Fig. 6.1a is applicable. It is comprised of a stable ground state $|g\rangle$, an excited state $|e\rangle$ with decay rate Γ and a meta-stable high-lying Rydberg state $|r\rangle$. When no excitations are present in the medium, an impinging photon resonant with the $|g\rangle \leftrightarrow |e\rangle$ transition (frequency ω_{ge}) will encounter the 'vacant' level diagram depicted in the figure. Here a control field of Rabi frequency Ω is resonant with the $|e\rangle \leftrightarrow |r\rangle$ transition (frequency ω_{er}) leading to transmission of the impinging photon due to electromagnetically induced transparency (EIT) [64], thus circumventing the decay channel of the excited state $|e\rangle$. This is reflected by the on-resonant dip in the absorption curve (solid plot in Fig. 6.1c). The accompanying positive slope in the dispersion curve near resonance (solid plot in Fig. 6.1d) leads to a reduction of the group velocity $v_{\mathrm{g}} \ll c$ in the medium and hence spatial compression of the incoming pulse by a factor of v_g/c (c being the speed of light in free space). The excitations propagating through the medium under these conditions are referred to as (slow-light) polaritons since they are coherent combinations of atomic and photonic excitation.

What we have described above is the standard EIT transmission experienced by the first photon entering the medium. However, once a polariton has been formed near the entrance, this excitation involving the Rydberg state $|r\rangle$ will impose a van der Waals interaction $V(r)$ on neighboring atoms [65]. This entails a shift in the transition frequency ω_{er} as shown in the 'blocked' level diagram of Fig. 6.1a, whereby the control field ceases to be resonant with that transition. This will affect subsequent incoming photon arriving in a region of 'blocked' atoms as these photons will experience an ensemble of two-level scatterers with decay rate Γ corresponding to the dashed curves in Fig. 6.1c&d. The size of the region blocked by a Rydberg excitation follows from the sharp van der Waals potential $V(r) = \hbar C_6/r^6$ with strength parameter C_6 and the single-atom EIT linewidth $\gamma_{\mathrm{EIT}} \equiv \Omega^2/\Gamma$, leading to the definition of the *blockade radius* r_{b} (see, e.g., [62, 66]),

$$V(r_{\mathrm{b}}) = \frac{\hbar\gamma_{\mathrm{EIT}}}{2} \Rightarrow r_{\mathrm{b}} = \left(\frac{2C_6}{\gamma_{\mathrm{EIT}}}\right)^{1/6}. \tag{6.1}$$

If the optical depth per blockade radius is large, $d_{\mathrm{b}} \gg 1$, then a photon arriving at a blocked medium will scatter in the course of its propagation through the blockaded region (the optical depth d_{b} is defined via the on-resonant 2-level attenuation $\propto e^{-d_{\mathrm{b}}}$ over a blockade radius). Hence, in the $d_{\mathrm{b}} \gg 1$ regime, the blockade precludes polaritons from coexisting in the medium at separations less than r_{b}.

Let us now envision the dynamics that would arise from the simple physical picture given above. Assuming the waist of the probe beam to be small compared to the blockade radius, we consider the one-dimensional scenario sketched in Fig. 6.1b of a bright light pulse impinging on the medium from the left. Those

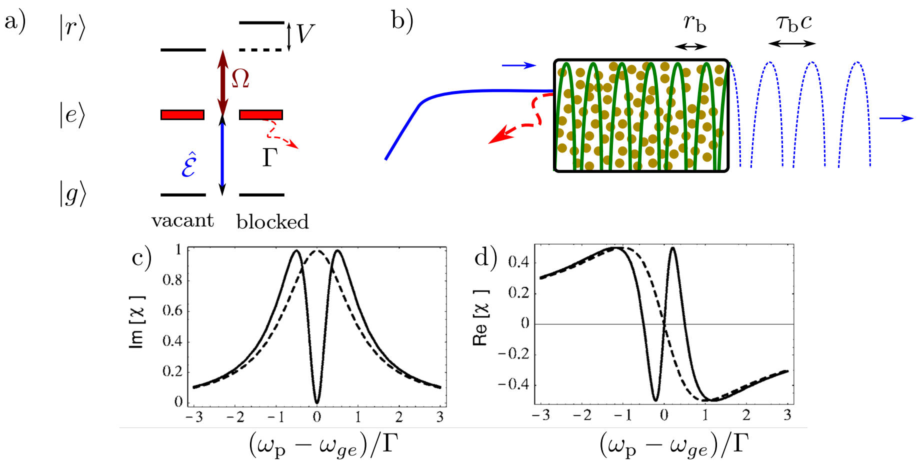

Figure 6.1: a) Atomic level diagram: Ground and Rydberg levels, $|g\rangle$ and $|r\rangle$, are long-lived compared to the lossy excited level $|e\rangle$, which has decay rate Γ. Outside the blockade radius of Rydberg polaritons, an incoming photon in the probe field $\hat{\mathcal{E}}$ enjoys EIT transmission ('vacant' set of energy levels). For atoms within the blockade region of a polariton, the Rydberg level $|r\rangle$ is shifted out of resonance with respect to the classical drive Ω causing an incoming photon encounter the 'blocked' levels and thus to scatter out of the excited state $|e\rangle$. b) A bright single-mode light pulse impinges on a Rydberg medium producing a train of propagating Rydberg polaritons (green peaks), separated by their blockade radius r_b, by scattering "superfluous" photons at the entrance (red dashed arrow) out of the forward-propagating mode. In turn, the polariton train emanates on the opposite end of the medium as a train of single photons spaced by the decompressed blockade radius $\tau_b c = r_b c/v_g$ (where v_g is the polariton group velocity in the medium). c&d) Absorption and dispersion curves for vacant (solid curve) and blockaded (dashed curve) media. They are plotted as a function of probe detuning from the transition frequency ω_{ge} between $|g\rangle$ and $|e\rangle$ in units of the linewidth Γ of $|e\rangle$. (Subfigures c&d are reproduced from Ref. [64]).

photons that successfully form polaritons upon entrance will propagate through the medium and emanate as an outgoing light field on the right. Due to the dissipative Rydberg blockade, photons entering the medium within a blockade radius of a polariton will not themselves form polaritons but instead scatter out of the forward-propagating mode due to the absence of EIT. Once formed, a polariton will block the entrance of the medium by its blockade radius for the duration of the *blockade time*,

$$\tau_{\mathrm{b}} = r_{\mathrm{b}}/v_{\mathrm{g}}. \tag{6.2}$$

Therefore, based on this simple picture we expect the outgoing light field to show anti-bunching with time-scale τ_{b} and, given sufficiently bright input, to form a pulse train of single photons as illustrated in Fig. 6.1b. While simple and appealing, we will see in the next section that the physical picture presented here is not fully sufficient to accurately describe experimental realizations of the system.

6.1.2 Experimental review

Here we will briefly review two key experiments studying the dissipative Rydberg blockade in cold atomic ensembles. One of the first realizations of effective photon-photon interactions using the technique of Rydberg-EIT was reported in Ref. [67]. In this study, the on-resonant transmission was observed to decrease with increasing probe intensity, a signature of the Rydberg blockade. A subsequent experimental study was performed using denser atomic media with optical depths per blockade radius $d_{\mathrm{b}} \gtrsim 1$ [66], thus approaching the $d_{\mathrm{b}} \gg 1$ regime discussed in Section 6.1.1. This study offers a more extensive characterization of resonant Rydberg-EIT media: In addition to observing saturation in the outgoing photon rates for high probe intensities, measurements of $g^{(2)}(\tau)$ were performed exhibiting anti-bunching of the optical output. While such anti-bunching is indeed a signature of the Rydberg blockade, the observed size of this feature significantly exceeded the blockade time τ_{b}, 6.2, counter to the naive expectation based on the discussion of Subsection 6.1.1. This discrepancy was attributed to the circumstance that the spectral features of width $\sim 1/\tau_{\mathrm{b}}$ generated by the Rydberg blockade exceeded the bandwidth of the EIT transmission window $B = \gamma_{\mathrm{EIT}}/\sqrt{8d}$; here d is the optical depth corresponding to the full length of the medium, $d = (L/r_{\mathrm{b}})d_{\mathrm{b}}$. As a consequence, the polaritons propagating through the medium experienced significant EIT filtering and dispersion, with the result of washing out the relatively sharp features created by the blockade. One of the main lessons of Ref. [66] is that these additional EIT effects are important in setting the limits of control for Rydberg-EIT media, as they will be detrimental to most applications.

6.1.3 Review of theoretical work

Several theoretical approaches to analyzing the dissipative Rydberg blockade can be found in the literature. A semi-classical theory has been derived in the limit of low probe intensity compared to the control field [68]. Within the regime of validity, its predictions agree with the transmission data of the experiment reported in Ref. [67] and mentioned above. Predictions agreeing

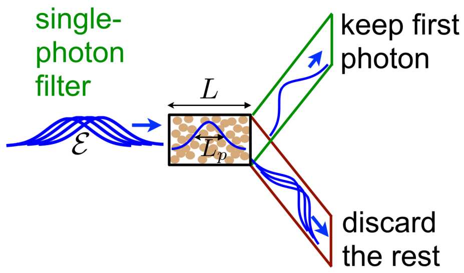

Figure 6.2: Dissipative Rydberg-EIT medium of length L acting as a single-photon filter on the probe pulse $\mathcal{E}$ of compressed length L_p. Only the photon arriving first propagates through the medium under EIT conditions, whereas the remaining photons scatter to the environment. (Adapted from Ref. [2])

with this data have also been obtained using a quantum theory that models the atomic ensemble as a collection of super atoms with radius r_b [69]. Also accounting for the quantum nature of light, Ref. [62] analyses the case of two strongly interacting photons. By deriving approximate analytical solutions to the Heisenberg-Langevin equations and verifying by full numerical simulations, it is demonstrated that dissipative Rydberg-EIT media subject to copropagating input photons will produce an output field exhibiting the avoided volume associated with blockade. The analysis was extended in Ref. [2] to include arbitrary multi-photon input states, providing an analytical approach to analyzing the quantum many-body regime.

Since the theory developed in Ref. [2] will serve as one the main foundations for the present work, we will now review it in some detail. The analysis considers a scenario similar to that in Fig. 6.1b, but assumes that the EIT-compressed input pulse (of length L_p) fits within a blockade radius r_b and the length of the medium L, i.e. $L_\mathrm{p} < r_\mathrm{b}, L$. In the limit of large optical depth per blockade radius, $d_\mathrm{b} \gg 1$, this causes the medium to act as a single-photon filter as illustrated in Fig. 6.2. In this limit, the single-polariton EIT transmission becomes ideal, i.e. we may ignore the decay and dispersion effects due to the polariton not fitting within the EIT window that were observed in the finite-d_b experiment of [66]. This permits a derivation of the wave function $|\psi_{\{\tau_2,\ldots,\tau_n\}}(t)\rangle$ for the polariton remaining after the entire pulse has entered the medium given knowledge of the scattering times $\{\tau_2, \ldots, \tau_n\}$ of the other photons. For an input pulse $h(t)$ in the Fock state $|n\rangle$, we will have $n-1$ (time-ordered) scattering events $\{\tau_2, \ldots, \tau_n\}$ occurring; the resulting (unnormalized) polariton wave function is [2],

$$|\psi_{\{\tau_2,\ldots,\tau_n\}}(t)\rangle = |\psi_{\tau_2}(t)\rangle = -\sqrt{v_\mathrm{g}} \int_{-\infty}^{\tau_2} dt_1 h(t_1) \hat{S}^\dagger \left(v_\mathrm{g}(t-t_1)\right) |0\rangle \tag{6.3}$$

in terms of the slowly-varying operator $\hat{S}^\dagger(z) \sim |r\rangle\langle g|$ creating a Rydberg excitation in the ensemble at position z [70] ($|0\rangle$ denotes the vacuum of the medium). Eq. (6.3) shows that the wave function only depends on the timing of the first scattering event (occurring at τ_2). Moreover, it has the straightforward interpretation of the first scattering event projecting the polariton into the medium, as it must have formed prior to τ_2, and that its wave function is given by the leading part of the pulse $h(t)$ that entered the medium before $t = \tau_2$. Hence, we draw two important conclusions about the dissipative Rydberg blockade in the limit $d_b \gg 1$: Firstly, the first photon to enter a vacant medium survives the blockade interaction with subsequent photons. Secondly, the scattering events amount to projective measurements on the polariton wave function. The later scattering events $\{\tau_3, \ldots, \tau_n\}$ do not enter Eq. (6.3) because they correspond to trivial projections, i.e. they carry no additional information about the polariton; this follows from the assumption that $L_p < r_b$ and hence the polariton could not have vacated the entrance of the medium. An implicit simplifying assumption here is that scattering events occur immediately upon entering the blockaded region, otherwise the non-zero propagation distance of the scattered photon would contain additional information about the distance to the blockading polariton leading to corrections to Eq. (6.3).

Under usual experimental circumstances, the scattered photons are difficult to detect, prompting us to trace out these degrees of freedom in the mathematical description. This amounts to constructing a density matrix $\hat{\rho}(t)$ from the wave functions (6.3) weighted by the probability density for the various scattering histories $\{\tau_2, \ldots, \tau_n\}$. By considering the retrieval of the spin-wave described by $\hat{\rho}(t)$ the effect of the finite EIT window for finite d_b was estimated, leading to the experimentally demanding criterion of $d_b \gtrsim 10^4$ for the success probability of generating a single photon from a coherent input state to exceed $\eta > 0.9$ [2]. This underscores the lesson from the experiment of Ref. [66] that the finite EIT window will play a significant role in most, if not all, realizations of the dissipative blockade in atomic ensembles.

6.1.4 Overview of chapter

In the remainder of this chapter we will construct and explore a model for the dissipative Rydberg blockade building on the approach of Ref. [2] reviewed above. Motivated by the experiment of Ref. [66], our model extends this work in two respects: Firstly, by dispensing with the constraint of the input pulse fitting into a blockade radius, $L_p < r_b$, we are allowed to consider continuous wave (CW) operation. Secondly, we incorporate the fact that single-polariton EIT decay releases the blockade, thereby allowing for the formation of a new polariton.

The model will be constructed in Section 6.2 based on the intuition harvested from previous work. We will subsequently test the resulting hypothesis by comparing its predictions to numerical simulations and experimental data to the extent available. To this end, we analyze in Section 6.3 the saturation behavior of the transmission through one-dimensional Rydberg-EIT media in the regime of non-perturbative single-polariton EIT-decay relevant to present-day experiments. The predictions of the theory are compared to the experimental data of Ref. [66] and numerical simulations of the full equations of motion. Next, in Section 6.4, we analyze a scheme for generating regular trains of single photons from CW input and derive its scaling behavior in the limit of perturbative single-polariton EIT-decay. Finally, we conclude and consider future directions in Section 6.6.

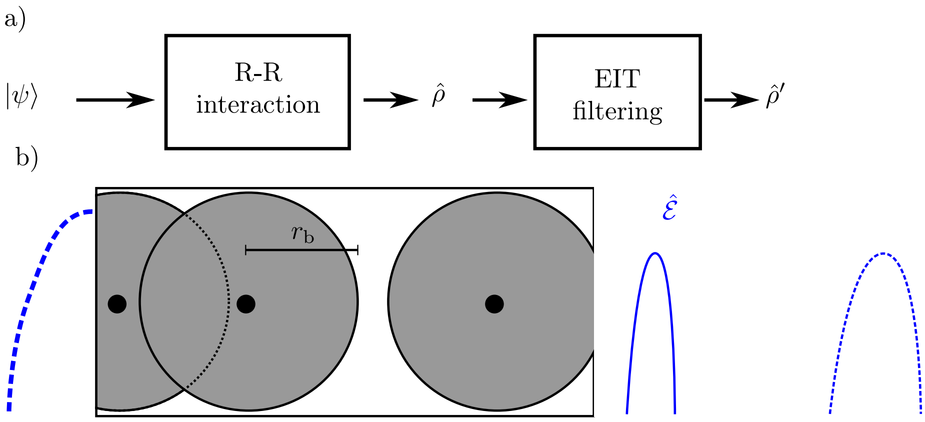

Figure 6.3: a) Serialization approximation of EIT filtering. The single-mode input state $|\psi\rangle$ is mapped into $\hat{\rho}$ according to the hard-sphere ansatz for the Rydberg-Rydberg (R-R) interaction. Subsequently, $\hat{\rho}$ is subjected to EIT filtering as it would occur in a linear EIT medium, producing the final density matrix $\hat{\rho}'$. In the exact evolution, to which $\hat{\rho}'$ is an approximation, these effects occur in a complex intermingled fashion. b) Localized polaritons in the "hard-sphere" model: Each Rydberg polariton (black dots) has a spherical blockade region (grey sphere) of radius r_b in which the formation of new polaritons is prohibited; however, blockade regions can overlap without entailing Rydberg-Rydberg scattering.

6.2 Quantum hard-sphere model for the dissipative blockade

In this section we propose a model for the dissipative Rydberg-Rydberg blockade in the 1-dimensional regime (see Figs. 6.1b and 6.2) and working in the limit of large optical depth per blockade radius, $d_b \gg 1$. The model involves two ingredients: Firstly, a hard-sphere ansatz for the Rydberg-Rydberg interaction and, secondly, accounting for the finite width of the EIT window by considering the linear EIT physics of individual polaritons. The idea is to separate the single-polariton EIT physics from the Rydberg-Rydberg interactions in a serialized manner as illustrated in Fig. 6.3a. This is based on the intuition that the sharp temporal features, leading to single-polariton EIT decay, are defined by the Rydberg-Rydberg interaction near the entrance of the medium, as we will discuss shortly.

6.2.1 Hard-sphere Rydberg-Rydberg interaction

We start by considering the limit of perfect single-polariton EIT, $d_b \ggg 1$, which allows us to discuss the hard-sphere interaction independently. The model we propose here for the Rydberg-Rydberg interaction is to approximate the blockade region of a polariton by a sharply defined sphere of radius r_b inside of which impinging photons will immediately scatter, whereas right outside the region the Rydberg-Rydberg interaction energy drops abruptly to zero as for a hard-sphere potential, see Fig. 6.3b. Note, as indicated in the figure, that this

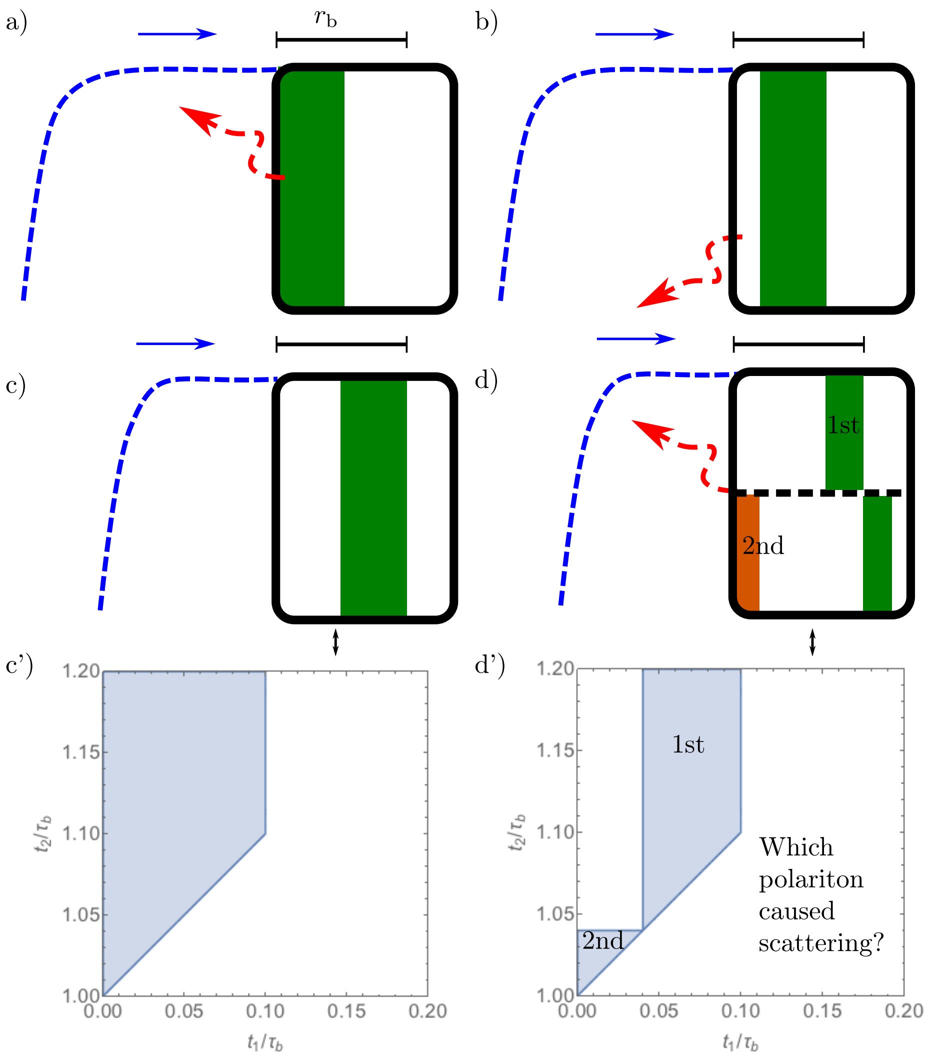

Figure 6.4: Formation of the polariton wave function by sequential projections of an incoming square pulse according to the hard-sphere model in the limit of perfect single-polariton EIT. a) An incoming probe photon is scattered (red dashed arrow) near the beginning of the medium thereby projecting a polariton in the medium. b) The polariton propagates further into the medium and at a subsequent time a second probe photon scatters, but since (in this instance) the polariton could not have left the first r_b of the medium, no additional projection of the polariton wave function ensues. c) The polariton is now about to leave the first blockade radius of the medium, prompting us to consider possible formation times t_2 of the second polariton as described by the two-photon wave function c'), assuming the pulse to arrive at $t = 0$. d) The first and second polaritons straddle the rear and front boundaries of the first blockade radius as a scattering event occurs; this causes a projection c') $\rightarrow$ d') on the two-body wave function producing a superposition state of the first and second polariton being the scatterer.

does not prevent the blockade spheres from overlapping insofar as the center of one sphere does not lie within another sphere. This figure is too simple, however, because these spheres are non-classical in the sense that their exact (center) positions are not fully determined, i.e. they are in a quantum superposition of being in different locations according to some wave function.

Within the hard-sphere model, the action of the Rydberg medium on pulsed input can be understood as described in the following, where, for sake of argument, we assume that we detect the scattering events. Consider Fig. 6.4: Photons enter the medium according to some temporal input mode $h(t)$ in a quantum state $|\psi_{\mathrm{in}}\rangle$; if a photon successfully enters the medium it creates a polariton excitation that propagates without loss at speed v_{g}. If another photon attempts to enter less than a time $\tau_{\mathrm{b}} = r_{\mathrm{b}}/v_{\mathrm{g}}$ after the polariton was created, the photon that attempts to enter will scatter into a mode of the environment. In terms of the time τ at which this scattering event took place, the environment effectively projects the wave function of the Rydberg excitation to be localized within the arrival time interval $[\tau - \tau_{\mathrm{b}}, \tau]$ (see Fig. 6.4a). As long as the polariton is within the first blockade radius of the entrance, subsequent scattering events will not localize the polariton further (see Fig. 6.4b). Once the polariton has propagated a distance r_{b} into the medium it can no longer cause scattering of incoming photons and a new polariton may be formed at the entrance of the medium. Within the validity of the hard-sphere model, scattering photons are ignorant as to the precise distance to the scatterer, since the scattering event constitutes a projective, binary distance measurement. As a consequence, when a polariton (whose temporal extent was defined near the entrance) straddles the rear of the first blockade radius of the medium, then a scattering event cannot distinguish whether the scattering was caused by this distant polariton, or whether the distant polariton had already left and the scattering was instead caused by a newly formed polariton near the entrance (see Fig. 6.4d). The resulting projection caused by the scattering hence acts simultaneously on the two polaritons leading to spatial entanglement.

When a polariton reaches the rear of the medium, it will map back onto an outgoing optical field. Ignoring dispersion, the output light signal is simply related to the polariton wave function by spatial decompression by a factor of c/v_{g}. For this reason, we may conveniently use the basis of definite time-ordered polariton formation times to specify the state of the output light field:

$$|\vec{t}_R\rangle \equiv |t_1, \ldots, t_R\rangle \equiv \hat{\mathcal{E}}^\dagger(t_1) \cdots \hat{\mathcal{E}}^\dagger(t_R)|0\rangle, \tag{6.4}$$

where $\hat{\mathcal{E}}^\dagger(t)$ is the outfield field creation operator, $|0\rangle$ is the vacuum and $t_1 \leq \ldots \leq t_R$ due to the assumed time ordering (subscript R in $\vec{t}_R$ indicates the dimension of the vector). According to the analogue situation of macroscopic objects with a large degree of interaction with the environment, it makes sense to think of the localized states (6.4) as forming a "classical basis". The wave nature of the polariton resides in coherences between these states, and it is this we must refer to in determining the EIT propagation of the polariton.

Note that the counting statistics that result from the hard-sphere model (assuming perfect single-polariton EIT) also appear in the subject of dead-time-distorted photo-detection [71]. For given input, a non-paralyzable photodetector with dead time τ_{b} produces the same counting statistics as the hard-sphere blockade with blockade time τ_{b} (measuring its output using an ideal photodetector). (Non-paralyzable means that photons arriving during dead time do not extend the current dead period.)

6.2.2 Single-polariton EIT decay

We will now consider how single-polariton EIT decay modifies the above picture. In the limit of many input photons per blockade time τ_b it seems reasonable to assume that the first projection of a given polariton occurs when its wave packet is localized in the vicinity of the entrance of the medium. During the subsequent propagation within the first blockade radius no additional projections occur (Fig. 6.4b) as discussed above and hence it is reasonable to assume that the effect of EIT decay during this interval is equivalent to linear EIT filtering. Should such a polariton decay event occur within the first blockade radius of the medium, it would immediately allow for a new polariton to be formed at the entrance. An implementation of these ideas will be considered in Section 6.3 below. In the limit of perturbative polariton EIT decay, we may take a simpler approach akin to that of Ref. [2] by considering the density matrix $\hat{\rho}$ predicted by the hard-sphere theory in the limit of perfect single-polariton EIT. Applying linear EIT filtering to $\hat{\rho}$ or its correlation functions then yields an estimate of the EIT transmission. This approach will also be applied in the course of the analysis. Note that we will not consider the effect of EIT dispersion.

In summary, the "quantum hard-sphere" model presented above captures the dualistic nature of light as it manifests itself in the Rydberg-EIT medium: In the atomically mediated photon-photon interaction light appears corpuscular due to the sharp $1/r^6$ interaction potential prohibiting polaritons to co-exist within a blockade radius of one another; meanwhile, the EIT-facilitated propagation of light through the medium can only be properly accounted for in reference to the wave nature of light. In this approach, photons that successfully enter the medium can be thought of as propagating blockade spheres, of radius equal to the Rydberg blockade radius r_b, whose centers are only localized to within a certain wave packet. The photonic wave packet of the quantum signal emanating from the ensemble will be determined by the projective measurements on the many-body state performed by the environment modes, taken to be all other modes than that of the forward-propagating signal.

6.3 Transmission behavior

We will now apply the approach described in Section 6.2 to analyze various scenarios involving dissipative Rydberg-EIT media in the 1-dimensional limit, where the transverse spot size of the impinging light fields is small compared to the blockade radius. As our first application, we will consider the transmission behavior for a medium subject to continuous-wave (CW) probe and control fields as a function of the input rate $\mathcal{R}_{\text{in}}$ of the probe.

6.3.1 Perfect single-polariton EIT

As a preliminary, let us first derive the output rate in absence of single-polariton EIT decay, i.e. only considering the R-R interaction (see Fig. 6.3a). The input flux $\mathcal{R}_{\text{in}}$ splits into two fractions, the part of the flux that makes it through the medium $\mathcal{R}_{\rm out}$ and a rate of Rydberg-Rydberg scattered photons, $\mathcal{R}_{\rm out}\tau_{\rm b}\mathcal{R}_{\rm in}$:[1]

$$\mathcal{R}_{\rm in} = \mathcal{R}_{\rm out} + \mathcal{R}_{\rm out}\tau_{\rm b}\mathcal{R}_{\rm in}; \tag{6.5}$$

$\tau_{\rm b}\mathcal{R}_{\rm in}$ is simply the average number of photons scattered by each Rydberg polariton, while $\mathcal{R}_{\rm out}$ is the rate of periods where the medium is blockaded. From Eq. (6.5) we find the desired result

$$\mathcal{R}_{\rm out} = \frac{1}{\tau_{\rm b} + (1/\mathcal{R}_{\rm in})}. \tag{6.6}$$

We see that the output rate is upper-bounded by the inverse blockade time as expected, $\mathcal{R}_{\rm out} \leq (1/\tau_{\rm b})$; the average temporal separation between input photons $1/\mathcal{R}_{\rm in}$ combines with $\tau_{\rm b}$ to determine (6.6).

6.3.2 Imperfect single-polariton EIT

We now turn to the more realistic case of imperfect single-polariton EIT, in which we must account for the finite transmission of polaritons that do not fit within the EIT window. If a polariton is EIT-scattered within the first blockade radius $r_{\rm b}$ of the medium its blockade ceases, hence allowing for the creation of a new polariton at the input of the medium. Therefore the average blockade time (during which Rydberg-Rydberg scattering occurs) per polariton $\bar{\tau}_{\rm b}$ is upper bounded by that of a polariton that makes it through the first $r_{\rm b}$ of the medium, $\bar{\tau}_{\rm b} \leq \tau_{\rm b}$. Introducing the average single-polariton EIT transmission $\bar{\eta}_{\rm EIT}[L]$ through a medium of length $L \geq r_{\rm b}$ and (for didactical reasons) the average Rydberg formation rate $\mathcal{R}_{\rm Rf}$, we again decompose the input rate in the spirit of Eq. (6.5),

$$\mathcal{R}_{\rm in} = \bar{\eta}_{\rm EIT}[L]\mathcal{R}_{\rm Rf} + (1-\bar{\eta}_{\rm EIT}[L])\mathcal{R}_{\rm Rf} + \mathcal{R}_{\rm Rf}\bar{\tau}_{\rm b}\mathcal{R}_{\rm in}, \tag{6.7}$$

where on the right-hand side the first term is the output rate,

$$\mathcal{R}_{\rm out} \equiv \bar{\eta}_{\rm EIT}[L]\mathcal{R}_{\rm Rf}, \tag{6.8}$$

the second term of (6.7) is the rate of polariton EIT decay, and the third term is the rate of Rydberg-Rydberg scattering events. We can decompose the average blockade time $\bar{\tau}_{\rm b}$ into contributions from polaritons that make it through the first $r_{\rm b}$ of the medium and those that do not

$$\bar{\tau}_{\rm b} = \bar{\eta}_{\rm EIT}[r_{\rm b}]\tau_{\rm b} + \bar{\tau}'_{\rm b}, \tag{6.9}$$

where $\bar{\tau}'_{\rm b}$ is the contribution from those polaritons that EIT-decay within the first blockade radius of the medium. Substituting Eqs. (6.8,6.9) into (6.7) and solving for the output rate, we find

$$\mathcal{R}_{\rm out} = \frac{\bar{\eta}_{\rm EIT}[L]/\bar{\eta}_{\rm EIT}[r_{\rm b}]}{\tau_{\rm b} + \frac{1}{\bar{\eta}_{\rm EIT}[r_{\rm b}]}\left[\frac{1}{\mathcal{R}_{\rm in}} + \bar{\tau}'_{\rm b}\right]}, \tag{6.10}$$

which, for finite EIT transmission $\bar{\eta}_{\rm EIT} < 1$, is less than the rate (6.6) for perfect single-polariton EIT. Eq. (6.10) shows that the part of the medium

[1] We neglect finite-pulse corrections that arise from the initial condition of the medium and a finite averaging time.

beyond the first blockade radius simply contributes a trivial damping factor in the numerator, whereas the denominator reflects only the dynamics of the first blockade radius.

To evaluate (6.10) we must estimate the functions $\bar{\eta}_{\rm EIT}[l]$ and $\bar{\tau}'_{\rm b}$ in terms of known quantities. Applying the serialization approach of Fig. 6.3a and the intuition of Fig. 6.3c&d, we take the temporal extent τ of a polariton to be defined by the first R-R event after its formation and denote its EIT transmission probability through a length l of the medium by $\eta_{\rm EIT}(\tau, l)$. (This assumption ignores the additional projections that can occur as the polariton leaves the first blockade radius of the medium; these projections will lessen the probability that the polariton makes it through the remaining part of the medium.) Averaging over the CW/Poisson distribution for τ this leads to,

$$\bar{\eta}_{\rm EIT}[l] = \langle \eta_{\rm EIT}(\tau, l)\rangle_\tau = \int_0^\infty d\tau \mathcal{R}_{\rm in}(\mathcal{R}_{\rm in}\tau)e^{-\mathcal{R}_{\rm in}\tau}\eta_{\rm EIT}(\tau, l). \tag{6.11}$$

We estimate $\bar{\tau}'_{\rm b}$ in a similar manner as

$$\bar{\tau}'_{\rm b} = \langle \int_0^{r_{\rm b}} dl(l/v_{\rm g})\,[-d\eta_{\rm EIT}(\tau, l)/dl]\rangle_\tau. \tag{6.12}$$

Approximating $\eta_{\rm EIT}(\tau, l)$ by the EIT transmission of a square pulse subjected to Gaussian filtering (see Appendix D.1), Eqs. (6.11,6.12) combined with (6.10) yields the following expression for the output rate,

$$\tilde{\mathcal{R}}_{\rm out} = \frac{\exp\left(4\frac{L}{r_{\rm b}}\frac{\tilde{\mathcal{R}}_{\rm in}^2}{d_{\rm b}}\right)\operatorname{erfc}\left(2\sqrt{\frac{L}{r_{\rm b}}}\frac{\tilde{\mathcal{R}}_{\rm in}}{\sqrt{d_{\rm b}}}\right)}{\frac{1}{\tilde{\mathcal{R}}_{\rm in}}\left[1+\sqrt{\frac{d_{\rm b}}{\pi}}\right]+\frac{d_{\rm b}}{4\tilde{\mathcal{R}}_{\rm in}^2}\left[\exp\left(\frac{4\tilde{\mathcal{R}}_{\rm in}^2}{d_{\rm b}}\right)\operatorname{erfc}\left(\frac{2\tilde{\mathcal{R}}_{\rm in}}{\sqrt{d_{\rm b}}}\right)-1\right]}, \tag{6.13}$$

where we have introduced dimensionless rates $\tilde{\mathcal{R}}_{\rm in/out} \equiv \mathcal{R}_{\rm in/out}\tau_{\rm b}$ and used the relation $\tau_{\rm b} = d_{\rm b}/(2\gamma_{\rm EIT})$; $\gamma_{\rm EIT} \equiv \Omega^2/\Gamma$ is the single-atom EIT linewidth in terms of the control field Rabi frequency Ω and the linewidth Γ of the intermediate level. We start by examining limiting cases of Eq. (6.13): First we note that this expression agrees with the result for perfect single-polariton EIT (6.6) in the limit of infinite optical depth per blockade radius,

$$\tilde{\mathcal{R}}_{\rm out}\Big|_{d_{\rm b}\to\infty} = \frac{1}{1+1/\tilde{\mathcal{R}}_{\rm in}}, \tag{6.14}$$

as expected. Considering instead the limit of infinite input rate $\tilde{\mathcal{R}}_{\rm in}$, we find from (6.13) that

$$\tilde{\mathcal{R}}_{\rm out}\Big|_{\tilde{\mathcal{R}}_{\rm in}\to\infty} = \frac{1}{2}\sqrt{\frac{r_{\rm b}}{L}}\frac{1}{1+\sqrt{\pi/d_{\rm b}}}; \tag{6.15}$$

hence this calculation predicts a finite asymptote in the high-intensity limit. The asymptotic value equals 1/2 for $r_{\rm b} = L$ and $\sqrt{d_{\rm b}/\pi} \gg 1$. That the asymptotic value (6.15) can be finite (rather than zero) can be explained by noting that while EIT decay tends to lessen the photonic output rate, its impact on the rate is diminished by the fact that a new polariton can be formed immediately after.

6.3.3 Comparison to experiment and numerical simulation

We plot (6.13) in Fig. 6.5 where it is compared to the experimental data of Ref. [66]. In plotting (6.13) we use effective values of d_b and L from the experiment, whereas the value of τ_b is obtained by fitting to the data; this is equivalent to fitting the single-atom EIT linewidth γ_EIT since d_b is fixed. The fitted values of τ_b are about a factor of 2 within those found by using the value of γ_EIT from the experiment. In Fig. 6.5 the data is also compared to the output rate $\mathcal{R}'_\mathrm{out}$ that would arise if all multi-photon events within a time-window $\Delta t = 0.8\mu$s are converted to single-photon events, assuming that this conversion happens independently in different time windows,

$$\mathcal{R}'_\mathrm{out} = \frac{1}{\Delta t}\left(1 - e^{-\Delta t \mathcal{R}_\mathrm{in}}\right). \tag{6.16}$$

This is the theoretical curve presented in Ref. [66] alongside the transmission data. Because $\mathcal{R}'_\mathrm{out}$ includes events where photons in neighboring time windows are separated by less than Δt, this rate exceeds the hard-sphere prediction for perfect single-polariton EIT, (6.6) or (6.14), when comparing for $\Delta t = \tau_\mathrm{b}$. Note that $\Delta t = 0.8\mu$s exceeds the value of τ_b found from experimental parameters by more than an order of magnitude. While the quantum hard-sphere result (6.13) is more motivated by the physics of the system than the simpler ad-hoc formula, (6.16), the experimental data considered here is insufficient to determine the precise saturation behavior of the output rate.

Numerical simulation of the quantum many-body problem considered here is computationally unfeasible for more than a few excitations, but considering the few-photon scenario is still a valuable benchmark for our model. Hence, to check the serialization approximation for EIT filtering, as illustrated in Fig. 6.3a, we compare against numerical simulations of the full set of equations of motion. We apply EIT filtering to the density matrix to obtain $\hat{\rho} \to \hat{\rho}'$ corresponding to the full length L of the Rydberg medium (taking $L = r_\mathrm{b}$); this yields a pessimistic estimate, since the sharp temporal features removed by the filter are in general created somewhere in the interior of the medium thus reducing the effective optical depth of the EIT-filtering effect. For the comparison we consider square-pulse Fock-state input with $n_\mathrm{in} = 2$ (which is reasonably feasible numerically). The numerical simulation uses the three-level model for the atoms shown in Fig. 6.1a. The density matrix $\hat{\rho}$ predicted by the hard-sphere ansatz applied to Fock-state input is given in Appendix D.2. The results are plotted Fig. 6.5b, showing good agreement for $d_\mathrm{b} \gtrsim 10$.

6.4 Generation of regular trains of single photons

As another application of the model, we will now consider schemes for generating regular pulse trains of single photons, see Fig. 6.6. The first scheme (Fig. 6.6a) will now be analyzed in some detail. It operates with the same CW probe and control input as considered in the transmission analysis above. The blockade sets a lower limit τ_b to the temporal separation of output photons leading to anti-bunching. To achieve regularity, we must also impose an upper bound on the (average) separation. This can be ensured by a sufficiently large input rate,

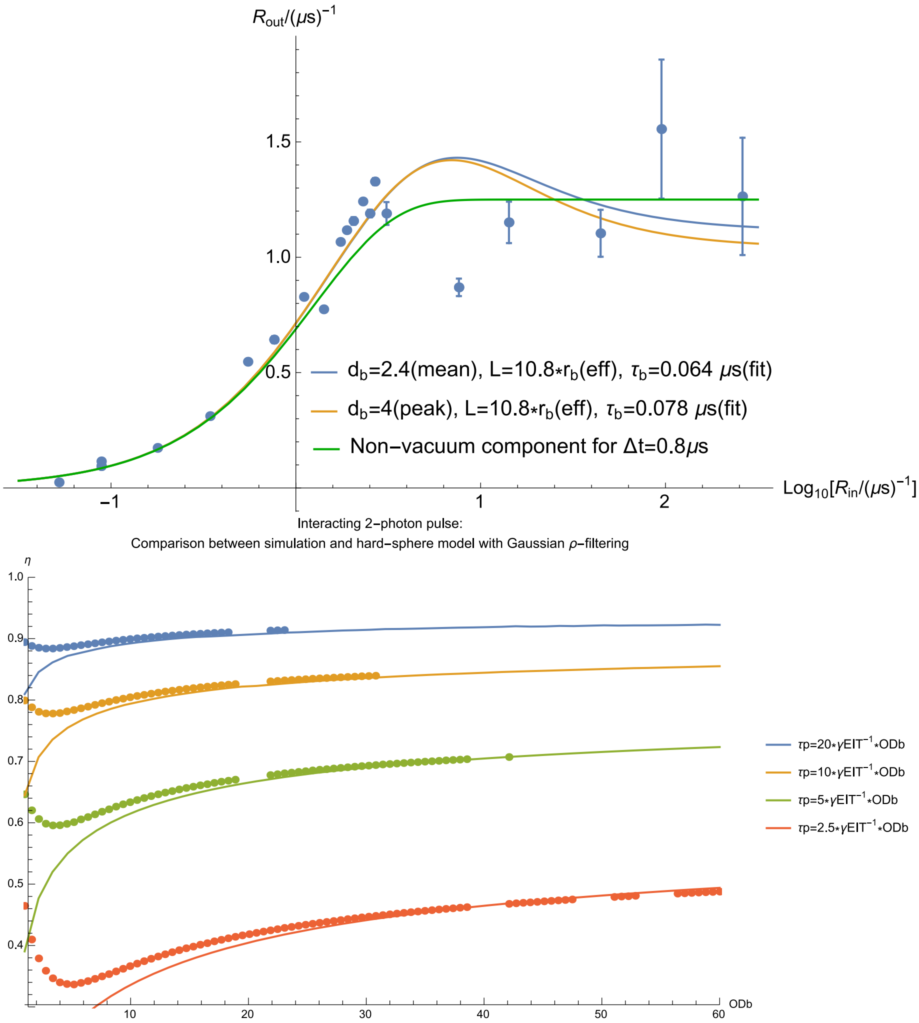

Figure 6.5: Transmission through a dissipative Rydberg-EIT medium. a) Output rate $\mathcal{R}_{\text{out}}$ as function of input rate $\mathcal{R}_{\text{in}}$. The data from Ref. [66] is compared to plots of (6.13) for two fixed values of d_{b} (blue and yellow) corresponding to mean and peak values of the Gaussian distribution in the experiment with axial spread σ_{ax}, effective length $L = 4.2 \cdot \sigma_{\text{ax}}$ and fitted values of τ_{b}. Also plotted (green curve) is the probability of having at least one photon in the time-interval $\Delta t = 0.8\mu s$, see Eq. (6.16). b) Comparison between full numerical simulation and hard-sphere ansatz with post-EIT filtering for the propagation of a two-photon square pulse through a Rydberg medium of length $L = r_{\text{b}}$. The numerical simulation was performed by Michael Gullans (JQI/NIST).

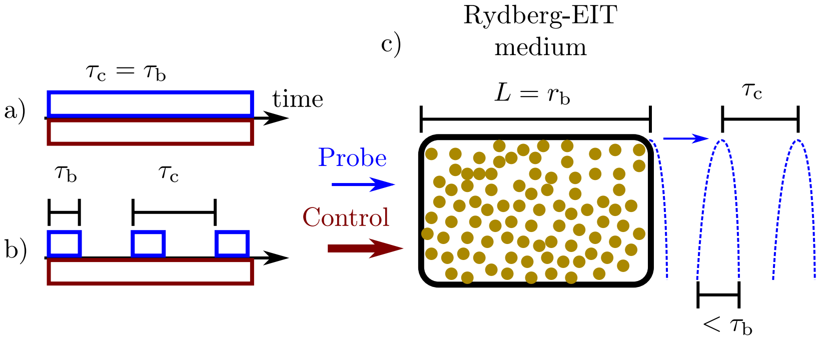

Figure 6.6: Generation of single-photon trains with period τ_c and pulse duration at most τ_b using a dissipative Rydberg-EIT medium with blockade time τ_b. a-b) Input pulse cycles for two different schemes with CW control fields. a) CW probe scheme. b) Pulsed probe scheme equivalent to repeated single-photon generation [2], see Fig. 6.2. c) 1-d Rydberg-EIT medium acting as a single-photon filter.

but only insofar as the effect of single-polariton EIT decay remains negligible (as discussed above, the average polariton EIT transmission $\bar{\eta}_{EIT}$ decreases with increasing input rate). Such a decay event will terminate the regularity of the pulse train (creating a "domain wall"), effectively resetting the process. These considerations imply that an optimum input rate exists as a trade-off between the input photons not being too far apart while keeping single-polariton EIT decay low. Moreover, to generate regular pulse trains containing an appreciable number of photons the probability of EIT decay must be small, i.e. we must be in the regime of perturbative single-polariton EIT decay. In this regime, we can meaningfully estimate the correlation functions of the outgoing light field by appropriately filtering the correlation functions of the density matrix $\hat{\rho}$ produced by the idealized R-R interaction (see Fig. 6.3a). These functions will be derived in the following using the intuition of hard-sphere projective scattering events (Fig. 6.3c&d).

6.4.1 Hard-sphere correlation functions in the limit of perfect single-polariton EIT

6.4.1.1 Diagonal elements

First we consider the ensemble-averaged intensity profile $\langle \hat{I}(\tau) \rangle_{\hat{\rho}} = \langle \hat{\mathcal{E}}^\dagger(\tau)\hat{\mathcal{E}}(\tau) \rangle_{\hat{\rho}} = G^{(1)}(\tau;\tau)$. Since it is the expectation value of an operator which is diagonal in the "classical basis", Eq. (6.4), it is indifferent to the wave nature of the polaritons and will coincide with the result of a suitably defined macroscopic analog involving, say, bowling balls. $\langle \hat{I}(t) \rangle_{\hat{\rho}}$ for square-pulse Poisson input of rate $\mathcal{R}_{in}$ can be derived inductively by propagating the initial condition that the medium is empty when the input pulse arrives at the medium at time τ_s (and using the fact that different chunks of the input pulse are uncorrelated). Let us first consider the probability density $P_1(t_1 - \tau_s)$ of the first Rydberg excitation occurring at a time $t_1 \geq \tau_s$; this is simply the product of the probability that no photons arrived during the interval $[\tau_s; t_1]$, i.e. $\exp[-\mathcal{R}_{in}(t_1 - \tau_s)]$ for the

Poisson distribution, and the arrival rate of photons $\mathcal{R}_{\text{in}}$, so that we have

$$P_1(\tau) = \theta(\tau)\mathcal{R}_{\text{in}} \exp[-r\tau]. \tag{6.17}$$

Next, let us construct the probability density $P_2(t_2 - \tau_{\text{s}})$ that the second Rydberg excitation occurs at time t_2. Note that per the hard-sphere ansatz this probability density can be non-zero only for $t_2 \geq \tau_{\text{s}} + \tau_{\text{b}}$. The *conditional* probability density of the second Rydberg occurring at t_2 conditioned on the first Rydberg arriving at t_1 is just $P_1(t_2 - t_1 - \tau_{\text{b}})$, where P_1 is given in Eq. (6.17); i.e. the first Rydberg excitation (at t_1) imposes an initial condition of an empty medium at $t_1 + \tau_{\text{b}}$ equivalent to the one at τ_{s}. The unconditional probability density $P_2(t_2 - \tau_{\text{s}})$ for the arrival of the second Rydberg at t_2 is then found by integrating the conditional density $P_1(t_2 - t_1 - \tau_{\text{b}})$ over $t_1 \in [\tau_{\text{s}}, t_2 - \tau_{\text{b}}]$ weighted by the probability density $P_1(t_1 - \tau_{\text{s}})$ we found above for t_1 (interestingly, the combined integrand is independent of t_1)

$$\begin{aligned} P_2(t_2 - \tau_{\text{s}}) &= \theta(t_2 - \tau_{\text{s}} - \tau_{\text{b}}) \int_{\tau_{\text{s}}}^{t-\tau_{\text{b}}} dt_1 P_1(t_1 - \tau_{\text{s}}) \cdot P_1(t_2 - t_1 - \tau_{\text{b}}) \\ &= \theta(t_2 - \tau_{\text{s}} - \tau_{\text{b}})\mathcal{R}_{\text{in}} \exp[-\mathcal{R}_{\text{in}}(t_2 - \tau_{\text{s}} - \tau_{\text{b}})] \cdot [\mathcal{R}_{\text{in}}(t_2 - \tau_{\text{s}} - \tau_{\text{b}})]. \end{aligned}$$

By iterating this argument we find the probability density for the arrival of the R'th Rydberg at time t_R to be given by (defining $t_0 \equiv \tau_{\text{s}} - \tau_{\text{b}}$ for convenience)

$$\begin{aligned} P_R(t_R - \tau_{\text{s}}) &= \theta(t_R - \tau_{\text{s}} - (R-1)\tau_{\text{b}}) \\ &\quad \times \mathcal{R}_{\text{in}} e^{-\mathcal{R}_{\text{in}}(t_R - \tau_{\text{s}} - (R-1)\tau_{\text{b}})} \frac{[\mathcal{R}_{\text{in}}(t_R - \tau_{\text{s}} - (R-1)\tau_{\text{b}})]^{R-1}}{(R-1)!}. \end{aligned} \tag{6.18}$$

$P_R(t_R - \tau_{\text{s}})$, Eq. (6.18), is the probability density of the creation of a polariton at time t_R conditioned on $R-1$ polaritons having been created in the preceding time interval $[\tau_{\text{s}}, t_R - \tau_{\text{b}}]$. This allows us to construct $G^{(1)}(\tau;\tau)$ simply by observing that its value at a time $\tau = t - \tau_{\text{s}}$ after the onset of the pulse only can have contributions from the first $\lceil (t-\tau_{\text{s}})/\tau_{\text{b}} \rceil$ polaritons created since τ_{s} per the hard-sphere ansatz; summing these contributions, Eq. (6.18), we find (for $t \geq \tau_{\text{s}}$)

$$\begin{aligned} G^{(1)}(t - \tau_{\text{s}}; t - \tau_{\text{s}}) &= \sum_{j=0}^{\lfloor (t-\tau_{\text{s}})/\tau_{\text{b}} \rfloor} P_j(t - \tau_{\text{s}}) \\ &= \sum_{j=0}^{\lfloor (t-\tau_{\text{s}})/\tau_{\text{b}} \rfloor} \mathcal{R}_{\text{in}} e^{-\mathcal{R}_{\text{in}}(t - \tau_{\text{s}} - j\tau_{\text{b}})} \frac{[\mathcal{R}_{\text{in}}(t - \tau_{\text{s}} - j\tau_{\text{b}})]^j}{j!}. \end{aligned} \tag{6.19}$$

We plot Eq. (6.19) in Fig. 6.7a for different combinations of the input rate $\mathcal{R}_{\text{in}}$ and the blockade time in units of pulse duration $\tau_{\text{b}}/\tau_{\text{p}}$. The width of the peaks are seen to increase with peak number while their heights decrease. This is a symptom of the decay of the initial condition of a vacant medium at τ_{s} when the pulse arrives, corresponding to the decay of photon-photon correlations in the output signal as we will return to later.

The second-order correlation function,

$$G^{(2)}(\tau_1, \tau_2; \tau_2, \tau_1) = \langle :: \hat{I}(\tau_1)\hat{I}(\tau_2) :: \rangle_{\hat{\rho}} = \langle \hat{\mathcal{E}}^\dagger(\tau_1)\hat{\mathcal{E}}^\dagger(\tau_2)\hat{\mathcal{E}}(\tau_2)\hat{\mathcal{E}}(\tau_1) \rangle_{\hat{\rho}},$$

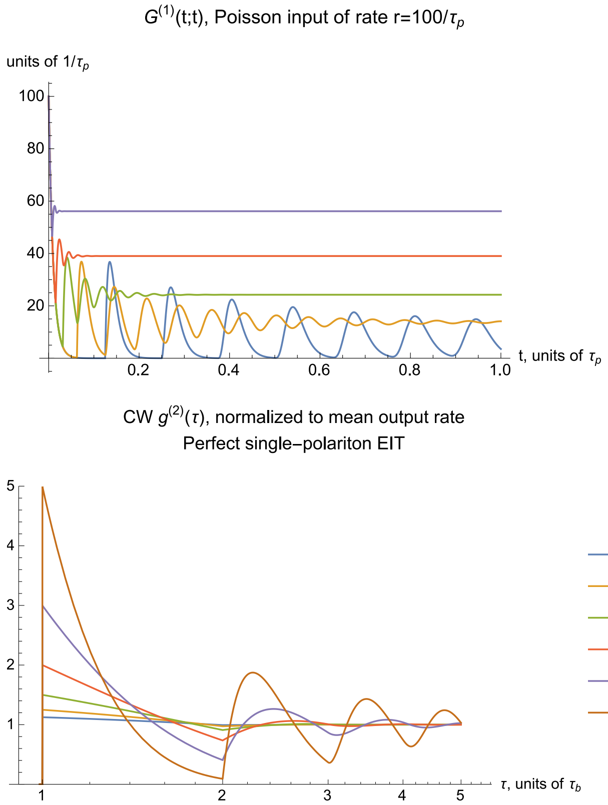

Figure 6.7: Correlation functions predicted by the hard-sphere model in the limit of perfect single-polariton EIT: a) Ensemble-averaged output intensity $\langle \hat{I}(t) \rangle \equiv G^{(1)}(t;t)$. Poisson distributed input with fixed mean number of photons $\mathcal{R}_{\rm in}\tau_{\rm p}$ for different ratios $\tau_{\rm b}/\tau_{\rm p}$. b) Steady-state 2-time correlation function $g^{(2)}_{\rm ss}(\tau)$, Eq. (6.21), exhibiting perfect anti-bunching for $|\tau| \leq \tau_{\rm b}$.

can be constructed from the diagonal elements $G^{(1)}(\tau;\tau)$ derived in Eq. (6.19) by pursuing a similar logic: As the product between the probability density of creating a polariton at time $\tau_\mathrm{s}+\min\{\tau_1,\tau_2\}$ conditioned on a vacant medium at τ_s and the probability density of creating a polariton at time $\tau_\mathrm{s}+\max\{\tau_1,\tau_2\}$ conditioned on a polariton having been created at $\tau_\mathrm{s}+\min\{\tau_1,\tau_2\}$. Importantly, the latter is independent of the event history of the time interval $[\tau_\mathrm{s};\tau_\mathrm{s}+\min\{\tau_1,\tau_2\}+\tau_\mathrm{b}]$. This is because the counting statistics of different time intervals of the CW input are uncorrelated and conditioning on having a Rydberg excitation created at $\tau_\mathrm{s}+\min\{\tau_1,\tau_2\}$ sets a boundary condition at $t'=\tau_\mathrm{s}+\min\{\tau_1,\tau_2\}+\tau_\mathrm{b}$ equivalent to the initial condition at τ_s of a vacant Rydberg medium. This argument leads to the expression:

$$\begin{aligned}G^{(2)}(\tau_1,\tau_2;\tau_2,\tau_1) &= \Theta(|\tau_2-\tau_1|-\tau_\mathrm{b})\\ &\times G^{(1)}(\min\{\tau_1,\tau_2\};\min\{\tau_1,\tau_2\})G^{(1)}(|\tau_2-\tau_1|-\tau_\mathrm{b};|\tau_2-\tau_1|-\tau_\mathrm{b}).\end{aligned} \tag{6.20}$$

The correlation functions considered thus far apply to the scenario of a square pulse arriving at the medium at time $t=0$. A more common quantity to consider in experiment is the steady-state correlation function $g^2_\mathrm{ss}(\tau)$,

$$g^{(2)}_\mathrm{ss}(\tau) \equiv \frac{\langle\hat{\mathcal{E}}^\dagger(0)\hat{\mathcal{E}}^\dagger(\tau)\hat{\mathcal{E}}(\tau)\hat{\mathcal{E}}(0)\rangle_\mathrm{ss}}{\langle\hat{\mathcal{E}}^\dagger(\tau)\hat{\mathcal{E}}(\tau)\rangle_\mathrm{ss}\langle\hat{\mathcal{E}}^\dagger(0)\hat{\mathcal{E}}(0)\rangle_\mathrm{ss}},$$

that ensues when the transients from the leading edge of the pulse and the initial condition of the medium have decayed. Taking the limit $\min\{\tau_1,\tau_2\}\to\infty$ in Eq. (6.20) and identifying the steady state mean output rate $\mathcal{R}_\mathrm{out}\equiv G^{(1)}(\tau;\tau)\big|_{\tau\to\infty}$ we find

$$g^{(2)}_\mathrm{ss}(\tau) = \Theta(\tau-\tau_\mathrm{b})\frac{G^{(1)}(\tau-\tau_\mathrm{b};\tau-\tau_\mathrm{b})}{\mathcal{R}_\mathrm{out}}, \tag{6.21}$$

which is seen to be closely related to the diagonal elements of $G^{(1)}$ (see plots in Fig. 6.7). The hard-sphere prediction for $g^2_\mathrm{ss}(\tau)$ in the perfect EIT limit, Eq. (6.21), shows perfect anti-bunching for $|\tau|\le\tau_\mathrm{b}$ as per construction.

The argument leading to Eq. (6.20) can be iterated to express the "diagonal" elements ($\tau_i=\tau_i'$) of the correlation function

$$G^{(N)}(\tau_1,\ldots,\tau_N;\tau_N',\ldots,\tau_1') \equiv \langle :: \prod_{i=1}^{N}\hat{\mathcal{E}}^\dagger(\tau_i)\hat{\mathcal{E}}(\tau_i') ::\rangle_{\hat{\rho}}$$

in terms of those of $G^{(1)}$ found in Eq. (6.19). Assuming a time-ordered set $\{\tau_1,\ldots,\tau_N\}$, Eq. (6.20) generalizes to (where $\tau_0\equiv-\tau_\mathrm{b}$ for convenience)

$$\begin{aligned}&G^{(N)}(\tau_1,\ldots,\tau_N;\tau_N,\ldots,\tau_1) =\\ &\qquad\prod_{i=1}^{N}\theta(\tau_i-\tau_{i-1}-\tau_\mathrm{b})G^{(1)}(\tau_i-\tau_{i-1}-\tau_\mathrm{b};\tau_i-\tau_{i-1}-\tau_\mathrm{b}).\end{aligned} \tag{6.22}$$

6.4.1.2 Off-diagonal elements

We now turn to the off-diagonal elements of the general first-order correlation function $G^{(1)}(\tau;\tau')=\langle\hat{\mathcal{E}}^\dagger(\tau)\hat{\mathcal{E}}(\tau')\rangle$ can be related to the diagonal elements

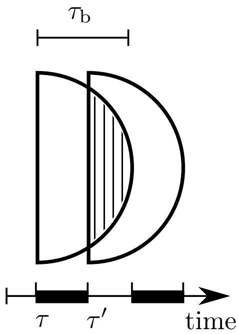

Figure 6.8: Since a polariton will only scatter photons arriving subsequent to itself, its effective blockade region is a hemisphere pointing forward in time. The overlap of effective blockade regions corresponding to polariton arrival times τ and τ' is indicated by shading. The forbidden region, during which scattering events would ruin the superposition between τ and τ', consists of the two disjoint time intervals shown as projections on the axis.

$G^{(1)}(\tau'';\tau'')$. Note that the operator $\hat{\mathcal{E}}^\dagger(\tau)\hat{\mathcal{E}}(\tau')$ is non-diagonal in the classical basis; it measures the quantum coherence between having a Rydberg excitation at different times at once (and the result differs from that of the bowling ball experiment in which $G^{(1)}(\tau;\tau') \propto \delta(\tau-\tau')G^{(1)}(\tau;\tau)$). To have such coherence, no scattering events must occur so as to determine whether the Rydberg excitation were formed at τ or τ'. We may construct $G^{(1)}(\tau;\tau')$ as the probability density for the creation of a polariton at $\min\{\tau,\tau'\}$ times the probability that no scattering events occur that allows the environment to distinguish whether the polariton was created at τ or τ'. The forbidden scattering times is the set obtained by subtracting the intersection of effective blockade regions of polaritons at τ,τ' from their union (assuming that the effective blockade region of the polariton is not truncated by the pulse ending), see Fig. 6.8. From the figure, we see that this requires that no photons impinge on the Rydberg medium for intervals of combined duration $2\min\{\tau_\mathrm{b},|\tau-\tau'|\}$. This is all the information we need for Poisson-distributed input, and therefore we find that (assuming $\tau,\tau' \leq \tau_\mathrm{p}-\tau_\mathrm{b}$, where τ_p is the pulse duration)

$$G^{(1)}(\tau;\tau') = G^{(1)}(\min\{\tau;\tau'\};\min\{\tau;\tau'\})e^{-2\mathcal{R}_\mathrm{in}\min\{\tau_\mathrm{b},|\tau-\tau'|\}}. \tag{6.23}$$

We plot Eq. (6.23) in Fig. 6.9 for two different values of $\mathcal{R}_\mathrm{in}$.

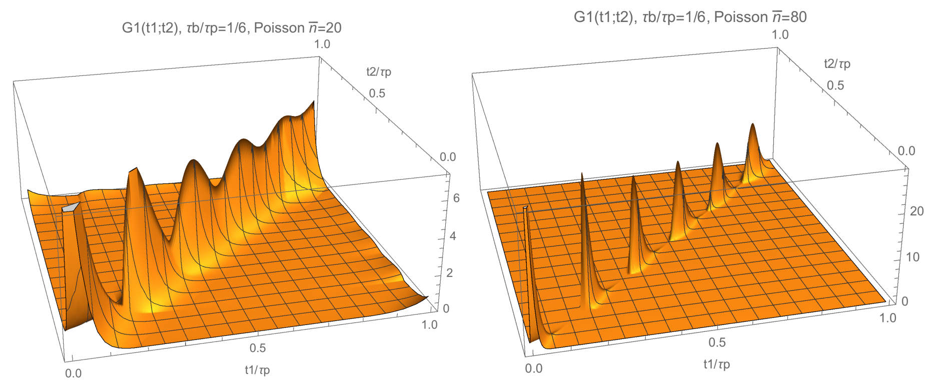

Figure 6.9: Plots of $G^{(1)}(t_1; t_2)$ according to the the hard-sphere ansatz without EIT filtering for coherent square-pulse input. The diagonal ridges are recognized as the diagonal elements of $G^{(1)}$ plotted in Fig. 6.7.

6.5 Conditions for generating pulse trains of single photons

We will now use the hard-sphere correlation functions derived above to analyze the generation of regular trains of single photons. The effect of EIT-filtering will be estimated by post-filtering of $G^{(1)}(\tau, \tau')$ in the spirit of Fig. 6.3a. We consider the experimentally relevant case of CW Poisson input characterized by mean input rate $\mathcal{R}_{\text{in}}$ impinging on a Rydberg medium with blockade time τ_{b}. We will mainly consider the signatures of regularity in $G^{(1)}$ as $G^{(N)}$ is simply related to this by Eq. (6.22).

6.5.1 Input rate requirement

To ease the analysis of $\langle \hat{I}(t-\tau_{\text{s}}) \rangle \equiv G^{(1)}(t-\tau_{\text{s}}; t-\tau_{\text{s}})$ we rewrite Eq. (6.19) as

$$\langle \hat{I}(t-\tau_{\text{s}}) \rangle = \sum_{p=0}^{\lfloor (t-\tau_{\text{s}})/\tau_{\text{b}} \rfloor} \tilde{I}_p(t-\tau_{\text{s}}), \tag{6.24}$$

in terms of the profile of the p'th peak

$$\tilde{I}_p(t-\tau_{\text{s}}) \equiv \mathcal{R}_{\text{in}} \frac{1}{p!} [\mathcal{R}_{\text{in}}(t-\tau_{\text{s}}-p\tau_{\text{b}})]^p e^{-\mathcal{R}_{\text{in}}(t-\tau_{\text{s}}-p\tau_{\text{b}})} \Theta(t-\tau_{\text{s}}-p\tau_{\text{b}}), \tag{6.25}$$

enumerating peaks as $\{0, 1, \ldots\}$. Considering the individual peak profiles $\tilde{I}_p(t-\tau_{\text{s}})$, the p'th peak is seen to be located at $t_p = \tau_{\text{s}} + p(\tau_{\text{b}} + 1/\mathcal{R}_{\text{in}})$ and hence the peak-to-peak separation is $\Delta t = \tau_{\text{b}} + \frac{1}{\mathcal{R}_{\text{in}}}$. In the high-intensity limit the peaks are well-separated and we can approximate Eq. (6.24) by

$$\langle \hat{I}(\tau \sim t_p - \tau_{\text{s}}) \rangle \approx \tilde{I}_p(\tau), \tag{6.26}$$

where $\tau \sim t_p - \tau_{\text{s}}$ means that τ is in the neighborhood of $t_p - \tau_{\text{p}}$ (or, more precisely, that p minimizes $|\tau - t_j + \tau_{\text{s}}|$). Note that each peak $\tilde{I}_p$, Eq. (6.25), has unit area. To derive a condition for well-separated peaks we consider the corrections to Eq. (6.26); from the exact Eq. (6.24) we see that these are simply the tails of the other $\tilde{I}_{p'}$:

$$\langle \hat{I}(\tau \sim t_p - \tau_\mathrm{s}) \rangle = \tilde{I}_p(\tau) + \sum_{j=0, j\neq p}^{\lfloor \tau/\tau_\mathrm{b} \rfloor} \tilde{I}_j(\tau).$$

As we shall see shortly, the width of $\tilde{I}_p(t)$ is sublinear in p ($\sim \sqrt{p}$) and hence grows slower than $t_p - \tau_\mathrm{s} \propto p$. For this reason it is sufficient to ensure that each peak $\tilde{I}_p(t)$ is well-separated from its nearest neighbors. Thus to have a well-separated crystal of $N = p + 1$ photons we must ensure that the width $(\delta t)_N$ of $\tilde{I}_N(t)$ is much less than the peak separation $\Delta t = \tau_\mathrm{b} + 1/\mathcal{R}_\mathrm{in}$. The p'th peak width (HWHM) can be approximated for $p \gg 1$ as

$$(\delta t)_p \approx \frac{\sqrt{\ln(4)p}}{\mathcal{R}_\mathrm{in}}. \tag{6.27}$$

From Eq. (6.25) we also find the p'th peak height to be,

$$\langle \hat{I}(t_p - \tau_\mathrm{s}) \rangle = \mathcal{R}_\mathrm{in} \frac{p^p}{p!} e^{-p} \approx \frac{\mathcal{R}_\mathrm{in}}{\sqrt{2\pi p}}, \tag{6.28}$$

using Sterling's approximation for $p \gg 1$. Notably, peak heights and widths are independent of τ_b.

We wish to have a parameter condition that determines whether all peaks of $\langle \hat{I}(t) \rangle_{\hat{\rho}}$ will be well-localized and regularly spaced. As discussed above that requires us to ensure that all N peaks are narrow compared to their nearest-neighbor separation. In turn, since the width grows with peak number, it suffices to consider the last peak of the crystal, i.e. make sure that the (HWHM) width of $\tilde{I}_N(\tau)$ obeys $(\delta t)_N < \tau_\mathrm{b} + 1/\mathcal{R}_\mathrm{in} \approx \tau_\mathrm{b}$ (working in the $N \gg 1$ regime we here take $N - 1 \approx N$). Demanding more specifically that $(\delta t)_N \leq \beta \tau_\mathrm{b}$ for some fraction β of the blockade time, Eq. (6.27) yields the input rate requirement

$$\mathcal{R}_\mathrm{in} \gtrsim \frac{\sqrt{\ln(4)N}}{\beta \tau_\mathrm{b}}. \tag{6.29}$$

Below we will use Eq. (6.29) with equality (rather than as a lower bound) because the detrimental effect of the finite EIT window becomes more severe with increasing r (as we will turn to shortly).

6.5.2 EIT filtering

EIT post-filtering can be carried out by filtering the ensemble-averaged quantum coherent single-Rydberg wave packet $G^{(1)}(t_1; t_2)$. Before proceeding, we take a look at some plots of $G^{(1)}(t_1; t_2)$ in Fig. 6.9. These plots appear as narrow ridges/strings of spikes along $t_1 = t_2$, decaying rapidly for $t_1 \neq t_2$ (i.e. the quantum coherence decays). Using Eq. (6.23) in the limit of well-separated peaks for which Eq. (6.26) is applicable, we define the single-Rydberg EIT transmission η_EIT in terms of the diagonal elements of the filtered $\tilde{G}^{(1)}$ (Gaussian

EIT approximation and assuming we can extend integration limits to infinity)

$$\eta_{\mathrm{EIT}} \equiv \int_{-\infty}^{\infty} d\tau \tilde{G}^{(1)}(\tau;\tau) \tag{6.30}$$

$$\tilde{G}^{(1)}(\tau;\tau) \equiv \int_{-\infty}^{\infty} d\delta \tilde{I}_p(\min\{\tau,\tau+\delta\}) e^{-2\mathcal{R}_{\mathrm{in}}\min\{\tau_{\mathrm{b}},|\delta|\}} \times \frac{1}{2\sqrt{\pi}\tau_{\mathrm{EIT}}} \exp\left(-\frac{\delta^2}{4\tau_{\mathrm{EIT}}^2}\right). \tag{6.31}$$

Eq. (6.30) can be evaluated analytically, but we restrict our attention to the limit $\tau_{\mathrm{EIT}} \ll 1/\mathcal{R}_{\mathrm{in}}, \tau_{\mathrm{b}}$ in which[2]

$$\eta_{\mathrm{EIT}} \approx 1 - \frac{4\mathcal{R}_{\mathrm{in}}\tau_{\mathrm{EIT}}}{\sqrt{\pi}} + \mathcal{O}[(\mathcal{R}_{\mathrm{in}}\tau_{\mathrm{EIT}})^2].$$

Tolerating an EIT loss fraction of at most $\epsilon = 1 - \eta_{\mathrm{EIT}}$, we are faced with an upper bound for $\mathcal{R}_{\mathrm{in}}$:

$$\epsilon \gtrsim \frac{4\mathcal{R}_{\mathrm{in}}\tau_{\mathrm{EIT}}}{\sqrt{\pi}} \Leftrightarrow \mathcal{R}_{\mathrm{in}} \lesssim \frac{\sqrt{\pi}}{4}\frac{\epsilon}{\tau_{\mathrm{EIT}}}. \tag{6.32}$$

Hence, the average crystal length allowed by the EIT filter is $N_{\mathrm{EIT}} \sim 1/\epsilon$.

6.5.3 Asymptotic scaling of the pulse-train length

We assume the optimal input rate $\check{r}$ to be the solution to $N_{\mathrm{EIT}} = N_{\mathrm{p}}$, where N_{p} is the N stemming from the peak width requirement, Eq. (6.29);

$$\check{\mathcal{R}}_{\mathrm{in}} = \sqrt[3]{\frac{\sqrt{\pi}\ln(2)}{2\tau_{\mathrm{EIT}}\beta^2\tau_{\mathrm{b}}^2}} = \sqrt[3]{2\ln(2)}\pi^{1/6}\beta^{-2/3}d_{\mathrm{b}}^{-5/6}\gamma_{\mathrm{EIT}},$$

having used $\tau_{\mathrm{b}} \equiv d_{\mathrm{b}}/(2\gamma_{\mathrm{EIT}})$ and $\tau_{\mathrm{EIT}} \equiv \sqrt{d_{\mathrm{b}}}/\gamma_{\mathrm{EIT}}$. Combining Eqs. (6.29) and (6.32) we find at $\mathcal{R}_{\mathrm{in}} = \check{\mathcal{R}}_{\mathrm{in}}$

$$N_{\max} = N_{\mathrm{EIT}} = N_{\mathrm{p}} \quad \Rightarrow \quad N_{\max} = \sqrt[3]{\frac{\pi\beta^2}{128\ln 2}d_{\mathrm{b}}}.$$

For this expression to reach $N_{\max} \gtrsim 1$ requires $d_{\mathrm{b}} \gtrsim 100$ for $\beta \approx 1/2$, whereas $N_{\max} \approx 10$ requires $d_{\mathrm{b}} \approx 10^5$. Hence we find the process of crystal generation to demand a very large optical depth per blockade radius.

Having discussed in detail the CW scheme of Fig. 6.6a, we will now consider the alternative scheme shown in Fig. 6.6b. While it retains the CW control field, it uses a pulsed input probe field (generated from a CW field by e.g. a beam chopper). The probe pulses are taken to be of duration τ_{b} so that each fits within the medium of length $L = r_{\mathrm{b}}$, i.e. the regime addressed by Ref. [2]. A main advantage of this scheme (over scheme 'a') is that a polariton EIT-decay event will only create a defect in the outgoing pulse train, whereas it will not affect the overall regularity which is ensured by that of the input

[2]The EIT loss determined here by post-filtering is found to be a factor of 2 worse than $\bar{\eta}_{\mathrm{EIT}}[r_{\mathrm{b}}]$ as given by Eq. (6.11). We ascribe this to the additional projections that can occur when a polariton leaves the first r_{b} of the medium (as opposed to entering it as in Fig. 6.3c).

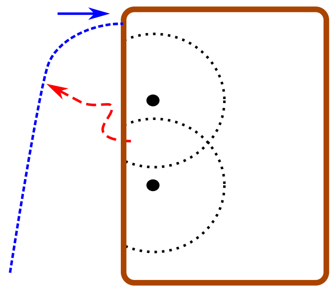

Figure 6.10: Multi-body Rydberg scattering event in a 3-d medium, where the waist of probe and control fields exceed the blockade radius, allowing polaritons to coexist "side by side".

probe field; moreover, this lessens the need for a large input rate. Hence, to assess this scheme we simply need to consider the probability of having a single output photon in a given duty cycle. In this way the asymptotic scaling of the defect probability is found to be $1 - \bar{\eta}_{\mathrm{EIT}} \propto 1/\sqrt{d_{\mathrm{b}}}$ for large d_{b} [2]. Both schemes considered here present requirements for d_{b} which are outside the reach of Rydberg media in magneto-optical traps, but which could be approached in Bose-Einstein condensates.

6.6 Conclusion and outlook

We have proposed a new model for analyzing the many-body physics of the dissipative Rydberg blockade in extended EIT media. The model accounts for the finite width of the EIT window, which is a significant effect in state-of-the-art experiments [66]. Analyzing the transmission through such systems, we found the predictions of the model to be compatible with numerical simulations and available experimental data. To further assess the model, it would be of interest to perform additional numerical simulations, like that presented in Fig. 6.5b, to explore the single- and zero-photon output manifolds starting from two-photon input. Moreover, additional experimental data for larger values of d_{b} would be of great value in establishing the precise saturation behavior of the blockade. The model was also applied to analyzing a scheme for generating pulse trains of single photons from CW input, whereby its asymptotic scaling was determined.

The results presented here lead us to conclude that the model has some merit and warrants further investigation. The model could provide valuable insight for tackling the difficult quantum many-body problem considered here so that, ideally, it could serve as the starting point for the rigorous derivation of effective many-body theories for Rydberg-EIT that go beyond the regime of validity of existing theories.

Finally, one can envision several extensions of the approach taken here: Storage and retrieval operations in Rydberg media can be modeled by translating time-varying control fields into a time-dependent blockade time τ_{b} of hard-sphere Rydberg polaritons. In 3-d Rydberg media multi-body Rydberg scattering events can take place when the blockade regions of transversely spaced polaritons overlap (see sketch in Fig. 6.10). One might also hope that the intuition gained here can somehow be extended to shed light on dispersive Rydberg interactions.

Bibliography

[1] T. Bagci, A. Simonsen, S. Schmid, L. G. Villanueva, E. Zeuthen, J. Appel, J. M. Taylor, A. Sørensen, K. Usami, A. Schliesser, and E. S. Polzik, "Optical detection of radio waves through a nanomechanical transducer," *Nature*, vol. 507, pp. 81–85, 03 2014.

[2] A. V. Gorshkov, R. Nath, and T. Pohl, "Dissipative many-body quantum optics in rydberg media," *Phys. Rev. Lett.*, vol. 110, p. 153601, Apr 2013.

[3] S. Schmid, T. Bagci, E. Zeuthen, J. M. Taylor, P. K. Herring, M. C. Cassidy, C. M. Marcus, L. Guillermo Villanueva, B. Amato, A. Boisen, Y. Cheol Shin, J. Kong, A. S. Sørensen, K. Usami, and E. S. Polzik, "Single-layer graphene on silicon nitride micromembrane resonators," *Journal of Applied Physics*, vol. 115, no. 5, pp. –, 2014.

[4] H. J. Kimble, "The quantum internet," *Nature*, vol. 453, pp. 1023–1030, 06 2008.

[5] J. Bochmann, A. Vainsencher, D. D. Awschalom, and A. N. Cleland, "Nanomechanical coupling between microwave and optical photons," *Nat Phys*, vol. 9, pp. 712–716, 11 2013.

[6] R. W. Andrews, R. W. Peterson, T. P. Purdy, K. Cicak, R. W. Simmonds, C. A. Regal, and K. W. Lehnert, "Bidirectional and efficient conversion between microwave and optical light," *Nat Phys*, vol. 10, pp. 321–326, 04 2014.

[7] M. Aspelmeyer, T. J. Kippenberg, and F. Marquardt, "Cavity optomechanics," *Rev. Mod. Phys.*, vol. 86, pp. 1391–1452, Dec 2014.

[8] M. Aspelmeyer, T. J. Kippenberg, and F. Marquardt, eds., *Cavity Optomechanics: Nano- and Micromechanical Resonators Interacting with Light*. Quantum Science and Technology, Springer-Verlag Berlin Heidelberg, 1 ed., 2014.

[9] T. Rocheleau, T. Ndukum, C. Macklin, J. B. Hertzberg, A. A. Clerk, and K. C. Schwab, "Preparation and detection of a mechanical resonator near the ground state of motion," *Nature*, vol. 463, pp. 72–75, 01 2010.

[10] J. D. Teufel, T. Donner, D. Li, J. W. Harlow, M. S. Allman, K. Cicak, A. J. Sirois, J. D. Whittaker, K. W. Lehnert, and R. W. Simmonds, "Sideband cooling of micromechanical motion to the quantum ground state," *Nature*, vol. 475, pp. 359–363, 07 2011.

[11] J. Chan, T. P. M. Alegre, A. H. Safavi-Naeini, J. T. Hill, A. Krause, S. Groblacher, M. Aspelmeyer, and O. Painter, "Laser cooling of a nanomechanical oscillator into its quantum ground state," *Nature*, vol. 478, pp. 89–92, 10 2011.

[12] E. Verhagen, S. Deleglise, S. Weis, A. Schliesser, and T. J. Kippenberg, "Quantum-coherent coupling of a mechanical oscillator to an optical cavity mode," *Nature*, vol. 482, pp. 63–67, 02 2012.

[13] T. A. Palomaki, J. W. Harlow, J. D. Teufel, R. W. Simmonds, and K. W. Lehnert, "Coherent state transfer between itinerant microwave fields and a mechanical oscillator," *Nature*, vol. 495, pp. 210–214, 03 2013.

[14] K. R. Brown, J. Britton, R. J. Epstein, J. Chiaverini, D. Leibfried, and D. J. Wineland, "Passive cooling of a micromechanical oscillator with a resonant electric circuit," *Phys. Rev. Lett.*, vol. 99, p. 137205, Sep 2007.

[15] Q. P. Unterreithmeier, E. M. Weig, and J. P. Kotthaus, "Universal transduction scheme for nanomechanical systems based on dielectric forces," *Nature*, vol. 458, pp. 1001–1004, 04 2009.

[16] A. D. O'Connell, M. Hofheinz, M. Ansmann, R. C. Bialczak, M. Lenander, E. Lucero, M. Neeley, D. Sank, H. Wang, M. Weides, J. Wenner, J. M. Martinis, and A. N. Cleland, "Quantum ground state and single-phonon control of a mechanical resonator," *Nature*, vol. 464, pp. 697–703, 04 2010.

[17] C. A. Regal and K. W. Lehnert, "From cavity electromechanics to cavity optomechanics," *Journal of Physics: Conference Series*, vol. 264, p. 012025, 2011.

[18] A. H. Safavi-Naeini and O. Painter, "Proposal for an optomechanical traveling wave phonon–photon translator," *New Journal of Physics*, vol. 13, no. 1, p. 013017, 2011.

[19] J. M. Taylor, A. S. Sørensen, C. M. Marcus, and E. S. Polzik, "Laser cooling and optical detection of excitations in a lc electrical circuit," *Phys. Rev. Lett.*, vol. 107, p. 273601, 2011.

[20] L. Tian, "Optoelectromechanical transducer: Reversible conversion between microwave and optical photons," *Annalen der Physik*, vol. 527, no. 1-2, pp. 1–14, 2015.

[21] K. Stannigel, P. Rabl, A. S. Sørensen, P. Zoller, and M. D. Lukin, "Optomechanical transducers for long-distance quantum communication," *Phys. Rev. Lett.*, vol. 105, p. 220501, Nov 2010.

[22] J. T. Hill, A. H. Safavi-Naeini, J. Chan, and O. Painter, "Coherent optical wavelength conversion via cavity optomechanics," *Nat Commun*, vol. 3, p. 1196, 11 2012.

[23] C. Dong, V. Fiore, M. C. Kuzyk, and H. Wang, "Optomechanical dark mode," *Science*, vol. 338, no. 6114, pp. 1609–1613, 2012.

[24] Y. Liu, M. Davanço, V. Aksyuk, and K. Srinivasan, "Electromagnetically induced transparency and wideband wavelength conversion in silicon nitride microdisk optomechanical resonators," *Phys. Rev. Lett.*, vol. 110, p. 223603, May 2013.

[25] M. Tsang, "Cavity quantum electro-optics," *Phys. Rev. A*, vol. 81, p. 063837, Jun 2010.

[26] L. Tian and H. Wang, "Optical wavelength conversion of quantum states with optomechanics," *Phys. Rev. A*, vol. 82, p. 053806, Nov 2010.

[27] Y.-D. Wang and A. A. Clerk, "Using interference for high fidelity quantum state transfer in optomechanics," *Phys. Rev. Lett.*, vol. 108, p. 153603, Apr 2012.

[28] L. Tian, "Adiabatic state conversion and pulse transmission in optomechanical systems," *Phys. Rev. Lett.*, vol. 108, p. 153604, Apr 2012.

[29] S. A. McGee, D. Meiser, C. A. Regal, K. W. Lehnert, and M. J. Holland, "Mechanical resonators for storage and transfer of electrical and optical quantum states," *Phys. Rev. A*, vol. 87, p. 053818, May 2013.

[30] K. Zhang, F. Bariani, Y. Dong, W. Zhang, and P. Meystre, "Optomechanical microwave sensor at the sub-photon level," *ArXiv e-prints*, Sept. 2014.

[31] S. Barzanjeh, M. Abdi, G. J. Milburn, P. Tombesi, and D. Vitali, "Reversible optical-to-microwave quantum interface," *Phys. Rev. Lett.*, vol. 109, p. 130503, Sep 2012.

[32] S. Weis, R. Rivière, S. Deléglise, E. Gavartin, O. Arcizet, A. Schliesser, and T. J. Kippenberg, "Optomechanically induced transparency," *Science*, vol. 330, no. 6010, pp. 1520–1523, 2010.

[33] A. H. Safavi-Naeini, T. P. M. Alegre, J. Chan, M. Eichenfield, M. Winger, Q. Lin, J. T. Hill, D. E. Chang, and O. Painter, "Electromagnetically induced transparency and slow light with optomechanics," *Nature*, vol. 472, pp. 69–73, 04 2011.

[34] X. Zhou, F. Hocke, A. Schliesser, A. Marx, H. Huebl, R. Gross, and T. J. Kippenberg, "Slowing, advancing and switching of microwave signals using circuit nanoelectromechanics," *Nat Phys*, vol. 9, pp. 179–184, 03 2013.

[35] A. M. Jayich, J. C. Sankey, B. M. Zwickl, C. Yang, J. D. Thompson, S. M. Girvin, A. A. Clerk, F. Marquardt, and J. G. E. Harris, "Dispersive optomechanics: a membrane inside a cavity," *New Journal of Physics*, vol. 10, p. 095008, 2008.

[36] F. Elste, S. M. Girvin, and A. A. Clerk, "Quantum noise interference and backaction cooling in cavity nanomechanics," *Phys. Rev. Lett.*, vol. 102, p. 207209, May 2009.

[37] F. Massel, S. U. Cho, J.-M. Pirkkalainen, P. J. Hakonen, T. T. Heikkilä, and M. A. Sillanpää, "Multimode circuit optomechanics near the quantum limit," *Nat Commun*, vol. 3, p. 987, 08 2012.

[38] A. Xuereb, C. Genes, and A. Dantan, "Strong coupling and long-range collective interactions in optomechanical arrays," *Phys. Rev. Lett.*, vol. 109, p. 223601, Nov 2012.

[39] A. B. Shkarin, N. E. Flowers-Jacobs, S. W. Hoch, A. D. Kashkanova, C. Deutsch, J. Reichel, and J. G. E. Harris, "Optically mediated hybridization between two mechanical modes," *Phys. Rev. Lett.*, vol. 112, p. 013602, Jan 2014.

[40] C. K. Law, "Interaction between a moving mirror and radiation pressure: A hamiltonian formulation," *Phys. Rev. A*, vol. 51, pp. 2537–2541, Mar 1995.

[41] S. H. Crandall, D. C. Karnopp, J. Edward F. Kurtz, and D. C. Pridmore-Brown, *Dynamics of mechanical and electromechanical systems.* McGraw-Hill, 1968.

[42] S. Schmid, C. Hierold, and A. Boisen, "Modeling the kelvin polarization force actuation of micro- and nanomechanical systems," *Journal of Applied Physics*, vol. 107, no. 5, p. 054510, 2010.

[43] C. M. Caves, "Quantum limits on noise in linear amplifiers," *Phys. Rev. D*, vol. 26, pp. 1817–1839, Oct 1982.

[44] Y. Tsaturyan, A. Barg, A. Simonsen, L. G. Villanueva, S. Schmid, A. Schliesser, and E. S. Polzik, "Demonstration of suppressed phonon tunneling losses in phononic bandgap shielded membrane resonators for high-q optomechanics," *Opt. Express*, vol. 22, pp. 6810–6821, Mar 2014.

[45] P.-L. Yu, K. Cicak, N. S. Kampel, Y. Tsaturyan, T. P. Purdy, R. W. Simmonds, and C. A. Regal, "A phononic bandgap shield for high-q membrane microresonators," *Applied Physics Letters*, vol. 104, no. 2, pp. –, 2014.

[46] C. W. Gardiner and P. Zoller, *Quantum Noise*, vol. 56 of *Springer series in synergetics.* Springer, second enlarged edition ed., 2000.

[47] E. Zeuthen, "Extending cavity-mechanical cooling via a hot LC electrical circuit & Framework for electromechanical coupling calculations," Master's thesis, The Niels Bohr Institute, University of Copenhagen, August 2012.

[48] C. O'Brien, N. Lauk, S. Blum, G. Morigi, and M. Fleischhauer, "Interfacing superconducting qubits and telecom photons via a rare-earth-doped crystal," *Phys. Rev. Lett.*, vol. 113, p. 063603, Aug 2014.

[49] L. A. Williamson, Y.-H. Chen, and J. J. Longdell, "Magneto-optic modulator with unit quantum efficiency," *Phys. Rev. Lett.*, vol. 113, p. 203601, Nov 2014.

[50] Y. Tabuchi, S. Ishino, A. Noguchi, T. Ishikawa, R. Yamazaki, K. Usami, and Y. Nakamura, "Coherent coupling between a ferromagnetic magnon and a superconducting qubit," *Science*, vol. 349, no. 6246, pp. 405–408, 2015.

[51] C. W. Gardiner and M. J. Collett, "Input and output in damped quantum systems: Quantum stochastic differential equations and the master equation," *Phys. Rev. A*, vol. 31, pp. 3761–3774, Jun 1985.

[52] D. L. Moehring, M. J. Madsen, K. C. Younge, J. R. N. Kohn, P. Maunz, L.-M. Duan, C. Monroe, and B. B. Blinov, "Quantum networking with photons and trapped atoms (invited)," *J. Opt. Soc. Am. B*, vol. 24, pp. 300–315, Feb 2007.

[53] L. Lin, R. Howe, and A. Pisano, "Microelectromechanical filters for signal processing," *Microelectromechanical Systems, Journal of*, vol. 7, pp. 286–294, Sep 1998.

[54] A. O'Connell and A. Cleland, *Microwave-Frequency Mechanical Resonators Operated in the Quantum Limit*, pp. 253–281. Springer Berlin Heidelberg, 2014.

[55] B. Yurke and J. S. Denker, "Quantum network theory," *Phys. Rev. A*, vol. 29, pp. 1419–1437, Mar 1984.

[56] M. H. Devoret, "Quantum fluctuations in electrical circuits," in *Quantum Fluctuations, Les Houches, Session LXIII, 1995* (S. Reynaud, E. Giacobino, and J. Zinn-Justin, eds.), Elsevier Science B.V., 1997.

[57] G. Burkard, R. H. Koch, and D. P. DiVincenzo, "Multilevel quantum description of decoherence in superconducting qubits," *Phys. Rev. B*, vol. 69, p. 064503, Feb 2004.

[58] D. M. Pozar, *Microwave Engineering.* John Wiley & Sons, Inc., 4th ed., 2012.

[59] V. Giovannetti and D. Vitali, "Phase-noise measurement in a cavity with a movable mirror undergoing quantum brownian motion," *Phys. Rev. A*, vol. 63, p. 023812, Jan 2001.

[60] A. A. Clerk, M. H. Devoret, S. M. Girvin, F. Marquardt, and R. J. Schoelkopf, "Introduction to quantum noise, measurement, and amplification," *Rev. Mod. Phys.*, vol. 82, pp. 1155–1208, Apr 2010.

[61] I. Friedler, D. Petrosyan, M. Fleischhauer, and G. Kurizki, "Long-range interactions and entanglement of slow single-photon pulses," *Phys. Rev. A*, vol. 72, p. 043803, Oct 2005.

[62] A. V. Gorshkov, J. Otterbach, M. Fleischhauer, T. Pohl, and M. D. Lukin, "Photon-photon interactions via rydberg blockade," *Phys. Rev. Lett.*, vol. 107, p. 133602, Sep 2011.

[63] M. F. Maghrebi, M. J. Gullans, P. Bienias, S. Choi, I. Martin, O. Firstenberg, M. D. Lukin, H. P. Büchler, and A. V. Gorshkov, "Coulomb bound states of strongly interacting photons," *Phys. Rev. Lett.*, vol. 115, p. 123601, Sep 2015.

[64] M. Fleischhauer, A. Imamoglu, and J. P. Marangos, "Electromagnetically induced transparency: Optics in coherent media," *Rev. Mod. Phys.*, vol. 77, pp. 633–673, Jul 2005.

[65] M. Saffman, T. G. Walker, and K. Mølmer, "Quantum information with rydberg atoms," *Rev. Mod. Phys.*, vol. 82, pp. 2313–2363, Aug 2010.

[66] T. Peyronel, O. Firstenberg, Q.-Y. Liang, S. Hofferberth, A. V. Gorshkov, T. Pohl, M. D. Lukin, and V. Vuletic, “Quantum nonlinear optics with single photons enabled by strongly interacting atoms,” *Nature*, vol. 488, pp. 57–60, 08 2012.

[67] J. D. Pritchard, D. Maxwell, A. Gauguet, K. J. Weatherill, M. P. A. Jones, and C. S. Adams, “Cooperative atom-light interaction in a blockaded rydberg ensemble,” *Phys. Rev. Lett.*, vol. 105, p. 193603, Nov 2010.

[68] S. Sevinçli, N. Henkel, C. Ates, and T. Pohl, “Nonlocal nonlinear optics in cold rydberg gases,” *Phys. Rev. Lett.*, vol. 107, p. 153001, Oct 2011.

[69] D. Petrosyan, J. Otterbach, and M. Fleischhauer, “Electromagnetically induced transparency with rydberg atoms,” *Phys. Rev. Lett.*, vol. 107, p. 213601, Nov 2011.

[70] A. V. Gorshkov, A. André, M. D. Lukin, and A. S. Sørensen, “Photon storage in λ-type optically dense atomic media. ii. free-space model,” *Phys. Rev. A*, vol. 76, p. 033805, 2007.

[71] J. W. Müller, “Some formulae for a dead-time-distorted poisson process: To andré allisy on the completion of his first half century,” *Nuclear Instruments and Methods*, vol. 117, no. 2, pp. 401 – 404, 1974.

[72] I. J. R. Aitchison and A. J. G. Hey, *Gauge Theories in Particle Physics.* Graduate Student Series in Physics, Institute of Physics Publishing, 2nd edition ed., 1989.

Appendix A

Appendix to Chapter 2

A.1 Membrane modes and their gauge masses

We will now show how the drum modes may be introduced into a Hamiltonian description of the vibrating membrane. Our starting point will be a classical Hamiltonian expressed as an area integral over the membrane, the integrand being a Hamiltonian density (see for instance Ch. 4 of Ref. [72])

$$H_{\text{mem}} = \iint_A d^2\vec{r} \left[\frac{\Pi^2(\vec{r})}{2\rho} + \frac{\rho v^2}{2} [\nabla z(\vec{r})] \cdot [\nabla z(\vec{r})] \right]; \tag{A.1}$$

here ρ is the uniform mass density (per area) and $\Pi(\vec{r}) = \rho \dot{z}(\vec{r})$ is the momentum density conjugate to the displacement $z(\vec{r})$, $\vec{r}$ being a 2-dimensional vector in the plane of the membrane. Specializing to clamped membranes, for which $z = 0$ at the boundary of A, we use the identity

$$\nabla \cdot [z \nabla z] = [\nabla z] \cdot [\nabla z] + z \nabla^2 z$$

and the divergence theorem to rewrite (A.1) in terms of the Laplacian

$$H_{\text{mem}} = \iint_A d^2\vec{r} \left[\frac{\Pi^2(\vec{r})}{2\rho} - \frac{\rho v^2}{2} z(\vec{r}) \nabla^2 z(\vec{r}) \right]$$

Assuming the shape of the membrane allows us to solve the spatial Helmholtz equation

$$(\nabla^2 + \omega_j^2/v^2) z(\vec{r}) = 0,$$

to determine a complete, countable set of orthogonal modes $\{u_j\}$ that obey the clamped boundary condition, $z = 0$; v is the speed of sound. Using this set of modes to expand the displacement and momentum density fields

$$z(\vec{r}) = \sum_j \beta_j u_j(\vec{r}), \quad \Pi(\vec{r}) = \rho \sum_j \dot{\beta}_j u_j(\vec{r}) \tag{A.2}$$

and exploiting orthogonality of the mode set,

$$\iint_A d^2\vec{r} u_j(\vec{r}) u_{j'}(\vec{r}) \propto \delta_{j,j'},$$

we find

$$H_{\text{mem}} = \sum_j \iint_A d^2\vec{r}\frac{u_j^2(\vec{r})}{A}\left[\frac{1}{2}m^*\dot{\beta}_j^2 + \frac{m^*}{2}\omega_j^2\beta_j^2\right] \tag{A.3}$$

where we have introduced the physical mass of the membrane $m^* \equiv \rho A$. In order for (A.3) to be a genuine Hamiltonian we must express it in terms of canonical position-momentum conjugate pairs representing the respective normal modes. In identifying these coordinate pairs there is a certain gauge freedom. A useful way to think of this freedom is the following: Assume for the sake of argument that only a single, given normal mode $u_j(\vec{r})$ is excited; tracking the motion of any fixed point $\vec{r}_j$ in the membrane plane as it undergoes oscillations amounts to tracking all points because they move in a perfectly correlated fashion according to the mode shape $u_j(\vec{r})$. The gauge freedom is the freedom to choose canonical coordinates $\{\beta_j, p_j\}$ so that β_j is the oscillation amplitude of the point $\vec{r}_j$ according to $u_j(\vec{r})$ as is be achieved by normalizing the modes so that $u_j(\vec{r}_j) = 1$ (there are additional choices of coordinates for which β_j does not correspond to the amplitude of any point on the membrane). In order to preserve the form of Eqs. (A.2), we note that any canonical scaling transformation $\{\beta_j, p_j\} \to \{\beta'_j = r_j\beta_j, p'_j = r_j^{-1}p_j\}$ must be accompanied by a rescaling of the normal modes $\{u_j\} \to \{u'_j = r_j^{-1}u_j\}$ and vice versa, so that e.g.,

$$z(\vec{r}) = \sum_j \beta_j u_j(\vec{r}) = \sum_j \beta'_j u'_j(\vec{r}). \tag{A.4}$$

The gauge freedom described above amounts to choosing the gauge mass m_j of the normal mode described by $\{\beta_j, p_j\}$. Demanding the form invariance (A.4) and choosing gauge masses $\{m_j\}$ we find that (A.3) only takes the canonical form of a sum of harmonic oscillator Hamiltonians in the position-momentum pairs $(\beta_j, p_j = m_j\dot{\beta}_j)$

$$H_{\text{mem}} = \sum_j \left[\frac{p_j^2}{2m_j} + \frac{1}{2}m_j\omega_j^2\beta_j^2\right], \tag{A.5}$$

by demanding the normal mode normalization

$$\iint_A d^2\vec{r}\frac{u_j^2(\vec{r})}{A} = \frac{m_j}{m_*}. \tag{A.6}$$

Conversely, for a set of modes normalized so that $\{u_j(\vec{r}_j) = 1\}$, Eq. (A.6) determines the gauge masses $\{m_j\}$ that must be chosen. For two gauge choices $\{m_j\}$ and $\{m'_j\}$, the position coordinates $\{\beta_j\}$ and $\{\beta'_j\}$ are related as

$$\sqrt{m_j}\beta_j = \sqrt{m'_j}\beta'_j. \tag{A.7}$$

Appendix B

Appendices to Chapter 3

B.1 Fourier transform convention

We will use the following convention for the Fourier decomposition of bosonic annihilation and creation operators (in the "lab frame")

$$\hat{a}(t) \equiv \frac{1}{\sqrt{2\pi}} \int_0^\infty d\omega \hat{a}(\omega) e^{-i\omega t}; \; \hat{a}^\dagger(t) \equiv \frac{1}{\sqrt{2\pi}} \int_0^\infty d\omega \hat{a}^\dagger(\omega) e^{+i\omega t}, \tag{B.1}$$

where $[\hat{a}(\omega)]^\dagger = \hat{a}^\dagger(\omega)$; i.e. Eqs. (B.1) are the positive- and negative-frequency parts of the Hermitian operator $\hat{a}(t) + \hat{a}^\dagger(t)$. In the presence of a drive field (of frequency $\omega_{\mathrm{d},i}$) applied to the mode $\hat{a}$ we will rather be interested in the Fourier decomposition of the rotating frame variables $e^{i\omega_{\mathrm{d},i}t}\hat{a}(t)$ and $e^{-i\omega_{\mathrm{d},i}t}\hat{a}^\dagger(t)$; considering the first of these, we find from Eq. (B.1)

$$\begin{aligned} e^{i\omega_{\mathrm{d},i}t}\hat{a}(t) &= \frac{1}{\sqrt{2\pi}} \int_0^\infty d\omega \hat{a}(\omega) e^{-i(\omega - \omega_{\mathrm{d},i})t} \\ &= \frac{1}{\sqrt{2\pi}} \int_{-\omega_{\mathrm{d},i}}^\infty d\Omega \hat{a}(\Omega + \omega_{\mathrm{d},i}) e^{-i\Omega t} = \frac{1}{\sqrt{2\pi}} \int_{-\omega_{\mathrm{d},i}}^\infty d\Omega \hat{\hat{a}}(\Omega) e^{-i\Omega t} \end{aligned} \tag{B.2}$$

where we have introduced the rotating frame frequency $\Omega \equiv \omega - \omega_{\mathrm{d},i}$ and made the notational shift $\hat{\hat{a}}(\Omega) \equiv \delta\hat{a}(\Omega + \omega_{\mathrm{d},i})$ (the signals of interest will be assumed to lie within a narrow bandwidth of the carrier for which $|\Omega| \ll \omega_{\mathrm{d},i}$). We read off the rotating frame Fourier transform from Eq. (B.2)

$$\mathcal{F}_{t\to\Omega}\{e^{i\omega_{\mathrm{d},i}t}\hat{a}(t)\} = \hat{\hat{a}}(\Omega). \tag{B.3}$$

In parallel to Eq. (B.2) we find for the Hermitian conjugate,

$$e^{-i\omega_{\mathrm{d},i}t}\hat{a}^\dagger(t) = \frac{1}{\sqrt{2\pi}} \int_{-\omega_{\mathrm{d},i}}^\infty d\Omega \hat{a}^\dagger(\Omega + \omega_{\mathrm{d},i}) e^{i\Omega t} = \frac{1}{\sqrt{2\pi}} \int_{-\omega_{\mathrm{d},i}}^\infty d\Omega \hat{\hat{a}}^\dagger(\Omega) e^{i\Omega t},$$

from which we read off

$$\mathcal{F}_{t\to\Omega}\{e^{-i\omega_{\mathrm{d},i}t}\hat{a}^\dagger(t)\} = \hat{\hat{a}}^\dagger(-\Omega). \tag{B.4}$$

B.2 Homodyne measurement and noise quadratures

Combining Eqs. (3.6) and (3.13) from the main text we find that the Fourier transformed heterodyne current has the following signal and noise components ($\Omega > 0$)

$$\hat{I}(\Omega)/|\alpha_{\mathrm{LO}}| = t_{\mathrm{s},\theta_{\mathrm{LO}}}(\Omega)\hat{a}_{\mathrm{in,s}}(\Omega) + \hat{\mathcal{N}}_{\theta_{\mathrm{LO}}}(\Omega)$$

where

$$t_{\mathrm{s},\theta_{\mathrm{LO}}}(\Omega) \equiv e^{-i\theta_{\mathrm{LO}}}U_{\mathrm{s}}(\Omega) + e^{i\theta_{\mathrm{LO}}}V_{\mathrm{s}}^{*}(-\Omega) \tag{B.5}$$

$$\hat{\mathcal{N}}_{\theta_{\mathrm{LO}}}(\Omega) \equiv e^{-i\theta_{\mathrm{LO}}}\hat{\mathcal{F}}(\Omega) + e^{i\theta_{\mathrm{LO}}}\hat{\mathcal{F}}^{\dagger}(-\Omega). \tag{B.6}$$

Integrating the photocurrent with a variable phase ϕ, we see that both input quadratures are contained in $\hat{I}(\Omega)$ obtained for a fixed value of θ_{LO}

$$\begin{aligned}\hat{Z}_{\phi,\theta_{\mathrm{LO}}}(\Omega) \equiv \frac{1}{|\alpha_{\mathrm{LO}}|}\int \hat{I}(t)\cos(\omega t+\phi)dt &= \frac{e^{i\phi}\hat{I}(\Omega)+e^{-i\phi}\hat{I}^{\dagger}(\Omega)}{2|\alpha_{\mathrm{LO}}|}\\ &= \frac{1}{\sqrt{2}}\left[|t_{\mathrm{s},\theta_{\mathrm{LO}}}(\Omega)|\hat{X}_{\mathrm{s},-(\psi+\phi)}(\Omega) + \hat{Y}_{\mathrm{n}}(\Omega)\right]\end{aligned} \tag{B.7}$$

where we have introduced the phase $\psi \equiv \mathrm{Arg}[t_{\mathrm{s},\theta_{\mathrm{LO}}}(\Omega)]$ of the quadrature transfer function (B.6) for the single-mode input signal quadratures

$$\hat{X}_{\mathrm{s},\varphi}(\Omega) \equiv \frac{e^{-i\varphi}\hat{a}_{\mathrm{in,s}}(\Omega) + e^{i\varphi}\hat{a}^{\dagger}_{\mathrm{in,s}}(\Omega)}{\sqrt{2}}, \tag{B.8}$$

obeying the canonical commutation relations $[\hat{X}_{\varphi}(\Omega), \hat{X}_{\varphi+i\pi/2}(\Omega')] = i\delta(\Omega-\Omega')$; the added quadrature noise in Eq. (B.7) is accounted for by the Hermitian operator

$$\hat{Y}_{\mathrm{n}}(\Omega) \equiv \frac{e^{i\phi}\hat{\mathcal{N}}_{\theta_{\mathrm{LO}}}(\Omega) + e^{-i\phi}\hat{\mathcal{N}}^{\dagger}_{\theta_{\mathrm{LO}}}(\Omega)}{\sqrt{2}}, \tag{B.9}$$

where $\hat{\mathcal{N}}_{\theta_{\mathrm{LO}}}$ was defined in Eq. (B.6).

B.3 Cauchy-Schwarz upper bound for heterodyne sensitivity

This section uses the optical homodyne quadratures defined in Appendix B.2 above. Referencing Eq. (B.7) to the input signal, we define the heterodyne sensitivity as the variance

$$\begin{aligned}P(\Omega)\delta(\Omega-\Omega') &\equiv \left\langle \left(\hat{X}_{\mathrm{s},-(\psi+\phi)}(\Omega) + \frac{\hat{Y}_{\mathrm{n}}(\Omega)}{|t_{\mathrm{s},\theta_{\mathrm{LO}}}(\Omega)|}\right)\left(\hat{X}_{\mathrm{s},-(\psi+\phi)}(\Omega') + \frac{\hat{Y}_{\mathrm{n}}(\Omega')}{|t_{\mathrm{s},\theta_{\mathrm{LO}}}(\Omega')|}\right)\right\rangle_{\mathrm{vac,s}}\\ &= \frac{1}{2}\delta(\Omega-\Omega') + \frac{\langle \hat{Y}_{\mathrm{n}}(\Omega)\hat{Y}_{\mathrm{n}}(\Omega')\rangle}{|t_{\mathrm{s},\theta_{\mathrm{LO}}}(\Omega)|^{2}},\end{aligned} \tag{B.10}$$

where we take the input on the signal port to be vacuum uncorrelated with the noise inputs. To evaluate $\langle \hat{Y}_\mathrm{n}(\Omega)\hat{Y}_\mathrm{n}(\Omega')\rangle$ we will make use of the property that the noise associated with $\hat{\mathcal{F}}$ is time-stationary, i.e.

$$\begin{aligned}\langle \hat{\mathcal{F}}^\dagger(\Omega)\hat{\mathcal{F}}(\Omega')\rangle \propto \delta(\Omega-\Omega'),\ \langle \hat{\mathcal{F}}(\Omega)\hat{\mathcal{F}}^\dagger(\Omega')\rangle \propto \delta(\Omega-\Omega')\\ \langle \hat{\mathcal{F}}(\Omega)\hat{\mathcal{F}}(\Omega')\rangle \propto \delta(\Omega+\Omega'),\ \langle \hat{\mathcal{F}}^\dagger(\Omega)\hat{\mathcal{F}}^\dagger(\Omega')\rangle \propto \delta(\Omega+\Omega'),\end{aligned} \tag{B.11}$$

as follows from the assumed form of $\hat{\mathcal{F}}$, (3.7) given in the main text, combined with the thermal expectation values of the input operators $\hat{a}_{\mathrm{in},i}(\Omega)$. From Eq. (3.7) of the main text we find in this way that

$$\begin{aligned}\langle \hat{Y}_\mathrm{n}(\Omega)\hat{Y}_\mathrm{n}(\Omega')\rangle &= \frac{1}{2}\left[\langle \hat{\mathcal{N}}_{\theta_\mathrm{LO}}(\Omega)\hat{\mathcal{N}}^\dagger_{\theta_\mathrm{LO}}(\Omega')\rangle + \langle \hat{\mathcal{N}}^\dagger_{\theta_\mathrm{LO}}(\Omega)\hat{\mathcal{N}}_{\theta_\mathrm{LO}}(\Omega')\rangle\right]\\ &= \left|\begin{pmatrix}\vec{u}^{(+)}\\ \vec{v}^{(+)}\end{pmatrix}\right|^2 + \left|\begin{pmatrix}\vec{v}^{(-)}\\ \vec{u}^{(-)}\end{pmatrix}\right|^2 + 2\mathrm{Re}\left[e^{-2i\theta_\mathrm{LO}}\left\langle \begin{pmatrix}\vec{u}^{(+)}\\ \vec{v}^{(+)}\end{pmatrix}^*, \begin{pmatrix}\vec{v}^{(-)}\\ \vec{u}^{(-)}\end{pmatrix}\right\rangle\right]\end{aligned} \tag{B.12}$$

where $\langle\cdot,\cdot\rangle$ denotes the inner product between vectors in $\mathbb{C}^n$ and we have defined the vectors

$$[\vec{u}^{(\pm)}]_i \equiv U_i(\pm\Omega)\sqrt{n_i(\pm\Omega+\omega_{\mathrm{d},i})+1/2},\quad [\vec{v}^{(\pm)}]_i \equiv V_i(\pm\Omega)\sqrt{n_i(\mp\Omega+\omega_{\mathrm{d},i})+1/2}.$$

As a side remark, we note that $P(\Omega)$ as given by Eq. (B.10) coincides with the definition given in the main text as can be seen using the first equality in (B.12) and the commutator $[\hat{\mathcal{N}}_{\theta_\mathrm{LO}}(\Omega), \hat{\mathcal{N}}^\dagger_{\theta_\mathrm{LO}}(\Omega')] = -|t_{\mathrm{s},\theta_\mathrm{LO}}(\Omega)|^2\delta(\Omega-\Omega')$. The Cauchy-Schwarz inequality on $\mathbb{C}^n$ implies that

$$\left|\left\langle \begin{pmatrix}\vec{u}^{(+)}\\ \vec{v}^{(+)}\end{pmatrix}^*, \begin{pmatrix}\vec{v}^{(-)}\\ \vec{u}^{(-)}\end{pmatrix}\right\rangle\right| \le \left|\begin{pmatrix}\vec{u}^{(+)}\\ \vec{v}^{(+)}\end{pmatrix}\right|\cdot\left|\begin{pmatrix}\vec{v}^{(-)}\\ \vec{u}^{(-)}\end{pmatrix}\right|, \tag{B.13}$$

which leads us to an upper bound of (B.12)

$$\langle \hat{Y}_\mathrm{n}(\Omega)\hat{Y}_\mathrm{n}(\Omega')\rangle \le \left(\left|\begin{pmatrix}\vec{u}^{(+)}\\ \vec{v}^{(+)}\end{pmatrix}\right| + \left|\begin{pmatrix}\vec{v}^{(-)}\\ \vec{u}^{(-)}\end{pmatrix}\right|\right)^2. \tag{B.14}$$

Note that $(\Omega,\Omega'>0)$

$$\begin{aligned}\left|\begin{pmatrix}\vec{u}^{(\pm)}\\ \vec{v}^{(\pm)}\end{pmatrix}\right|^2\delta(\Omega-\Omega') &= \frac{\langle \hat{\mathcal{F}}^\dagger(\pm\Omega)\hat{\mathcal{F}}(\pm\Omega')\rangle + \langle \hat{\mathcal{F}}(\pm\Omega)\hat{\mathcal{F}}^\dagger(\pm\Omega')\rangle}{2}\\ &= \left[\eta(\pm\Omega)N(\pm\Omega) + \frac{1\mp\eta(\pm\Omega)}{2}\right]\delta(\Omega-\Omega')\end{aligned} \tag{B.15}$$

since from the bosonic commutation relations and (3.6) we have (for $\Omega,\Omega'>0$)

$$[\hat{a}_{\mathrm{out,e}}(\pm\Omega), \hat{a}^\dagger_{\mathrm{out,e}}(\pm\Omega')] = \delta(\Omega-\Omega') \Rightarrow [\hat{\mathcal{F}}(\pm\Omega)\hat{\mathcal{F}}^\dagger(\pm\Omega')] = [1\mp\eta(\pm\Omega)]\delta(\Omega-\Omega').$$

Combining (B.10) with (B.14) and (B.15) we arrive at the upper bound for P_s, given as Eq. (3.16) in the main text.

B.4 Conditional entanglement generation

One of the highly desired protocols for quantum communication is entanglement generation between distant atom-like systems conditioned on one or more clicks in photo-counting detectors [52]. The schemes discussed here are related to their more familiar quantum optical analogs by the replacement of actual atoms by artificial ones such as superconducting qubits with typical transition frequencies in the microwave domain. This is of particular interest for (entanglement-based) quantum repeaters, which may allow for the realization of a long-ranging quantum internet based on an optical fiber infrastructure. To achieve this based on super-conducting systems, transduction between microwave and optical frequencies is required.

The entanglement schemes involve the emission of single photons from the (artificial) atoms which need to be transduced to optical frequencies for fiber transmission (see Fig. B.1). The transduction efficiency for a single signal quantum is given by

$$\eta = \eta_h \int_0^{\Delta T} |h_{\text{out}}(t)|^2 dt \tag{B.16}$$

with η_h defined as in the main text. For simplicity, we will perform the analysis assuming $|V_i(\Omega)| \approx 0$, so that the transducers act as beam splitters. In the end we will take the limit $\eta \ll 1$ where it is very unlikely that a single incoming signal quantum generates more than one quantum at the exit port. In this limit the expressions remain valid even in the presence of the amplification noise resulting from $|V_i(\Omega)| > 0$. The inevitable transduction of noise photons amounts to an additional equivalent dark count probability P_d related to the noise rate r_N defined in the main text; here we shall take this to be the only source of dark counts for simplicity. Moreover, we assume unit detection efficiency. To simplify the analysis we make the assumptions that the noise photons are distinguishable and hence do not bunch upon combination on the beamsplitter; this amounts to assuming that $1/\Delta T$ is much smaller than the bandwidth. From this assumption it follows that each transducer contributes an average dark count rate of $r_\text{N}\Delta T/2$ in each detector, whereby the probability for at least one dark count in a particular detector is $P_\text{d} = 1 - (e^{-r_\text{N}\Delta T/2})^2 = 1 - e^{-r_\text{N}\Delta T} \approx r_\text{N}\Delta T$ for $r_\text{N}\Delta T \ll 1$.

The basic idea of the schemes to be considered here is to symmetrically excite the artificial atoms into a state of the form

$$(\sqrt{1-P_\text{e}}|0\rangle_{\text{A},1}|0\rangle_{\text{P},1}+\sqrt{P_\text{e}}|1\rangle_{\text{A},1}|1\rangle_{\text{P},1})\otimes(\sqrt{1-P_\text{e}}|0\rangle_{\text{A},2}|0\rangle_{\text{P},2}+\sqrt{P_\text{e}}|1\rangle_{\text{A},2}|1\rangle_{\text{P},2}), \tag{B.17}$$

where $|n\rangle_{\text{A},i}$ denotes the atomic state of atom i and $|n\rangle_{\text{P},i}$ the photonic Fock states corresponding to the emitted light from atom i. The photonic states are transduced by individual electro-optomechanical transducers and mixed in a mode-matched fashion at a 50:50 beamsplitter, thereby withholding the which-way information from the subsequent photodetection measurement (see Fig. B.1). Hence, in absence of imperfections, if a single click is obtained the atomic system is projected into an entangled state of either atom being in its $|1\rangle_{\text{A},i}$ state (while we would like to condition on exactly one click in a single detector, photon number resolution is typically not achievable in practice):

$$|\Psi_\pm\rangle = \frac{1}{\sqrt{2}}(|0\rangle_{\text{A},1}|1\rangle_{\text{A},2} \pm |1\rangle_{\text{A},1}|0\rangle_{\text{A},2}), \tag{B.18}$$

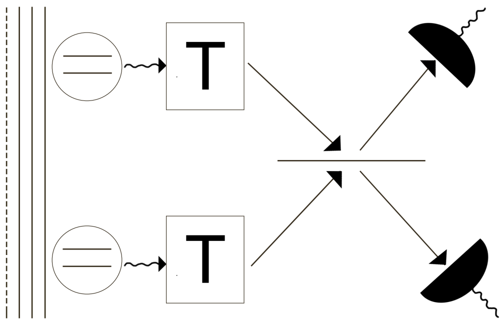

Figure B.1: Sketch of the setup for conditional remote entanglement generation between microwave qubits via optics. The two qubits are symmetrically and coherently excited by a control pulse. The microwave radiation resulting from subsequent decay is transduced into the optical domain and interfered on a symmetric beam splitter and the output is measured by photodetection. A click in one of the detectors is an indication that the single-click scheme has succeeded. Subsequently applying a symmetric π-pulse to the qubits and conditioning on a second click in a two-click scheme decreases the sensitivity to transduced noise photons.

with the sign determined by which detector clicks. The two-click scheme adds a subsequent π-pulse along with the condition of an additional click; this serves to verify that the atomic systems are in the state (B.18). This added step mitigates the effect of dark counts, imperfect transduction $\eta < 1$ and atomic double excitations, hence allowing $P_\mathrm{e} = 1/2$.

We now calculate the conditional fidelities F_{ic}, $i \in \{1, 2\}$ for Bell-state generation by means of these single-click and two-click variants (illustrated in Fig. B.1). This conditional fidelity is defined as the average overlap between the generated and desired states given that the relevant click condition was fulfilled. Upon fulfillment of the condition, the system is described by a certain density matrix $\hat{\rho}_{ic}$. Starting with the single-click condition, we will now determine the conditional fidelity of achieving either of the states $|\Psi_\pm\rangle$. This may be calculated by imagining that if we obtain $|\Psi_-\rangle$, we rotate it into $|\Psi_+\rangle$; denoting the corresponding rotated density matrix $\hat{\rho}'_{ic}$, the desired conditional fidelity is given by:

$$F_{i\mathrm{c}} = \mathrm{Tr}[\hat{\rho}'_{ic}|\Psi_+\rangle\langle\Psi_+|]. \tag{B.19}$$

By considering the various possible outcomes compatible with fulfillment of the condition in the limit $P_\mathrm{d}/\eta \ll P_\mathrm{e} \ll 1$ and $\eta \ll 1$, we arrive at (using the abbreviated notation $|i\rangle_{A,1}|j\rangle_{A,2} \equiv |ij\rangle$)

$$\begin{aligned}\hat{\rho}'_{1c} = \frac{1}{\mathcal{N}_1}\Bigg[& \overbrace{(1-P_e)^2 2P_d(1-P_d)|00\rangle\langle 00|}^{\text{Neither emits, dark count in one arm}} \\ & + \overbrace{2P_e(1-P_e)\eta(1-P_d)|\Psi_+\rangle\langle\Psi_+|}^{\text{One atom emits and is detected, no dark count in other arm}} \\ & + \overbrace{P_e(1-P_e)(1-\eta)2P_d(1-P_d)[|01\rangle\langle 01| + |10\rangle\langle 10|]}^{\text{One emits but is not detected, dark count in one arm}} \\ & + \overbrace{P_e^2([1-(1-\eta)^2] + (1-\eta)^2 2P_d)(1-P_d)|11\rangle\langle 11|}^{\text{Both emit, if detected no dark count in other arm}}\Bigg], \end{aligned} \tag{B.20}$$

where $\mathcal{N}_1$ is the appropriate normalization factor ensuring that $\mathrm{Tr}[\hat{\rho}'_{1c}] = 1$. Using Eqs. (B.18) and (B.20) to evaluate the conditional fidelity (B.19), we find

$$F_{1c} = \frac{2P_e(1-P_e)\eta + P_e(1-P_e)(1-\eta)2P_d}{P_e\eta(1-2P_d)[2-P_e\eta] + 2P_d}. \tag{B.21}$$

expanding Eq. (B.21) in the limit $P_e, P_d \ll 1$, $P_d \ll P_e$ it reduces to

$$F_{1c} \approx 1 - P_e(1-\eta/2) - \frac{P_d}{\eta P_e} \tag{B.22}$$

The choice of P_e that maximizes F_{1c} as given by (B.22) is

$$P_e^{(\mathrm{opt})} = \sqrt{\frac{P_d}{\eta(1-\eta/2)}}$$

yielding the fidelity

$$F_{1c}^{(\mathrm{opt})} = 1 - 2\sqrt{\left(\frac{1}{\eta} - \frac{1}{2}\right)P_d} \approx 1 - 2\sqrt{\left(\frac{1}{\eta} - \frac{1}{2}\right)\eta_0^{(+)} N_0^{(+)} B\Delta T}. \tag{B.23}$$

Next, we consider the two-click scheme. The scheme works in two steps and we will take as our condition that at least one click in exactly one arm occurs in each of the two steps. In the first step the two atoms are excited symmetrically to the state (B.17) with $P_e = 1/2$ (which maximizes the fidelity), preferably only one of the atoms emit a photon. In the next step, a π-pulse is applied symmetrically to the two atoms such that an atom in the $|0\rangle_A$ state is transferred to $|1\rangle_A$ while emitting a photon; meanwhile, an atom in the $|1\rangle_A$ state is left unchanged by the pulse. In the absence of dark counts and for perfect transduction, $P_d = 0$, $\eta = 1$, fulfillment of the two-click condition that either of the states entangled atomic states $|\Psi_\pm\rangle$, Eq. (B.18), have been generated with unit conditional fidelity (whether the first click occurs in detector one or two reveals which of the two states where generated). For finite dark count probability P_d, the conditional fidelity drops below 1 according to an expression to be determined shortly. Fulfillment of the two-click condition corresponds to the density matrix (rotating $|\Psi_-\rangle$ into $|\Psi_+\rangle$ for purposes of calculating F_{2c},

$\hat{\rho}_{2\mathrm{c}} \rightarrow \hat{\rho}'_{2\mathrm{c}})$

$$\hat{\rho}'_{2\mathrm{c}} = \frac{1}{\mathcal{N}_2}\left[(1-P_\mathrm{e})^2 2P_\mathrm{d}(1-P_\mathrm{d})\left([1-(1-\eta)^2](1-P_\mathrm{d}) + (1-\eta)^2 2P_\mathrm{d}(1-P_\mathrm{d})\right)|00\rangle\langle 00|\right.$$
$$+P_\mathrm{e}(1-P_\mathrm{e})\left[(\eta(1-P_\mathrm{d}) + (1-\eta)2P_\mathrm{d}(1-P_\mathrm{d}))^2 - \eta^2(1-P_\mathrm{d})^2\right][|01\rangle\langle 01| + |10\rangle\langle 10|]$$
$$\left. 2P_\mathrm{e}(1-P_\mathrm{e})\eta^2(1-P_\mathrm{d})^2|\Psi_+\rangle\langle\Psi_+| + P_\mathrm{e}^2\left((1-\eta)^2 2P_\mathrm{d} + (1-(1-\eta)^2)\right)2P_\mathrm{d}(1-P_\mathrm{d})^2|11\rangle\langle 11|\right].$$

From this the conditional fidelity for entanglement generation in the two-photon scheme is, from Eq. (B.19), (evaluating at the optimum excitation probability $P_\mathrm{e} = 1/2$)

$$F_{2\mathrm{c}}^{(\mathrm{opt})} = \frac{2P_\mathrm{d}^2(1-\eta)^2 + 2P_\mathrm{d}(1-\eta)\eta + \eta^2}{8P_\mathrm{d}^2(1-\eta)^2 + 2P_\mathrm{d}(4-3\eta)\eta + \eta^2}. \tag{B.24}$$

Juxtaposing the single-click and two-click schemes, we find in the limit $P_\mathrm{d}, P_\mathrm{d}/\eta \ll 1, \eta_0^{(+)} N_0^{(+)} B\Delta T \ll 1$ that

$$\begin{aligned} F_{1\mathrm{c}} &\approx 1 - 2\sqrt{\left(\frac{1}{\eta} - \frac{1}{2}\right)\eta_0^{(+)} N_0^{(+)} B\Delta T} \\ F_{2\mathrm{c}} &\approx 1 - \left(\frac{6}{\eta} - 4\right)\eta_0^{(+)} N_0^{(+)} B\Delta T. \end{aligned} \tag{B.25}$$

From these expressions, Eqs. (B.25), we see that the dependence of the fidelities on the efficiency η is rather weak in both cases: It serves to determine a prefactor to $N_0^{(+)}$ varying by at most a factor of 2 for $F_{1\mathrm{c}}$ and at most a factor of 3 for $F_{2\mathrm{c}}$, where we have set $\eta = \eta_0^{(+)}$ to focus on the $N_0^{(+)}$ dependence (other values would not change the main conclusions). This reflects that the conditional fidelity is determined by the probability to detect the good transduced photons relative to the noise photons, which is exactly determined by the added noise $N_0^{(+)}$. The expressions for $F_{i\mathrm{c}}$ given as (3.20) in the main text follow from (B.25) by taking the low-efficiency limit $\eta = \eta_0^{(+)} \rightarrow 0$. From the expressions (B.25) it is clear that the two-photon scheme has a smaller sensitivity to added noise than the one-photon scheme in the interesting regime $N_0^{(+)} B\Delta T \ll 1$. On the other hand the two-photon scheme will have a lower success probability if the transducer has a low efficiency since it requires the detection of two photons. If we are only interested in the quality of the produced entanglement $N_0^{(+)}$ is the important quantity to consider. As opposed to the situation for heterodyne detection, where a single mode was measured, there is, however, an additional factor coming from the fact the photo-detectors are not mode selective. Since efficient transduction requires $B\Delta T > 1$ this factor puts an additional requirement on the the added noise for photo-detection schemes compared to the continuous-variable schemes. On the other hand, photo-detection schemes can give useful output even with limited efficiency.

Appendix C

Appendices to Chapter 5

C.1 From serial to parallel resistance

The ohmic resistance R_L of the inductor L naturally appears in series with the latter. For the case of a parallel RLC, it is convenient to approximate the serial connection of R_L and L by a parallel connection of effective circuit elements $R_{L,\text{eff}}$ and L'. Assuming that we are only interested in a narrow band of frequencies $\delta\omega$ around the signal carrier ω_s, $|\delta\omega|/\omega_\text{s} \ll 1$, we find by Taylor expansion of the small quantity $1/Q_L \equiv R_L/(\omega_\text{s}L) \ll 1$ that

$$\begin{aligned}\frac{1}{-i\omega L + R_L} &= \frac{1}{-i\omega L}\frac{1}{1+\frac{R_L/L}{-i\omega}} \\ &\approx \frac{1}{-i\omega L}\left[1 - \frac{R_L/L}{-i\omega} + \left(\frac{R_L/L}{-i\omega}\right)^2\right] \approx \frac{1}{-i\omega L}\left[1 - \frac{1}{Q_L^2}\right] + \frac{R_L}{\omega_\text{s}^2 L^2},\end{aligned}$$

from which we can read off $L' = L(1 - 1/Q_L^2)^{-1}$ and $R_{L,\text{eff}} = \omega_\text{s}^2 L^2/R_L = R_L Q_L^2$. This makes clear that the resonance of the parallel RLC (in absence of electromechanical coupling)

$$\left[\frac{1}{-i\omega L + R_L} - i\omega\bar{C}_\text{c}\right]^{-1} \approx \left[\frac{1}{-i\omega L'} - i\omega\bar{C}_\text{c} + \frac{1}{R_{L,\text{eff}}}\right]^{-1}$$

occurs at the frequency $\omega_\text{LC} = (L'\bar{C}_\text{c})^{-1/2}$ within the stated approximations.

C.2 Homodyne measurement

C.2.1 Photo-current, $\hat{I}(\Omega)$

Homo- or heterodyne measurement of a signal requires mixing the relatively weak output signal of the transducer, as given by its scattering relation (3.6), with a large coherent-state LO $\alpha_\text{LO} = |\alpha_\text{LO}|e^{i\theta_\text{LO}}$, where the phase θ_LO will determine which quadrature is being measured. The mixing serves to down-convert the optical signal by the LO frequency ω_LO, whereby the sidebands will contribute to the photo-current at frequencies $\sim \omega_\pm - \omega_\text{LO}$; therefore it is convenient to work with field operators in a rotating frame wrt. ω_LO. Denoting the output fluctuation signal for the exit port $\hat{a}_{\mathrm{out,e}}$, the annihilation operator $\hat{a}_{\mathrm{h}}$ for the field impinging on the photodetector of the heterodyne interferometer is (in a rotating frame wrt. ω_{LO}) $\hat{a}_{\mathrm{h}}(t) = \alpha_{\mathrm{LO}} + \hat{a}_{\mathrm{out,e}}(t)$, the associated photocurrent being represented by the operator $\hat{I}(t) \equiv \hat{a}_{\mathrm{h}}^{\dagger}(t)\hat{a}_{\mathrm{h}}(t)$. Ignoring the DC contribution from the LO alone, $|\alpha_{\mathrm{LO}}|^2$, this leads to the following expression for the frequency components of the photo-current,

$$\hat{I}(\Omega) \approx \alpha_{\mathrm{LO}}^{*}\hat{a}_{\mathrm{out,e}}(\Omega) + \alpha_{\mathrm{LO}}\hat{a}_{\mathrm{out,e}}^{\dagger}(-\Omega), \tag{C.1}$$

where $\hat{a}_{\mathrm{out,e}}(\Omega)$ is in a rotating frame wrt. ω_{LO}. Eq. (C.1) shows that the photocurrent spectral component $\hat{I}(\Omega)$ has contributions from the optical signal at the two absolute frequencies $\omega_{\mathrm{LO}} \pm \Omega$ as illustrated in Figs. 3.2. In particular, this allows for the two-sideband homodyning scheme depicted in Fig. 3.2c) where a linear combination of the red and the blue optical sidebands at $\omega_{\pm}$ is measured. Importantly, as is clear from Eq. (C.1), the LO phase $\theta_{\mathrm{LO}} = \mathrm{Arg}[\alpha_{\mathrm{LO}}]$ will determine the relative phase with which the sidebands enter the linear combination. The LO amplitude $|\alpha_{\mathrm{LO}}|$, on the other hand, is in principle immaterial as long as it dominates other contributions at ω_{LO}.

C.2.2 Sideband interference and noise contributions

This section relies on the definitions of the homodyne quadratures given in Appendix B.2. Using the thermal expectation values for $\hat{\mathcal{F}}$, Eqs. (B.11), we find via the definitions (B.9,B.6) that the added noise $\hat{Y}_{\mathrm{n}}(\Omega)$ is phase-insensitive wrt. the integration phase ϕ while it does in general depend on the relative phase with which the output sidebands are combined as can be tuned via θ_{LO} (for $\Omega, \Omega' > 0$)

$$\begin{aligned}
\langle \hat{Y}_{\mathrm{n}}(\Omega)\hat{Y}_{\mathrm{n}}(\Omega')\rangle &= \frac{1}{2}\left[\langle \hat{\mathcal{N}}_{\theta_{\mathrm{LO}}}(\Omega)\hat{\mathcal{N}}_{\theta_{\mathrm{LO}}}^{\dagger}(\Omega')\rangle + \langle \hat{\mathcal{N}}_{\theta_{\mathrm{LO}}}^{\dagger}(\Omega)\hat{\mathcal{N}}_{\theta_{\mathrm{LO}}}(\Omega')\rangle\right] &\text{(C.2)}\\
&= \frac{\langle \hat{\mathcal{F}}^{\dagger}(\Omega)\hat{\mathcal{F}}(\Omega')\rangle + \langle \hat{\mathcal{F}}(\Omega)\hat{\mathcal{F}}^{\dagger}(\Omega')\rangle}{2} &\text{(C.3)}\\
&\quad + \frac{\langle \hat{\mathcal{F}}^{\dagger}(-\Omega)\hat{\mathcal{F}}(-\Omega')\rangle + \langle \hat{\mathcal{F}}(-\Omega)\hat{\mathcal{F}}^{\dagger}(-\Omega')\rangle}{2} &\text{(C.4)}\\
&\quad + \mathrm{Re}\left[e^{-2i\theta_{\mathrm{LO}}}\left(\langle \hat{\mathcal{F}}(\Omega)\hat{\mathcal{F}}(-\Omega')\rangle + \langle \hat{\mathcal{F}}(-\Omega)\hat{\mathcal{F}}(\Omega')\rangle\right)\right] &\text{(C.5)}
\end{aligned}$$

The first two terms of Eq. (C.3) correspond to the symmetrized noise of the upper and lower optical sidebands while the third represents their interference. Rather than evaluating $\langle \hat{Y}_{\mathrm{n}}(\Omega)\hat{Y}_{\mathrm{n}}(\Omega')\rangle$ using (C.3), we make use of the reduced equivalent circuit to rewrite the homodyne photocurrent, (5.33). By means of the effective OM input-output relations (4.91,4.92) we have (in mechanical units)

$$\hat{I}(\Omega)/|\alpha_{\mathrm{LO}}| = g(\theta_{\mathrm{LO}})\delta\hat{x}(\Omega) + e^{-i\theta_{\mathrm{LO}}}\hat{a}_{\mathrm{in}}^{(\mathrm{eff})}(\omega_{\mathrm{l}} + \Omega) + e^{i\theta_{\mathrm{LO}}}\hat{a}_{\mathrm{in}}^{(\mathrm{eff})\dagger}(\omega_{\mathrm{l}} - \Omega),$$
$$g(\theta_{\mathrm{LO}}) \equiv -i\frac{2g_{\mathrm{OM}}}{\sqrt{\kappa}}\frac{\sqrt{\eta_{\mathrm{opt}}}}{x_{\mathrm{ZPF}}}\left[e^{-i(\theta_{\mathrm{LO}}-\theta_{+})}\mathcal{L}_{+} - e^{i(\theta_{\mathrm{LO}}-\theta_{-})}\mathcal{L}_{-}\right],$$

where $\theta_{\pm} \equiv \mathrm{Arg}[\mathcal{L}(\pm\Omega_{\mathrm{m}})]$. Considering the mechanical response to the mechanical $\hat{F}_{\mathrm{m}}$, Johnson $\hat{F}_{\mathrm{e}}$ and optical $\hat{F}_{\mathrm{o}}$ back-action forces, where the $\hat{F}_i \equiv 2\bar{C}_{\mathrm{c}}G\hat{V}_i$

are given by Eqs. (4.10) and (5.19-5.21), as well as the transmission line signal

$$\delta\hat{x}(\Omega) = \chi_{\mathrm{m,eff}}(\Omega)[\hat{F}_{\mathrm{m}}(\Omega) + \hat{F}_{\mathrm{e}}(\Omega) + \hat{F}_{\mathrm{o}}(\Omega) - \frac{\hbar}{x_{\mathrm{ZPF}}}\sqrt{\eta_{\mathrm{el}}\gamma_{\mathrm{EM},+}}\hat{b}_{\mathrm{in}}^{(\mathrm{tx})}(\omega_{\mathrm{d}} + \Omega)],$$
$$\chi_{\mathrm{m,eff}}^{-1}(\Omega) = m\left[\Omega_{\mathrm{m}}^2 - \Omega^2 - i(\gamma_{\mathrm{m},0} + \Gamma_{\mathrm{EM}} + \Gamma_{\mathrm{OM}})\Omega\right]$$

where $\chi_{\mathrm{m,eff}}(\Omega)$ is the effective mechanical susceptibility corresponding to the damped oscillator of Fig. 5.1c, we can separate the noise contributions to $\hat{I}(\Omega)$ and properly reference them to the input

$$\hat{I}(\Omega)/|\alpha_{\mathrm{LO}}| = -\frac{\hbar}{x_{\mathrm{ZPF}}}\sqrt{\eta_{\mathrm{el}}\gamma_{\mathrm{EM},+}}g(\theta_{\mathrm{LO}})\chi_{\mathrm{m,eff}}(\Omega)\Bigg[\hat{b}_{\mathrm{in}}^{(\mathrm{tx})}(\omega_{\mathrm{d}} + \Omega)$$
$$+\frac{1}{-\frac{\hbar}{x_{\mathrm{ZPF}}}\sqrt{\eta_{\mathrm{el}}\gamma_{\mathrm{EM},+}}}\left(\hat{F}_{\mathrm{m}}(\Omega) + \hat{F}_{\mathrm{e}}(\Omega) + \hat{F}_{\mathrm{o}}(\Omega) + \frac{e^{-i\theta_{\mathrm{LO}}}\hat{a}_{\mathrm{in}}^{(\mathrm{eff})}(\omega_{\mathrm{l}} + \Omega) + e^{i\theta_{\mathrm{LO}}}\hat{a}_{\mathrm{in}}^{(\mathrm{eff})\dagger}(\omega_{\mathrm{l}} - \Omega)}{g(\theta_{\mathrm{LO}})\chi_{\mathrm{m,eff}}(\Omega)}\right)\Bigg]$$

Comparing to Eq. (5.33) we see that $t_{\mathrm{s},\theta_{\mathrm{LO}}}(\Omega) = -\frac{\hbar}{x_{\mathrm{ZPF}}}\sqrt{\eta_{\mathrm{el}}\gamma_{\mathrm{EM},+}}g(\theta_{\mathrm{LO}})\chi_{\mathrm{m,eff}}(\Omega)$ and identify the optical component $\hat{\mathcal{N}}_{\theta_{\mathrm{LO}}}^{(\mathrm{o})}(\Omega)$ of the noise operator $\hat{\mathcal{N}}_{\theta_{\mathrm{LO}}}(\Omega) = \sum_i \hat{\mathcal{N}}_{\theta_{\mathrm{LO}}}^{(i)}(\Omega)$, (B.6),

$$\hat{\mathcal{N}}_{\theta_{\mathrm{LO}}}^{(\mathrm{o})}(\Omega) = -\frac{t_{\mathrm{s},\theta_{\mathrm{LO}}}(\Omega)}{\frac{\hbar}{x_{\mathrm{ZPF}}}\sqrt{\eta_{\mathrm{el}}\gamma_{\mathrm{EM},+}}}\left(\hat{F}_{\mathrm{o}}(\Omega) + \frac{e^{-i\theta_{\mathrm{LO}}}\hat{a}_{\mathrm{in}}^{(\mathrm{eff})}(\omega_{\mathrm{l}} + \Omega) + e^{i\theta_{\mathrm{LO}}}\hat{a}_{\mathrm{in}}^{(\mathrm{eff})\dagger}(\omega_{\mathrm{l}} - \Omega)}{g(\theta_{\mathrm{LO}})\chi_{\mathrm{m,eff}}(\Omega)}\right), \tag{C.6}$$

as well as the electrical and mechanical components,

$$\hat{\mathcal{N}}_{\theta_{\mathrm{LO}}}^{(\mathrm{e})}(\Omega) = -\frac{t_{\mathrm{s},\theta_{\mathrm{LO}}}(\Omega)}{\frac{\hbar}{x_{\mathrm{ZPF}}}\sqrt{\eta_{\mathrm{el}}\gamma_{\mathrm{EM},+}}}\hat{F}_{\mathrm{e}}(\Omega) \tag{C.7}$$

$$\hat{\mathcal{N}}_{\theta_{\mathrm{LO}}}^{(\mathrm{m})}(\Omega) = -\frac{t_{\mathrm{s},\theta_{\mathrm{LO}}}(\Omega)}{\frac{\hbar}{x_{\mathrm{ZPF}}}\sqrt{\eta_{\mathrm{el}}\gamma_{\mathrm{EM},+}}}\hat{F}_{\mathrm{m}}(\Omega). \tag{C.8}$$

Note that the noise operators (C.6,C.7,C.8) are mutually uncorrelated.

Appendix D

Appendices to Chapter 6

D.1 Linear EIT transmission for a square pulse

We estimate the averaged quantities $\bar{\eta}_{\mathrm{EIT}}$ and $\bar{\tau}'_{\mathrm{b}}$ by applying Gaussian filtering to a square pulse. We introduce the EIT transmission of a square pulse of duration τ through a medium of length l

$$\begin{aligned}\eta_{\mathrm{EIT}}(\tau,l) \equiv &\int_{-\infty}^{\infty} dT \int_{-\infty}^{\infty} dt_1 \int_{-\infty}^{\infty} dt_2 \frac{1}{2\pi\tau_{\mathrm{EIT}}^2(l)} e^{-\frac{(t_1-T)^2}{2\tau_{\mathrm{EIT}}^2(l)}} e^{-\frac{(t_2-T)^2}{2\tau_{\mathrm{EIT}}^2(l)}} \\ &\times \frac{1}{\tau}\left[\Theta(t_1)\Theta(\tau-t_1)\Theta(t_2)\Theta(\tau-t_2)\right] \\ &= \mathrm{erf}\left[\frac{\tau}{2\tau_{\mathrm{EIT}}(l)}\right] + \frac{2}{\sqrt{\pi}}\frac{\tau_{\mathrm{EIT}}(l)}{\tau}\left(-1+\exp\left[-\frac{\tau^2}{4\tau_{\mathrm{EIT}}^2(l)}\right]\right), \quad \text{(D.1)}\end{aligned}$$

in terms of the length-dependent EIT time parameter

$$\tau_{\mathrm{EIT}}(l) \equiv \frac{\sqrt{(l/r_{\mathrm{b}})d_{\mathrm{b}}}}{\gamma_{\mathrm{EIT}}} \quad \text{(D.2)}$$

where $\gamma_{\mathrm{EIT}} \equiv \Omega^2/\Gamma$ is the single-atom EIT linewidth in terms of the control field Rabi frequency Ω and the linewidth Γ of the intermediate level. Taking the pulse length to be defined by the first Rydberg-Rydberg scattering event, we average $\eta_{\mathrm{EIT}}(\tau,l)$ over the corresponding Poisson distribution

$$\begin{aligned}\bar{\eta}_{\mathrm{EIT}}[l] = \langle \eta_{\mathrm{EIT}}(\tau,l)\rangle_\tau = &\int_0^{\infty} d\tau \mathcal{R}_{\mathrm{in}}(\mathcal{R}_{\mathrm{in}}\tau)e^{-\mathcal{R}_{\mathrm{in}}\tau}\eta_{\mathrm{EIT}}(\tau,l) \\ &= \exp\left([\mathcal{R}_{\mathrm{in}}\tau_{\mathrm{EIT}}(l)]^2\right)\mathrm{erfc}\left(\mathcal{R}_{\mathrm{in}}\tau_{\mathrm{EIT}}(l)\right), \quad \text{(D.3)}\end{aligned}$$

which we will use to evaluate $\bar{\eta}_{\mathrm{EIT}}[L]$ and $\bar{\eta}_{\mathrm{EIT}}[r_{\mathrm{b}}]$ that appeared above.

Next, to determine $\bar{\tau}_{\mathrm{b}}$ we need to average over both the position l at which the polariton dies and the temporal polariton extent τ. We perform the first averaging using the assumption that the probability density for polariton decay can be found from Eq. (D.1) as $-d\eta_{\rm EIT}(\tau,l)/dl$

$$\begin{aligned}\bar{\tau}_{\rm b} &= \langle\int_0^\infty dl\,\min\{l/v_{\rm g},\tau_{\rm b}\}\left[-\frac{d\eta_{\rm EIT}(\tau,l)}{dl}\right]\rangle_\tau \\ &= \langle\tau_{\rm b}\eta_{\rm EIT}(\tau,r_{\rm b})+\int_0^{r_{\rm b}} dl\frac{l}{v_{\rm g}}\left[-\frac{d\eta_{\rm EIT}(\tau,l)}{dl}\right]\rangle_\tau \qquad \text{(D.4)} \\ &= \tau_{\rm b}\bar{\eta}_{\rm EIT}[r_{\rm b}]+\langle\int_0^{r_{\rm b}} dl\frac{l}{v_{\rm g}}\left[-\frac{d\eta_{\rm EIT}(\tau,l)}{dl}\right]\rangle_\tau, \qquad \text{(D.5)}\end{aligned}$$

where we have used (D.3) and where we recognize the decomposition (6.9), so that the second term in (D.5) is $\bar{\tau}'_{\rm b}$. We determine this quantity using (D.1) and the same distribution for τ as in (D.3)

$$\begin{aligned}&\bar{\tau}'_{\rm b} = \langle\int_0^{r_{\rm b}} dl\frac{l}{v_{\rm g}}\left[-\frac{d\eta_{\rm EIT}(\tau,l)}{dl}\right]\rangle_\tau \\ &= \tau_{\rm b}\left(\frac{\gamma_{\rm EIT}}{\mathcal{R}_{\rm in}\sqrt{d_{\rm b}}}\left(\frac{2}{\sqrt{\pi}}-\frac{\gamma_{\rm EIT}}{\mathcal{R}_{\rm in}\sqrt{d_{\rm b}}}\right)+\exp\left(\frac{\mathcal{R}_{\rm in}^2 d_{\rm b}}{\gamma_{\rm EIT}^2}\right)\operatorname{erfc}\left(\frac{\mathcal{R}_{\rm in}\sqrt{d_{\rm b}}}{\gamma_{\rm EIT}}\right)\left[\frac{\gamma_{\rm EIT}^2}{\mathcal{R}_{\rm in}^2 d_{\rm b}}-1\right]\right).\end{aligned} \qquad \text{(D.6)}$$

We note that $\bar{\tau}'_{\rm b}/\tau_{\rm b}$ and $\bar{\tau}_{\rm b}/\tau_{\rm b}$, (D.6) and (D.5), only depend on the dimensionless parameter $\mathcal{R}_{\rm in}\sqrt{d_{\rm b}}/\gamma_{\rm EIT}=\mathcal{R}_{\rm in}\tau_{\rm EIT}(r_{\rm b})$. The results (D.3) and (D.6) were used to arrive at the result for $\tilde{\mathcal{R}}_{\rm out}$, Eq. (6.13), in the main text.

D.2 Hard-sphere density matrix for two-photon input

According to the hard-sphere ansatz, the density matrix when the entire pulse has entered the medium is (assuming that $h(t)=0$ for $t<0$ and $t>\tau_{\rm end}$ and that $\tau_{\rm end}\geq\tau_{\rm b}$)

$$\begin{aligned}\hat{\rho}(t) &= \overbrace{2\int_0^{\tau_{\rm end}} d\tau_1\int_{\max\{\tau_1-\tau_{\rm b},0\}}^{\tau_1} dt_1 h^2(\tau_1)h^2(t_1)|\tilde{\psi}_{\tau_1}(t)\rangle\langle\tilde{\psi}_{\tau_1}(t)|}^{\text{one scattering event}} \\ &\quad \overbrace{+2\int_0^{\tau_{\rm end}-\tau_{\rm b}} dt_1\int_{t_1+\tau_{\rm b}}^{\tau_{\rm end}} dt_2 h^2(t_1)h^2(t_2)|\tilde{\psi}_\emptyset(t)\rangle\langle\tilde{\psi}_\emptyset(t)|}^{\text{no scattering event, }\emptyset},\end{aligned}$$

where the normalized wave functions are

$$|\tilde{\psi}_{\tau_1}(t)\rangle = \frac{-\sqrt{v_{\rm g}}}{\sqrt{\int_{\max\{\tau_1-r_{\rm b}/v_{\rm g},0\}}^{\tau_1} dt'_1 h^2(t'_1)}}\int_{\max\{\tau_1-r_{\rm b}/v_{\rm g},0\}}^{\tau_1} dt_1 h(t_1)\hat{S}^\dagger[v_{\rm g}(t-t_1)]|0\rangle$$

$$\begin{aligned}|\tilde{\psi}_\emptyset(t)\rangle &= \frac{v_{\rm g}}{\sqrt{\int_0^{\tau_{\rm end}-r_{\rm b}/v_{\rm g}} dt'_1\int_{t'_1+r_{\rm b}/v_{\rm g}}^{\tau_{\rm end}} dt'_2 h^2(t'_1)h^2(t'_2)}} \\ &\times\int_0^{\tau_{\rm end}-r_{\rm b}/v_{\rm g}} dt_1\int_{t_1+r_{\rm b}/v_{\rm g}}^{\tau_{\rm end}} dt_2 h(t_1)h(t_2)\hat{S}^\dagger[v_{\rm g}(t-t_1)]\hat{S}^\dagger[v_{\rm g}(t-t_2)]|0\rangle.\end{aligned}$$